Development of charged particle detection systems for materials analysis with rapid ion beams : large solid angle detectors and numerical nuclear pulse processing

Víctor Alarcón Díez

▶ **To cite this version:**

Víctor Alarcón Díez. Development of charged particle detection systems for materials analysis with rapid ion beams : large solid angle detectors and numerical nuclear pulse processing. Physics [physics]. Université Pierre et Marie Curie - Paris VI, 2016. English. NNT : 2016PA066489 . tel-01512657

HAL Id: tel-01512657

https://theses.hal.science/tel-01512657v1

Submitted on 24 Apr 2017

HAL is a multi-disciplinary open access archive for the deposit and dissemination of scientific research documents, whether they are published or not. The documents may come from teaching and research institutions in France or abroad, or from public or private research centers.

L'archive ouverte pluridisciplinaire **HAL**, est destinée au dépôt et à la diffusion de documents scientifiques de niveau recherche, publiés ou non, émanant des établissements d'enseignement et de recherche français ou étrangers, des laboratoires publics ou privés.

Université Pierre et Marie Curie

Ecole doctorale Physique et Chimie des Matériaux – ED 397

Institute de NanoScience de Paris - UMR7586

Couches nanométriques : formation, interfaces et défauts

Development of Charged Particle Detection Systems for Materials Analysis With Rapid Ion Beams

Large solid angle detectors and numerical nuclear pulse processing

Par Víctor Alarcón Díez

Thèse de doctorat de Physique

Dirigée par Ian C. Vickridge

Présentée et soutenue publiquement le 14-12-2016

Devant un jury composé de :

Dr. DOEBELI, Max	Chercheur, ETH Zurich	Rapporteur
Dr. ZUCCHIATTI, Alessandro	Professeur, UAM	Rapporteur
Dr. ALQUIE, Georges	Professeur emerite, UPMC	Examinateur
Dr. KHODJA, Hicham	Chercheur, CEA	Examinateur
Dr. MONCOFFRE, Nathalie	Chercheur, CNRS	Examinatrice
Dr. VICKRIDGE, Ian	Chercheur, CNRS	Directeur de thèse

Except where otherwise noted, this work is licensed under
http://creativecommons.org/licenses/by-nc-nd/3.0/

Development of Charged Particle Detection Systems for Materials Analysis With Rapid Ion Beams[1]

Large solid angle detectors and numerical nuclear pulse processing

Développent de système de détection de particules pour analyse de matériaux avec faisceau d'ions

Détecteur de grande angle solide et traitement numérique des impulsions nucléaires

Par Víctor Alarcón Díez

[1] This thesis has been supported by Marie Curie Actions – Initial Training Networks (ITN) within the project Supporting Postgraduate Research with Internships in Industry and Training Excellence (SPRITE) under EC contract No. 317169.

“El mundo es como aparece ante mis cinco sentidos, y ante los tuyos que son las orillas de los míos”

— Miguel Hernández —

Glossary

AB	Atomic Bremsstrahlung
ADC	Analogue to Digital Converter
BCP	Bathocuproine
BI	Bayesian Inference
CCE	Charge Collection Efficiency
DBP	tetraphenyldibenzoperiflanthene
DDA	Digital Data Acquisition
DPP-PHA	Digital Pulse Processing – Pulse Height Analysis
EBS	Elastic Backscattering Spectrometry
EHP	Electron Hole Pair
ERDA	Elastic Recoil Detection Analysis
EXAFS	Extended Xray Absorption Fine Structure
FPGA	Field Programmable Gate Array
FWHM	Full Width at Half Maximum
GR	Guard Ring
HOMO	Highest Occupied Molecular Orbital
IBA	Ion Beam Analysis
IBIC	Ion Beam Induced Chargfe
ITO	Indium Tin Oxide
LUMO	Lowest Unoccupied Molecular Orbital
MBE	Molecular Beam Epîtaxy
MEIS	Medium Energy Ion Scattering
NDF	Nuno's Data Furnace
NIM	Nuclear Instrumentation Module
NRA	Nuclear Reaction Analysis
NRP	Narrow Resonance Profiling
OPV	Organic PhotoVoltaic
PCB	Printed Circuit Board
PHD	Pulse Height Defect
PIGE	Particle-Induced Gamma Emission
PIPS	Passivated Implanted Planar Silicon

PIXE	Particle-Induced X-ray Emission
QFEB	Quasi Free Electron Bremsstrahlung
QL	Quintuple Layer
QSH	Quantum Spin Hall effect
RBS	Rutherford Backscattering Spectrometry
SAFIR	Système d'Analyse par Faisceaux d'Ions Rapides
SEB	Secondary Electron Brehmsstrahlung
SegDet	Segmented Detector
SIMS	Secondary Ion Mass Spectrometry
SA	Simulated Annealing
TFU	Thin Film Unit (10^{15} cm^{-2})
TI	Topological Insulator
TMO	Transition Metal Oxide
TR	Time Reversal
TSS	Topological Surface State
WF	Work Function
XRF	X-ray Fluorescence

Contents

Abstract 3

Résumé 4

Resumen 16

Acknowledgements 17

1. Introduction 19

1.1 Ion beam Analysis (IBA) Techniques 20

1.1.1 Rutherford Backscattering Spectroscopy (RBS) 22

1.1.2 Channelling 28

1.1.2.1 Surface peak 29

1.1.2.2 Beyond the surface peak 33

1.1.3 Particle Induce X-ray Emission (PIXE) 37

1.1.4 Nuclear Reaction Analysis (NRA) 39

1.1.5 Ion Beam Induction Charge (IBIC) 41

1.2 Topological Insulators (TI) 43

1.3 Organic Semiconductor Devices 46

2. Charged Particle Detection 48

2.1 Semiconductor Detectors 48

2.1.1 Single Detector 49

2.1.2 Segmented Detector 52

2.1.2.1 Charge Collection Efficiency: Publication I 55

2.1.2.2 Segmented Detector first results 68

2.1.3 Annular Detector 72

2.2 Signal Acquisition and Treatment 76

2.2.1 Preamplifier 77

2.2.2 Data Acquisition: from analogue to digital 78

2.2.2.1 Analogue system 78

2.2.2.2 Digital system 80

2.2.2.3 Acquisition System comparison 83

3. IBA in Topological Insulators 86

3.1 Motivation 86

3.2 Samples and Experimental Setup 87
3.3 Results: Publication II 89
3.4 Results: Non-published 95
3.4.1 Composition quantification: NDF Fitting 95
3.4.2 Channelling 98
3.4.3 Segmented Detector in TI 101
3.4.3.1 Channelling with SegDet 103
3.5 Conclusions and perspectives concerning TI 104
4. MoO_x and Organic Semiconductors Devices 107
4.1 Motivation 107
4.2 Samples and Experimental Setup 108
4.3 Results and Discussion 110
4.3.1 MoO_x oxidation: stoichiometry and external oxygen characterisation 110
4.3.2 Organic semiconductor: overcoming classical RBS limitations 116
4.4 Conclusions of the MoO_x/DBP study 119
5. Conclusions and Perspectives 122
Annex I: NDF DataFurnace and Total IBA 125
Annex II: Ion Damage 128
Bibliography 131
Figures 139
Tables 144

Abstract

This thesis presents the technical improvements made in IBA (Ion Beam Analysis) for the SAFIR platform (UPMC-INSP, Paris, France), and a selection of associated scientific applications. The main improvements are the increased solid angle in a custom silicon-based semiconductor segmented detector and the associated data acquisition system. These improvements open the way to substantially improved spectrum statistics for a given analysing beam fluence, and the possibility to perform realistic analyses with very low beam fluences, for example on very sensitive samples, or with beams of very low intensity.

IBA has been used for materials characterisation since the 1970's, mainly focused on semiconductor technology which is the base for the electronic technology used nowadays. In the beginning of the XXI century new technological challenges (lower power consumption, more storage, higher speed…) are imposed and new materials beyond classical semiconductors, are emerging (spin tuneable materials, topological insulators, organic semiconductors…). IBA needs to evolve to meet the challenges in analysing some of these new materials since detection and data acquisition systems have not been really updated for years.

The large solid angle Segmented Detector (SegDet) overcomes some of the limitations related to the charged particle detection system. IBA techniques exploit the different ion-matter interactions (Rutherford, nuclear reaction, x-rays production…) and the statistical nature of these interactions means that the statistics of the detected particles is a critical parameter. A larger detector solid angle – e.g. for RBS Rutherford Backscattering Spectrometry, more than 50 times that of a standard detector – represents a great improvement. The large detector area has to be segmented in order to maintain good energy resolution. Our device was divided into 16 side-to-side segments separated by a voltage guard ring. This requires 16 independent particle spectroscopy channels, which is complicated and expensive to implement using the classical analogue systems. We have demonstrated the possibility to use a low cost and highly reproducible Digital Data Acquisition (DDA) system through numerical nuclear pulse processing for each individual segment and shown performance at least equivalent to that of an analogue system. The SegDet was completely characterised in terms of depletion thickness, leakage current, charge collection efficiency and energy resolution.

Very ionisation sensitive materials, such as the organic compounds, were not possible to study since the ion beam modify or destroy the samples before the statistics were satisfying to be interpreted; using the SegDet are now available to analyse. Furthermore the samples with small amount of matter, such as ferromagnetic doped materials for spintronic or oxidation processes, can be analysed within a reasonable beam fluence giving good statistical results. In this thesis we demonstrate both applications getting valuable results for iron-contain Bi_2Se_3 topological insulator, transition metal oxide MoO_x oxidation process and organic semiconductor tetraphenyldibenzoperiflanthene (DBP) elemental analysis. Moreover the statistical improvement has been used to extend the maximum capabilities for a single ended 2 MV Van de Graaff accelerator by using the doubly charged ions such as $^4He^{2+}$ produced at very low fluences by the RF ion source to perform RBS at energies up to 4 MeV.

Résumé

Cette thèse présente un travail visant à l'amélioration des techniques d'IBA (Ion Beam Analysis – Analyse par Faisceau d'Ions) pour la plateforme SAFIR de l'INSP (Institute de NanoScicence de Paris, UPMC) basée sur un détecteur segmenté de grand angle solide, avec un système tout numérique de traitement de signaux associé. Les possibilités d'analyse du système ainsi mis en œuvre sont démontrées à travers quelques applications dans le domaine de la physique et la science de matériaux. L'augmentation de l'angle solide de détection est le principal avantage, permettant une diminution considérable de l'incertitude liée à la statistique de comptage pour une fluence donnée d'ions incidents. Ce développement ouvre la voie à des études de très faibles quantités de matière ou des pics de faible intensité sur un fond important ; à l'étude de matériaux sensibles aux dégâts induits par le faisceau incident ; ou encore à l'exploitation de faisceaux de très faible intensité.

La thèse est divisée en trois grandes parties : une première partie théorique qui présente les concepts physiques sous-entendant les différentes techniques IBA ; une deuxième partie plus technique détaillant les développement et la mise en œuvre du système de détection, ainsi que le traitement 'self-consistent' de la grande quantité d'information recuillie avec ce nouveaux système ; et une troisième partie présentant les premiers résultats obtenus en sciences des matériaux en appliquant le système ainsi mis en œuvre.

Introduction aux techniques IBA

L'IBA est une méthode de caractérisation des matériaux développée depuis les années 1970 généralement pour l'étude des semi-conducteurs, mais également avec applications en géologie, sciences du patrimoine et médecine entres autres. Dans tous les cas, les ions génèrés à partir d'un gaz ionisé ou par pulvérisation sont accélèrés aux énergies entre 0.1 et 10 MeV et sont dirigés sous vide avec des champs magnétiques ou électriques sur l'échantillon objet de l'anayse, normalement situé lui aussi dans une chambre sous vide. Les ions peuvent donner lieu à plusieurs types d'interactions avec les atomes l'échantillon et c'est en mesurant le nombre des produits de ces interactions, ainsi que leurs spectres en énergie, que l'analyse de la composition et dans certains cas de la structure cristalline de l'echantillon s'effectue. La mesure des ions retrodiffusés élastiquement est à la base de la méthode RBS (Rutherford Backscattering Spectrometry). La mesure des rayons X caractéristiques induit par les ions incidents est à la base de la méthode PIXE (Particle Induced Xray Emission). Enfin la mesure des produits de réactions nucléaires est à la base des méthodes PIGE (Particle Induced Gamma Emission), NRA (Nuclear Reaction Analysis), et dans le cas spécifique où une section efficace d'une réaction nucléaire présente des résonances étroites, à la méthode NRP (Narrow Resonance Profiling).

Toutefois, la téchnologie derrière ces méthodes d'analyse est née au début de la deuxième moitié du XXème seigle, quand le principal sujet d'étude était la physique nucléaire, via les réactions nucléaires etudiées avec des accélérateurs électrostatiques d'ions, de tension de l'ordre du méga-Volt. Les besoins d'études en physique nucléaire vers les plus hautes énergies

et l'état de connaissance de cette discipline aux basses énergies ont permi de reconvertir les « petits» accélérateurs à des fins d'analyses de la matière condensée. Il s'agira, cette fois, d'identifier une atome de une cible[2] à partir d'une particule inciedente connue. De plus, il était tentant de ne pas abandonner ces petits accélérateurs qui avaient fait l'objet d'investissements importants. Ainsi, les techniques IBA sont nées et sont maintenant largement utilisées pour l'analyse de la composition et de la structure de la région superficielle des matériaux. Dans les années 1960, l'accélérateur de SAFIR était le premier au monde à être conçu spécifiquement pour l'IBA, et être installé, non plus dans un centre de recherches nucléaires, mais dans un laboratoire de physique des solides.

Dans cette thèse trois techniques majeures de l'IBA sont exploitées : RBS, PIXE et NRA. Après une présentation de la perte d'énergie continue des particules dans la matière, qui est un processus commun à toutes les techniques IBA, ces trois techniques sont présentées plus en détails dans la section qui suit. La technique d'Ion beam Induced Charge (IBIC) est présenté dans la section du résumé dédiée à la caractérisation du détecteur segmenté, tandis qu'une présentation détaillée de la canalisation des particules dans un monocristal dépasse le cadre de ce résumé. Le lecteur est référé à la section 1.1.2 de la thèse pour plus de détails.

Pouvoir d'arrêt

L'interaction la plus probable entre un ion et la matière qu'il traverse est la perte d'énergie électronique, et cette interaction est importante pour toutes les méthodes IBA. En effet, l'ion incident subit un grand nombre de chocs avec les électrons – quelques chocs pour chaque nm traversé, en perdant une faible quantité d'énergie dans chaque choc. On distingue, donc, pour des interactions avec une atome de la cible, des chocs élastiques (l'énergie cinetique est conservée) et des chocs inélastiques (une partie de l'énergie cinétique de la collision est absorbée pour arracher l'électron de son site). À une échelle macroscopique, cette perte d'énergie électronique peut être considrée comme étant continue. La perte moyenne par unité de longueur, fonction du matériau et de la vitesse de l'ion, est donc définie de manière différentielle, en le nomant le pouvoir d'arrêt $s = dE/dx$. Un proton de 1 MeV travsersant le silicium perd 41 eV par nm traversé. A cette perte devrait s'ajouter également la perte d'énergie dûe aux interactions faibles avec les noyaux atomiques – également constituée d'une série d'interactions avec une faible perte dans chaque interaction. Ces pertes nucléaires sont négligeables devant les pertes électroniques. Le pouvoir d'arrêt est donc donné par $s = s_n + s_e$ où $s_n \ll s_e$ dans le domaine de l'IBA.

[2] Si pour les physiciens nucléaires, il s'agit d'envoyer des ions sur une cible, pour l'analyste il s'agit d'envoyer des ions sur un échantillon. Du fait de l'héritage 'nucléaire' de l'IBA, on parle encore parfois d'une cible même pour l'analyse.

RBS – Rutherford Backscattering Spectrometry – Spectrométrie de la Rétrodiffusion de Rutherford

La RBS est sans doute la technique la plus utilisée dans le domaine d'IBA. Ici on profite de l'interaction élastique entre les ions légers (chargés positivement) et les noyaux atomiques de la cible, où la section efficace de rétrodiffusion est Rutherford - analytique et bien connue. Si la fluence du faisceau incident (nombre d'ions par unité de surface) est connue on peut remonter quantitativement à la composition de la cible.

En RBS, on peut considérer que l'ion incident subit une interaction purement Coulombienne (et donc ayant la section efficace de Rutherford) avec un noyau atomique. La quantité de mouvement et l'énergie cinétique sont conservées, ce qui permet de déduire facilement la section efficace de l'interaction, ainsi que l'énergie de l'ion après l'interaction (et par conséquent aussi l'énergie cédée au noyau cible) – la cinématique de l'interaction. La section efficace de Rutherford est proportionnelle au carré du numéro atomique du noyau cible et est donc très avantageuse pour des noyaux lourds, mais limitée pour des noyaux légers. En cas de rétrodiffusion (la trajectoire de l'ion est déviée de plus de 90°), plus le noyau est lourd plus l'ion incident garde son énergie initiale. Si le noyau était infiniment lourd l'ion ne cédérait aucune énergie au noyau et conserverait donc son énergie initiale. Dans le cas contraire, où le noyau cible aurait la même masse que l'ion incident, la rétrodiffusion serait impossible – l'ion reviendrait avec 'zéro' énergie. Un spectre en énergie des ions rétrodiffusés est ainsi une sorte de spectrométrie de masse des noyaux de la cible. Notons ici que cette sensibilité à la masse donne donc une sensibilité aux différents isotopes. De plus, les ions perdent leur énergie via le processus quasi-continu du pouvoir d'arrêt. Un ion rétrodiffusé sur un noyau à la surface de la cible revient avec l'énergie donnée par la cinématique, alors qu'un ion rétrodiffusé par le même noyau à une certaine profondeur dans la cible aura perdu de l'énergie, sur les trajets aller et retour dans la cible, et reviendra donc avec moins d'énergie. Le spectre en énergie contient donc aussi des informations sur la profondeur à laquelle s'est trouvé le noyau cible et ainsi constitue aussi une mesure de profil de concentration en profondeur. Du fait que les interactions sont parfaitement connues, la RBS est absolument quantitative.

Toutefois, la résolution en masse et la résolution en énergie de la RBS sont limitées par la résolution en énergie du détecteur. La sensibilité est limitée par la statistique de comptage pour un pic caractéristique – soit isolé, soit sur un fond provenant d'autres noyaux dans la cible. C'est dans ce dernier cas que la grand angle solide du détecteur segmenté donne un avantage consdérable par rapport aux détecteurs de particules classiques.

PIXE – Particle Induced X ray Emission – Emission de rayons X Induis par Particules

Avec une probabilité beacoup plus petite que celle d'une interaction de perte d'énergie éléctronique, l'ion peut ioniser une atome cible dans une couche électronique interne. Un photon est émis quand un électron d'une couche extérieur tombe dans le trou laissé par l'electron éjecté, et son énergie est caractéristique de l'atome ionisé. À la différence avec la RBS, l'energie du rayon X est une signature atomique, et pas isotopique. Pour un élément donné

l'ionisation peut se faire dans une diverses couches et sous-couches internes, et l'électron qui va combler le trou peut provenir lui aussi d'une des diverse couches et sous-couches externes donnant lieu à des rayons X de différentes énergies et intensités. Le processus étant très similaire à celui à la base de la fluorescence X, le nomenclature des raies y est identique. Notons ici que l'énergie des rayons X ne depend pas de la profondeur à laquelle ils ont été induits : un spectre PIXE ne contient aucune information sur les profils de concentration des éléments détectés.

Le PIXE nécessite un détecteur spécialisé, typiquement un détecteur à sémiconducteur d'une grande épaisseur pour aborber les rayons X d'énergie jusqu'à 20 keV, et refroidi afin d'obtenir une résolution en énergie suffisante.

De par les sections efficaces d'ionisation et d'emission des rayons X, le PIXE est particulièrement bien adapté pour la déterminations de concentrations d'éléments de masse moyenne (Si jusqu'à Ag) et peut être un complément intéressant à la RBS dans les cas où la résolution en masse de ce dernier est insuffisante, ou alors où dans les cas où le signal d'un élément en RBS est noyé dans un grand fond.

NRA – Nuclear Reaction Analysis – Analyse par Réactions Nucléaires

Les ions incident sur les noyaux de la cible peuvent induire des réactions nucléaires, telle que $^{18}O(p,\alpha)^{15}N$. Ici, un proton incident sur un noyau ^{18}O produit une particule alpha et laisse le noyau résiduel ^{15}N. Dans une réaction nulcéaire il y a réorganisation de la structure interne des nouyaux impliqués. Il peut y avoir échange de nucléons, excitation des états nucléaires internes, et/ou émission de produits de réactions – particules, photons, particules sub-nucléaires. La réaction peut consommer (réaction endothermique) ou relacher (réaction exothermique) de l'énergie. La réaction n'est plus élastique car l'énergie cinétique n'est pas conservée ; seule la masse-énergie est conservée. NRA est la technique IBA qui utilise les produits des réactions nucléaires exothermiques (et dont par conséquent les produits de réaction sont assez énergétiques) pour déterminer la quantité de matière dans une cible. Ces réactions typiquement ont une section efficace assez basse par rapport à la rétrodiffusion de Rutherford. Les connaissances de la physique nucléaire ne permettent pas encore de calculer leurs sections efficaces à priori. De plus, ces sections efficaces peuvent varier fortement avec la nature et l'énergie des ions incidents et en fonction de l'angle de détection. Toutefois, une fois la chaleur de réaction connue, la cinématique suit des lois de collisions classiques analogues à la RBS. Notons ici que les réactions nucléaires sont spécifiques aux expèces nucléaires, et donc aux isotopes. La NRA est par conséquent adaptée à la caractérisation des isotopes. La gamme d'éléments détectables avec la NRA est très large, mais c'est utilisé surtout pour les éléments plus légers où d'autres techniques d'IBA ne sont pas adaptées.

Du fait que les sections efficaces sont faibles, de grandes fluences sont nécessaires afin d'obténir des statistiques de comptage convenables, et de grands currents de faisceau (plusieurs centaines de nA) sont utilisés. Ceci engendre un très grand flux de particules diffusées élastiquement qui peuvent saturer le détecteur et les chaines d'acquisition. Les produits des

réactions nucléaires utilisées en NRA sont suffisamment énergétiques qu'il suffit de placer devant le détecteur une feuille suffisamment épaisse pour arrêter les particules diffusées élastiquement, mais suffisamment mince pour laisser passer les produits des réactions nucléaires. A ce détail près, la détection de ces particules et les chaines d'acquisition de données sont identiques à celles utilisées pour la RBS. Les explications détaillées dans la prochaine section restent donc aussi valables pour le NRA.

Système de détection et traitement de données

Nous avons vu l'importance de la section efficace dans les techniques d'IBA. Toutes ces techniques sont fortement dépendantes de la statistique donnée pour leurs sections efficaces respectives. Ces sections efficaces étant fixées par la nature, pour augmenter le taux de comptage (et donc améliorer les statistiques de la mesure) il faut soit augmenter la fluence d'ions incidents, soit augmenter l'angle solide de détection. Dans le premier cas, bien que possible, il y a un risque d'endommagement de la cible (avec, dans des cas extrêmes, formation de bulles d'hydrogène dans la cible, ou alors exfoliation de couches minces). On peut aussi augmenter la durée des expériences qui deviennent alors prohibitoires. Dans cette thèse nous présentons les améliorations des statistiques de comptage apportées au système de détection de particules chargées (donc pas en PIXE) dans la plateforme SAFIR.

Les détecteurs à l'état solide[3] de particules, normalement réalisés en silicium sous forme d'une diode Schottky, sont basés sur la création de paires électron-trou par le passage d'une particule chargée, et la mesure de la charge induite qu'ils génèrent dans un champ électrostatique. Ce sont des dispositifs semi-conducteurs qui sous une différence de potentiel inversé génèrent une zone de déplétion ou il n'y a pas de porteurs libres, comme cela se passe dans un condensateur à plaques parallèles. Quand une particule chargée arrive, l'équilibre dans la zone de déplétion est perturbé et des paires électron-trou sont créés. Pour une particule complètement arrêtée dans la zone de déplétion, le nombre de paires créés est proportionnel à l'énergie de cette particule. Comme le semi-conducteur est sous un champ électrique, les électrons et les trous vont se déplacer sous l'effet du champ et ainsi induire une charge mesurable sur les électrodes du détecteur.

Augmenter simplement l'angle solide en construisant de plus grands détecteurs n'est pas satisfaisant, car la résolution en énergie du détecteur (et du préamplificateur de charge associé) dépend de la capacité et du courant de fuite du détecteur. Plus grande est la surface, plus grandes sont ces deux derniers, et plus mauvaise est la résolution en énergie. Pour des résolutions en énergie atteignables aujourd'hui (10 keV), la surface du détecteur est typiquement limitée à 25 mm^2. De plus, même si l'on imagine un détecteur de petite surface placé très près de la cible pour augmenter l'angle solide de détection sans pour autant dégrader la résolution en énergie, la dispersion cinématique (variation en énergie des particules diffusées à différents angles) elargerait le spectre en énergie et conduirait à une perte effective de résolution.

[3] Il y a également des détecteurs d'ionzation de gaz, très intéressants mais hors du cadre de cette thèse.

De fait, l'angle solide d'un détecteur RBS est limité à 1-2 msr. Cependant, il y a de fortes motivations pour augmenter l'angle solide de détection sans compromettre la résolution en énergie ou accepter une plus grande dispersion cinématique. Tout d'abord, comme la précision de la mesure dépend de la statistique de comptage, on peut améliorer la précision de la RBS (toute autre chose étant égale) même dans le cas d'un pic isolé sans fond. Ceci permet également de repousser les limites de détection. Dans le cas d'un pic de faible intensité sur un fond important une amélioration de la précision statistique passe par une encore plus forte augmentation du taux de comptage – un ordre ou deux de grandeur en angle solide est nécessaire pour apporter une amélioration significative.

Dans le cas de matériaux qui sont endommagés par le faisceau – soit par perte de matière ou changements de structure discernable par la mesure IBA (dégâts de type I, voir Annex II: Ion Damage) – soit avec des changements de sa structure de bande ou alors de sa réactivité chimique (dégâts de type II) qui ne sont pas discernables lors de la mesure IBA, il est évident qu'il est souhaitable d'obtenir l'information analytique avec une fluence qui n'endommagera pas, ou alors beaucoup moins la cible. Il serait même appréciable de pouvoir analyser des cibles tellement sujettes à l'endommagement que leur analyse est aujourd'hui impensable – telles que des cibles biologiques, des polymères peu robustes, ou des cristaux avec de faibles énergies de cohésion.

Enfin, il n'est pas possible d'augmenter la fluence d'ions à souhait, et une grand angle solide permettrait peut-être d'exploiter à des fins analytiques des faisceaux de très faible intensité, tels que des faisceaux d'ions multi-chargés.

Afin d'y parvenir, nous avons adopté une approche nouvelle, avec un prototype de détecteur de grand angle solide, divisé en segments individuels pour limiter la capacitance et le courant de fuite. Celui-ci a été initialement développé à l'INSP dans le cadre du projet Européen SPIRIT. Au sein du projet SPRITE, nous sommes partis du prototype, le développant pour le rendre suffisamment performant pour envisager une utilisation systématique pour l'IBA. Le détecteur segmenté est composé d'un substrat de silicium sur lequel sont gravés 16 détecteurs indépendants côte-à-côte. Tous les segments sont entourés par un anneau de garde (structure assez standard pour les détecteurs de particules) qui, polarisé à la même tension que le détecteur, permet de contrôler le courant de fuite et assurer la minimisation des effets de bord autour de chaque segment. Avec cette configuration on a les bénéfices d'avoir une grande surface de détection (760 mm²), donc une augmentation de l'angle solide (vers 130 msr pour notre détecteur), mais sans perte de résolution en énergie. La configuration des segments est choisie afin de limiter aussi la dispersion cinématique. Par ailleurs, le fait d'avoir différents angles de rétrodiffusion peut résoudre l'ambigüité masse/profondeur inhérente dans un spectre RBS. En résumé, le détecteur segmenté fournit une amélioration dans l'incertitude des mesures déjà faisables pour IBA et permet d'étudier des matériaux qui ne sont pas mesurables avec le système classique.

Le fait d'avoir un grand nombre de segments s'accompagne aussi d'un grand nombre de systèmes d'acquisition. Le système d'acquisition classique pour le RBS (et la majorité de techniques IBA) est basé sur l'amplification analogique des impulsions de charge avec un

changement en forme semi-gaussien, que sont ensuite traitées par un convertisseur analogique-digital sensible aux pics semi-gaussiens. La hauteur du pic, qui est proportionnelle à la quantité de charge induit dans le détecteur et donc à l'énergie de la particule est donc représentée numériquement et peut être stockée dans un système informatique, contribuant ainsi à l'accumulation du spectre en énergie. Un tel système pour notre détecteur nécessiterait 16 chaines d'acquisition indépendantes, chacune coûtant plus de 10k€, un prix mettant en cause la rentabilité de son déploiement pour le détecteur segmenté. Cependant il existe depuis peu des systèmes basés sur la numérisation rapide du signal issu directement du préamplificateur et traitement numérique afin d'en extraire le signal donnant l'énergie de la particule. L'installation est beaucoup plus simple et confortable et parfaitement compatible avec les besoins d'un détecteur segmenté, avec un coût nettement inférieur, de l'ordre de 1 k€ par chaine. Nous avons également conçu et mis en œuvre un banc de préamplificateurs adaptés aux détecteurs segmentés.

Dans un mesure RBS classique un seul spectre est obtenu par mesure. L'interprétation d'un tel spectre se fait par ajustement itératif aux données de courbes simulées pour une structure de cible supposée. Cette approche n'est plus possible avec 16 spectres, obtenus à des angles de détection différents, et une autre approche est nécessaire. L'outil NDF DataFurnace qui interprète les données RBS de manière self-consistent par un algorithme de recuit simulé est l'approche plus convenable pour notre système. D'ailleurs l'approche de recuit simulé permet d'inclure les données obtenues par d'autres techniques IBA aboutissant à un résultat optimisé et auto consistent avec toutes les données. Cette manière de traiter les données est tellement puissante que nous avons introduit une annexe dédiée aux explications détaillées (Annex I: NDF DataFurnace and Total IBA).

Dans le Chapitre 2 nous présentons des informations détaillées sur le fonctionnement des détecteurs à semi-conducteurs classiques, avec les concepts physiques de fond, ainsi que les améliorations introduites pour le détecteur segmenté. Nous y présentons également une étude et une caractérisation exhaustives des propriétés du détecteur (avec une conférence orale présentée au congrès international ECAART 12 et une publication en cours sur la collection de charge dans le zone entre segments, Sous-section 2.1.2.1). Enfin, dans le cadre du projet SPRITE, nous avons conçu un nouveau détecteur segmenté annulaire destiné à être réalisé par nos collègues de HZDR – Helmholtz-Zentrum Dresden-Rossendorf. Les explications détaillées sur les systèmes analogiques et numériques d'acquisition de données, avec une comparaison des deux systèmes, sont également inclues dans ce chapitre.

Applications

Les trois applications les plus importantes où le détecteur segmenté a été utilisé sont : La RBS avec les ions doublement chargés, l'IBA pour l'étude de la composition et structure de l'isolant topologique Bi_2Se_3, et une étude des dispositifs photovoltaïques organiques, basés sur des oxydes de métaux de transition (injecteurs de trous) et le photo-absorbeur tetraphenyldibenzoperiflanthene (DBP, donneur semi-conducteur organique).

Faisceaux de faible intensité

L'exploitation des très faibles courants d'ions doublement chargés (dans la Subsection 2.1.2.2) permet de doubler la gamme d'énergie utilisable par des accélérateurs électrostatiques. Dans le cas de SAFIR, avec une tension maximale au terminal de 2.2 MV, la limite supérieure d'énergie pour les ions une fois chargé est d'environ 2.2 MeV. La source radiofréquence d'ions de SAFIR produit très majoritairement des ions une fois chargé, avec de très faibles intensités d'ions multichargés. Avec un bon ajustement des paramètres de transport du faisceau, il est possible de diriger sur la cible un courant faible (inférieur au nA) de He^{2+}. Il est probable que des faisceaux d'ions plus hautement chargés (par exemple Ar^{3+}) puissent également être produits. Le courant observé pour He^{2+} est trop faible pour être exploité actuellement, mais le grand angle solide du détecteur segmenté permet de surmonter cette limitation et rend faisable l'exploitation de ce faisceau de faible intensité – avec une énergie de 4.4 MeV. Nous avons démontré cette possibilité en relevant des spectres RBS à 4 MeV, ou l'on observe de fortes déviations de la section efficace de Rutherford, ouvrant la voie à de multiples applications de la RBS non-Rutherford (ou, plus succinctement, Elastic Backscattering Spectrometry EBS).

Isolants Topologiques

Les isolantes topologiques, TI, (Section 1.2 et Chapitre 3) sont des matériaux avec une structure de bande électronique de type isolant conventionnel en volume (gap de quelques dixième d'eV) mais qui possèdent des états électroniques conducteurs en surface (cône de Dirac au centre de la zone de Brillouin et avec une hélicité sur la texture de spin). Ces états électroniques de Dirac de bords ont une symétrie d'inversion temporelle et une robustesse vis-à-vis du désordre. La nature topologique de cette différence entre surface et volume est extrêmement intéressante dans la perspective d'utilisation de ces matériaux quand ils sont dopes ferromagnétiquement dans la technologie électronique, par exemple en informatique quantique ou alors dans des dispositifs spintroniques. Le Bi_2Se_3 est un isolant topologique aux températures ambiantes à cause de son gap relativement important (~ 0.3 eV). Le matériau se cristallise dans le système rhomboédrique, selon la séquence d'empilement des plans atomiques : Se-Bi-Se-Bi-Se qui constitue le feuillet de base (QL : quintuple layer). Les liaisons sont covalentes à l'intérieur du feuillet et les feuillets successifs sont reliés entre eux par des forces de Van der Waals. La croissance par épitaxie par jets moléculaires de ce composé lamellaire sur GaAs(111) permet d'obtenir des échantillons de bonne qualité structurale et de contrôler l'épaisseur au feuillet près.

Il y a intérêt pour l'utilisation du détecteur segmenté pour deux raisons : 1) Les forces Van der Waals entre les QL sont tout à fait plus faibles que celles présentes dans un matériau inorganique typique, donc le Bi_2Se_3 est peut-être susceptible d'être endommagé par le faisceau d'ions. 2) Le relativement faible niveau de dopage ferromagnétique nécessaire pour faire ressortir des états exotiques provenant des TI est aussi susceptible d'être dosé uniquement par un système comme le nôtre.

Nous avons étudié des couches de Bi_2Se_3, élaborées par épitaxie par jets moléculaire sur substrats de GaAs, d'épaisseur entre 50 et 100 nm, soient non-dopées, soient dopées avec du fer à un des trois différents niveaux. Chaque échantillon est protégé par une des trois différents couches de protection, à savoir ZnSe, Se et Au.

Dans un premier temps, nous avons effectué une étude en profondeur de ces TI avec une configuration RBS classique ; quelques résultats ont été présentés au congrès francophone IBAF 2014 et au congrès international IBA 2015, ce dernier donnant lieu à une publication (Section 3.3). Dans cette publication nous montrons également les résultats des mesures dans la configuration de canalisation, ce qui permet la caractérisation de l'ordre atomique dans les réseaux cristallins, ainsi que la mesure de l'endommagement du ce structure induit par le faisceau. Nous avons ensuite continué la caractérisation avec un système classique incorporant les mesures de PIXE pour les TI avec les plus petites quantités de fer (invisible dans les spectres RBS) – mesures qui ont pu être intégré dans l'optimisation par recuit simulé de NDF. Enfin, une fois opérationnelle, le détecteur segmenté a été utilisé afin de compléter la caractérisation par canalisation (Section 3.4) avec une statistique de comptage bien supérieure à celle obtenue avec le système classique.

Selon les résultats obtenus, les dégâts générés par le faisceau d'analyse, bien qu'observables en canalisation, sont négligeables dans des conditions standard pour le RBS. Toutefois, le désordre atomique observé est spérieur à celui attendu d'un bon monocristal. Les meilleures échantillons pour faire de la canalisation sont ceux recouvert de ZnSe et Se, car ces couches de recouvrement sont cristallisées tandis que l'Au est amorphe et peut donc engendre une augmentation de la dispersion angulaire du faisceau incident avant même d'atteindre la couche Bi_2Se_3 d'intérêt. Les échantillons sans Fe montrent un excès en Se par rapport à la stœchiométrie idéal. Cet observation est comme étant le résultat de la condition de croissance, qui nécessite un environnement riche en Se, mais cet écart de stœchiométrie n'a pas eu d'implications pour les propriétés électroniques mesurées dans ces couches. Les échantillons dopés ont été mesuré avec RBS et PIXE, car pour les échantillons avec la plus faible quantité de Fe la RBS est insuffisamment sensible pour effectuer un mesure adéquat. Pour ces échantillons contenant du fer nous avons trouvé de nouveau un excès de Se, mais qui cette fois augmente avec la quantité de Fe. La diffraction de rayons X a mis en évidence l'existence de phases $FeSe_x$, et des mesures magnétiques ont montré la présence de la phase Fe_3Se_4, ce qui est en accord avec les mesures RBS.

Par ailleurs, l'utilisation du détecteur segmenté pour l'étude du Bi_2Se_3 a révélé un comportement du détecteur jusqu'à la insoupçonné. En effet, les signaux importants et isolés provenant du Bi ont permis de mettre en évidence un fond dans le spectre, s'étendant jusqu'aux plus basses énergies à partir du pic de Bi. Ce comportement n'a pas encore pu être investigué en détails.

Dispositifs Photovoltaïques Organiques

Les dispositifs optoélectroniques basés sur matériaux organiques (Section 1.3 et Chapitre 4) sont très prometteurs pour les technologies futures du développement durable. Il y a de multiples applications, telles que dans les domaines de l'électronique de basse consommation ou le diagnostique médical, mais dans cette thèse nous portons notre attention sur un système destiné à l'exploitation de l'énergie solaire. Les cellules solaires les plus commercialisées aujourd'hui sont basées sur les technologies de semi-conducteurs inorganiques, essentiellement le Si et le GaAs, mais les prix élévés de fabrication et les contraintes pour les installations nécessaires rendent cette industrie peu compétitive par rapport à l'exploitation des sources d'énergie fossiles. Le développement des matériaux semi-conducteurs organiques qui sont produits aux bas coûts économique et environnementale pourrait être un facteur clé pour l'exploitation des sources d'énergie renouvelables telles que l'énergie solaire. Par contre il y a des limitations intrinsèques pour ces matériaux ; les faibles quantité et mobilité des porteurs de charge, le gap élévé, et l'instabilité chimique sous les conditions environnementales de fonctionnement. Nous considérerons ici le tetraphenyldibenzoperiflanthene (DBP), un des semi-conducteurs organiques qui a des caractéristiques pouvant en faire un élément fondamental dans la fabrication de dispositifs optoélectroniques organiques.

La faible mobilité des porteurs dans les semi-conducteurs organiques peut être surmontée à travers de la déposition d'échangeurs de charge. Les oxydes de métaux de transition ont été démontrés comme étant de bons échangeurs de charge compatibles avec les semi-conducteurs organiques grâce à leur structure atomique et propriétés de transport de porteurs. Concrètement, le oxyde MoO_x est un candidat très prometteur pour être utilisé comme injecteur de trous dans les semi-conducteurs organiques de type p. Les propriétés de conduction de ce matériau sont fortement liées à sa stoechiométrie et, à ce propos, comprendre l'interaction de ce matériau avec un environnement oxydant (son environnement de fonctionnement sera en toute probabilité oxydant) est essentiel pour la maîtrise de son intégration dans des dispositifs opérationnels.

DBP et le détecteur segmenté

Typiquement un matériau comme le DBP, $C_{64}H_{32}$, n'est pas analysable par IBA à cause des dégâts générés par le faisceau d'analyse. Notre but ici est de démontrer l'efficacité du détecteur segmenté pour l'analyse d'une structure organique. Le système d'acquisition a été configuré pour le stockage numérique en mode 'liste', de l'énergie et du temps pour chaque particule qu'arrive au détecteur ; il est ensuite possible, à partir de cette liste, de reproduire des spectres en énergie pour des fenêtres de temps souhaitées, et ainsi tracer l'évolution du nombre d'atomes dans la couche en fonction de la fluence du faisceau.

Nous avons montré que le DBP ne présente pas de dommage de Type I, dommage visible par l'évolution des spectres en fonction de la fluence – par exemple par la perte de carbone. En revanche, la couche organique devient transparente (donc dommage de Type II) après même une faible fluence. La limite de fluence au-delà de laquelle cet endommagement n'est plus visible est de $1.2 \cdot 10^3$ atomes/nm² (0.2 μC dans un faisceau de 1 mm²). Pour cette fluence on a

trouvé une incertitude de 60% statistique (±1σ) sur la mesure de la quantité de carbone avec 6 segments du détecteur tandis que pour un détecteur simple l'incertitude statistique est de 98%. Notons que la précision obtenue avec le détecteur segmentée serait encore améliorée avec les 16 segments en jeu, et dans les deux cas (détecteur simple et détecteur segmenté) l'incertitude pourrait être encore amélioré avec le raffinement de quelques paramètres, telles que la diminution du courant, l'augmentation du diamètre du faisceau ou l'utilisation des données accumulées de diffèrentes points de la cible, supposé homogène.

Oxydation dans le MoO_x

Nous avons étudié le processus d'oxydation du MoO_x ayant différentes stœchiométries (x = 2.57, 3 et 3.14) par la RBS et la NRA. Les échantillons furent élaborés par la technique de pulvérisation réactive à courant continu avec une cible de Mo métallique et différentes pressions partielles d'oxygène dans le bâti de pulvérisation par l'équipe de NanoSYD à l'Université du Sud de Denmark. Nous avons recuit ces échantillons sous $^{18}O_2$ afin de distinguer l'oxygène provenant du gaz de celui déjà présent dans les échantillons, et investigué le taux d'incorpration ou d'échange d'oxygène avec des analyses par RBS et par NRA. Nous considérons quatre types d'échantillons : « as deposited » sans aucun autre traitement ; traités avec un procédé de nettoyage de surface ; nettoyage de surface et recuits sous $^{18}O_2$; nettoyage de surface, cristallisation par traitement thermique et ensuite oxydés sous $^{18}O_2$. Le nettoyage de surface consiste en un traitement sous vide de 30 minutes à 150°C suivi d'un deuxième pour 30 minutes à 200°C. L'oxydation a été réalisée pendant une heure à 300° C sous 200 mbar de $^{18}O_2$, tandis que la cristallisation se réalisé en 5 minutes à 500°C sous vide.

Le nettoyage et oxydation sous $^{18}O_2$ ont été executés dans un four à pression contrôlée disponible à l'INSP et entre ces traitements l'exposition à l'air des échantillons a été minimisée. Tant la RBS que la NRA ont la capacité de mesurer les isotopes. Pour la NRA, la réaction nucléaire utilisée ici est $^{18}O(p,\alpha)^{15}N$, où nous avons mesuré les particules alpha ($^4He^+$) résultants. Les spectres obtenus par les deux techniques ont été ajustés de manière self-consistent avec NDF. Nous avons utilisé le détecteur segmenté pour ces deux techniques, donc il y a 14 spectres (2 des 16 segments étant inoperationnels) par mesure dans le cas des échantillons non traités sous $^{18}O_2$, et 28 spectres pour ceux traités sous $^{18}O_2$. Nous avons ainsi pu mesurer la quantité d'oxygène d'origine externe ainsi que son profil de diffusion dans le MoO_x.

Les résultats montrent l'absence d'une perte de molybbdene ou de l'oxygène originalement présent dans les couches lors des diffèrent recuits. Ils confirment également qu'il n'y a pas eu d'oxydation atmosphérique incontrôlée lors de manipulations. Les échantillons oxydés ont été caractérisés et analysés avec succès par les deux techniques IBA. Pour tous les échantillons recuits sous $^{18}O_2$, la quantite de ^{16}O (originalement présent dans les couches) reste inchangée, et il y a incorporation de ^{18}O. Ceci permet de conclure qu'il n'y a pas d'échange entre l'oxygène de la couche et celui du gaz (l'oxygène dans les couches est fortement lié) et conforte la vue que les couches 'as deposited' contient une forte concentration de lacunes d'oxygène.

Les échantillons cristallisés ne présentent pas d'effets de canalisation en RBS, donc ils ne sont pas des monocristaux mais auront une structure plutôt polycristalline. De plus, la quantité de ^{18}O trouvé dans ces échantillons cristallisés est plus grande que celle trouvée dans les couches amorphes. Nous postulons donc que les joints de grain facilitent le transport et agissent comme pièges pour l'oxygène.

Les échantillons amorphes, quelque soit leur contenu original en oxygène, présentent toutes une stoechiometrie finale de $x = 3.35 \pm 0.2$ (pour MoO_x). Ce montant n'est pas limité par la cinétique et représente donc une limite thermodynamique supérieure pour x.

Conclusions et perspectives

Nous avons implémenté avec succès un détecteur de particule à 16 segments ayant une surface de détection de 760 mm² accompagné d'un système d'acquisition de donnes tout numérique pouar la détection de particules chargées dans l'IBA. Des études intensives sur les caractéristiques et l'optimisation du détecteur segmenté (résolution en énergie, collection de charge, système de blindage, installation dans une chambre d'analyse, etc.) ont été effectuées pendant cette thèse et les avantages de ce système ont été vérifiés par comparaison avec les systèmes de détection classiques. L'utilisation de l'outil d'ajustement NDF a été démontrée comme étant le plus efficace (probablement l'unique) manière de traiter et analyser de manière self-consistent le grandre nombre de spectres obtenus.

Nous avons appliqué notre système amélioré pour l'acquisition en conditions de très basse intensité de faisceau (les ions doublement chargés $^4He^{2+}$) ; pour l'caractérisation de la structure du réseau atomique de l'isolant topologique Bi_2Se_3 contenant du fer (que nous avons également étudié avec le système classique); pour la démonstration des possibilités ouvertes pour l'IBA pour la caractérisation de matériaux organiques, comme le DBP, notamment en repoussant les limites imposées par le endommagement dû au faisceau d'analyse par rapport aux systèmes classiques ; et pour la caractérisation du processus de oxydation dans les échangeurs de porteurs nécessaires pour l'électronique organique.

Il y a encore des ajustements à réaliser pour la complète implantation et l'utilisation systématique dans l'INSP. Il faut développer le software d'acquisition ainsi que quelques perfectionnements dans le hardware pour l'optimisation de la résolution en énergie. Le comportement du détecteur segmenté avec les signaux provenant des couches épaisses et/ou des éléments lourds, mis en évidence en toute fin de thèse, reste incompris, mais des expériences sont déjà envisagées pour élucider cet effet. Nous sommes convaincus que les laboratoires d'IBA vont passer de plus en plus aux configurations comme la nôtre, donc l'outil NDF mériterait d'être plus développé pour les détecteurs segmentés, par exemple en permettant de lier certaines variables telles que les angles entre les segments, ou la fluence (qui est rigoureusment identique pour chaque segment), lors des recuits simulés.

Resumen

Esta tesis presenta las mejoras técnicas realizadas en el campo de la IBA (Ion Beam Analysis – Análisis por Haz de Iones) en la plataforma SAFIR (UPMC-INSP, Paris, Francia), y una selección de aplicaciones científicas asociadas. Las principales mejoras están en el incremento del ángulo solido en un detector segmentado de silicio y el sistema de adquisición a él asociado. Estos adelantos abren el camino para la mejora substancial desde el punto de vista estadístico en las técnicas de IBA que utilizan partículas cargadas como fuente de información.

Las técnicas de IBA han sido utilizadas por la caracterización de materiales desde los años 70 del siglo pasado, esencialmente enfocados a las tecnologías semiconductoras en que hoy día se basa la electrónica. En este comienzo del siglo XXI nuevos retos tecnológicos deben ser afrontados (bajo consumo, mayor velocidad, durabilidad) y nuevos materiales más allá de los semiconductores clásicos están emergiendo (materiales spintronicos, aislantes topológicos, semiconductores orgánicos, etc.). Por tanto, las técnicas IBA deben adaptarse y evolucionar para hacer frente a estos nuevos necesidades analíticas de estos materiales, puesto que mucha de la instrumentación utilizada no ha sido renovada durante anos.

El detector segmentado de gran ángulo solido supera algunas de las limitaciones relacionadas con el sistema de detección de partículas cargadas. Las técnicas IBA utilizan las diferentes formas en las que interaccionan iones y materia (retrodifusion, reacciones nucleares, producción de rayos X…) para darnos información sobre el material bajo estudio. Estas interacciones tienen una naturaleza estadística intrínseca y por lo tanto su medición depende, en última estancia, del ángulo solido con el que son detectadas; en nuestro caso aumentado la superficie de detección, el ángulo solido es más 50 veces el de un detector clásico. Sin embargo el aumento de la superficie de detección genera ruido electrónico que compromete la resolución de nuestra medida, para solventarlo utilizamos la segmentación del área total en 16 segmentos individuales alineados verticalmente con un anillo de guardia entre ellos para separarlos. La manera más eficaz de adquirir las señales generadas por un dispositivo multicanal (uno por cada segmento) como este es la aproximación digital, más económica y manejable que el clásico sistema analógico.

Los materiales sensibles a la ionización, como los compuestos orgánicos o monocristales, no son posibles de estudiar mediante las configuraciones clásicas de IBA, ya que antes de tener estadísticas suficientes la muestra queda dañada e incluso destruida; con la utilización de un detector segmentado las estadísticas necesarias pueden ser tomadas con una menor fluencia de iones incidentes, evitando así el daño. El incremento estadístico puede ser útil para aquellas muestras en las que la cantidad de materia sea muy pequeña o esté superpuesta con otra señal. En esta tesis mostramos las posibilidades del detector segmentado en ambos casos, obteniendo interesantes resultados del análisis del aislante topológico Bi_2Se_3, el óxido de metal de transición MoO_x y la molécula foto absorbente DBP. También demostramos la utilidad de nuestro sistema para configuraciones de baja intensidad del haz como el caso de los iones doblemente cargados de $^4He^{2+}$ a 4 MeV en un acelerador Van de Graaff de 2 KV.

Acknowledgements

This thesis has been a work that I could not do alone, it has involved a lot of people who I had the great pleasure to meet and work with. The first big acknowledgment is for my supervisor Ian, he has the trust placed on me and, somehow, that changes my life. His advice and support have been invaluable during all this period and his way to transfer the scientific knowledge and his personality have perfectly matched on me. I have an unpayable debt with him.

I would like to thank the jury members to give me some of their time reading the thesis and coming to the defense. Special mention for the examinators who had to give even more time writing the thesis report and coming from outside France; tausend dank Max Doëbeli, Grazie mille Alessandro.

Pendant le période que j'ai été en France, déjà 4 ans, j'ai eu l'opportunité de connaitre et travailler avec de très intéressantes et gentilles personnes. Tous les membres de l'équipe CONFID de l'INSP de Jussieu m'ont aidé de manière désintéressé et très compréhensives (je suis arrivé sans parler aucun mot en français) dans le long et coûteux chemin de une thèse. Ainsi que nos voisins de couloir de l'équipe SIMPA, avec lesquels pendant les moments de cantine on a eu toutes sortes des très intéressantes conversations. Un spécial remerciement doit être fait à Emrick Briand et Sébastien Steydli pour la mise en place de l'accélérateur (avec l'alignement des lignes de faisceau, las chambres d'analyse, etc.) après les travaux de rénovation et le système d'acquisition. Aussi à Jean-Jacques Ganem pour les discussions scientifiques et son aide pour la rédaction en français ; et Isabelle Trimalle pour son aide dans les petites mais très importantes tâches de la préparation de échantillons et mesures optiques et électroniques.

En dehors de l'équipe, le travaille avec Mahmoud Eddrief sur les isolants topologiques a été très enrichissante et fondamental pour la thèse. Ma marraine Nadine Witkowski a été aussi très importante en la recherche de sujet scientifiques pour l'application du détecteur segmenté. Ainsi que toute l'équipe de gestion et secrétariat qui rendent la vie administrative un peu plus facile. Aussi je suis très reconnaissant à l'équipe de l'accélérateur ALTAÏS à Namur pour le bon accueil pendant le temps de la rénovation de notre accélérateur, grâce à vous j'ai été capable de faire une présentation orale devant un congrès international (probablement la plus important dans le domaine) et publier un article.

The SPRITE project has been the key of this thesis. I would like to thank to Karen Kirkby, Helena Kondryn and Francine Elson-Vining for their project administration work during these years. The academic and personal (and economic) support has to be greatly recognised since all the people involved know the difficulties that can be found in an international project like this. Obviously I am very grateful as well to all my spriters colleagues for whom I wish all the best and I hope that we can, no matter how, meet again. The SPRITE workshops are already legendary.

I am very grateful to the people who took care of me during the different secondments around Europe. A Julien Colaux pour son aide avec le NDF, pas seulement à Surrey mais aussi par

courrier électronique. L'outil est clairement compliqué à utiliser mais un peu plus jouable merci à toi. To Max Doëbeli and Arnold Müller (sorry about not writing this in German…) during the ETH Zurich secondment, where I learn so many things being accompanied by these great scientist and people. Grazie anche a tutto il equipo di CAEN en Viareggio, il periodo là ha stato explendido e la coperatione con voi una ampia esperienza. Finally thank you to all the RBI in Zagreb (sorry for not being able to write this in Croat) especially to Milko Jakšić, Ivan Sudic and Valentin Stoytschew.

Finalmente, en mi lengua materna, quiero agradecer el inestimable y siempre cariñoso apoyo que siempre he recibido de mis padres y mi hermano, y aunque estuviésemos geográficamente lejos siempre los he sentido muy cerca; sin ellos nada de esto habría sido posible. También quiero agradecer al resto de mi familia, especialmente a mis abuelos; los que ya no están, que se sentirían muy orgullosos, y mi abuela Florencia que tanto me quiere; todos me han hecho disfrutar cada vez que volvía a casa. Un agradecimiento muy especial para Sylvia que ha estado desde el momento que nos conocimos a mi lado, aunque no fuese físicamente, y ha sido como un rayo de luz en la noche más oscura.

Doy las gracias a todos los amigos y amigas de "trejcan", de la UAM y de las vicisitudes de la vida en general, siempre fue un placer, y un alivio, volver a casa y encontraros, tal vez no exactamente igual que cuando me fui, pero con las mismas cosas que nos hicieron ser buenos amigos. También a la gente que he encontrado durante mi estancia en Paris, donde hemos disfrutado de nuestro exilio, especialmente a Juan "el perillas" y Carla, Tanya, Edu y Amaya; muy importantes en los primeros tiempos parisinos.

Sin todos vosotros y vosotras, en una medida u otra, esto no lo hubiese conseguido.

1. Introduction

This thesis is dedicated to improving Ion Beam Analysis (IBA) as a set of material characterisation techniques with a broad application both in research and industry. We have made several improvements in the detection and acquisition system for the SAFIR[4] platform – INSP-UPMC – aimed at routine and systematic use. We present both the technical improvements (detection and acquisition), and several scientific applications that make use of them.

In this work we installed and developed a large solid angle Segmented Detector (SegDet) for particle detection in IBA techniques. The solid angle of around 48 times that of the classical IBA detectors increases the statistical performance for the experiments which opens a new range of potential material characterisation applications: samples with small amount of some elements or samples composed of elements that give signals on the substrate background which cannot be studied with enough accuracy in a reasonable experimental time; delicate materials which can be easily damaged or even destroyed under the ion beam (e.g. organic materials) before they can be properly measured; or experiments where the beam intensity is so small that classical IBA systems are not able to get satisfactory results (e.g. use of 4 MeV $^4He^{2+}$ ion beam in 2 MV single ended accelerators). The segmentation – 16 segments in the case of the present SegDet – makes the analogue acquisition system very costly and complicated to setup. A modern digital acquisition approach is proposed to overcome this difficulty. In a classical RBS measurement usually one, or more rarely two or three spectra are collected from detectors placed at various scattering angles. The use of the 16 channel SegDet generates 16 spectra for each measurement, which must be treated in a self-consistent manner to deduce afterwards the sample composition. A fitting tool to manage that amount of data in a self-consistent way, such as the DataFurnace (NDF) [1] is necessary.

The thesis shows two different analytical applications: iron-contain Topological Insulator (TI) Bi_2Se_3 and organic semiconductor devices. The TI are an electronic state of the matter with particular surface quantum states, which are currently the object of intense experimental and theoretical work. Bi_2Se_3 is a layered structure, with the layers bonded via the weak Van der Waals forces which are therefore potentially easily damaged by the analysing beam. Bi_2Se_3 may also be ferromagnetically doped, so as to introduce ferromagnetic behaviour in view of applications in spintronics. RBS, PIXE and ion channelling were applied to study the effect of beam damage during analysis, and to characterise the stoichiometry and the ferromagnetic doping. In the organic semiconductor we focus first on the Transition Metal Oxide MoO_x hole extractor, in which the stoichiometry is a critical parameter determining the electronic behaviour. The oxidation process (deliberate or unintentional environmental modification of x in MoO_x) has to be well understood. The organic dye tetraphenyldibenzoperiflanthene (DBP) responsible for conversion of light into charge is impossible to study with a classical particle

[4] Système d'Analyse par Faisceaux d'Ions Rapides (FR) – Fast ion beam analysis system (EN)

detector. We show how the use of the SegDet makes it possible to perform elemental characterisation even of this sensitive organic compound.

The thesis is divided into 6 chapters. Chapter 1 presents a thorough introduction to IBA techniques (Section 1.1), with special attention paid to those used in the thesis, together with an introduction to the applications in which the system has been used (Sections 1.2 and 1.3). After a general overview of charged particle detection and data acquisition systems, the new detection system, based on a segmented detector and fully digital data acquisition is presented in Chapter 2, and compared with the standard detector (Section 2.1) and data acquisition (Section 2.2) systems. The Publication I presents a study of the charge collection characteristics of the SegDet in the interstrip regions. Chapters 3 and 4 are dedicated respectively to IBA characterisation of Topological Insulators and Molybdenum Oxide thin films for organic semiconductor solar cells – in which our system makes enhancements in (or even makes possible) the material IBA study. Chapter 5 presents overall conclusions and the contributions in the IBA field made by the author.

Finally, Annex I: NDF DataFurnace and Total IBA explains details of the data analysis procedure and the software used. Annex II: Ion Damage presents an overview of damage induced by the analysing ion beam, which is an important concept throughout the thesis.

1.1 Ion beam Analysis (IBA) Techniques

IBA techniques have been widely used for characterisation of materials from semiconductors to organic polymers since the 1970's, since they provide direct and absolutely quantitative measurements, in principle without the use of standards. The energy of the scattered incident beam particles, recoiled particles, or nuclear reaction events provides information on the atomic or nuclear species that has interacted with incident beam. The number of detected interaction products (for a given incident beam fluence) provides information on the concentration of the target nucleus or atomic species, and in cases where the detected particle also loses energy traversing the solid target, the energy spectrum also provides information on the depth distribution of the target nucleus. Figure 1 shows a summary of the possible ion-matter interactions which are encompassed by IBA:

- Rutherford Backscattering Spectrometry (RBS) where the fundamental event is elastic backscattering of the incident ion. Light ions at medium energies (0.5-2.5 MeV) are the most commonly used since at higher energies the cross section is no longer Rutherford although the interaction remains elastic (in this case the term EBS, Elastic Backscattering Spectrometry, is often used in the literature). It is interesting for medium and heavy target elements, Z~(8, 90). Depth profiles can be extracted. Medium Energy Ion Scattering (MEIS) is a variant of RBS in which an electrostatic detector, under ultra-high vacuum, is used to improve energy (and hence depth) resolution. The best depth resolution is obtained with ions near the maximum of the stopping power curve – around 100 keV for protons and 400 keV for $^{4}He^{+}$.

- In Elastic Recoil Detection Analysis (ERDA) a target particle recoiled by the beam is detected. The incident ion has to be chosen according to the target element, with typical incident energies in the range 2-100 MeV. Depth profiles can be extracted.

- Particle Induced X-ray Emission (PIXE) where the x-rays resulting from the interactions between the atomic shell electrons and the ion beam are collected. Light incident ions are used at medium energies (1-3 MeV). It is used to study light-medium elements, Z~(11-60). No depth profile can be extracted.

- Particle Induced Gamma-ray Emission (PIGE) is similar to PIXE but using the gamma rays generated in ion-nucleus interactions. Light ions at medium energies (1-3 MeV) are used. It is used for light element identification Z~(3-20). Depth profiles can be obtained when the cross section has narrow resonant structures, by scanning the incident beam energy in the vicinity of the resonant structure. In this case the method is referred to as Narrow Resonance Profiling (NRP).

- In Secondary Ion Mass Spectrometry (SIMS) the target components are sputtered by the ion beam and they are classified according to their mass using a mass spectrometer. It is interesting for surface characterisation, giving nanometre scale depth profile. Typically, heavy ions of energies in the range 2 keV to 20 keV are used since the required instrumentation is at a modest scales and sputtering yields are sufficient.

- In Nuclear Reaction Analysis (NRA) charged particles or gamma rays resulting from nuclear reactions with the ion beam are detected. Because nuclear reaction cross sections generally vary quite strongly with ion energy and detection angle, the incident ion, its energy, and the detection angle have to be chosen according to the element being analysed; for example carbon can be detected using a deuterium beam at 1.2 MeV, where the reaction $^{12}C(d,p_0)^{13}C$ will take place, giving a proton as a residual ejected particle. If, as is most conveniently the case, the nuclear reaction is exothermic then the elastically scattered primary beam can be stopped by a mylar (Polyethylene terephthalate) film that is still thin enough to allow passage of the higher energy nuclear reaction products. Depth profiles can be extracted.

- Ion Beam Induced Charge (IBIC): Unlike the above ion beam techniques IBIC is not an elemental materials characterisation but rather a tool to study the electronic behaviour within a material. It is used for wide bandgap materials such as semiconductors junction (p-n, Schottky) insulators and semi-insulators materials. It has a great interest to measure and map transport properties such as carrier concentration, mobility and lifetime, diffusion processes, depletion region thickness, the charge collection efficiencies and charge drift length, as well as lattice dislocations, point or extended defects and radiation induced damage.

The techniques used in this thesis (RBS, PIXE, NRA and IBIC) will be presented in more detail in next subsections. Channelling (subsection 1.1.2) is not mentioned above since it is not an extra technique but a different experimental configuration of the other techniques.

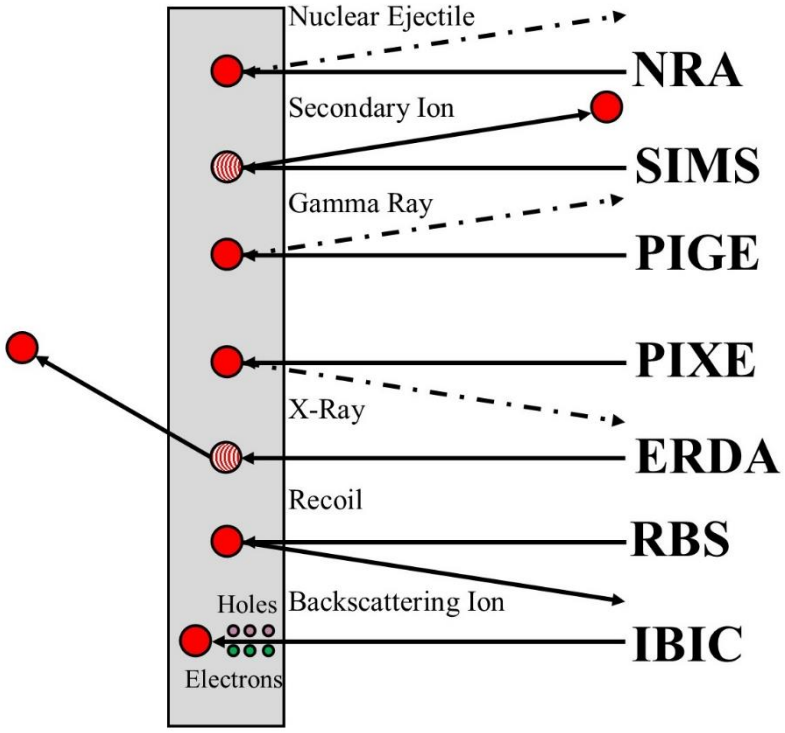

Figure 1: Ion interactions with matter.

These techniques are powerful tools by themselves, however a combination of them is one of the aims of this work in order to extract all the possible information that IBA can give. For that reason, we have used NDF DataFurnace [1] which allows self-consistent treatment of the data obtained by different IBA techniques from a given sample, applying the idea of Total IBA [2]. More detailed information about NDF and its use is given in Annex I.

1.1.1 Rutherford Backscattering Spectroscopy (RBS)

Rutherford Backscattering Spectroscopy or *RBS* is the most common IBA technique. It is used to do a quantitative elemental – and isotopic – characterisation of matter, being able to extract thickness information and depth homogeneity. The measurements are direct and absolutely quantitative so in principle standards are not needed, although in practice it is common to use an standard sample to determine the detector solid angle.

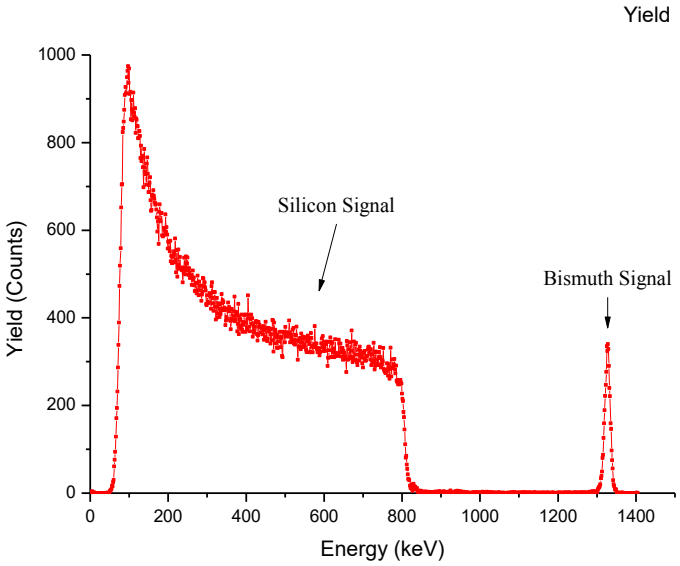

Figure 2: RBS ($^4He^+$ - 1500 keV normal incident beam at 165° scattering angle) spectra of bismuth thin film (peak between 1300-1350 keV) on silicon substrate (lower energy, up to 800 keV).

The backscattering ions arrive at the particle detector where their energy is deposited giving rise to a charge pulse, of magnitude proportional to the ion energy, for each ion. Charged particle detector operation is presented in more detail in Chapter 2. A typical RBS energy spectrum is shown in Figure 2. The backscattered particle energy depends on the elastic collision with the target nucleus and the energy lost along the path (ingoing and outgoing) inside the sample, mainly due to collisions with electrons. The probability for an incident particle to be backscattered is given by the Rutherford Backscattering Cross Section (σ).

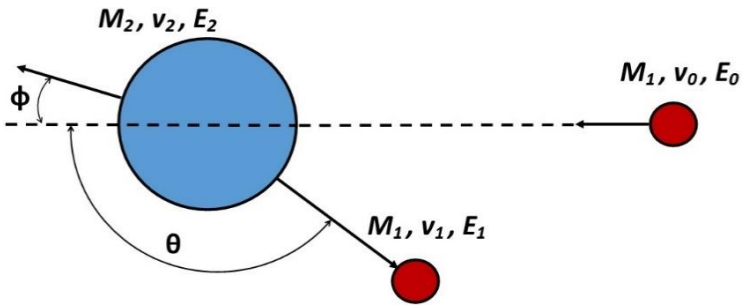

Figure 3: Schema elastic collision. Where $E_{0,1,2}$ is energy, $M_{1,2}$ mass and $v_{0,1,2}$ velocity for the incident particle and target, while θ and ϕ are angles, in the laboratory frame.

The incident ion energy are at relatively low energy (500-5000 keV), i.e. it is a non-relativistic system and therefore the interaction between incident ion and target nuclei is a classical mechanics elastic collision. In Figure 3 is represented the simple elastic two-body collision, which is expressed as the conservation of energy and momentum

$$E_0 = E_1 + E_2 \Rightarrow \frac{1}{2}M_1 v_0^2 = \frac{1}{2}M_1 v_1^2 + \frac{1}{2}M_2 v_2^2 \qquad 1.1$$

$$\vec{p}_0 = \vec{p}_1 + \vec{p}_2 \Rightarrow \begin{cases} M_1 v_0 = M_1 v_1 \cos\theta + M_2 v_2 \cos\phi \\ 0 = M_1 v_1 \sin\theta + M_2 v_2 \sin\phi \end{cases} \quad 1.2$$

Through the equation 1.1 and 1.2 is obtained:

$$\frac{v_1}{v_0} = \left(\frac{(M_2^2 - M_1^2 \sin^2\theta)^{1/2} + M_1 \cos\theta}{M_2 + M_1} \right) \Rightarrow \quad 1.3$$

$$\Rightarrow \frac{E_1}{E_0} = \left(\frac{(M_2^2 - M_1^2 \sin^2\theta)^{1/2} + M_1 \cos\theta}{M_2 + M_1} \right)^2 \equiv K \quad 1.4$$

Where *K* is known as *Kinematic factor*.

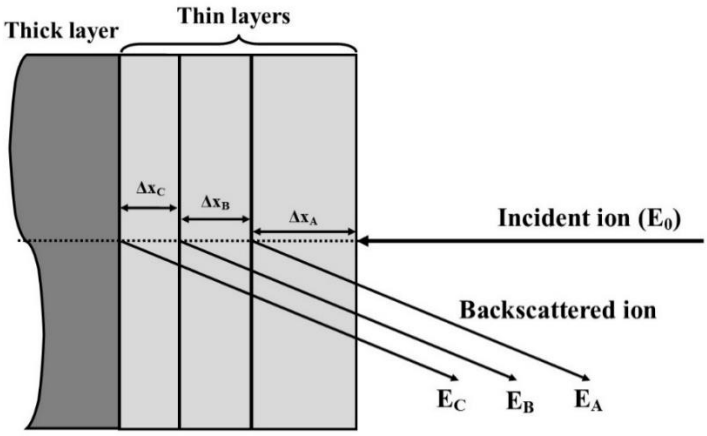

Figure 4: Three element/compound (A, B, C) thin layers on thick layer substrate target; incident and backscattered ion beam. $\Delta E = E_0 - E_{n=A,B,C\ldots}$

However the incident particle penetrates into the sample, losing some energy, until the particle-nuclei collision occurs (Figure 4). The *Stopping Power*, $\mathrm{d}E/dx$, which represents the average energy loss per unit length, is the physical quantity to take this fact into account. Here it is convenient to introduce the concept of *stopping cross section*, s, which is simply the stopping power per atom. It has two different components: 1) due to the electronic cloud (*electronic stopping power*) and 2) related to the nuclear collision (*nuclear stopping power*). The *electronic stopping power* is an inelastic interaction due to generation of plasmons (collective electron excitations) and single ion-electron (localised) interactions. The equation 1.5, Bethe (1930), established an approximation taking into account the first order quantum perturbation and non-relativistic velocities [3] which can give us a fairly accurate estimate.

$$s_e = \frac{1}{N}\frac{\mathrm{d}E}{dx}\bigg|_e = \frac{4\pi Z_1^2 e^4 N Z_2}{m_e v_1^2} \ln\frac{2m_e v_1^2}{I} \quad 1.5$$

Where I is the target averaged ionisation potential – since this process is ionising the matter along the incident particle path– which can be taken from experimental data or calculated by dipolar oscillator forces, as was done by Bloch (1933) [4].

On the other hand, the nuclear stopping is related to the elastic interaction with the atom, which has much lower cross section. Nevertheless the implications for the incident ion path can be very important. It is responsible for the ion scattering, in any direction – including the backscattering process which is the main interaction in RBS – changing the trajectory dramatically. Here the interaction is coulombian – it is a non-ionising interaction – but the electrons which are bound to the nucleus cannot be ignored since they may screen the nuclear charge from the ion. Screening corrections to the Rutherford cross section are introduced by Ziegler (1988) [5], Andersen (1980) [6] or L'Ecuyer [7] to cite just three. The s_n values are tabulated using experimental data or may be calculated by computer simulation methods such as the widely used semiempirical binary collision approximation (TRIM/SRIM [8]) and, less used, molecular dynamics simulation [9].

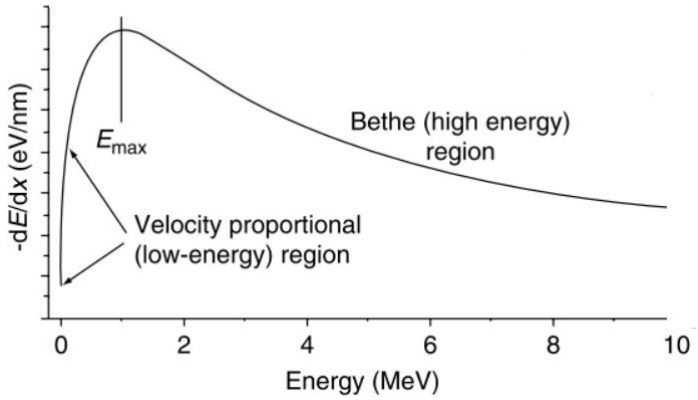

Figure 5: Example of electronic stopping power using the Bethe formula for incident high energetic $^4He^+$ in Ni [10].

In the non-relativistic regime $s = s_e + s_n \Rightarrow \frac{dE}{dx} = \left.\frac{dE}{dx}\right|_e + \left.\frac{dE}{dx}\right|_n$, where the stronger term is s_e due to the higher number of interaction (assuming SRIM for 2 MeV alpha ion beam ($^4He^+$) in Ni: s_e= 619.2 keV/µm and s_n= 0.7 keV/µm). Assuming that dE/dx is known for a given target and incident ion type and energy, an energy-depth relationship is established in Equation 1.6.

$$x_n = \int_{\bar{E}_{n=A,B,C\ldots}}^{E_0} \left(\frac{dE}{dx}\right)^{-1} dE = (E_0 - E)\left(\frac{dE}{dx}\right)^{-1}\Bigg|_{\bar{E}_n} \qquad 1.6$$

Where $\bar{E}_n$ is the average energy, $\bar{E}_n = \frac{1}{2}(E_n + E_0)$, n being each element/compound. When a film is composed of a mix of element A_i in proportions a_i so that the composition is $A_1a_1A_2a_2$ ..., with $\sum_i a_i = 1$, the Bragg rule of linear additivity may be applied to estimate the compound stopping power s_c from the elemental stopping powers s_i:

$$s_c = \sum_i a_i\, s_i \qquad 1.7$$

It is the basic relationship between the energy and the depth, which makes RBS a powerful technique in films characterisation and material science.

The energy loss is the result of a large number of energy loss events between the particle and the electrons of the solid (here we ignore the nuclear contribution which is negligible for the light ions and energies used in RBS). The number of such interactions follows a Poisson distribution, and in each event the energy lost follows a probability distribution. These two probability distributions thus lead to variations in the actual energy lost for each ion traversing a given material thickness. This is called energy straggling, and we denote the distribution for the loss of energy u after traversing a thickness x of matter by $g(u;x)$. In the cases encountered here, $g(u;x)$ may be assumed to follow a Guassian distribution of which the standard deviation σ_g may be estimated from

$$\sigma_g = \Omega\sqrt{x} \qquad 1.8$$

Where Ω is termed the straggling constant. The straggling constant may be estimated theoretically, although good measurements are more reliable then the theoretical estimates. Bohr (ref) derived the straggling constant for the idealised case of free electrons to be $\Omega_B = 8.85$ keV/(mg/cm^2)$^{1/2}$. If elemental straggling constants are known, they may be linearly combined with an analogie of the Bragg rule for stopping powers.

Focusing in the ion-nucleus interaction, we have seen that the amount of energy transferred (kinematics) is shown in Equation 1.4 and the interaction is through Coulomb potential (with screening correction). We now consider the frequency of these interactions – i.e. their *differential scattering cross section* $d\sigma/d\Omega$, which takes in account both the Rutherford scattering cross section[5] (σ) and the detector solid angle (Ω), Equation 1.8 shows the expression where N is the number of atoms per cm² in the target, x is the target thickness, N_i number of incident particles, $Z_{1,2}$ incident and target atomic number and e is normalised electron charge[6].

$$\frac{d\sigma}{d\Omega} = \frac{1}{Nx}\left(\frac{(dN_i/d\Omega)}{N_i}\right) = \qquad 1.9$$

[5] Lord Ernest Rutherford (1871-1937) used a classical coulomb interaction to describe in 1911 [104] the backscattered alpha particles observed by his students, Hans Geiger and Ernest Marsden, in 1909 [105] and thus he gave us the first proof of the atomic nucleus. In the Geiger-Marsden experiment a radium alpha source was placed in front of foils of several materials and they measured the scintillations produced by the backscattered alpha particles in a zinc sulphide screen. They observed a very small number of these backscattered particles compared with the transmitted and lightly deflected particles, and further noted an increase in the alpha yield from targets of larger atomic number and from thicker foils. Rutherford explained this fact by a positive-positive repulsion due to coulomb force, which could be just possible if a very small positive charged zone were in the atoms of the foils, contrary to the Thomson model, which supposed a great positive ball with small negative zones within it. The Rutherford model was improved by Niels Bohr in 1913 taking in account quantum mechanics [18, 19, 20] giving the Rutherford-Bohr atomic model well implanted nowadays.

[6]Throughout this thesis we use $e^2 = \frac{q_e^2}{4\pi\varepsilon_0} = 14.4\ keV\ cm = 14.4\ eV$ Å , where q_e is the electron charge

$$= \left(\frac{Z_1 Z_2 e^2}{2E_i}\right)^2 \frac{4}{\sin^4\theta} \left\{ \left[1 - \left(\left(\frac{M_1}{M_2}\right) \sin\theta \right)^2 \right]^{\frac{1}{2}} + \cos\theta \right\}^2 \left\{ \left[1 - \left(\left(\frac{M_1}{M_2}\right) \sin\theta \right)^2 \right]^{\frac{1}{2}} \right\} \quad 1.10$$

This equation can be simplified when $M_1 \ll M_2$, giving Equation 1.11:

$$\frac{d\sigma}{d\Omega} \approx \left(\frac{Z_1 Z_2 e^2}{2E_i}\right)^2 \left[\sin^{-4}\frac{\theta}{2} - 2\left(\frac{M_1}{M_2}\right)^2 \right] \quad 1.11$$

This statistics of the number of detected particles follows a Poisson distribution, since the probability, cross section, is small and the events are independent. The standard deviation of a Poisson distribution is the square root of the mean, and this uncertainty limits the precision with which an RBS measurement may be performed. For example, to determine the area of a peak to within 1% precision requires at least 10000 events to have been recorded in the peak.

Finally, a schematic RBS system is shown is Figure 6. Here the detected particles are the backscattered ones, hence the θ is large (between 140° to 170°) in order to get the maximum which is led by the cross section. The total number of detected particles (N_d) is expressed in Equation 1.12 where α is the incident beam angle:

$$N_d = \frac{\sigma\Omega \cdot N_i \cdot Nx}{\cos\alpha} \quad 1.12$$

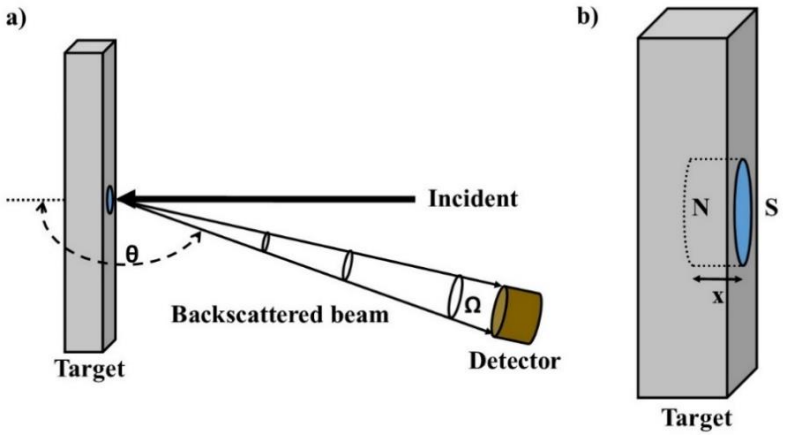

Figure 6: a) General RBS schema: the incident ion beam impact with the sample (target) and ions are backscattered to the detector with a frequency given by $d\sigma/d\Omega$; b) incident beam zone in target; beam surface S and x is penetration distance; N is the number of atoms per unit volume.

1.1.2 Channelling

The next IBA configuration introduced is *Channelling*. Actually channelling is a phenomenon that can occur for any IBA technique, however we are going to present just the RBS case – in which the sample holder is installed on a goniometer in order to align the ion beam with an axis or plane of a monocrystalline material. It is a powerful technique to study crystalline material surfaces, lattice order and non-ionising ion damage (see Annex II: Ion Damage). Unlike diffraction techniques – X-Rays or electrons – channelling is the result of highly local interactions and is best described in real space. Explanations about the physical behaviour in this configuration will be done below.

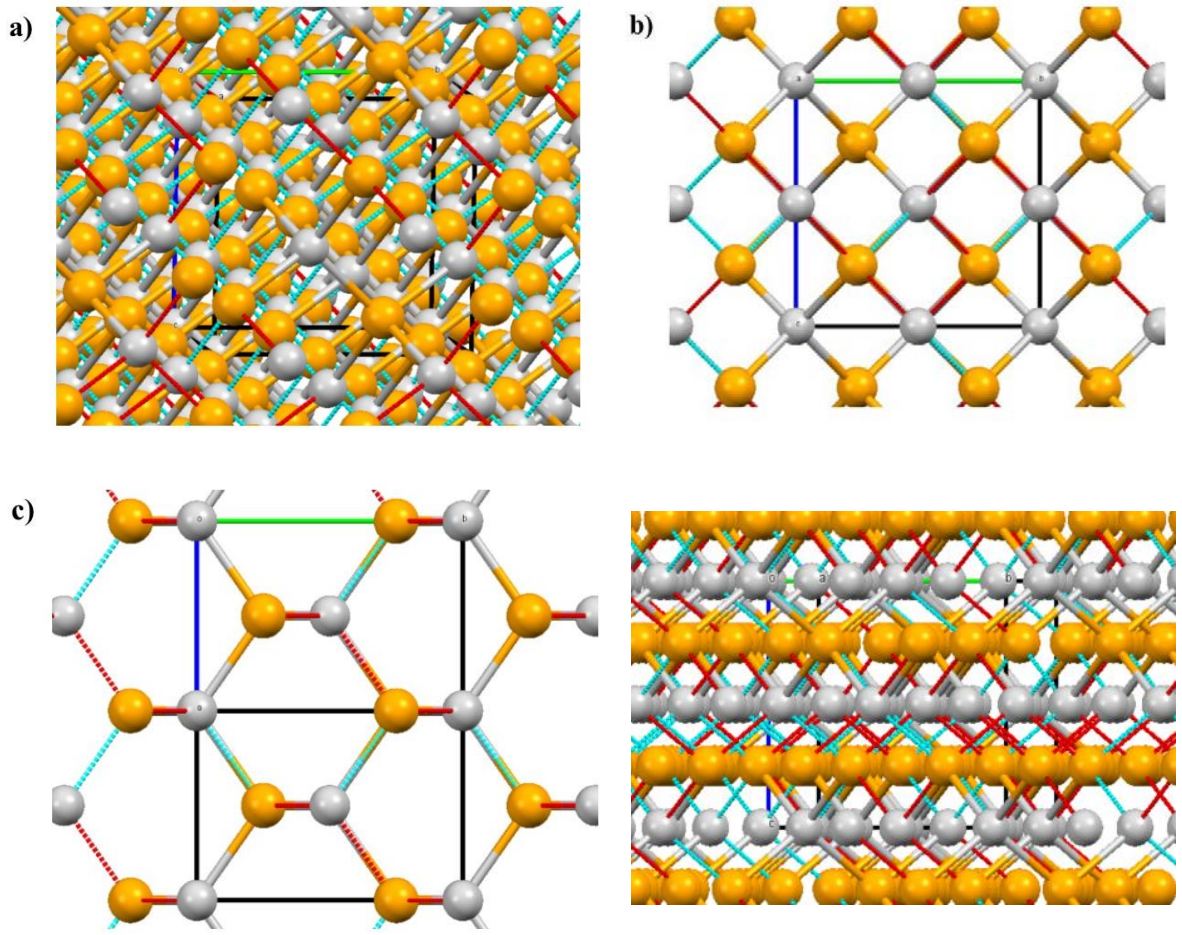

Figure 7: GaAs atomic structure a) in random configuration, b) channelled in axis <0 0 1>, c) channelled in axis <1 0 1> and d) plane [0 0 1]

In a non-channelled single crystal RBS measurement, the sample has to be oriented well away from any major crystalline axis or plane, so that all the incident ions can see all the atoms in the sample with the same probability[7]. This configuration is called *random* and it is illustrated in

[7] A perfect random is quite complicated to get and an accurate angle scan has to be done. In practice a quick angle scan is enough and some channelling corrections are implanted in the offline data treatment.

Figure 7.a for GaAs. When the ion is aligned with an axis (Figure 7.b and c) or planes (Figure 7.d) we are in the *channelling* configuration.

1.1.2.1 Surface peak

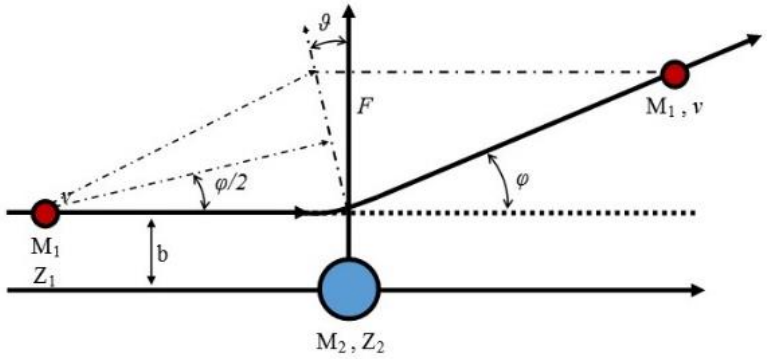

Figure 8: Scattering interaction between ion and first atomic layer

The ion flux is uniform and there is no shadowing for the first atomic layer and so this layer always contributes fully to the backscattering yield. By considering the deflections from the ions in the first and successive layers, we can estimate the probabilities of scattering from the successive atomic layers. Let us first consider just the surface atomic layer. As in RBS the interaction, channelling is ruled by the Coulomb force, hence the incident ions will be scattered with an angle φ (Figure 8) where the momentum difference is

$$\Delta p = 2M_1 v \sin\left(\frac{1}{2}\varphi\right) \tag{1.13}$$

And

$$\Delta p = \int F\cos(\vartheta)\,dt = \int \frac{Z_1 Z_2 e^2}{r^2}\cos(\vartheta)\,d\vartheta\,\left(\frac{dt}{d\vartheta}\right) \tag{1.14}$$

Using the angular momentum conservation we can write r as a function of ϑ

$$M_1 r^2 \frac{d\vartheta}{dt} = M_1 v b \implies r^2 = vb\frac{dt}{d\vartheta} \tag{1.15}$$

Substituting in Equation 1.14 and changing $\vartheta = \frac{\varphi}{2} + \frac{\pi}{2}$ we obtain

$$\Delta p = \int \frac{Z_1 Z_2 e^2}{vb}\cos\left(\varphi - \frac{\pi}{2}\right)d\varphi = \frac{2\,Z_1 Z_2 e^2}{vb}\cos\left(\frac{\varphi}{2}\right) \tag{1.16}$$

The combination of 1.13 and 1.16 gives

$$\tan\frac{\varphi}{2} = \frac{2\,Z_1 Z_2 e^2}{M_1 v^2 b} = \frac{Z_1 Z_2 e^2}{2E_i b} \tag{1.17}$$

Where E_i is the incident ion kinetic energy. Further in the ion trajectory, the ion will interact with the second atom along the atomic row, which is a distance d from the first one. The ion position there is expressed as

$$r_2 = b + \varphi d \tag{1.18}$$

In the Equation 1.17 we found an expression for the scattering angle as a function of the impact parameter b[8]. It is reasonable assume that the angle φ is small enough to consider that $\tan\varphi \approx \varphi$, therefore Equation 1.18 can be rewritten as

$$r_2 = b + \frac{Z_1 Z_2 e^2 d}{Eb} \tag{1.19}$$

Thus a shadowing effect is generated, with cylindrical symmetry, due to the first atom as is shown in Figure 9. It is possible to calculate the radius for this *shadow cone* (R_C) through the r_2 minimum

$$\left.\frac{dr_2}{db}\right|_{R_C} = 0 \Longrightarrow R_C = \sqrt{\frac{4Z_1 Z_2 e^2 d}{E}} \tag{1.20}$$

The shadow cone will generate a forbidden zone which depends on the interatomic spacing along the row, where no ion can penetrate and it is, ultimately, the cause of the surface peak existence. It has a value of the order of 10^{-1} Å.

Furthermore we can also express the ion fluence distribution, $f(b)$, as a function of incident fluence Φ_0, and the impact parameter b

$$f(b) = \begin{cases} 0 & r < R_C \\ \Phi_0 \frac{b}{r}\frac{db}{dr} & r > R_C \end{cases} \tag{1.21}$$

[8] This concept has been applied, although not shown, in the previous section about RBS. It is included in the electronic stopping power, the Rutherford cross section and straggling disertations.

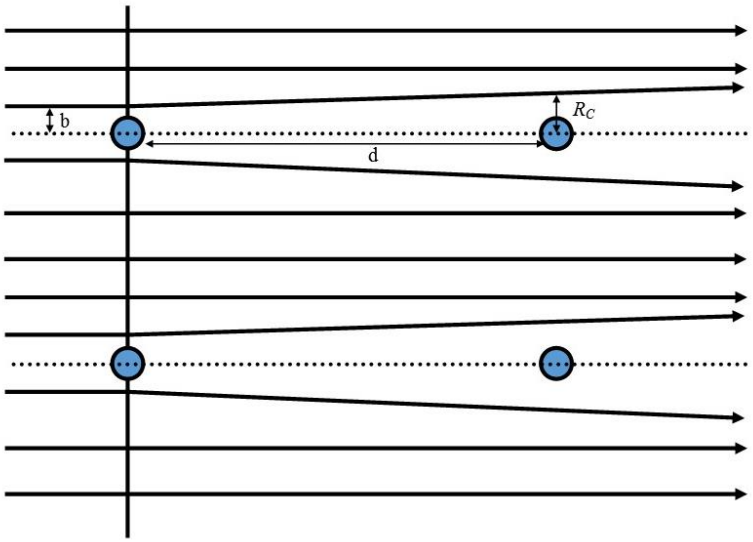

Figure 9: Incident ion fluence distribution in the two first layers

However the explanation above is just valid to have a qualitative idea of the channelling process in the material surface since there is not taken in account a) the vibrations of the atomic nucleus in a lattice; where the amplitude is within 10^{-1} - 10^{-2} Å, hence it is close to the R_C values, and b) the screening corrections in the Coulomb force due to the atomic electrons.

Thermal vibrations in crystalline solids can be explained by the Debye model [P. Debye, 1912] where there are three vibrations modes (one longitudinal and two transversals) in the Bravais lattice with frequency ω^* and state (modes) density associated $g(\omega^*)$ [11]. The probability density of these modes, ρ, is ruled by Bose-Einstein statistics [S. Bose, 1920 and A. Einstein, 1924] and, when the system is in thermodynamic equilibrium and in contact with a thermostat at temperature T, that density is expressed as a Gaussian [12]. It can be projected on one random direction, here will use u_{1D}, allowing us to have an analytical expression and extract the displacement average using the Debye-Waller factor, W, [13] as follows

$$\langle u^2 \rangle^{1/2} = \left\{ \frac{3\hbar^2}{k_B M_2 \Theta_D} \left[\frac{1}{4} + \frac{T}{\Theta_D} W\left(\frac{\Theta_D}{T}\right) \right] \right\}^{1/2} \qquad 1.22$$

Where the values ($\langle u^2 \rangle^{1/2} = \langle x^2 \rangle^{1/2} = \langle y^2 \rangle^{1/2} = \langle z^2 \rangle^{1/2}$ or combinations) are between 0.05 and 0.2 Å. If $\langle u^2 \rangle^{1/2} \ll R_C$ the ion path will not be perturbed by the second atom. However if $\langle u^2 \rangle^{1/2} \approx R_C$ the ion will be likely scattered once again, until the ion position r_i, where i indicates the atom number or atomic layer if we are in 3-D, where big enough in comparison with the lattice vibration displacement. Thus channelling is a great technique to characterise material surfaces, as we will see below[9].

[9] Debye Model is convenient to have a first approximation understanding of the lattice vibration behaviour, however it is not completely realistic since the displacements considered above are isotropic and axis independent, but actually they are not. Monte Carlo calculations are needed to take in account these correlated displacements.

The screening effect will change the potential seen by the ion, which will no longer be purely Coulomb, so the angle φ and R_C calculations will be affected. A reasonable correction, but not unique, is to apply the Thomas-Fermi Model (L. Thomas and E. Fermi, 1927) for the atomic potential with the Molière approximation (G. Molière; 1947), where the potential is expressed as follows

$$U_M(r) = \frac{Z_1 Z_2 e^2}{r}\left(0.1e^{-\frac{6r}{a}} + 0.35e^{-\frac{0.3r}{a}} + 0.55e^{-\frac{1.2r}{a}}\right) \quad 1.23$$

Where a is the Molière screening radius which depends with the Bohr's radius a_0 as follows

$$a = 0.8853a_0\left(Z_1^{1/2} + Z_2^{1/2}\right)^{-2/3} \xrightarrow{Z_1 \ll Z_2;\, E \approx 1\, MeV} a = 0.8853a_0(Z_2)^{-1/3} \quad 1.24$$

From here we obtain the Molière Cone radius R_M where $R_M/R_C \geq 0.8$ [14].

Once the corrections are applied, the number of atoms per row can be calculated, so a surface characterisation can be done. The yield for the first two atoms will be given by the convolution of the ion fluence, Equation 1.21, and the position distribution, $P(\vec{r})$, which is a Gaussian function. Unfortunately this convolution has no analytical solution further than the third atom in the row due the complexity of $r_i(b)$ when the corrections are included (Equation 1.18). To get analytical results Monte Carlo calculations have to be done obtaining the yield per atom in the row. This is called *Close Encounter Approximation* [15] where the fluence; uniform and perpendicular to the surface plane, has a Dirac distribution with $\delta(\vec{b}_n)$, for an incident particle n; giving a *normalised yield* of backscattering particles for one atom

$$\chi = \sum_{n=1}^{\mathfrak{N}} \int f(\vec{b}_n) P(\vec{b}_n) d\vec{b}_n = (2\pi N_V d\mathfrak{N}\langle u_{1D}^2\rangle)^{-1} \sum_{n=1}^{\mathfrak{N}} e^{-\frac{|\vec{b}_n|^2}{2\langle u_{1D}^2\rangle}} \quad 1.25$$

Where $\mathfrak{N}$ is the number of interactions and N_V the volumetric atomic density[10]. To note that an associated area with a radius R_0 around the row can be defined which gives us a geometrical radial symmetry as:

$$\pi R_0^2 = \frac{1}{N_V d} \quad 1.26$$

Extending χ for all the successive atoms, indicated by j, we obtain an expression for the atoms per row, L, which indicate the number of measured atoms in RBS-channelling corresponding to the material surface. Some results are shown in [11, 12].

[10] There is expressed $\langle u_{1D}^2\rangle$ as the thermal vibrations in one dimension, from here will be distinguish the vibration amplitude depending the degrees of freedom.

$$L = \sum_{j=1}^{\infty} \chi_j \qquad 1.27$$

From the experimental point of view, it is measured by the areal integration of the surface peak, subtracting a triangle which base is the line between the peak centre (E_p) and the minimum energy peak (E_M), and the height is the yield in E_M as it is shown in Figure 10. The limit in the measurement is given by the detector resolution (see Subsection 2.1.1).

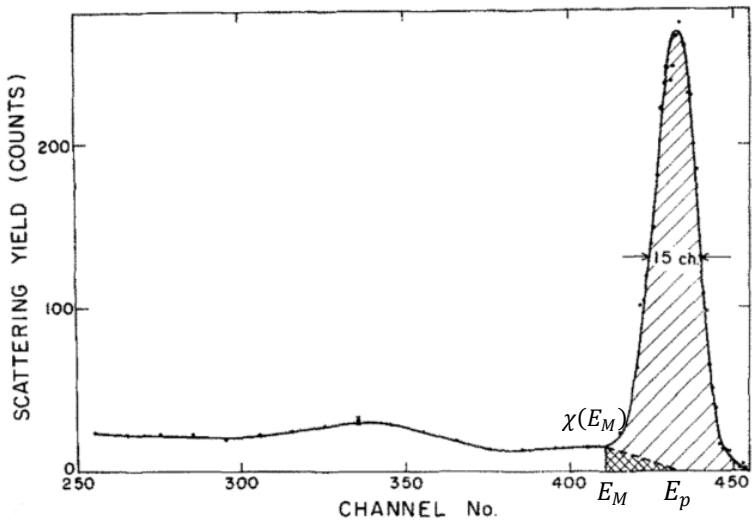

Figure 10: RBS-Channelling spectrum for 2 MeV He^+ ion beam on Pt <1 1 0> axis. Striped area corresponds to the atoms in the surface [16].

1.1.2.2 Beyond the surface peak

The above description involves the first atomic layers (~5 nm), where the characteristic surface peak is created. After that the ion propagates through the crystal via the interatomic row channels. This was described by Lindhard [17] using quasi continuum potential, $U_L(r)$, along the atomic rows, known as *Continuum Model*, instead of the binary interaction.

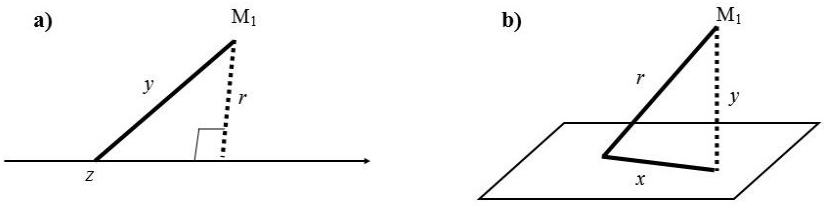

Figure 11: Channelling geometries a) axial channelling, where the axis z generates the linear potential in the ion M_1 and b) planar channelling, where the plane x-z generates the planar potential in M_1.

Channelling can be done in two geometries, axial and planar (Figure 11). For axial channelling, the continuum potential is written by

$$U_{LL}(r) = \frac{Z_1 Z_2 e^2}{d} \ln\left(1 + \left(C \cdot \frac{a}{r}\right)^2\right) \quad 1.28$$

Where $y^2 = r^2 + z^2$, C is a numerical coefficient, close to 3, and a is the Molière screening radius. There the atomic row is seen as a continuous single string with a screening effect (logarithmic part) due to atomic electrons. For planar channelling the average density of charge is $\sigma = Z_2 e N_V d_p$, with d_p interplanar distance, and $r^2 = y^2 + x^2$, hence the potential is

$$U_{LP}(y) = Z_1 Z_2 e^2 d_p N_V (\sqrt{y^2 + C^2 a^2} - y \quad 1.29$$

The projection of the ion momentum in the transverse plane, $p_\perp$, for small incident angle ψ is proportional to the it, $p_{\perp L} = p_r = \psi p$ for axial and $p_{\perp P} = p_y = \psi p$ for planar, and supposing no energy losses, we can apply energy conservation to obtain

$$E_{\perp L} = \frac{p_\perp^2}{2M_1} + U_{LL}(r) = E\psi + U_{LL}(r)$$
$$E_{\perp P} = \frac{p_\perp^2}{2M_1} + U_{LP}(y) = E\psi^2 + U_{LP}(y) \quad 1.30$$

Where $E_\perp$ is the *transverse energy*. The longitudinal energy $E_\parallel$ is just kinetic since it is related to the motion along the channel, $p_\parallel$, as it is shown in Figure 12. For an axial channelled particle, the movement along the channel is an anharmonic oscillation within it. In the planar case it is approximately harmonic.

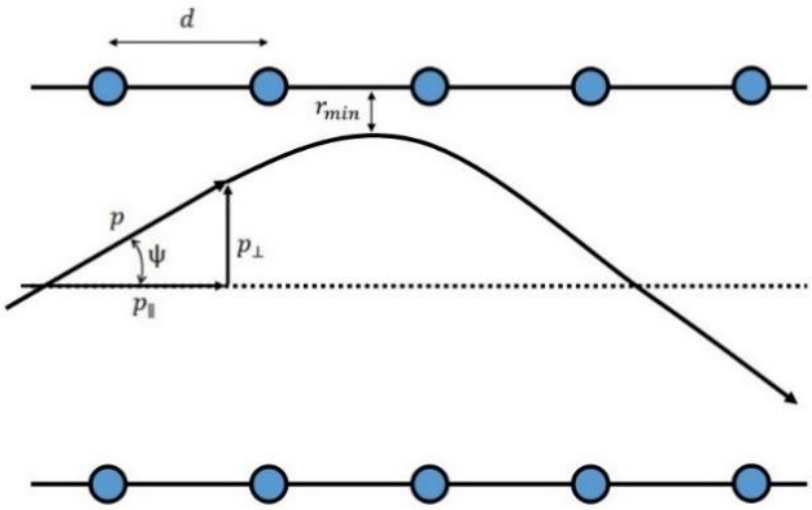

Figure 12: Incident ion momenta schema

The minimum ion distance of approach to the row, is r_{min}, where $\psi = 0$. It is taken equal to the average lattice vibration amplitude, so from Equation 1.22 $r_{min} = 2\langle u_{2D}^2 \rangle^{1/2}$. We can define the maximum inclination for an incident ion from where it can start to be channelled. An ion

has a potential $U_L = 0$ just before it interacts with the sample, therefore applying the transverse energy conservation through Equation 1.30

$$E_{incident} = E_{r_{min}} \Longrightarrow E\psi_c^2 = U_L(r_{min})$$

$$\psi_c = \sqrt{\frac{Z_1 Z_2 e^2}{Ed} \ln\left[1 + \left(\frac{Ca}{r_{min}}\right)^2\right]} = \frac{\psi_1}{\sqrt{2}} \ln\left[1 + \left(\frac{Ca}{r_{min}}\right)^2\right]^{1/2} \quad 1.31$$

Which is called the *critical incident angle*. If $\psi > \psi_c$ channelling will not happen. Also we define ψ_1 as the critical angle in the first order approximation for light and fast ions. Doing an analogue procedure for planar channelling equation 1.32 is obtained

$$\psi_c = \sqrt{\frac{2\pi N_V d_p Z_1 Z_2 e^2}{E} [(\langle y^2 \rangle + C^2 a^2)^{1/2} - \langle y^2 \rangle^{1/2}]} \quad 1.32$$

Experimentally the measurement of the critical angle is made through the close encounter probability yield as function of the incident angle measured by the goniometer, $\chi(\psi)$. There we have to take the *angular width at the half minimum*, $\psi_{1/2}$, i.e. $\chi(\psi_{1/2}) = 1/2$, as is shown in Figure 13. In the figure we can note a normalized yield higher than 1 in the wings of the angular distribution. This is because of the higher fluence around the rows which generates a bigger scattering contribution. Critical angles calculated this way overestimate measured values by about 15% [14], which is rather good given the various approximations that we have used. Due to the dependence with d, the critical angle can be used to define the lattice structure of the sample.

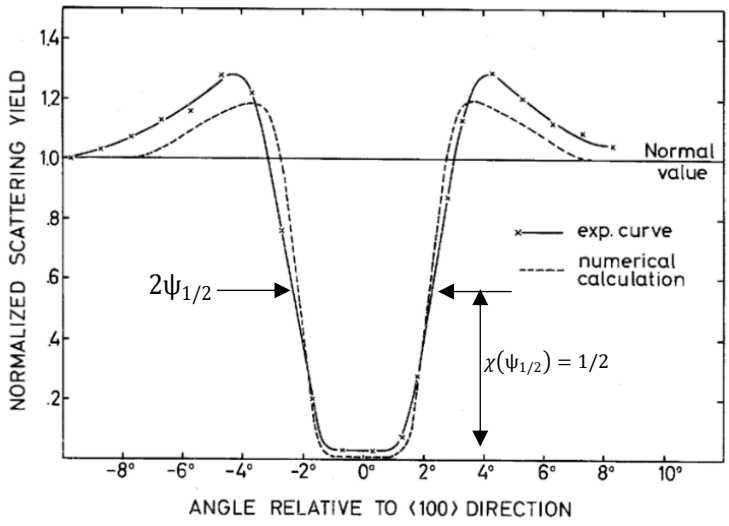

Figure 13: Yield as function of the incident angle, $\chi(\psi)$, for 480 keV protons on W crystal along <1 0 0> axis [14]

To complete the channelling parametrisation is necessary to introduce the definition of *minimum yield*. It is the physical quantity which will give the amount of disorder and corresponds to the minimum backscattered particle yield within the interatomic row channels.

In axial geometry, the reference [14] shows that for a parallel incident ion ($\psi = 0$) with a fluence $f(r)$ and position distribution $P(r)$ – analogue to Equation 1.25 – the minimum yield χ_{min} is:

$$\chi_{min}(\psi = 0) = \int_0^{R_0} f(r)P(r)dr = \int_0^{R_0} \ln\left(\frac{R_0^2}{R_0^2 - r^2}\right) \cdot \frac{r}{\langle u_{2D}^2 \rangle} e^{-\frac{r^2}{2\langle u_{2D}^2 \rangle}} dr = \\ = \frac{\langle u_{2D}^2 \rangle}{R_0^2} = 2\langle u_{2D}^2 \rangle N_V \pi d \quad 1.33$$

In an experiment, this parameter can be measured integrating an energy window in the RBS channelling spectrum just before the surface peak, on the bulk zone, and dividing the area by the random spectrum area in same window, i.e. $\chi_{min}^{exp} = \chi_{cha}/\chi_{rdm}$.

Experimental measurements give an underestimation of factor of about 3 in comparison with the calculations. A correction to solve this deviation, based on numerical simulations using the Molière potential, without continuum model or transverse energy conservation, was introduced by Barrett (J.H. Barrett, 1971). It is shown in [15].

The minimum yield provides us a lot of information about crystal quality. The minimum yield may increase due to *dechannelling*, which depends on the thermal vibrations and electronic stopping power – and is therefore present even in an ideal monocrystal – as well as the displaced atoms due to defects. Defects can be localised, such as interstitial atoms or extended such as dislocations, stacking faults, or amorphous zones. Characterising the dechannelling effects can give remarkable information (qualitative and quantitative) about the crystal structure. Furthermore, channelling effects can also occur for the outgoing particle. If the detector is placed at an angle corresponding to a major axis or plane (Figure 14) then the yield is further reduced due to blocking effects. In the case of dual channelling and blocking alignment the number of backscattered particles further decreases and the minimum yield is reduced quadratically. $\chi_{min}^{Dual} = \chi_{min}^2$.

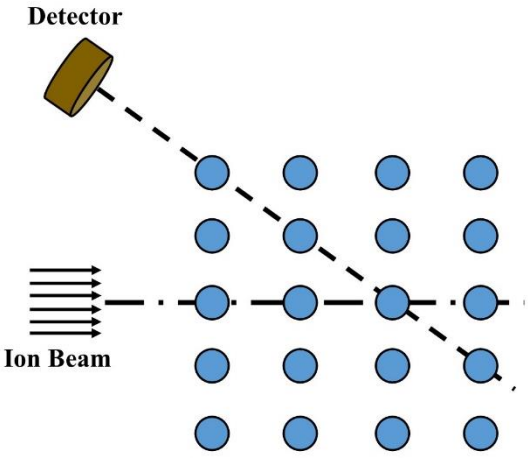

Figure 14: ion beam and particle detector aligned with two different crystal axis to generate the blocking effect.

More detailed information and examples can be found in [16], [18], [19].

1.1.3 Particle Induce X-ray Emission (PIXE)

In *PIXE*, the X-rays generated when an inner shell electron is ejected and an outer electron takes its place shedding its energy via energetic X-rays in the process, are detected. The main information that can be extracted is the elemental composition for light-medium elements. The acquisition chain is different than that for RBS, since here an X-ray detector is used, which requires a different kind of preamplifier (more information about acquisition in Section 2.2), however after the preamplifier it is completely compatible with an RBS acquisition chain in parallel. Both techniques combined with the NDF Data treatment [1] are a powerful materials physics tool [2]. It also can be used with a microprobe, generating X-Y spatial maps, even in non-vacuum environments [20]. PIXE using an external beam has extended the range of samples able to be studied, beyond just material physics (or science), to archaeological samples (archaeometry) environmental samples or cultural heritage materials.

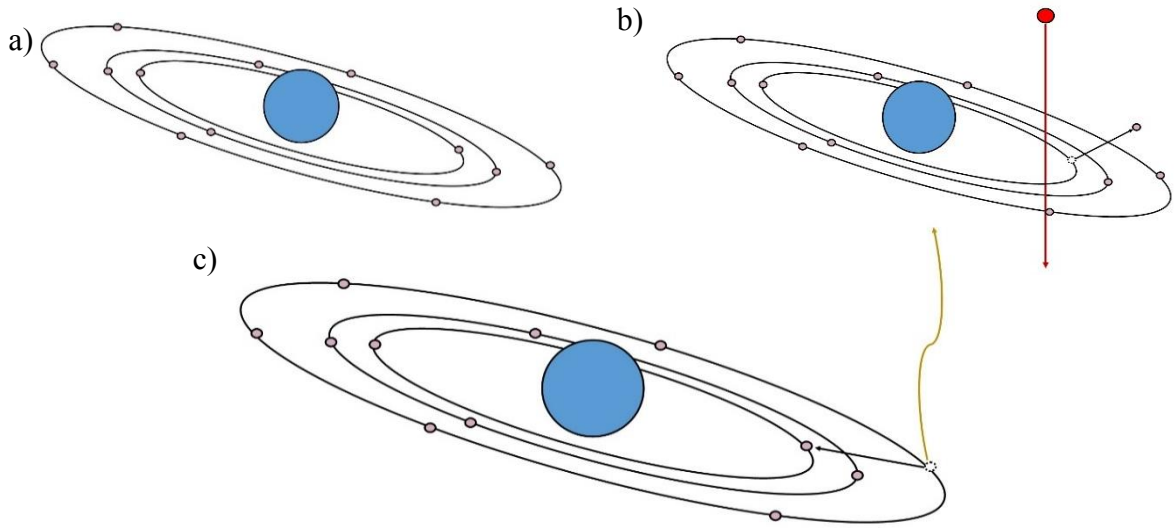

Figure 15: PIXE basic interaction: a) a sample atom, b) incident ion (red ball and its path is the red line) removes an inner electron, c) an outer electron takes the removed electron place emitting an X-ray (yellow line)

The X-ray production process (Figure 15) is initiated when the incident beam ionises the atom by ejecting an inner shell electron. The atom is then unstable, and the inner shell hole is filled by an electron from an outer shell, which sheds its energy in the form of an X-ray. Those X-ray energies are determined by the atomic electronic shell structure and are characteristic of the elemental species. Characteristic X-ray energies are tabulated in [21], and the nomenclature of the X-ray lines is shown in Figure 16.

The probability of X-ray generation is thus proportional to the *ionisation cross section*, σ_i. After the inner electron is removed one of three process can occur: production of fluorescence X-Rays, production of Auger electrons or Coster-Kronig transitions. *Fluorescence X-Rays* are the X-rays generated in the transition when an outer electron takes the place of the inner electron removed by the ion beam. *Auger electrons* (Auger, 1925) are emitted when the energy of the transition is no longer shed as an X-ray but rather transferred to another electron in the outer layer. The relative number of fluorescence X-rays is given by the *fluorescence yield*, ω. The relative numbers of transitions from the various outer shells is represented by the *relative*

transition probability, k. There can also be subshell transitions between outer shells. These are called *Coster-Kronig transitions,* (Coster and Kronig, 1935) and these probabilities are represented by *branching fractions*, b.

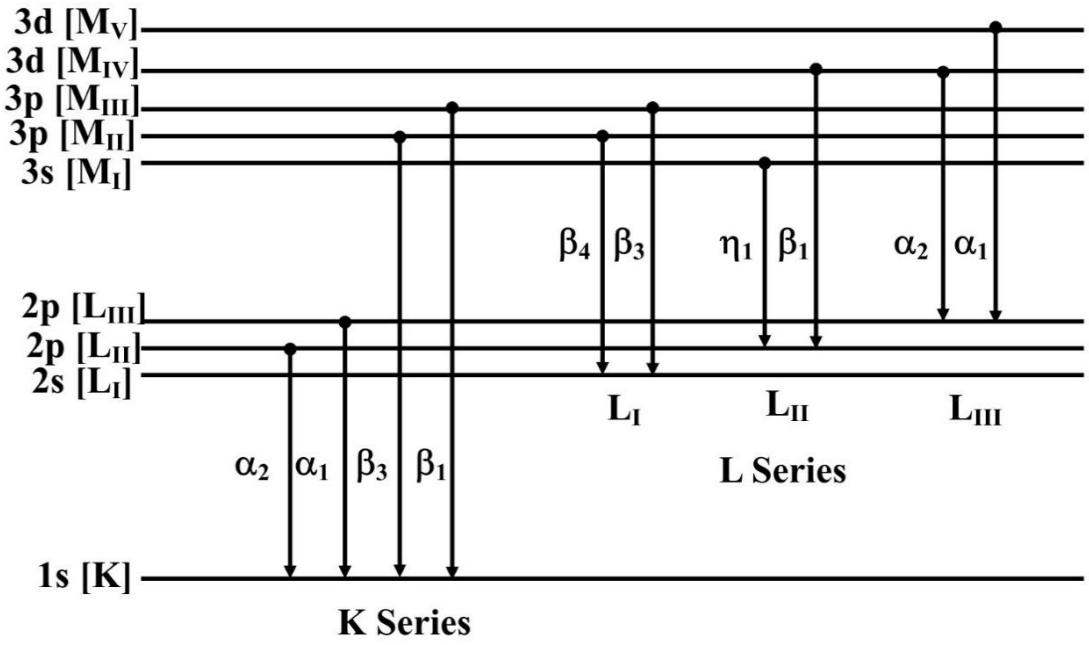

Figure 16: Atomic x-rays transmission

There are some models, for protons in K transitions [22]–[25], however when the subshells appear, the theory becomes very complicated and the results have to be constrained with the empirical data [26]–[29]. Anyway the next transitions (M, N…) are not so useful for PIXE since they overlap in the spectra and the uncertainly becomes difficult to manage.

The X-ray background is quite different to the particle background in RBS. In RBS, it is due to the backscattered ions which go deep in the substrate. In contrast for PIXE it is mainly due to the *bremsstrahlung effect*. This effect occurs as a result of the momentum changes of the incident ions and ejected secondary electrons. This is the source of one of the big advantages of PIXE over electron beam induced fluorescence. Protons are some 2000 times heavier than electrons, and so they suffer much less violent deceleration as they slowdown in the target, producing orders of magnitude less bremsstrahlung background since its cross section depends inversely on the mass square. Eventually, another source of background is the gamma rays emitted in nuclear reactions. The cross section of these background contributions is complicated to model – but there are some fair attempts [30] – therefore is necessary to use experimental data to supress it properly in the later analysis. The ejected electrons and secondary electrons generated by the ion beam are further sources of Bremsstrahlung. The three main contributions are Quasi-Free-Electron bremsstrahlung (QFEB), Secondary-Electron Bermsstrahlung (SEB) and Atomic Bermsstrahlung (BA). In QFEB the ions have high speed in comparison with the atomic electrons, hence they can be considered as free electrons. Their energy distribution is then given by classical kinematics and their spectrum contribution is at low energy ($\sim 1\ keV$) but with high intensity. The SEB occurs when the ejected electron losses energy through

Coulomb scattering within the target. This Coulomb interaction places the background signal in the medium part of the energy spectrum ($\sim 5\ keV$) with also medium intensity. The AB, in other hand, occurs when the electron comes back to the initial state. The contribution is across the whole PIXE energy spectrum but with a very low intensity.

The detector characterisation has to be done carefully in PIXE – here it is more critical than in RBS. A typical X-ray detector is the lithium drifted silicon (Si(Li)), which is a *p-i-n* diode of around 5 mm thickness. The i-type layer (insulator) is there in order to avoid high acceptor concentration. This detector has to be cooled down typically to liquid nitrogen temperature and biased at high voltage (-1000 V). A thin ohmic contact film is on the surface (To check *dead layer* concept see Subsection 1.1.5 and Section 2 below). A thin window, usually made of beryllium (tens of micrometre thickness) is needed to avoid backscattered ions reaching the detector and inducing damage, and interfering with the X-ray detection. In some cases, if the studied elements are heavy in a light elemental matrix for instance, an absorber is placed to eliminate the lower energetic X-rays where the bremsstrahlung background is higher. Often two detectors are used, with different windows, allowing optimal detection of both light and heavy elements. Detailed knowledge of the window thicknesses and composition, dead layer, and detector active zone thickness is necessary for reliable data analysis, since the detector *efficiency*, ϵ, depends on these elements [31].

Equation 1.34 describes the number of arriving X-rays in to the detector, where t is the absorber transmission factor, A atomic mass, N_{av} Avogadro's number, N target element concentration and $T(E)$ transmission factor related to the detector; remaining components have been presented above. However this equation is strictly valid for the two first X-ray lines (K and L) and does not take in account the secondary fluorescence.

$$N_D = \frac{N_{av}\ \omega\ b\ t\ \epsilon \left(\frac{\Omega}{4\pi}\right) N_I\ N}{A} \int_{E_0}^{E_f} \frac{\sigma_i(E) T(E) dE}{S(E)} \qquad 1.34$$

The usual PIXE spectra are treated with fitting tools (such as GUPIX [32], [33] or GeoPIXE [34]) which can subtract the background and the pile-up to convert the peak spectrum areas in elemental concentration. More information about PIXE and applications are in [16], [31].

1.1.4 Nuclear Reaction Analysis (NRA)

NRA is a technique which uses the exothermic nuclear reaction products to characterise target elements. The nuclear interaction here is neither elastic nor analytically described since it is ruled by quantum nuclear mechanics [35]. The instrumentation is very similar to that used for RBS and it is a technique complementary to those explained above, since the nuclear reaction cross sections primarily exist for light elements that cannot be measured otherwise. It is possible to include NRA data in NDF and thus to extend the self-consistent analysis to RBS, PIXE and NRA measurements (see Annex I: NDF DataFurnace and Total IBA).

The incident ion overcomes the nuclear coulomb barrier and interacts with the nuclei via nuclear potentials. The ion excites the nucleus, breaking the nuclear bonds and producing new elements

or isotopes. These may either be in the nuclear ground state or in an excited state; e.g. $^{28}Si(^{2}H^{+},H_0^{+})^{29}Si$ where ^{29}Si nuclei are the ground state while in $^{28}Si(^{2}H^{+},H_1^{+})^{29}Si$ the ^{29}Si atoms finish in the first excited nuclear state. Mass is not necessarily conserved. The energy consumed or produced in the reaction is labelled Q, so that $Q = [(M_1 + M_2) - (M_3 + M_4)]c^2$ and the reaction may be exothermic ($Q > 0$) or endothermic ($Q < 0$). The residual ejected particle (usually the light reaction product) energy is measured by the charged particle detector (Figure 17).

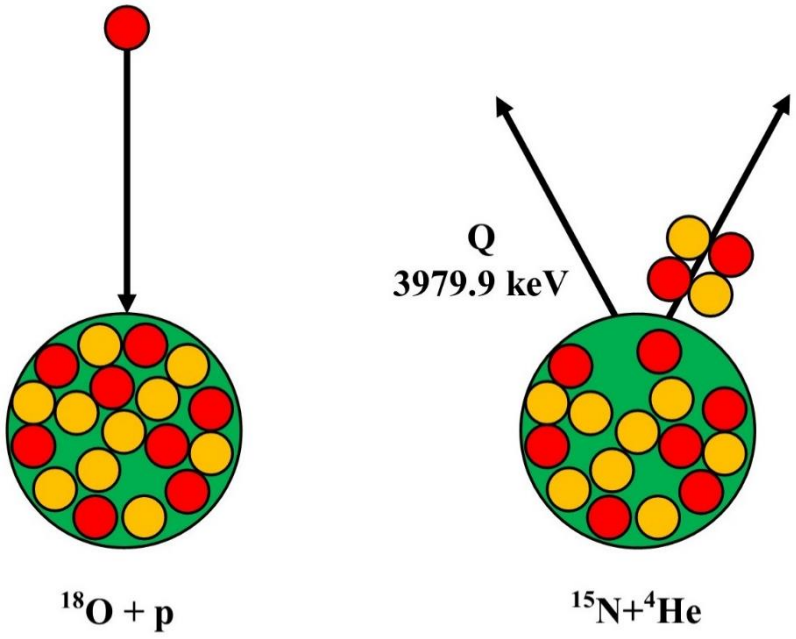

Figure 17: Ion-Nucleus reaction scheme for $^{18}O(H^{+},^{4}He^{+})^{15}N$. Yellow balls are neutrons and protons are red ones. This reaction is exothermic with a Q=3979.9 keV.

The cross section is no longer Rutherford, rather it is a non-analytical cross section with values up to 10^3 times smaller than the Rutherford, and hence NRA uses high ion fluxes in comparison to RBS, with typical ion current and beam spot around 200 nA and 2 mm diameter respectively. The NRA cross section has to be treated through the nuclear forces, which due to their quantum nature cannot be analytically described. Nevertheless there is a great experimental database provided by International Atomic Energy Agency (IAEA) constantly updated (IBANDL, https://www-nds.iaea.org/exfor/ibandl.htm). Moreover a semi-empiric cross section code, SigmaCalc is available, with reliable and useful results [36]. Nevertheless there are some common features with the RBS – EBS – that makes easier to understand and manage the information given by this technique. The particles detected follow the same Equation 1.12 as the RBS does. The stopping power has to be treated in the same way, since the nature of the ions is essentially the same.

NRA usually uses the light particle (proton, deuterium or alpha) produced in the nuclear reaction. For high Q values, this particle can have much higher energy than the backscattered particle measured in RBS previously shown. Particles with this amount of energy generate longer ionisation path within the detector that may be larger than the depletion zone thickness (see next Subsection 1.1.5 and 2.1.1) and the particle charge incompletely collected.

Furthermore due to the high incident ion flux the backscattered ions can overload the data acquisition, and so a foil of thickness sufficient to stop the backscattered particles, but thin enough to transmit the higher energy nuclear reaction products (5 to 50 μm) is placed in front of the detector. In exchange we obtain an extra stopping power contribution and the depth resolution is deteriorated. This configuration is called *Non-Resonant NRA* and it is very convenient to quantitatively characterise light elements or isotopes which cannot be measured with RBS. In the other hand *Resonant NRA* is the best to measure depth profiles of those light elements. Resonant NRA uses nuclear resonances at certain energy, e.g. 629 keV $^{18}O(H^+,{}^4He_0{}^+)^{15}N$, and varying the incident ion energy the depth profile can be obtained [37], [38]

Further NRA experimental setup information and physic explanation are in [16], [39].

1.1.5 Ion Beam Induction Charge (IBIC)

Contrasting with the above IBA techniques, in *IBIC* the measurements are not done through an outgoing reaction product after the sample interaction. In IBIC the information source is the charge generated by the ion beam within the sample and the electronic signal that is created is the output. The experimental setup changes since an ion microprobe is needed in order to have small beam currents (~fA) in a well located zones within the sample. The beam may be scanned to generate X-Y maps of the IBIC signals.

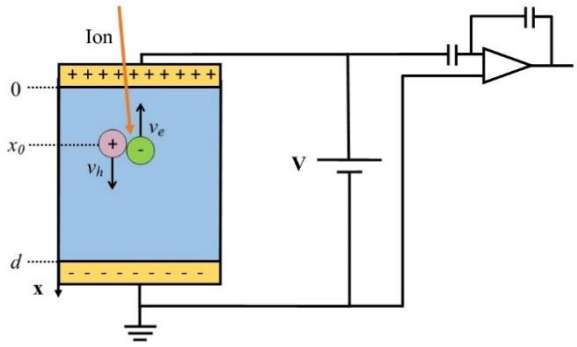

Figure 18: Charge induction schema. The ion creates the electron-hole pair which is instantly broken through the electric field and an inducted charge is generated. The signal is amplified and converted to voltage signal through a charge sensitive preamplifier.

The ion-matter interactions explained in Subsection 1.1.1 are also valid here, however we are going to focus on the electronic response of the sample itself so the output is obtained from the sample directly, no detector being needed. As we saw, the electronic stopping power decreases the ion energy until either the particle is backscattered from a nucleus (RBS, NRA) or it comes to rest in the sample. When an energetic ion travels through the matter it generates a charge track in which a great number of electron-hole pairs (EHP) is created [40]. The energy required to create one electron-hole pair in a semiconductor is directly related to the material energy gap e.g. 3.6 eV for silicon at 300 K (around 3 times the energy gap) and it is independent on the ion characteristics. After, there is a relaxation time, as known as *recombination*, in which the neutrality comes back. Also some carriers can be trapped in the material defects, which is called

trapping, contributing to increase the relaxation time. When a potential difference is applied, an electric field within the material is generated (Figure 18) and the EHP generated breaks away and a charge is induced. However the dielectric relaxation time in semiconductors is smaller than the carrier lifetime, i.e. the recombination – combining with trapping – process is very quick, so there is no time to induce charge by the carriers. The induced charge by EHP can be measured just when the material is in the relaxation regime [41]. The relaxation regime is reached in the wide bandgap materials or semiconductor junctions, where the potential difference applied in the material terminals produce a behaviour like a capacitor. Here the carrier movement can be treated electrostatically due to their low speed. The potential difference is called *bias voltage*, and it generates the active zone, called *depletion zone* (x_d), in which the electrostatic field is generated. This will be treated in more detail in Section 2.1.

The canonical example, which is used here too, is a *pn* semiconductor junction. There a highly doped semiconductor is in contact with a lightly oppositely doped one (high n and light p or vice versa). This is basically the structure of a typical charged particle detector, which will be explained in Subsection 2.1.1. The main interaction here is the charge induced by the incident ion, which is governed according to the *Shockley–Ramo theorem* (W. Shockley, 1938 [42] and S. Ramo, 1939 [43]), which was generalised by Gunn [44]. There the general expression for an induced charge and its current are given by

$$I_i = -q\vec{v} \cdot \frac{\partial \vec{E}(r)}{\partial V_i} \tag{1.35}$$

$$\Delta Q_i = e\left(\left.\frac{\partial \Upsilon(r)}{\partial V_i}\right|_{r_f} - \left.\frac{\partial \Upsilon(r)}{\partial V_i}\right|_{r_0} \right) \tag{1.36}$$

Where $\vec{v}$ is the moving charge velocity; $\partial \vec{E}(r)/\partial V_i$ is the *weighting field*; $\partial \Upsilon(r)/\partial V_i$ is the *weighting potential* for the electrode i, and q is the electron charge. $\vec{E}(r)$ and $\Upsilon(r)$ represent the external electric field and potential. From there we can see that the induced charge just depends on the initial and final position of the carrier. In the case illustrated in the Figure 18, parallel plate model, we can rewrite 1.35 and 1.36 as

$$\Delta Q = e\frac{\Delta x}{d} = \begin{cases} \dfrac{-ex_0}{d} \longmapsto \text{electrons} \\ \dfrac{e(x_0 - d)}{d} \longmapsto \text{holes} \end{cases} \tag{1.37}$$

$$i = e\frac{v(t)}{d} \tag{1.38}$$

In the RBS explanation (Subsection 1.1.1) the relationship between the ion path and the energy through the stopping power was shown. Here it is the same process, the induced charge depends on the ion path and it is related to the energy deposited using the stopping power. However it is an ideal case, since the lifetime of the carriers and the possible trapping processes which can

occur are not considered. We thus introduce the *charge collection efficiency* (*CCE*) concept in order to define the real charge collected versus the charge induced [45]. Therefore the energy measured in the detector, E_d, can be written as

$$E_d = \int_0^{x_0} CCE(x) \frac{dE}{dx} dx \qquad 1.39$$

Where $CCE(x)$ can be experimentaly calculated dividing the detected energetic pulse by the incident energy. The integral is defined between x=0, when the ion enters in the material, and x_0, where the ion has come to rest. This is also an ideal case due to the fact that the highly doped zone in the top and/or the ohmic contact produces a so called *dead layer*, in which the stopping power is different. A realistic mathematical treatment has to also take this into account. From the experimental point of view, the output signal is given as a voltage, V_d, which is scaled into an energy using the electron-hole creation energy (E_{eh}) and the preamplifier feedback capacitance (C):

$$E_d = \frac{V_d E_{eh} C}{q} \qquad 1.40$$

If the ion has a range greater than the depth of the depletion region, recombination can occur in the non-depleted region. Then the *diffusion length* (L) of the material plays a special role. It contains the average time of the free carriers, *lifetime*, and the *diffusion coefficient* [20]. The equation 1.39 becomes into

$$E_d = \int_0^{x_d} CCE(x) \frac{dE}{dx} dx + \int_{x_d}^{x_0} CCE(x) \frac{dE}{dx} \exp - \left(\frac{x - x_d}{L}\right) dx \qquad 1.41$$

For IBIC with light ions, the inherent damage due to the beam (see Annex II: Ion Damage) is reduced since the range in the sample can be long without a great amount of energy. On the other hand, using heavy ions the sample suffers more ionisation damage in a smaller depth. However the contrast in an X-Y scan map is higher, since the charge deposited is bigger and more sensitive to potential CCE defects. Charge funnelling, which is the increase in deposited charge and the higher localisation due to the plasma track generated by the incident ion [46], is greater when the ion mass gets bigger, so its effects may become significant when we are using heavy ions.

1.2 Topological Insulators (TI)

The first attempt to apply our segmented detector was for analysis of a three-dimensional *Topological Insulator* (TI) material. A TI is an electronic state of the matter which presents an insulator/semiconductor behaviour in the volume (bulk band), but a conductive nature on the surfaces. Furthermore these conductive surfaces have the property to confine the electron movement in just two different senses (Figure 19). This is due to the special surface electronic band present in these sort of materials. TI are closely related to the Quantum Spin Hall Effect

(QSH) – actually a material with QSH is a two-dimensional TI[11] – which is the effect to have the integer quantum Hall effect without an external magnetic field. It was predicted by F. Duncan M. Haldane [47] and finally theorised by C.L. Kane and E.J. Mele [48] in that case for the graphene. Both kind of materials, TI and QSH, have a topological invariant (Chern invariant) which ensures that the system stays in the same state under *Time-Reversal* (TR) perturbation; i.e. topological states are very robust under smooth changes, such as atomic structure defects [49].

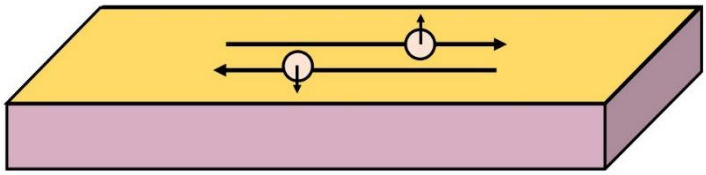

Figure 19: A Topological Insulator has an insulator behaviour in the bulk (purple) and conductive beaviour on the surfaces (yellow), the electron movement there is fixed in two senses depending on the electron spin

The bulk electronic band is a trivial insulator (or semiconductor), however the surface electronic band is a gapless Dirac cone kind, with massless Dirac fermion carriers within, which generates the quantum state called *Topological Surface State* (TSS) as shown in Figure 20. It is similar to the graphene structure but with an even number of these cones whereas in the TI are an odd number [49]. There the electrons spin-momentum vector is locked; therefore the linear movement is spin dependent, restricting the carrier conduction to just two directions. That is called *helicity* and it happens because the spin-orbit coupling of the atomic outer shell electrons generates a band inversion through overlapping conduction and valence bands, producing TR symmetric states. In comparison with graphene, the TI states are less dependent on atomic structure, offering a more tuneable material to be used for example in spintronic technology.

Inducing a perturbation in the TSS which breaks the TR symmetry, such as external electric/magnetic field or ferromagnetic impurities on the surface, the Dirac cone can be opened. There the interchange between TSS and ferromagnetic states is crucial for possible applications not just in spintronic technology [50], but exotic quantum phenomena or fundamental particle physics as well [51]–[53]. Here is where the RBS with a large solid angle segmented detector can be useful, since the small amount of ferromagnetic doping may be directly measured with lower uncertainty using the same measurement time (deeper explanations about Segmented Detector in Subsection 2.1.2).

[11] In order to have a more confortable read, TI along this thesis is refered to three-dimension topological insulators.

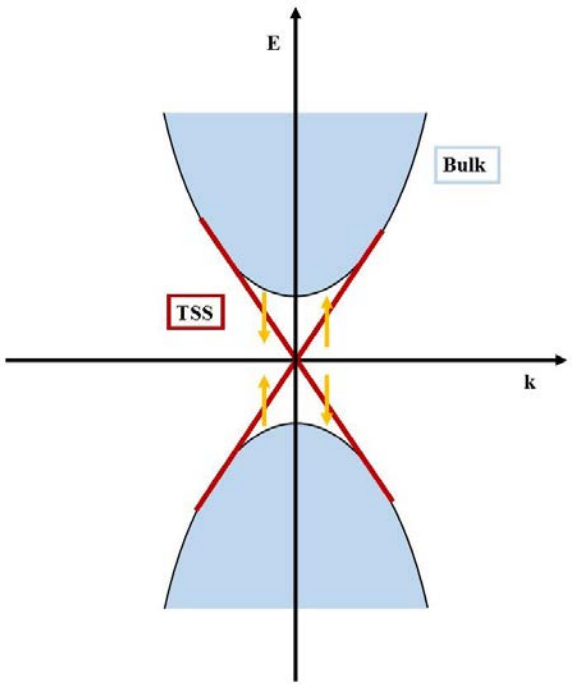

Figure 20: Topological insulators band structure. The bulk contribution (blue) is a trivial insulator while the Topologic Surface States (TSS) are a gapless Dirac cone (red lines) with spin-orbit locked massless Dirac fermions

The TI compound used is the Bi_2Se_3, due to the simplicity in its band structure (just one Dirac cone) and the electronic properties which make it functional at ambient temperature with a 0.3 eV energy gap [54]. The atomic structure is based on a rhomboidal unit cell with 5 atoms. The Bi and Se atoms are intercalated within Quintuple Layers (QL) along the z direction and bonded by Van der Waals forces [55], as is represented in Figure 21.

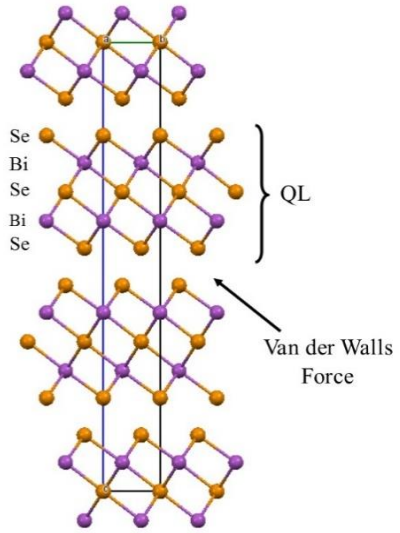

Figure 21: Bi_2Se_3 atomic lattice structure

The Van der Waals forces are weaker than other kind of bounds (such as ionic or covalent bonds), therefore the Bi_2Se_3 may be damaged easily with an ion beam, so it is good candidate

to be studied with a large solid angle detector which reduces the beam fluence needed (and thus the incident ion damage) to obtain spectra of given statistics (also see more in Subsection 2.1.2).

Chapter 3 presents the work done on the elemental characterisation of the Bi_2Se_3 (as deposited and Fe-containing) and the related publications.

1.3 Organic Semiconductor Devices

Optoelectronics has been an interesting topic in the last decades and when is combined with *organic semiconductor* technology, the scope is huge in terms of future sustainable development with multiple applications, such as organic photovoltaic solar cells, organic electronic and optoelectronic devices or gas and chemical sensors. They would have a big impact in multiple fields, from the conventional use technology (eco-friendly electronic devices) to medical diagnosis (malignant corps detection in the body). However some issues related with the intrinsic properties of these kinds of materials have to be overcome, such as low conductivity and carrier mobility, or instability under environmental condition. Deeper research about the physicochemical behaviour of these materials and their combination with inorganic compounds have been ongoing in many research groups for years [56].

The semiconductor behaviour in organic materials arises from the π and π^* (bonding and antibonding) molecular orbitals which are generated by the p_z component in the sp^2 atomic orbitals. The bonding π orbital represent the *Highest Occupied Molecular Orbital* (HOMO) whereas the antibonding is the *Lowest Unoccupied Molecular Orbital* (LUMO). These orbitals can be understood as conduction band, HOMO, and valence band, LUMO, making an analogy with the inorganic semiconductors. However energy gap between them is quite big to be considered as a semiconductor material (2-5 eV) and the carrier mobility is low (1 $cm^2\ V^{-1}\ s^{-1}$); therefore a certain amount of charge has to be injected (or extracted) to turn this insulator behaviour into a useful semiconductor. That can be done by molecular doping as well as layer junction with carrier exchange properties [57].

Transition Metal Oxides (TMO) have been demonstrated as great charge exchangers for organic semiconductor technologies due to their electronic structure, where the strong orbit-orbit interaction generates unusual orbital filling, which leads to interesting carrier transport properties since they have deep uncompleted atomic orbitals. The TMO reduces the hole extraction barrier through its *Work Function* (WF)[12] and the organic molecule *Ionisation Energy* (IE)[13] [58], [59]. Nevertheless there is a limitation: the WF of TMO varies with the stoichiometry, therefore there is a dependency with any stoichiometric change, e.g. the external oxidation due to the environmental exposition, which has to be well understood to have realistic chances generalising the use of organic semiconductor technology outside the academic world.

[12] Intrinsic characteristic of a solid material which represents the energy required to move an electron away from it.

[13] Energy required to remove a valence electron form a neutral atom.

Two interesting applications involve the TMO and the organic compounds: Organic Photovoltaic (OPV), using the TMO as a hole extractor; and organic transistors, light emitters, chemical and gas sensors devices where the TMO has a hole injector role. The OPV solar cell technology has a very promising future; although nowadays the efficiency is around 11%, quite lower compared with the 30% in thin film GaAs solar cells [60], the tendency is increasing, since in the last years a big effort is being made by the scientific community and some public institutions. However there are some underlying aspects that need to be understood in order to describe the physics of the organic semiconductor and to improve manufacturing processes. The organic (or hybrid organic/inorganic) devices are promising to slow down – or even stop – the extreme semiconductor dependency, decreasing costs and power consumption in the same time as the detrimental potential residues are also reduced. In any case the charge exchangers are needed to overcome the conduction limitations given by the organic compounds; the thermal stability and the reliability under real environmental conditions are key to make these materials an available replacement for the hydrocarbon-based energy or inorganic electronic devices. Figure 22 shows the layout for an OPV based on TMO MoO_x.

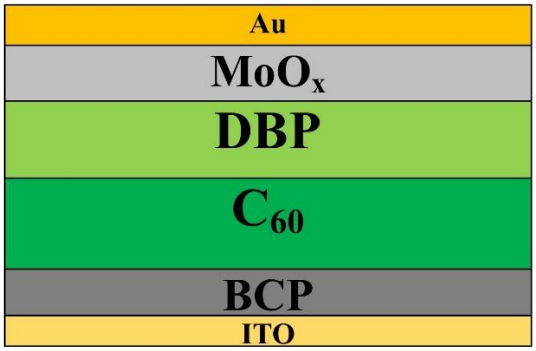

Figure 22: OPV layout; MoO_x is the TMO working as a hole extractor for the DBP organic p-type semiconductor, BCP Bathocuproine is the electron extractor for the Fullerene C60 n-type organic semiconductor. Au and ITO are the device anode/cathode.

Chapter 4 shows how we used the new enhanced charged particle detection system to study both materials. In particular we have focused on the Tetraphenyldibenzoperiflanthene (DBP), which has been demonstrated as a good organic semiconductor donor [61], [62] and the binary compound MoO_x as a good candidate as hole injector/extractor for the organic devices via HOMO level [58]. Here we present IBA measurements of the oxidation process in the TMO MoO_x with different stoichiometry's, which is extremely important for the WF controlled tuning and, therefore, for the charge exchange process. Moreover we demonstrate the capabilities of the Segmented Detector in the organic compound measuring the DBP carbon quantity using IBA techniques.

2. Charged Particle Detection

One of the central preoccupations of this thesis is the instrumentation used for IBA since it has been a great improvement in the particle detection and data acquisition Therefore a complete description concerning physical principles and our remarkable enhancements are necessary to have a general point of view about these two topics in IBA techniques. Section 2.1 is about semiconductor charged particle detectors, explaining how they work (Subsection 2.1.1) and which were the developments reached during this thesis: Segmented Detector (SegDet) characterisation and installation at SAFIR (Subsection 2.1.2). The study of charge collection efficiency in our detector is presented in the manuscript NIMB_PROCEEDINGS-D-16-00174 which was presented at the 12th European Conference on Accelerators in Applied Research and Technology (ECAART) and is submitted for publication. A proposed design for an annular segmented detector is presented in Section 2.1.3.

Section 2.2 presents the data acquisition systems which involves the signal amplification (Subsection 2.2.1) and the pulse processing after the charge collection is explained in Subsection 2.2.2, with an explanation of the different parts in the acquisition chains for both the old fashion analogue method and the digital system as well as a comparison between them.

2.1 Semiconductor Detectors

The semiconductors charged particle detectors have been widely used during the second half of the 20th century. Firstly, in early 1960s, they were made from commercial germanium diodes (thin Surface Barrier detector) and they were mainly dedicated to nuclear physics, the hottest topic in those days. They replaced the Gas Ionisation Chambers used until then. These semiconductor solid state detectors provided a great advantage in comparison with ionisation chambers due to enhancement in energy resolution and the possibility to reduce the size since the studied particles are stopped at shorter distance and larger energy loss, increasing thus the sensitivity.

Rapidly, in the late 1960s, the germanium was replaced with silicon, since the former had to be cooled to keep the leakage current low while the silicon properties – larger energy gap – made it possible to work at room temperature. It was also possible to build light-proof detectors, depositing an aluminium thin film on the surface, giving the possibility to study particles within a lighted environment. Such detectors were installed in the Voyager spacecraft (launched in 1977) to study cosmic rays outside the solar system (and it is still acquiring data!).

These detectors were used for nuclear or fundamental physics, mainly gamma rays and charged particles coming from nuclear reactions. In 1970s, two facts made possible and extremely convenient the use of the charged particle detector to IBA for material science. On one side, the semiconductor technology development increased dramatically, with better and cheaper semiconductor detectors and electronic devices; and on the other side the nuclear processes knowledge within the materials was good enough to start to apply this knowledge in the material description and characterisation. Furthermore, the nuclear and particle physicists could not use any more those “small” particle accelerators, since to continue their works higher energies were

necessary, therefore the conversion of those facilities into material and solid state physics was as natural as needed.

This development has been keeping until now, improving resolution, packaging size, data acquisition systems, etc. going from the great ATLAS detector in CERN to tiny low-cost *p-i-n* detectors.

2.1.1 Single Detector

Different techniques and materials are used to build up semiconductor detectors, however we will focus on Passivated Implanted Planar Silicon (PIPS) detectors, since they have optimal characteristics (price, resolution, size...) and are now the most commonly used. These detectors are based on a semiconductor silicon wafer (*p* or *n* type) doped by ion implantation technique on the front and/or back side, with p or n ion species, hence letting free holes or electrons, in order to make a *p-n* junction (Figure 23.a). The thickness is typically from 200 to 1000 μm and the surface area from 25 to up to 1200 mm^2. When a reverse bias voltage is applied – hence an ohmic contact or high carrier density has to be added on both detector sides – an electric field is created perpendicular to the wafer plane surface direction. This electric field generates a *depletion region* or active zone, in which free electrons in the conduction band go from the p type into n type material and holes go into n type from the p type, so they are all are matched within the electric field as is shown in Figure 23.b.

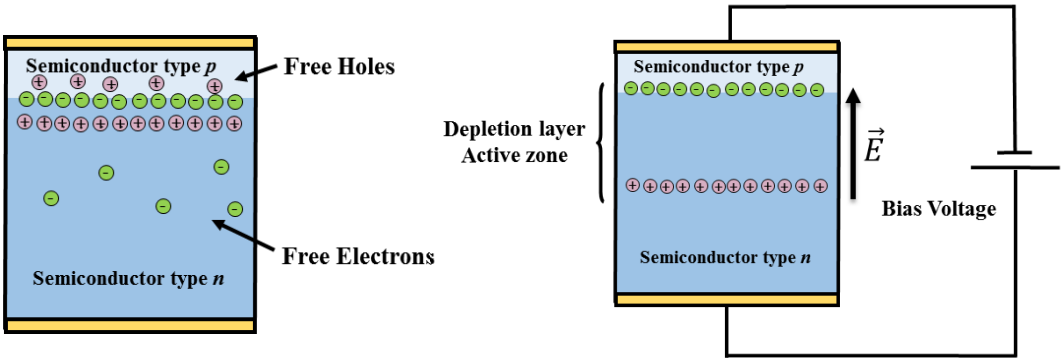

Figure 23: On the left p-n junction schema. On the right reverse bias applied in p-n junction.

Therefore detectors could be understood as capacitors and its behaviour is governed the well-known equation 2.1.

$$C = \varepsilon \frac{A}{\omega_d} \qquad 2.1$$

Where ε is the dielectric constant (in Si $\varepsilon = 11.9\varepsilon_0$, where ε_0 is the vacuum permittivity), A is detector surface area and ω_d is depletion layer thickness. This layer is the active part of a detector, with thickness that can be controlled through the applied reverse bias voltage. The depletion thickness can be calculated by:

$$\omega_d = \sqrt{\frac{2\varepsilon(V_b + V')}{e \cdot n}} = \sqrt{2\varepsilon\mu\rho(V_b + V')} \qquad 2.2$$

where n, μ and ρ are carrier number, mobility and resistivity respectively. We can approximate all of them to silicon wafer type carrier so as to simplify. Note as well that V_b is reverse bias voltage, V' is intrinsic potential difference due to *p*-*n* junction[14] and e is electron charge.

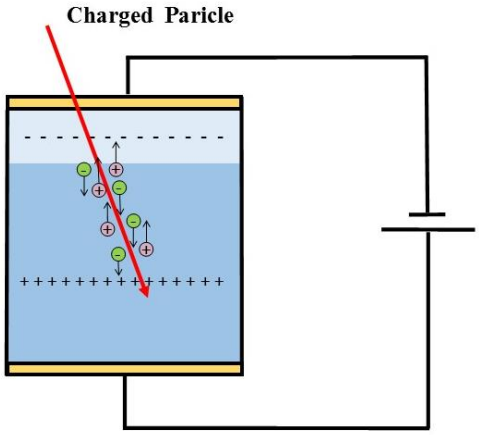

Figure 24: Electron-hole generation through the ion path due to ionising excitation.

In this state the carriers are in equilibrium, with no free electrons or holes. When a charged particle enters within this zone, the equilibrium can be broken if the energy is enough and excites the valence electrons. Those excited electrons can jump to the conduction band, generating then free electron-holes pairs as is represented in Figure 24[15]. Once an electron-hole pair is produced, an induced charge q is generated within the electric field, due to the Shockley-Ramo theorem [63], as was explained in Subsection 1.1.5. Thus the relationship between energy deposited and signal size is given by Equation 2.3.

$$q_s = \frac{E}{E_i} q_e \qquad 2.3$$

Where q_s is average induced signal charge, E deposited energy, E_i energy required to ionise the atoms in the semiconductor and create electron-hole pair (3.6 eV for silicon) and q_e is the electron charge. After a pair is produced and the signal is created, this has to be amplified and digitally treated in order to extract a spectrum in the computer. These following steps will be explained below in Section 2.2.

However there exists some elements which perturb the simple physics explained above. Firstly the incident particle has to pass through the ohmic or highly doped front contact, essential for the charge collection, where energy will be lost without ionisation, resulting in a shift in the

[14] In the *p*-*n* junction, without any external applied voltage, carriers are diffused thermally and electrons and holes can be matched just where *p* and *n* zone are touching (Figure 23.a), therefore there exists an intrinsic depletion zone.

[15] Description of how a detector works is valid for all kind of semiconductor detectors.

energy spectrum. This generates the so called *dead layer*. Furthermore some of the particles will be backscattered from the detector atoms. To take into account these corrections for non-ionizing energy loss a *Pulse-Height Defect* (*PHD*) model [64] has been successfully developed and widely used.

Several considerations must be made to give a full account of the performance of the charge collector i.e. compromise between energy resolution and number of collected events. The energy resolution equation with all the contributions would be as is shown in Equation 2.4, where the terms are statistically independent.

$$\Delta E = \sqrt{\Delta E_{elec}^2 + \Delta E_{stat}^2 + \Delta E_{CCL}^2 + \Delta E_{dl}^2 + \Delta E_{kin} + \Delta E_{sys}} \qquad 2.4$$

The very first contribution is the electronic noise (ΔE_{elec}). The electronic noise is an addition of two main contributions: electronic and thermal fluctuations. The source of them in the detectors are the leakage current and the capacitance in the *p-n* junction, because the detector is working as a non-ideal capacitor and there they both have a detector surface dependence [65]:

$$\Delta E_{elec} \propto \sqrt{I_D(A) + C_D^2(A)} \qquad 2.5$$

Another important contribution to the energy resolution is the statistical fluctuation of the number of electron-hole pairs created (ΔE_{stat}), i.e. intrinsic energy uncertainty, due to statistical processes involved in the charge collection. The incident ions are statistically independent and their interactions can be expressed with Poisson statistics, however although every ion loses exactly all of its energy in the detector, the fluctuations in the number of charge pairs produced deviates from the Poisson distribution. This is taken into account via the *Fano factor* [66] which accounts for loses ending up in secondary e-h pairs, created by the primary ones, which interact with the phonon modes [67], [68]. Thus the fluctuations in the measured energy for given incident energy (E) can be expressed as function of the Fano factor (F) and the material ionisation energy (E_I); and it is independent of the incident ion nature:

$$\Delta E_{stat} = 2.35 \cdot \sqrt{FEE_I} \qquad 2.6$$

Charge collection losses (ΔE_{CCL}) are due to the carrier trapping by detector crystal bulk (silicon) impurities. The dead layer (ΔE_{dl}) is a non-active area on the detector surface which is due to the ohmic surface contact and the entrance window (highly doped top layer), where a certain amount of energy is lost. For a commercial PIPS detector-preamplifier system[16] in standard conditions (with 50 mm^2 of area and 400 μm of depletion zone, capacitance ≈ 13 pF, leakage current ≈ 20 nA, at room temperature[17]) the energy resolution is around 15 keV.

[16] Preamplifiers will be discuss in Section 2.2.

[17] Values taken from the widely used Ortec silicon PIPS detector data sheet.

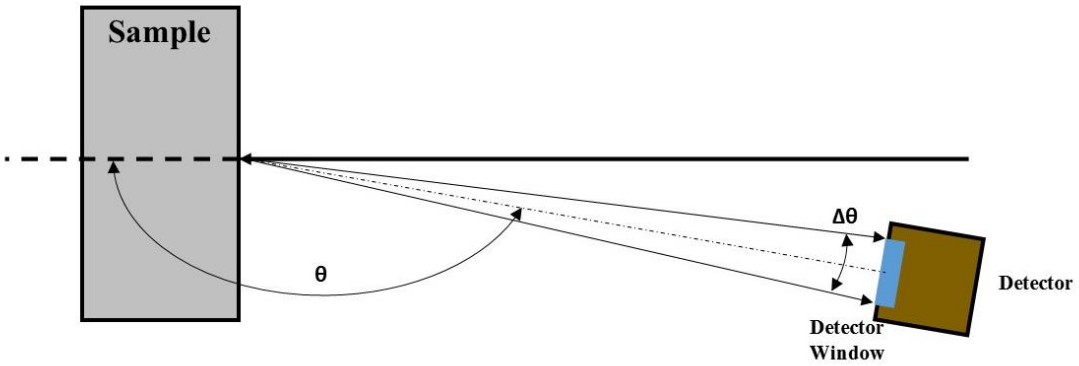

Figure 25: Angle spread schema. θ is the backscattering angle and $\Delta\theta = \theta_f - \theta_i$ is the detector window width.

The geometrical system has a contribution to take in account since there is an angular spread for a given backscattering angle due to the detector window width, which is called kinematic spread (ΔE_{kin}),. In Figure 25 the range of possible backscattering angles is represented by $\Delta\theta$. The mathematical expression is based on the Rutherford backscattering cross section variation with the energy at different angles and assuming a Gaussian energy distribution. It is expressed by Equation 2.7, where θ_i and θ_f are the extreme angles for a given detector and the summation has to be done taking angle steps between them.

$$\Delta E_{kin}(\theta) = \\ = 2.35 \cdot \sum_{\theta=\theta_i}^{\theta_f} \sqrt{E(\theta) - \sum_{\theta'=\theta_i}^{\theta_f} E(\theta') \left(\frac{\left(\frac{\sigma(\theta')}{\sigma(\theta_i)}\right) \cdot (E_{\theta'+1} - E_{\theta'})}{\sum_{\theta''=\theta_i}^{\theta_f} \left(\frac{\sigma(\theta)}{\sigma(\theta''_i)}\right) \cdot (E_{\theta''_i+\theta''_{i+1}} - E_{\theta''_i})} \right)^{-1}} \cdot \\ \cdot \sqrt{\left(\frac{\sigma(\theta)}{\sigma(\theta_i)}\right) \cdot (E_{\theta+1} - E_{\theta})} \qquad 2.7$$

Also the environmental system conditions are a noise source (ΔE_{sys}) (hard to measure and control, such as microphonic vibrations, environmental signals, etc.).

Furthermore, when two simultaneous particles arrive at the same time, the charge induced will be the addition of the real particle charges and these two events will be counted as one. There exists both on-line and off-line methods to suppress or simulate this phenomena. Below, in Section 2.2, the experimental and analytical treatment solutions will be presented.

2.1.2 Segmented Detector

In this thesis a large solid angle Segmented Detector (SegDet) has been used in order to improve the performance of a typical single PIPS detector (Figure 26). It was designed and built within the European project SPIRIT, however was modified and improved during the SPRITE project, in which this thesis is undertaken.

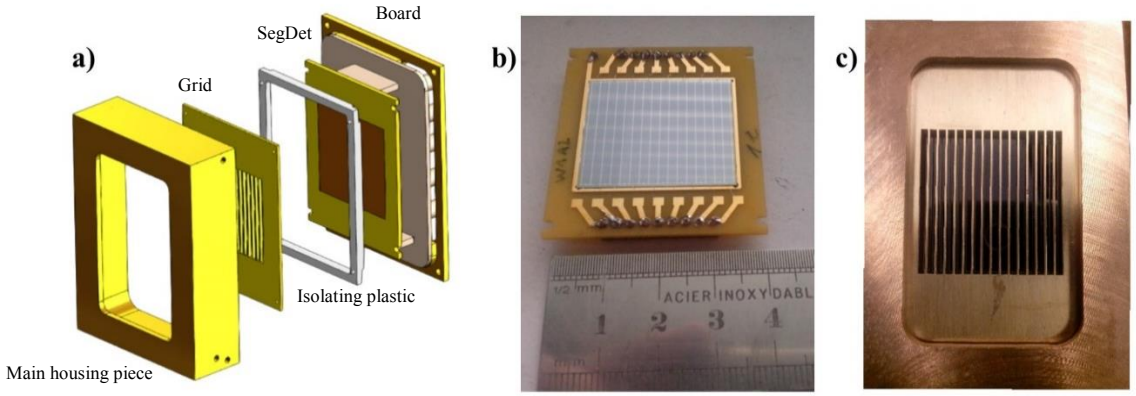

Figure 26: SegDet appearance. a) SegDet and housing schema, b) SegDet and print circuit picture, c) SegDet completely mounted

There are several reasons to develop and use a large solid angle segmented detector in ion beam analysis techniques. Firstly a large solid increases the counts number for a given incident ion fluence. The solid angle is proportional to the surface area of the detector, A, ruled by

$$\Omega = \frac{A}{r^2} \qquad 2.8$$

Where r is the distance between the sample and the detector. The number of particles detected N_d is proportional to the solid angle as is shown in Equation 1.12. In our case the detector surface active area is 763 mm^2. In comparison with a 50 mm^2 detector, using a 8x2 mm^2 collimator in front of it to avoid kinematic spread (it is a classical RBS detector configuration), a SegDet segment is more than 3 times bigger solid angle and the total SegDet is more than 48 times; therefore the number of detected particles is augmented and statistics improved for a given beam fluence. However the bigger surface area reduces the energy resolution due to the electronic component (both leakage current and capacitance depend on the area), the kinematic spread (larger backscattering angle range) and the pile-up (simultaneous events). The optimal way to keep the large solid angle avoiding those problems is segmenting the detector. In our case, the detector was longitudinally divided in 16 side-to-side segments (29x1.64 mm²). Furthermore, use of several backscattering angles helps solve the intrinsic mass-energy ambiguity typical for IBA[18]. A Guard Ring (GR), at the same voltage as the detector bias, surrounds the segments to isolate them, keeping the leakage current low, thus the edge current is captured and the impedance reduced. In Figure 27 are shown the GR and interstrip region structure. The segmentation multiplies the data measured, but also the system to get this data, the well-established analogue system cannot face the 16 acquisition channels in a cheap and comfortable way; Section 2.2 contains the approach used to acquire data with the SegDet.

[18] The energy can be lost by two factors: elastic collision (K) and stopping power (s). In a single IBA experiment is not possible to discern between them, however using several backscattering angles K will change, since it depends on the angle, while s remains the same. In NRA the energy tranfer is not elastic, but the principle is the equivalent.

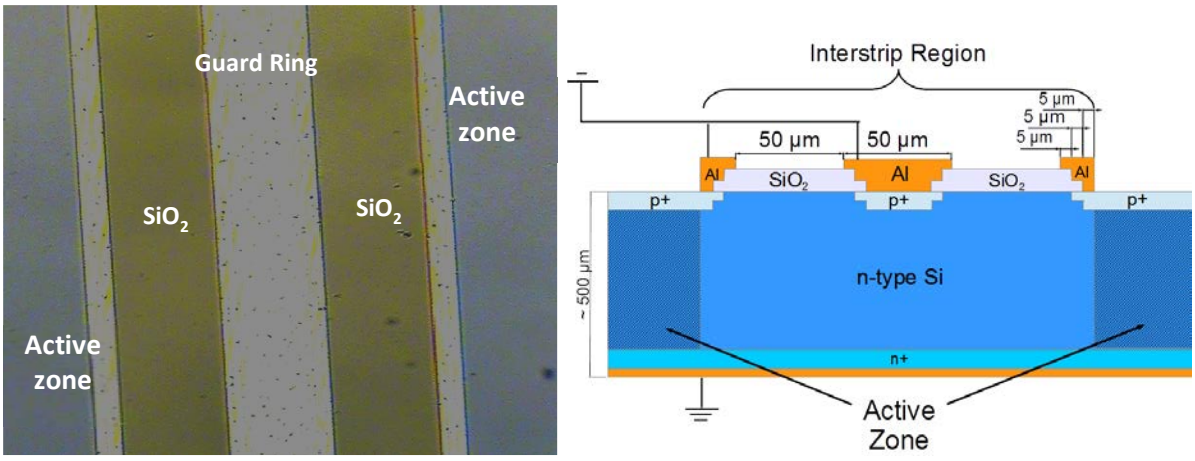

Figure 27: Guard Ring and interstrip region microscopic view (left) and a cross section schema (right)

The direct implication of the statistical improvement keeping an optimal resolution conditions is the possibility to study samples with small quantity of matter such as small peaks of light elements built on the background signal or heavy elements with small intensity. Another enhancement using our SegDet is the damage reduction to the sample due to the incident beam. An ion beam are accelerated charged particles, therefore they are irradiating all around their path. Also interactions between beam ions and sample atoms (both electrons and nucleus) create defects in the materials, even more when these materials are conductors or semiconductors with crystallised structures or insulators such as organic tissues. With the SegDet we are able to analyse these kind of fragile materials under ion beam. Further explanations about damage induced by ion beams are in Annex II: Ion Damage.

In the following Subsubsection 2.1.2.1 is a paper submitted as ECAART 12th proceedings, in which is presented the SegDet characterisation (leakage current and depletion thickness), focusing on the interstrip behaviour responses for the Charge Collection Efficiency (CCE) and the role of the GR in the detection system.

The initial detector housing design, inherited from the EC project SPIRIT, was not completely installed in the vacuum chamber; therefore it was not tested under real experimental conditions. The detector grounding has to be properly chosen since such a big detector generates some undesirable antenna behaviour which produces parasitic noise. Moreover, the board, where the detector is mounted and the preamp connection is made, was not made in the cleanest way and constituted an extra noise source. The changes that were made, extra information about the detector characterisation – non-included in the article – and first results using several segments simultaneously are shown in Subsection 2.1.2.2. Moreover, the large solid angle can give the possibility to perform very low fluence experiment such as $^{4}He^{2+}$ beam up to 4 MeV in small single ended accelerators such as the SAFIR facility which has 2 MV maximum terminal voltage, corresponding to 2 MeV $^{4}He^{+}$ in classical operation. Some results of this operational mode are shown in Subsection 2.1.2.2 as well.

2.1.2.1 Charge Collection Efficiency: Publication I

Charge Collection Efficiency in a Segmented Semiconductor Detector Interstrip Region

Alarcon-Diez, V.[1*], Vickridge, I.[1,2] Jakšić, M.[3], Grilj, V.[3], Schmidt, B.[4], Lange, H.[4]

[1]Sorbonne Universités, UPMC Univ Paris 06, UMR7588, INSP, F-75005, Paris, France

[2]CNRS, UMR7588, INSP, F-75005, Paris, France

[3]Department of Experimental Physics, Ruđer Bošković Institute, P.O. Box 180, 10002, Zagreb, Croatia

[4]Institute of Ion Beam Physics and Materials Research, Helmholtz-Zentrum Dresden-Rossendorf, P.O Box 510119, Dresden, Germany

Keywords: Segmented Detector, IBIC, Charge Collection Efficiency, Interstrip

Abstract

Charged particle semiconductor detectors have been used in Ion Beam Analysis (IBA) for over four decades without great changes in either design or fabrication. However one area where improvement is desirable would be to increase the detector solid angle so as to improve spectrum statistics for a given incident beam fluence. This would allow the use of very low fluences opening the way, for example, to increase the time resolution in real-time RBS or analysis of materials that are highly sensitive to beam damage. In order to achieve this goal without incurring the costs of degraded resolution due to kinematic broadening or large detector capacitance, a single-chip segmented detector (SEGDET) was designed and built within the SPIRIT EU infrastructure project. In this work we present the Charge Collection Efficiency (CCE) in the vicinity between two adjacent segments focusing on the interstrip zone. Microbeam Ion Beam Induced Charge (IBIC) measurements were used to perform X-Y mapping of CCE with different ion masses and energies, as a function of detector operating conditions (bias voltage changes, detector housing possibilities and guard ring configuration). We show the CCE in the active area edge region and have also mapped the charge from the interstrip region, shared between adjacent segments. The results indicate that the electrical extent of the interstrip region is very close to the physical extent of the interstrip and guard ring

* Corresponding author Tel. : +33 1 44 27 46 88
E-mail address : victor.alarcon@insp.upmc.fr (V. Alarcon-Diez)

structure with interstrip impacts slightly contributing to the complete spectrum. The interstrip contributions to the spectra can be substantially reduced by an offline anti-coincidence criterion applied to list mode data, which should also be easy to implement directly in the data acquisition software.

Introduction

The advance of IBA towards studying more complex materials, together with new technical possibilities are driving factors for the development of detection and data acquisition systems. In particular, the statistics of charged particle detection play a great role in the quantity and quality of the information that can be extracted from a given RBS or NRA experiment [1]. Increasing the detector solid angle will allow increased statistics for a given beam fluence, which will allow to overcome some limitations: detection or determination of elements present at or below the detection or quantification limit, measurement on materials sensitive to ion beam damage (such as some monocrystals or organic samples [2], [3], and use of very low ion currents, such as doubly charged alphas from a standard RF ion source to double the beam energy in a single ended electrostatic accelerator. Increasing the overall detection solid angle must be accomplished whilst maintaining a low kinematic energy spread. A limited detector surface area is also desirable since a large detector surface will generate significant electrical and thermal noise, and under standard analysis conditions the count rate could be very high, leading to significant deadtime and pileup. A segmented detector design – composed of an array of individual detectors of appropriately chosen geometries meets these criteria so long as a suitable number of pulse-shaping and data acquisition channels are also available. A segmented detector will also contribute to resolving the mass-depth ambiguity in RBS since spectra will be collected for several detection angles [4].

In the present work, we have studied Charge Collection Efficiency (CCE) of a large solid angle semiconductor segmented strip detector (SegDet) built in the framework of the SPIRIT EU project at HZDR. The active detector is $29x29\,mm^2$ size and composed of 16 individual segments with a Guard Ring (GR) dividing them. We focus on the charge collection in the interstrip region between two adjacent segments, applying the Ion Beam Induced Charge (IBIC) technique with a scanning ion microprobe. We have investigated how the charge may be shared in the interstrip region as well as the GR role, using different incident ions and energies.

Instruments and methodology

The SegDet used in this work is made by standard semiconductor processing techniques: ion implantation, lithography, thermal oxidation and metal deposition, annealing and so on. As a substrate a (100)-oriented, n-type Si wafer ($N_D \approx 1 \cdot 10^{12}\ cm^{-3}$, $\rho = 5500\ \Omega cm$) is used. The implanted donor in the p+ entrance window is B+ ($10\ keV$, $N_D = 5 \cdot 10^{14} cm^{-2}$) and the acceptor is P+ in the rear n+ contact ($50\ keV$, $N_D = 5 \cdot 10^{14} cm^{-2}$). The implantation was done through a SiO2 layer ($60\ nm$) which was removed after the implantation. Al was deposited to create the ohmic contacts. The schema of two adjacent segments with the interstrip region in between is shown in Figure 1. The complete detector area is $29x29\ mm^2$, divided into 16 segments ($29x1.79\ mm^2$), as is shown in Figure 2.a. The microscopic view of the interstrip region is shown in Figure 2.b; where two adjacent segments are the active areas (Segment A and B), SiO2 is the passivation zone which delimits the segment border, and the central part is the aluminium GR which is intended to isolate the segments – avoiding as much as possible the crosstalk, keeping the electric field at the edge under control and reducing the leakage current.

To characterize the detector electronically, the leakage current was measured under different bias and GR configurations – GR biased by the same voltage as the segments, GR no biased and GR floating – and the segment depletion thicknesses were measured via standard C-V curves.

The IBIC technique has been used to study the CCE in the last two decades for different semiconductor devices [5], [6]. It consists in the measurement of the charge carriers induced by the incident high energy ion in the depletion region of the p-n junction (Figure 3). In our case it was done in the Ruđer Bošković Institute, using a microprobe of $1x1\ \mu m^2$ size and scanning lengths from $250\ \mu m$ up to $650\ \mu m$ in X and Y axis (Figure 3). The incident ions used were $^{1}H^{1+}$ at $4.5\ MeV$, $^{12}C^{3+}$ at $5.5\ MeV$ and $^{12}C^{4+}$ at $6\ MeV$, where the differences in the charge state for C ions are negligible. The incident ion fluxes were between $10^2 - 10^3\ s^{-1}$. Two classical analogue charge acquisition channels were used to

acquire the induced charge as a function of the X-Y scan position. For the C ions three different GR configuration were used: GR bias as the segments, GR no bias and GR floating.

Results and discussion

The main subject of this study is the role of the GR in the SEGDET, therefore the first stage is to measure the electronic response without beam. The leakage current through both segments and the GR was measured and plotted as a function of GR bias as is shown in Figure 4. There are three different GR configurations: floating GR, GR no bias and GR with the same bias as the segments. Note that the 'no bias' configuration is when the power supply plug in the GR is switch off, but nevertheless a parasitic voltage due to the adjacent segment electric field appears in the display (when the segment voltage is $-80\ V$, for example, the GR voltage is $-10.9\ V$). In the graph can be seen that almost no leakage current on the segments has been found when the GR is biased, no matter which voltage is implemented, however the current is great when there is no bias on the GR. When GR is floating we are in an intermediate case. Since the energy resolution depends on the leakage current [4], the optimal configuration so far is biasing the GR.

Figure 5 shows the C-V curve and the p-n junction depletion thickness as functions of segment bias. The maximum depletion thickness of $260\ \mu m$ is reached at $-100\ V$ applied bias. For the main bias voltages -20 V, $-30\ V$, $-80\ V$ used in the later IBIC experiments the depletion thicknesses are $162\ \mu m$, $192\ \mu m$, $255\ \mu m$, respectively. Note, that at $0\ V$ segment bias there is an intrinsic depletion thickness of $32\ \mu m$.

Regarding the IBIC experiments, measurements were normalised by taking the charge collection efficiency (CCE) within the segments (detector active zone) as equal to 1 at the highest bias voltage ($-80\ V$), neglecting the energy loss in the dead layer ($\sim 100\ nm$). Figure 6 shows the CCE evolution in the segments with respect to the applied bias voltage when a $^{1}H^{+}$ $4.5\ MeV$ beam is used. The ion range in silicon given by SRIM [7] in this case is $180\ \mu m$. We note that CCE reach the maximum at a bias of $-20\ V$, which corresponds to a depletion region of $162\ \mu m$ as measured above. The 10% difference

can be explained since the protons are only completely stopped in the depletion zone at about $-25\ V$, which corresponds to $180\ \mu m$, but at $-20\ V$ the charge induced beyond the depletion zone can still be collected. The two adjacent segments showed identical behaviour.

The CCE behaviour in the interstrip region has been studied by extracting a line scan across the interstrip region from the 3D IBIC map to represent a 2D graph with the average CCE values projected in the Y axis, as is shown in Figure 7 for $^{1}H^{+}$ incident ions at $4.5\ MeV$ keeping the GR floating and bias segments at -30 V. Three zones can be identified: A) Detector segment, where $CCE = 1$, B) SiO_2 passivation, in which the CCE is slowly decreasing, and C) GR, where the CCE drops drastically and the signal is present in both acquisition channels. In between these zones are interfaces or transition regions, where the CCE change the previous tendency more softly. Furthermore the number of events present simultaneously in both acquisition channels was calculated using an off line coincidence data treatment, and showed that the charge induced is shared (i.e. adjacent segments cross talk). The coincident events decrease with the bias from $5 \cdot 10^{-2}$ to $2.4 \cdot 10^{-2}\ \% coincidences/\mu m^2$; therefore, taking in account that the active detector area is in the order of $10^5 - 10^6\ \mu m^2$, these events are negligible.

To define the different zones within the interstrip region more clearly it is desirable to use a heavier incident ion since it increases the CCE contrast in the X-Y maps [8]. Here we used $^{12}C^{3+}$ and $^{12}C^{4+}$ ions, both equivalent in the point of view of induced charge at $5.5\ MeV$ for $^{12}C^{3+}$ and $6\ MeV$ for $^{12}C^{4+}$. SRIM gives ion ranges in silicon of $5.42\ \mu m$ and $5.86\ \mu m$, respectively. Using the same line scan averaging as above, Figure 8 shows the CCE for the three different GR configuration when the segments are biased at $-30\ V$. Regarding the GR bias (blank), the electric field edge in both segments is well defined, and the crosstalk has been eliminated. However the CCE within the segments is 15% lower. On the other hand both the floating and the no bias configurations represent a $CCE > 1$ in the interstrip region and surroundings. That might be explained by the highly charged states of the C ions and high charge density along the ion tracks which this set up involves, where either light generation in the SiO_2 or

electron cascades could generate extra charge inside the detector interstrip resulting in a $CCE > 1$. To characterize this behaviour further studies using CCE simulations and systematic experiments with different device configurations are needed. Nevertheless, these heavy ions in those last GR configuration are giving us more information about the interstrip structure. When the GR is no biased, the CCE vs Y graph is mostly symmetric, where the $CCE > 1$ is extending around $15 - 20\ \mu m$ into the detector segment; then CCE is stable in the Al contact region, increasing up to 1.6 in the SiO_2 passivated zone. Approximately in the medium part of the SiO_2 the CCE starts to drop dramatically until the zone bellow the GR is reached. The charge is shared from the SiO_2 edge, however the number of these coincident events is very low, around $3 \cdot 10^{-4}\ \% \ coincidences/\mu m^2$. The GR floating case is more asymmetric since there is no reference for the generated electric field. Nonetheless, a CCE peak can be seen in the Al contact edge, instead a continuous more slowly drop than in the no bias case. Here the number of shared events is even smaller, around $1 \cdot 10^{-4}\ \% \ coincidences/\mu m^2$.

Conclusions

The GR role for our SEGDET has been clarified for the correct installation and routine use. We have shown that GR biased with the same voltage as the segment reduces the leakage current significantly, hence electrical and thermal noise contribution for the energy resolution is also reduced. For $^{1}H^{1+}$ ions, the CCE variation with applied bias seems to be in good agreement with the C-V measurements.

The charge generated in the interstrip region may be shared by two adjacent segments, however the number of these events is very small and can be either treated by anticoincidence methods or even neglected. Nevertheless biasing the GR shows the more effective configuration to reduce this charge sharing, and therefore, there is no need for any external segment shield (such as strip mask in front of the detector interstrip regions) to avoid crosstalk between the segments.

The CCE >1 generated by the ^{12}C ions in the interstrip region cannot be unequivocally explained with the present experimental results. Detailed electric field calculations and device simulations may shed further light on these observations.

Acknowledgements

This work has been supported by Marie Curie Actions - Initial Training Networks (ITN) as an Integrating Activity Supporting Postgraduate Research with Internships in Industry and Training Excellence (SPRITE) under EC contract no. 317169. We are very grateful to Isabelle Trimalle from INSP for the kind assistance in the C-V and microscopy measurements. Also we thank Ivan Sudić from RBI for his very kind welcome in Zagreb and the excellent help during the IBIC measurements.

Bibliography

[1] M. N. Yongqiang Wang, *Handbook of Modern Ion Beam Materials Analysis*. Materials Research Society, 2010.

[2] F. D. Auret, J. D. Comins, C. M. Comrie, T. E. Derry, and E. Wendler, "Mechanisms of damage formation in semiconductors," *Nucl. Instruments Methods Phys. Res. Sect. B Beam Interact. with Mater. Atoms*, vol. 267, no. 16, pp. 2680–2689, 2009.

[3] D. Benzeggouta and I. Vickridge, "Handbook on Best Practice for Minimising Beam Induced Damage during IBA," no. March, 2011.

[4] H. Spieler, *Semiconductor Detector Systems*. OUP Oxford, 2005.

[5] E. Vittone, "Semiconductor Characterization By Scanning Ion Beam Induced Charge," vol. 2013, 2013.

[6] M. B. H. Breese, E. Vittone, G. Vizkelethy, and P. J. Sellin, "A review of ion beam induced charge microscopy," *Nucl. Instruments Methods Phys. Res. Sect. B Beam Interact. with Mater. Atoms*, vol. 264, no. 2, pp. 345–360, Nov. 2007.

[7] J. F. Ziegler, "SRIM-2003," *Nucl. Instruments Methods Phys. Res. Sect. B Beam Interact. with Mater. Atoms*, vol. 219–220, pp. 1027–1036, Jun. 2004.

[8] M. B. H. Breese, D. N. Jamieson, and P. J. C. King, *Materials analysis using a nuclear microprobe*. 1996.

List of Figures

Figure 1: Two adjacent segments and interstrip region schema

Figure 2: a) Segmented Detector photos. b) Detailed interstrip region view: Segment A and B, SiO_2 passivation and Guard Ring

Figure 3: a) IBIC technique basic fundaments schema. b) X-Y scanning interstrip region schema

Figure 4: Leakage current vs applied bias in a segment (equivalent value in all segments) using three different GR configuration: floating (black), GR no bias (red) and bias as the segments (blue)

Figure 5: Capacitance (right Y axis, black) and depletion thickness (left Y axis, blue) vs bias voltage in segment A. equivalent values are found in all the segments.

Figure 6: CCE for two adjacent segments in GR floating configuration using $4.5\ MeV$ incident protons

Figure 7: CCE using $^{1}H^{+}$ at $4.5\ MeV$ (GR floating) and $-30\ V$ segment bias through the interstrip region and the comparison with its schematic structure. There are three zones: A) detector segment, B) SiO_2 and C) GR

Figure 8: CCE using $^{12}C^{3+}$ at 5.5 MeV and $^{12}C^{4+}$ at 6 MeV, with -30 V bias in each segment. There are the three GR configuration: black line, Bias; red line, no bias and blue line floating.

Figure *1*

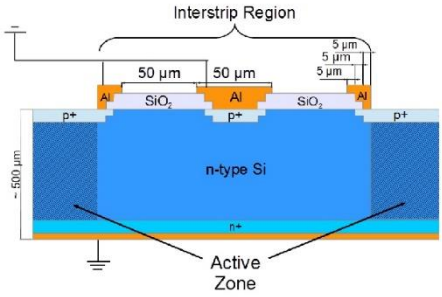

Figure 2

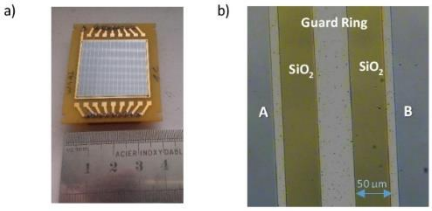

Figure 3

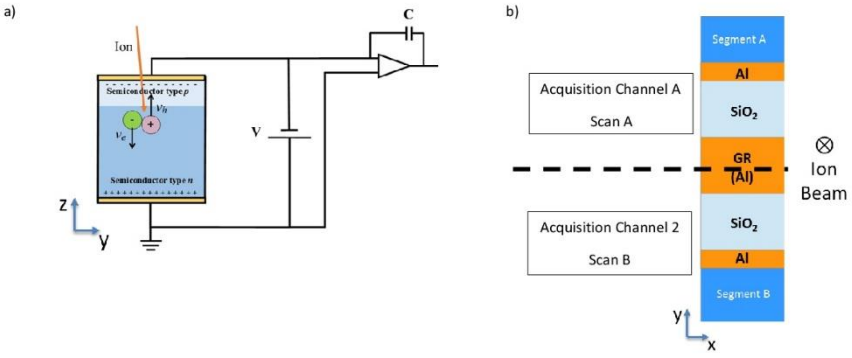

Figure 4

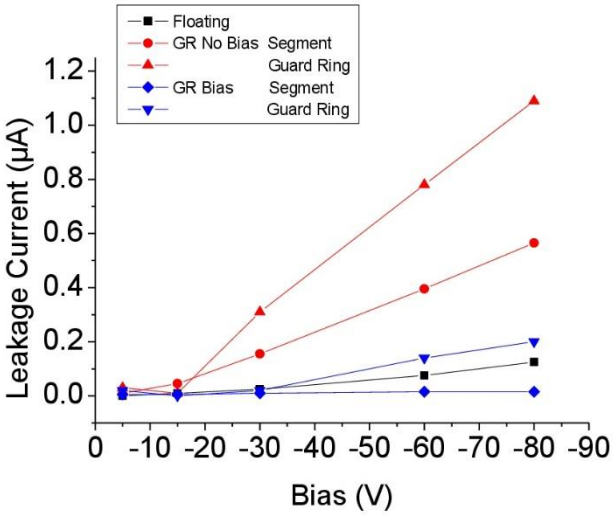

Figure 5

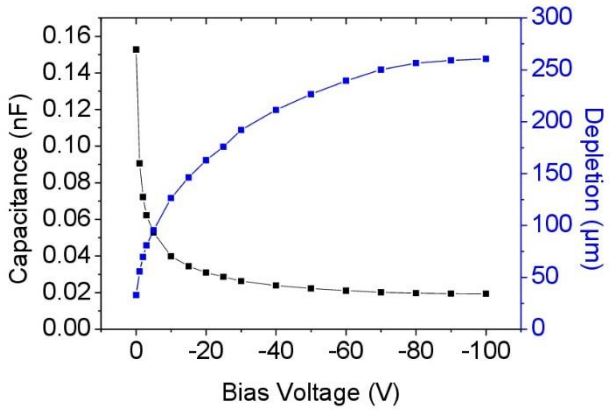

Figure 6

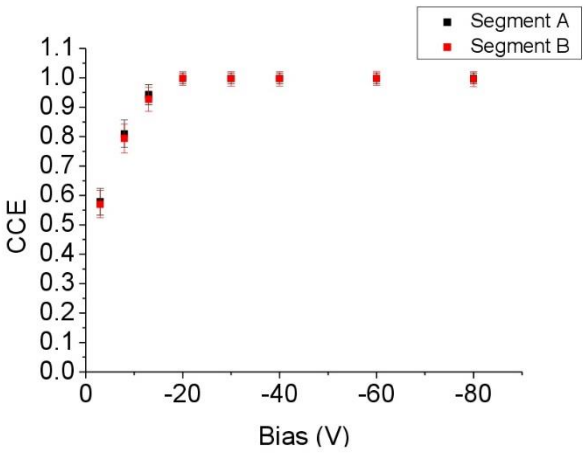

Figure 7

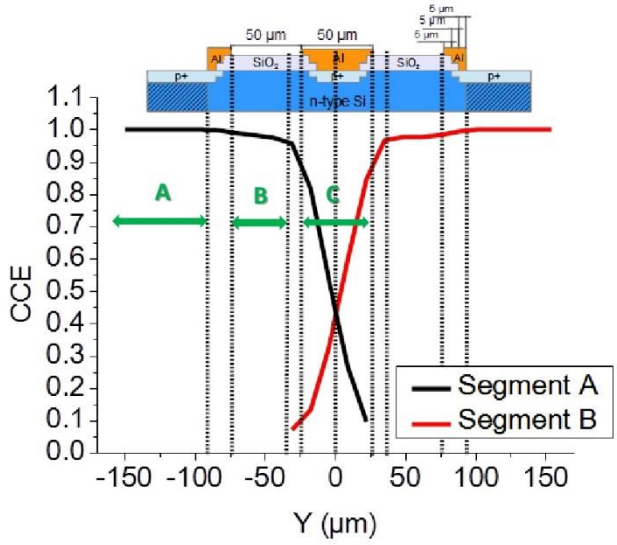

Figure 8

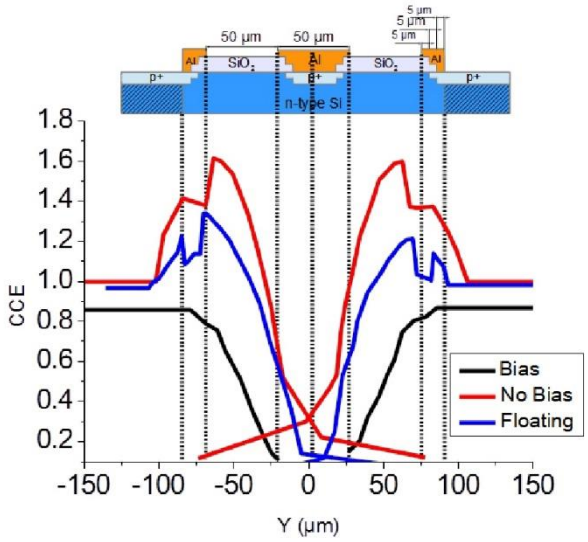
5 µm
5 µm
5 µm
50 µm
50 µm
Al
SiO2
Al
SiO2
Al
p+
p+
n-type Si
1.8
1.6
1.4
1.2
1.0
0.8
0.6
0.4
0.2
CCE
-150
-100
-50
0
50
100
150
Y (µm)
Bias
No Bias
Floating

2.1.2.2 Segmented Detector first results

In the Subsection above is shown the results presented and published, however during this thesis more work has been done in order to increase and improve the knowledge about these kind of detectors. In Figure 28 is represented the segment organisation and nomenclature in the SegDet.

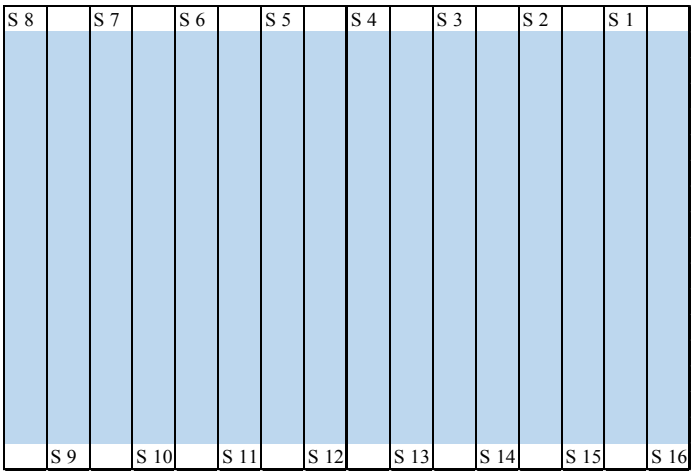

Figure 28: Segment organisation within SegDet

Previously to the detector installation in the experimental vacuum chamber and in order to understand better the operational behaviour and optimize its benefits, some tests were done in the electronic workshop. Using a pulse generator and under ambient pressure, the energy resolution and its dependence with the GR configuration was measured. In Figure 29 are represented six different configurations that were used: everything floating (EF), studied segment biased (Bias), studied segment biased while the two side segments are biased as well (B+2S), studied segment floating and GR biased (GR), studied segment and GR biased at same voltage (Bias+GR) and studied segment and GR and two sides segments biased (B+GR+2S). Using these configurations we could measure the resolution without either any source of environmental noise, dead layer shift or uncontrolled experimental perturbation; since the effect of the pulse generator, unlike a real ion, has just the electronic noise contribution of the Equation 2.4. The uncertainties are those due to the capacitor tolerance (20%) in the preamplifier test input. Through that capacitance we are able to convert the pulse voltage in energy[19]. Also the uncertainty in the measured voltage (40±1 mV) is taken in account. The bias voltage used was -40 V, the response is the same as for any other voltage after -5 V, where the depletion region is already sufficiently thick that detector capacitance is no longer the limit to energy resolution.

The results give us an idea of how the electric field is confined in the SegDet and applied voltage role. In the figure is shown the great GR impact, in which the energy resolution is even lower than in just the segment biased (20 keV for bias versus 15 keV in GR). That is because no e-h pairs are created and the charge induced is purely collected; the only important factor here is the leakage current and detector capacitance. The best configurations are bias and GR with the

[19]The conversion follows $E = \frac{E_i V C}{q_e}$; where E_i is the energy needed for the e-h pair, V is the input voltage, C the preamp test input capacitance and q_e the electron charge. In this case $E = 1350 \pm 300$ keV.

same polarisation, and bias, GR and two adjacent side segments with the same polarisation: both are equivalent, with 10 keV energy resolution.

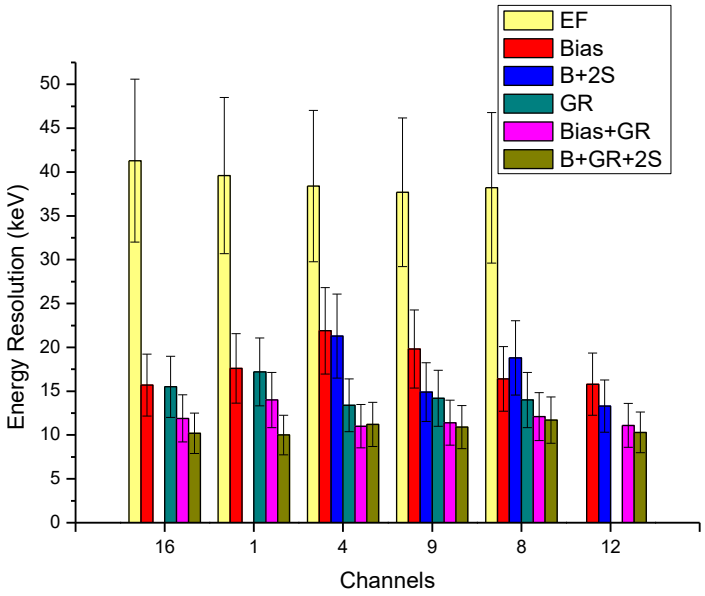

Figure 29: Segment energy resolution for several segment and guard ring configurations in the SegDet using a pulse generator and -40 V bias voltage. The uncertainty bars represent the uncertainty in the capacitance for the charge injection, and the uncertainty in the size of the voltage step applied to generate the charge. The non-shown segments were not available due to broken gold wire connection.

Once the preliminary test were done, we installed the detector (with all the housing components shown in Figure 26.a) in a vacuum chamber, without beam, using a pulse generator instead. The detector-preamp output signal was incredibly noisy due to the housing electrical shielding and poor detector board connectivity. A new board was designed and built applying the experience gained in the experimental environment (we designed the board and it was built by Nolam Embedded Systems). The metallic (brass) detector housing can be understood as an antenna; therefore the possible electromagnetic noise in the experimental environment could generate interferences in the detector signal. This can be avoided improving the electronic shielding through a better grounding choice. It has to be done carefully since for a good beam fluence measurement the chamber and the housing have to be connected between them and isolated from any other part. On the other hand the detector itself has to be completely isolated (if not the signal would not be generated), the figure shows the plastic isolating piece which makes an electrical barrier between the detector and the grid. The grid was designed to protect the thin gold wires (which make the connection for the bias and the output signal) as well as to separate the segments. The publication above demonstrates that the grid is not needed for segment separation, instead it can create unwanted scattering effects in the strip edges and generate spectrum distortions[20]. Therefore the grid was replaced by a brass mask which covers

[20] The incoming ion can collide and be scattered with the grid strip edge. The result is particles with less energy (more yield in the low energy part of the spectrum) and even changes in the segment, since the trajectory can be completely changed. Moreover the shape and straightness in the strips is not homogeneous, which is an extra complexity in a potential correction factor for these effects.

the gold wires but with a 30x30 mm² hole opened in the detector area. For shielding reasons this mask has to be grounded with the detector and isolated from the rest of the housing.

After the noise optimisation, the detector was ready to be applied in a real experimental test. Figure 30 shows an RBS experiment performed using 4 segments simultaneously, using the preamplifiers and data acquisition explained below in this chapter (Section 2.2), on a SiO_2 sample with a Carbon substrate. We used a $^4He^+$ beam at 800 keV incident energy. The backscattering angle is referenced by the SegDet centre (between Segment 12 and 4, so called S12 and S4).

It is possible to observe the silicon (around 400 keV) and oxygen (around 250 keV) peaks with slight differences in energy in the left part of the figure where both angles, S4 and S12, are very close ($\Delta\theta = \theta_{S12} - \theta_{S4} = 1.17°$) while the energy shift in the right part is more pronounced ($\Delta\theta = \theta_{S15} - \theta_{S8} = 18.4°$). There is also an extra peak just next to the substrate signal, below 200 keV, which corresponds to the carbon deposition from the beam due to the poor vacuum done during the measurements.

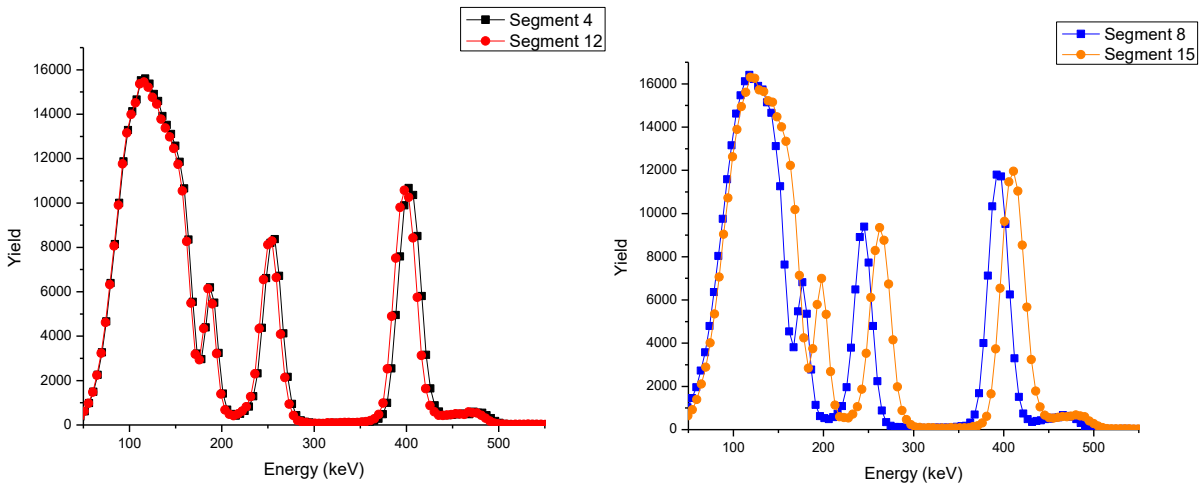

Figure 30: spectra taken simultaneously from four segments of the SegDet. Two from the centre segments (left, red and black) and two far between each other (right, blue and orange). RBS done using $^4He^+$ at 800 keV on SiO_2 on C substrate.

The large solid angle opens the way to reach higher energy using double charged ions, as commented above. In our case, SAFIR is a 2 MV High Voltage accelerator facility with 50 years of extraordinary service, it is well-known in the community for the high beam current and energy stability. Nevertheless the limitations in the terminal voltage limit the ion beam energy and thus excludes some interesting analytical possibilities. This is the case for example for the EBS resonance at 3.05 MeV for alpha particles on oxygen, ^{16}O (^4He, $^4He_0$) ^{16}O, that is widely used in in studies of oxidation processes.

One possibility to reach such energies with a small single ended accelerator is to use the doubly charged ions generated in the RF ion source, however the beam current of doubly charged ions from the source is some 10^2 to 10^3 times smaller than that of the singly charged ions – practically inexploitable for the traditional analysis systems. Here the SegDet can be extremely helpful

since by increasing the solid angle the measurement becomes feasible in a reasonable experimental time. Figure 31 shows bismuth on silicon substrate spectrum which was the first taken in SAFIR with a doubly charged alpha particle beam, $^4He^{2+}$, at 4 MeV using a 25 mm² single PIPS detector with a 6x1 mm² window in the front to avoid kinematic spread. The spectrum acquisition time was 20 minutes. From the known Bi areal density and a geometrical estimate of the detector solid angle, the incident $^4He^+$ beam fluence was estimated to be 0.64 μC (1.4 ions/nm² in the 2 mm diameter beam spot)[21], which implies a $^4He^+$ beam current of about 530pA. For an RBS experiment to give spectra with reasonable statistics, typically about 5 μC (5 ions/nm²) is required to obtain adequate statistics, and since here the measurement time was 20 minutes, a manageable experiment with this configuration would take about three hours for each spectrum. Although possible, it is probably more efficient to find a higher energy accelerator on which to perform such measurements.

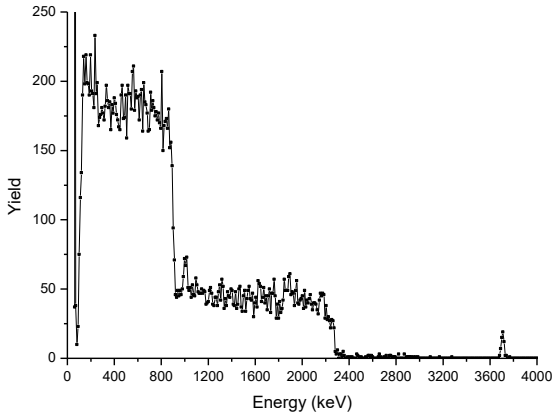

Figure 31: Bi (5.53 TFU) on Si substrate spectrum with a classical single PIPS detector (25mm²) for 4 MeV $^4He^{2+}$ ion beam. The signals up to 900 keV are HH^+ beam contribution at 2 MeV which is mixed with $^4He^{2+}$.

Note that up to 900 keV the yield is 4 times bigger. This is due to the HH^+ molecules present in the ion source, which have practically the same charge to mass ratio as the $^4He^{2+}$ and thus almost the same trajectory in the magnetic field of the analysing magnet. When the magnet and beamline elements are carefully tuned to avoid this contamination, the $^4He^{2+}$ beam current is reduced even further.

Figure 32 shows 4 MeV RBS spectra obtained with SegDet for a thin alloy (AuAgCu) film on a carbon substrate and same beam configuration as before, but with the magnet optimised to avoid the HH^+ beam component. Note that the carbon signal is 6 times higher than that expected for Rutherford scattering, since that is the cross section increase for ^4He in carbon at this higher energy. There are two SegDet segments (S5 and S12) taken simultaneously during 30 minutes. As was done above for the 4 MeV spectrum obtained with the PIPS detector, we can calculate the incident beam fluence and the $^4He^{++}$ current to be about 0.95 μC (2.1 ions/nm²) and 530 pA respectively. The spectrum obtained even with just one segment is already readily exploitable and when the spectra are obtained simultaneously for all 16 segments, equivalent information

[21] The values here are just approximations taking the number of particles in the spectra and acquisition time.

would be obtained in around 2 minutes. To obtain this information with the standard PIPS detector would again take on the order of three hours.

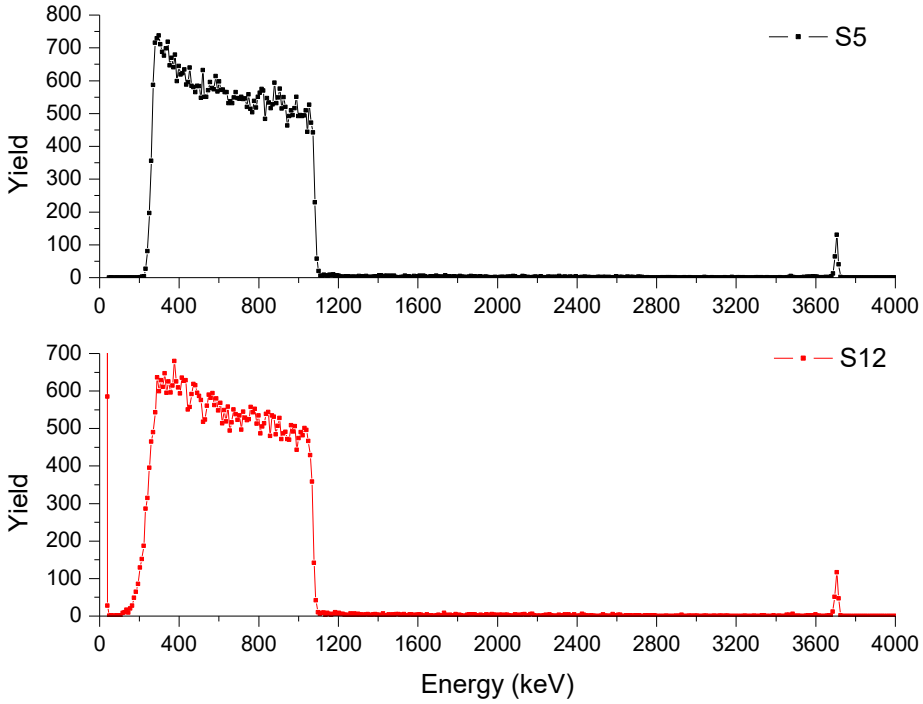

Figure 32: $Au_{0.78}Ag_{0.15}Cu_{0.07}$ (3.77 TFU) on C substrate spectra from SegDet, segment 5 on top and 12 on bottom, for 4 MeV $^{4}He^{2+}$ ion beam.

2.1.3 Annular Detector

In a first approach to obtain even higher solid angles within the SPRITE project (Marie Curie Actions) an annular segmented detector has been designed in collaboration with HZDR Rosendorff[22]. The main structure is similar to that of the SEGDET, which has been shown to operate well. The main improvement from such a detector is the increase of the solid angle for Ion Beam Analysis (IBA) techniques based on charged particle detection (Rutherford Backscattering Spectroscopy, RBS; Nuclear Reaction Analysis, NRA; Elastic Recoil Detection Analysis, ERDA; etc.), as was explained above. Furthermore, for backscattering techniques, the proposed annular design allows a large backscattering angle, since the beam passes through a hole in the centre of the detector (Figure 33) which is the optimal configuration because a detector with enlarged surface area can be used, increasing the count rate. The detector is divided into annular segments in order to keep the capacitance low, which also keeps the electronic noise low, as was shown above, and to follow cylindrical symmetry. As a segmented detector, it can also of course resolve the mass /depth ambiguity inherent in RBS spectra.

[22] Milestone 2.3: Develop design of annular segmented detector

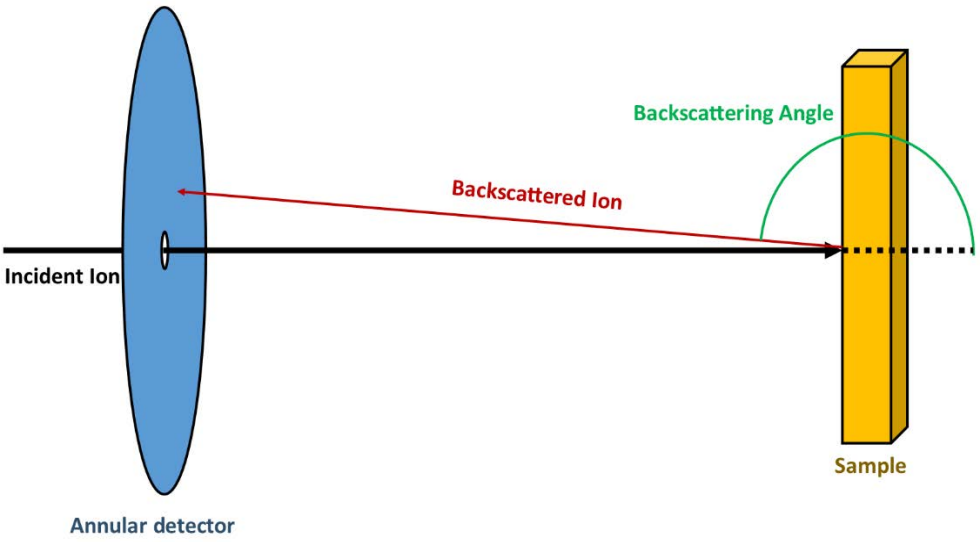

Figure 33: RBS and annular segmented detector schema.

The layout of the detector has to be carefully chosen. As the detector capacitance and leakage current significantly influence the energy resolution, the area of the single detector segments should kept low. Furthermore it is important to minimize the kinematic spread due to the segment width, where the backscattering angle covers a range $\Delta\theta$ between maximum and minimum values. The detector energy resolution has been explained above (Subsection 2.1.1). For a commercial PIPS 50 mm^2 detector at room temperature with a 400 µm of depletion zone (capacitance ≈ 13 pF, leakage current ≈ 20 nA) and standard preamplifier system, the typical energy resolution for the statistically independent contribution is around 10 keV[23]. In our design segment areas are 50 mm^2 and 400 µm depletion layer (17 pF, 15 nA) have been used, hence here it is reasonable to expect an energy resolution of about 10 keV[24] as well.

The design presented here has been arrived at by imposing an energy resolution for the kinematic spread smaller than 4 keV for light elements such as silicon, for which the kinematic spread is the greatest. In most practical cases there are also other system contributions for the energy uncertainty which may be difficult to control since they are associated with the measurement system which is reasonably valued at 1 keV, but which can be negligible in very low noise environments (for more details see Subsection 2.1.1). Therefore in our design the total energy resolution taking in account all the contributions is around 15 keV.

[23] Those values are based on the semiconductor PIPS detector Ortec data sheet.

[24] Electronic energy resolution is $\Delta E_{elec} \sim \sqrt{I_D + C_D^2}$ (Equation 2.5). Leakage current (I_D) is smaller in our case than in the reference, between 0.7 to 0.8 times. The square capacitance in our case is between 1.5 to 2 times bigger. Therefore the differences are $\sqrt{0.7}$ and $\sqrt{0.8}$ smaller for current and $\sqrt{0.5}$ and $\sqrt{1}$ bigger for capacitance, hence is reasonable to consider no changes in these contributions in energy resolution.

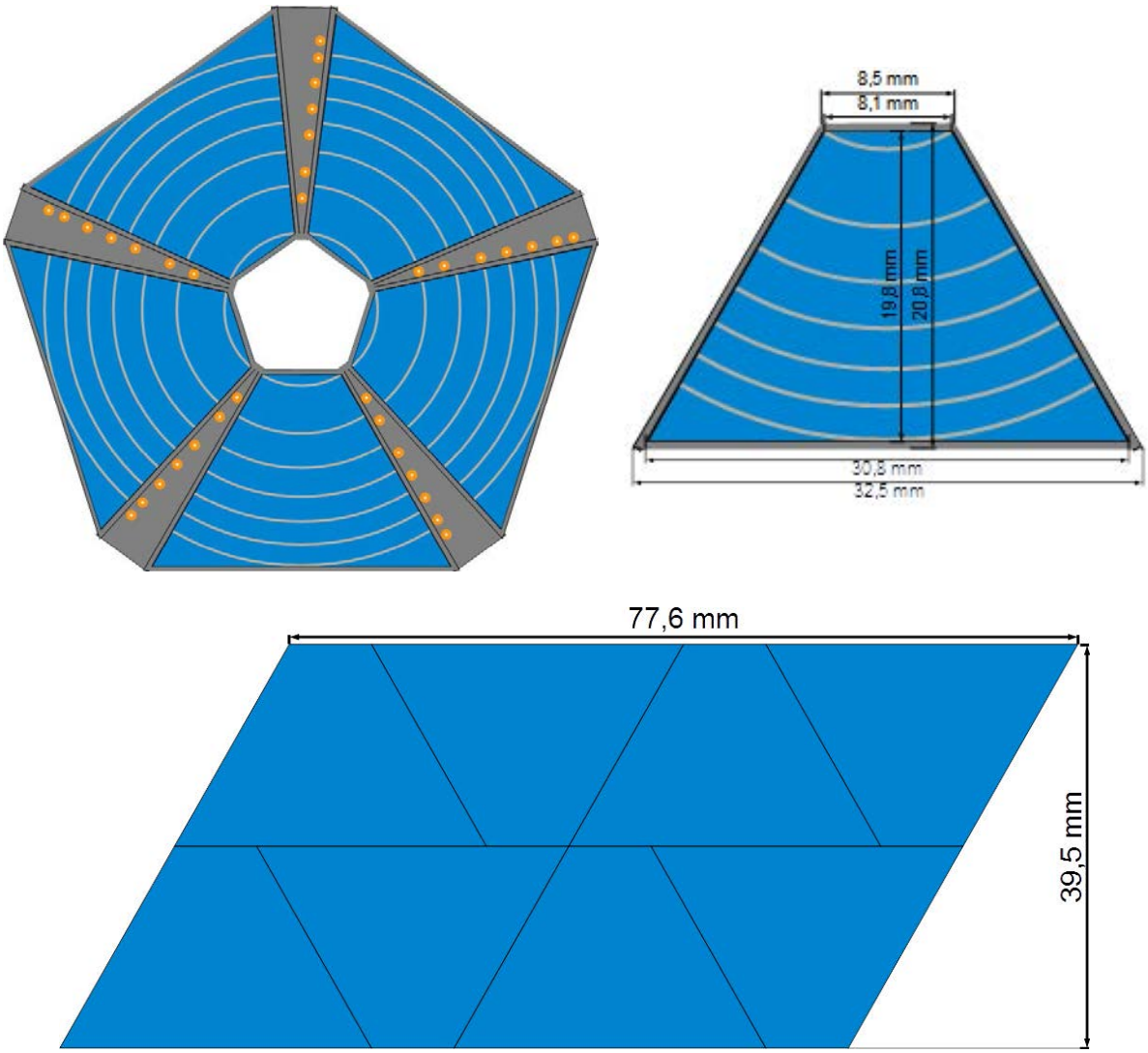

Figure 34: On the top-left is the annular detector design. The detector active area is blue and the detector mounting boards with copper signal paths are grey. On the top-right is a detector section on the PCB. On the bottom is shown the proposed pattern for fabrication of 6 detector sectors in a 77.6 x 39.5 mm silicon wafer.

The detector design is shown in Figure 34, where the detector is composed of 6 annular segments, each divided into 5 sectors giving a total of 30 segments for the array. Each segment is surrounded by a 280 µm wide guard ring zone, with a 30 µm guard ring, in order to confine the electric field in the vicinity of the detector edges [65]. It is usually biased at the same voltage as the detector bias. In Figure 35 is shown the guard ring structure.

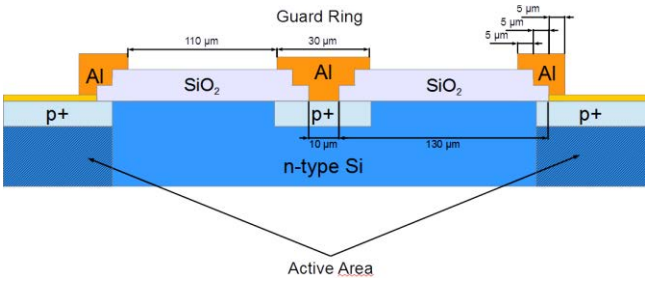

Figure 35: Interstrip schema: guard ring and passivated zone. Detector active areas are in left and right sides.

For a normally incident beam and 70 mm between the target and the detector, the backscattering angles (θ) go from 173° to 159°, the complete area for the active zone is 250 mm² and the total solid angle is 282 msr. In Figure 35 are shown the specifications for the segments in each part.

The five silicon sectors are independent and have to be mounted on a printed circuit board (PCB). The PCB schema, front and back side, is shown in the top of Figure 36. The front side is divided in insulator (in grey) and detector grounding zone (in orange). The grounding part is where the detector would be glued with silver paste. It is covered with a cooper thin layer to have an ohmic contact. There is also a pad-hole connection for the grounding between both sides. In the back side of the PCB the pad-holes are connected between them in order to have a common ground.

Table 1: Segment specifications. R (max and min) is segment radius, r is segment width, and area is calculated for the segment from one of the 5 sectors. The sold angle (Ω) of each segment is calculated for the segment from one of the 5 sectors for a target-detector distance of 70 mm.

Segment	**θ_{max} (°)**	**θ_{min} (°)**	**R_{max} (mm)**	**R_{min} (mm)**	**r (mm)**	**Ω (msr)**
1	173,48	169,77	8.00	12,63	4,63	9,88
2	169,56	166,98	12,90	16,18	3,28	9,69
3	166,77	164,71	16,45	19,14	2,69	9,49
4	164,5	162,76	19,41	21,73	2,32	9,31
5	162,56	161,02	22,00	24,07	2,07	9,13
6	160,83	159,46	24,34	26,23	1,89	8,95

To make the p-n junction, $5 \cdot 10^{14}$ atoms/cm^2 of boron (p-type) would be implanted into the wafer front side and $5 \cdot 10^{14}$ atoms/cm^2 of phosphorus (n-type) would be implanted at 50 keV into the wafer back side. Aluminium ohmic contacts are also required on both sides and a passivation oxide added around the guard ring in order to avoid current leakage at the edges [65].

The above detector design may be fabricated using standard semiconductor processing techniques (ion implantation, lithography, CVD, etc.) as was the case for the SPIRIT/SPRITE linear segmented detector array (Subsection 2.1.2).

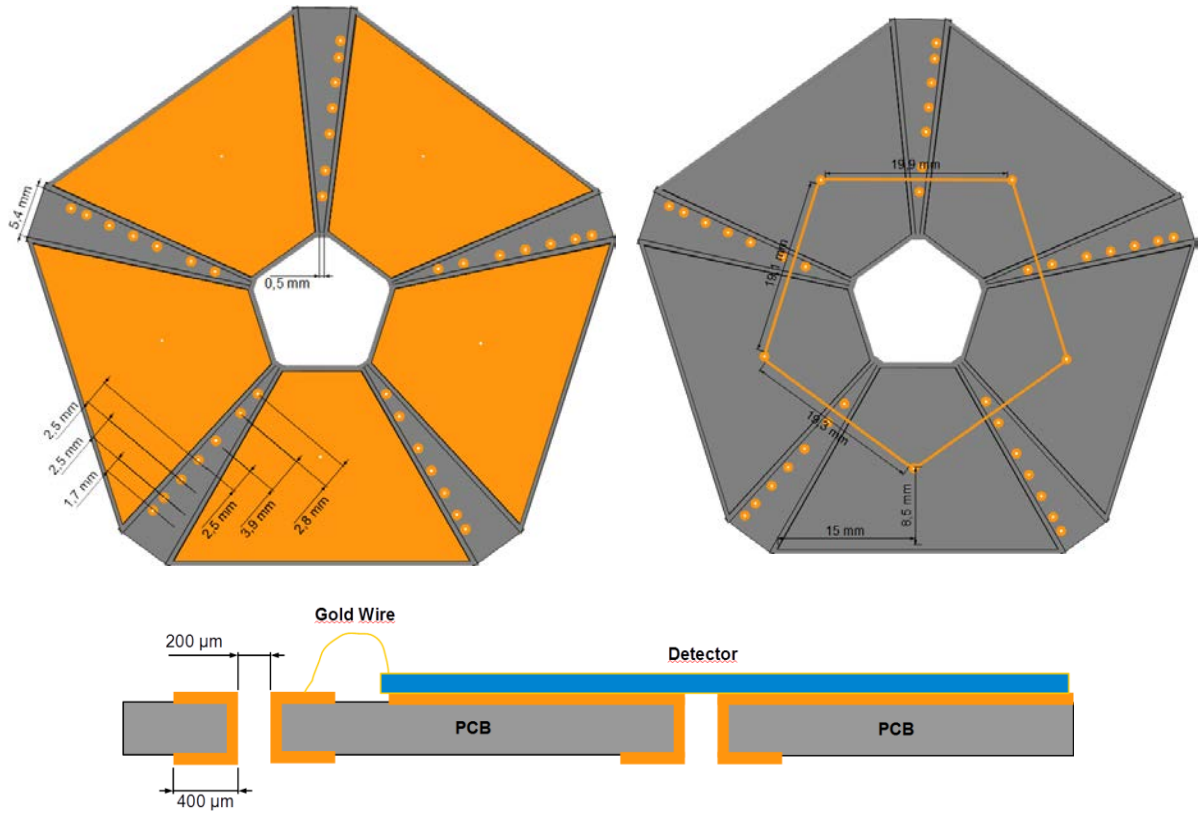

Figure 36: On the top-left, PCB front side where are the pad-hole connections in the insulator part (grey) – with geometrical dimensions – and cooper covered for the back detector side grounding. On the top-right, PCB back side with a common ground connection. On the bottom, Contact pad-hole schema for detector output signal, input guard ring voltage and detector back side grounding connection.

2.2 Signal Acquisition and Treatment

Once the SegDet is operative a proper procedure is needed to treat the signal that comes from it. The typical IBA acquisition system is shown in Figure 37, it is composed by a preamplifier, just after the detector; signal shaping and digitalisation. The standard method for shaping is a semi-Gaussian shape through an analogue signal amplifier and a digitisation after that [69]. However in our system we used a digital shaping approach provided by CAEN S.p.A, SPRITE partner[25].

[25] VAD undertook a secondment (SPRITE Internship Mobility Partnerships (IMPs) at the main CAEN facility in Viareggio (Italy) during this PhD.

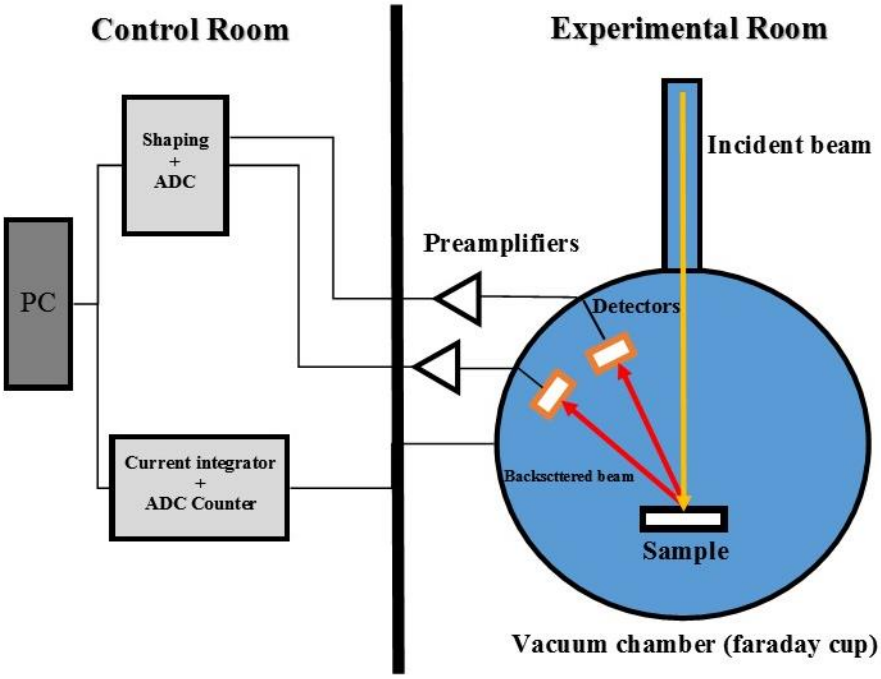

Figure 37: Data acquisition system schema.

2.2.1 Preamplifier

The charge Q induced in the detector by the passage of a charged particle is typically too small (~fC) to be directly digitised and must therefore undergo an initial analogue amplification. This is accomplished with a charge sensitive preamplifier which is, basically, a linear current integrator with an operational amplifier (opamp) where the current signal is converted into a voltage step, of height V_o given by

$$V_o = G\frac{Q}{C_f} \qquad 2.9$$

Where G is the opamp gain and C_f is the value of the feedback capacitor. A preamplifier circuit schema is shown in Figure 38. The capacitor C_f gets charged quickly, i.e. short *rise time*, after which the current has to pass by the feedback resistor R_f which discharges the capacitor slowly, i.e. long *decay time*. This approach minimizes the effect of noise in the detector signal. The detector polarisation voltage is applied via a current-limiting resistor in the preamps. The preamps is placed as close as possible to the detector and the packaging has to be kept small in order to minimize the cable capacitance and limit microphonic noise and environmental pickup.

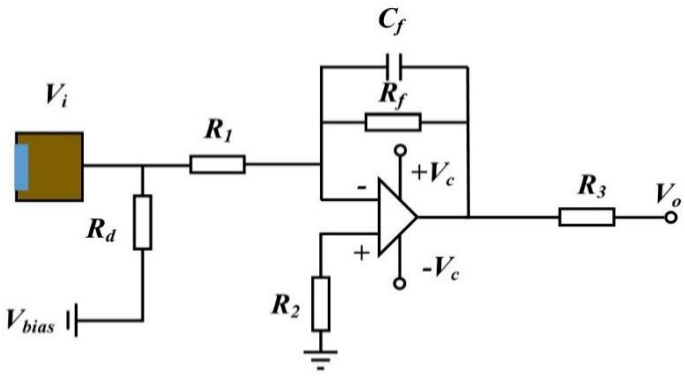

Figure 38: Preamplifier circuit. Input detector voltage, V_i, induced by the charge deposited and the output voltage, V_o, would be prepared for the shaping. R_f and C_f are the op amp positive feedback to increase de voltage and R_d is the detector bias resistor.

In our system, 16 acquisition channels have to be available, therefore two 8 channel preamplifiers were designed[26] based on the Cremat CR110 hybrid preamplifier modules[27]. In The preamp board is shown in Figure 39.a the detector polarisation is daisy chainable for multiple boards, and provision is also made for applying the polarisation to the guard ring. The power supply is also daisy-chainable, and protected by pi-filters.

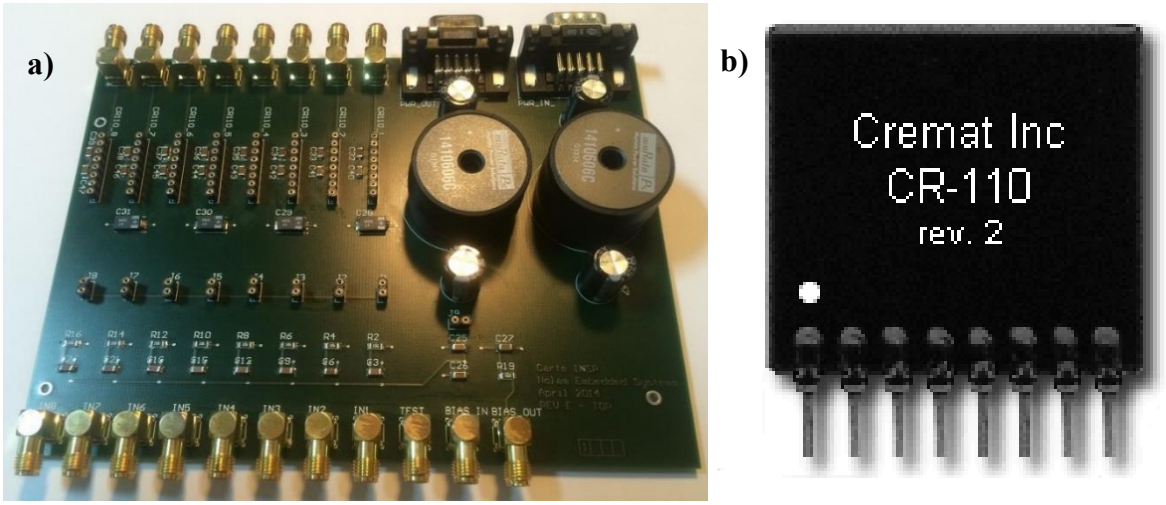

Figure 39: a) INSP-Nolam preamp board picture. b) Cremat CR-110 preamplifier.

2.2.2 Data Acquisition: from analogue to digital

2.2.2.1 Analogue system

In the standard IBA experiment data acquisition is performed through a shaping amplifier (semi-Gaussian shape) and a peak sensing analogue-digital convertor. The digitised pulse height signal is treated by a multichannel analyser installed in a computer, which represents

[26] in collaboration with Nolam Embedded Systems, Creteil, France

[27] https://www.fastcomtec.com/fwww/datashee/amp/cr-110.pdf

these data as a histogram (see Figure 2 in Subsection 1.1.1). A diagram of such a signal treatment and acquisition system is shown in Figure 40.

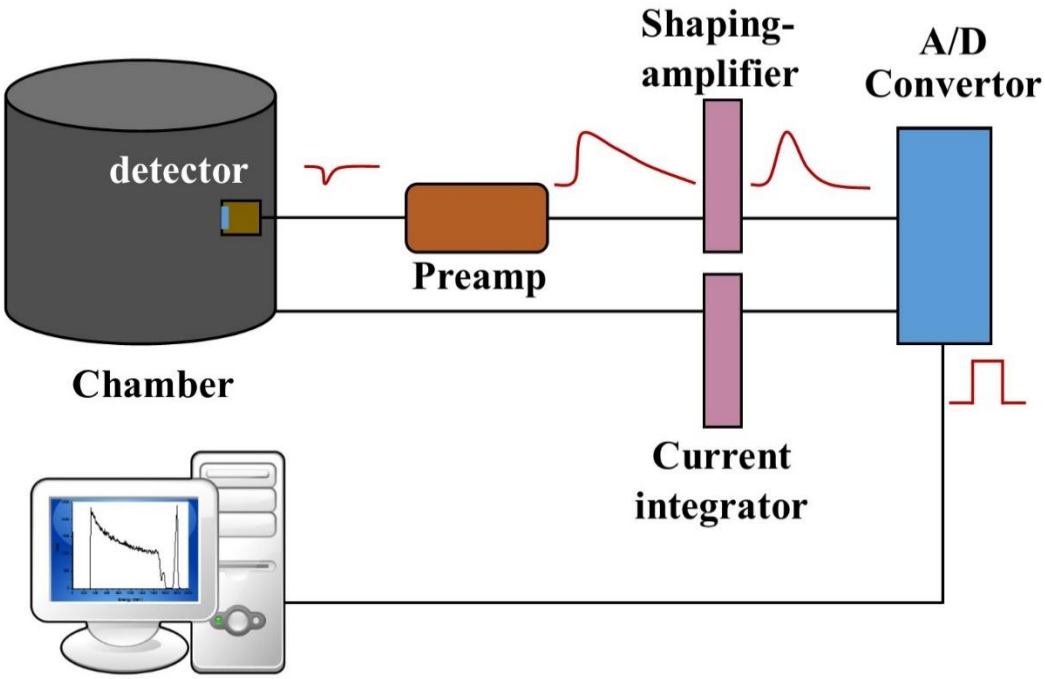

Figure 40: Analogue data acquisition system. Red lines are the signal shape after each step. The current integrator is used to measure the charge deposited, the input comes from the chamber and the output goes to A/D Converter.

The first step post-preamplifier in the acquisition is the pulse shaper which mainly functions to smooth the sharp step signal coming from the preamp and to attenuate the noise, effectively improving the signal-to-noise ratio through an optimised frequency filter. The signal treatment can be considered in reciprocal space using the Fourier transformation. It is based on high pass, differentiator, and low pass filters, and an integrator (CR-RC). The convolution of both generates the semi-Gaussian signal. The amplitude of this signal is proportional to the incoming ion energy. CR and RC time constant parameters have to be optimised for the experiment since the noise bandwidth and signal amplitude are related to them. The optimal configuration of differentiator time, τ_{dif}, and the integrator time, τ_{int}, have to be equal, $\tau_{dif} = \tau_{int} = T_p$. Thus T_p is the maximum output pulse value, which is called *shaping time* or *peaking time*. Increasing T_p allows averaging over a greater time and so results in less noise and better resolution. However increasing T_p also increses the time window in which a second particle can arrive and interfere with the treatment of the signal from the first particule, resulting in pulse pile-up, meaning it is necessary to find the optimum compromise between noise attenuation and single event measurement. In an extreme case, the next event will be overlapping the first one to the extent that the pulse height of the composite event will be the sum of the heights of the two events. Even choosing optimum time parameters pulse pile-up cannot be completely avoided, and the amplifier/shapers usually have further pile-up rejection circuit installed. This feature uses fast electronics to identify piled up pulses and establishes a time window within which the ADC is inhibited (and thus contributes to the ADC deadtime), however pulses which arrive too

closely together to be identified as piled up cannot be rejected and the remaining pileup needs to treated in spectrum simulations [70], [71].

Three other parameters in the acquisition are important. The *threshold* establishes the minimum pulse voltage height to be take into account as an event. This will reduce the false signals due to the white noise (high frequency). It has to be fixed high enough to discriminate those possible false events but low enough to count the real incoming ions. The second parameter is the *baseline*, which sets the zero amplitude of the shaping amplifier, restoring it just after each event, and is crucial to have an accurate pulse height measurement. The last one is the *pole-zero* tail cancelation which optimally damps the signal from the shaping amplifier through the use of an additional tuneable resistor so that the signal returns as rapidly as possible to zero, without overshoot or undershoot.

The last step in the chain is the peak sensing ADC, which converts the pulse height into a digital signal which can be classified by the multichannel analyser, obtaining the final histogram.

The second part of the system is related to integrating the current of the incident ion beam. The measured charge is proportional to the number of incident ions, and then to the charge. In our system the chamber acts as a faraday cup and so must be completely isolated from ground, where the ions colliding with the sample (total incident ions, N_i) are generating a current. The current integrator outputs a pulses for each incremental amount of charge, which may be counted.

2.2.2.2 Digital system

The analogue data acquisition has been used for decades since it has a great robustness and a quite reliable performance. Usually the after-preamp equipment is in the control room powered by a NIM (Nuclear Instrument Module) power supply (22x48x27 cm, 5 kg). Furthermore the cost per acquisition channel is very elevated (>10k€/channel).

In our case we have been using the 16 segments SegDet, so a standard data acquisition method would have a very high cost. Instead we employ a Digital Pulse Processing – Pulse Height analysis (DPP-PHA) provided by CAEN Spa (Viareggio, Italy) in the SAFIR facility. There the external analogue amplifier and ADC are not necessary anymore, since all the electronics after the preamp is within the digitiser box. A diagram of the acquisition chain is shown in Figure 41.

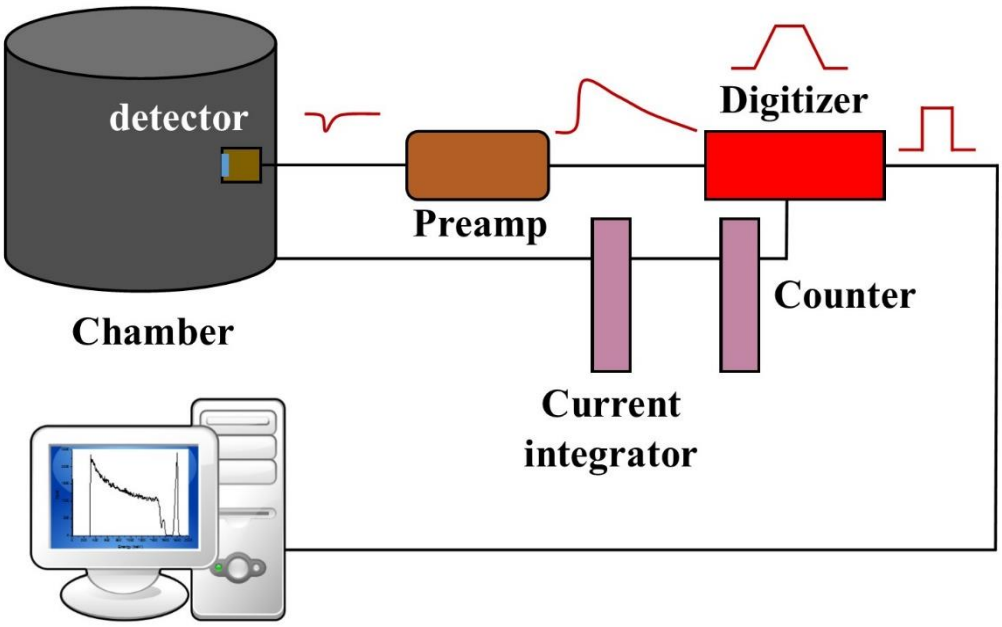

Figure 41: Digital acquisition system using the digitiser provided by CAEN S.p.A

In the digital approach the ADC is the first step after the preamplifier, using a 14-bit 250MSample/s flash ADC followed by a FPGA (Field-Programmable Gate Array) where the digital signal will be treated and prepared to be displayed in a PC. From here the first advantages arise. In our system we used two CAEN DT5725 modules, which are very compact (20x20x5 cm), with 8 spectroscopy channels each. Furthermore, the price per channel, including preamplifiers, is less than 1k€, unachievable for the analogue systems where the price would be over 10 times more. Further advantages are that all the event data may easily be recorded in list-mode for detailed off-line treatment and that all the acquisition settings can be easily saved and recalled.

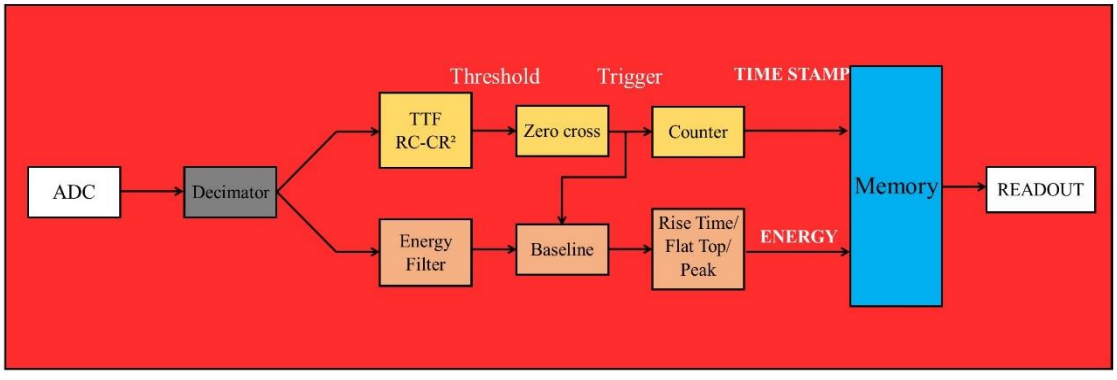

Figure 42: Digital signal treatment schema.

The signal treatment within the DPP CAEN digitiser, shown in Figure 42, starts in the flash ADC, where the analogue signal coming from the preamp is digitalised. After that, a decimation filter is placed in order to rescale the time parameters if the signal is very slow. Usually for IBA

applications it is not the case. The next step are the filters, one dedicated to timing and another for energy.

In the timing branch a trigger and a time stamp are generated when an event comes. There the noise will be reduced, avoiding false pulses (*smoothing factor* and *trigger threshold*) due to high frequency noise and subtracting the *baseline* after the event to minimize the pile-up. It is working like the CR-RC filter in the analogue system, but with a bipolar treatment, being actually, a RC-CR² filter. The bipolar approach improves the event identification since the zero crossing is detected irrespective of the pulse amplitude. The minimum time interval, *delay*, between two events may be set.

The energy filter is where the digital CAEN approach differs most from the analogue. Instead of a semi-Gaussian shaping, trapezoid shaping is used [72]. Here, as with the analogue system the height of the shaped signal is proportional to the preamp pulse height. The trapezoid timing is divided in three steps: *rise time* (T_R), *flat top* (T_{FT}) and fall time. Fall and rise time (which are always equal) and the flat top width can be adjusted. They have an analogous function to the pulse shaping time in the analogue shaping amp, and therefore they have to be well chosen in order to optimize resolution and to avoid pile-up. During ($2T_R + T_{FT}$), if a second event arrives, the pile-up rejecter will reject both pulses, however these pulses can be counted as pile-up events and included in the *dead time*, which was not possible in the analogue system. The rejecter cannot function the case of two very close events (during the CR-RC² filter time) and there will be a real pile-up event. However there exist *hold-off* and *live time correction* settings which can be programmed to establish a no recording time after the trigger and avoid even these pile-up events.

When this time ($2T_R + T_{FT}$) finishes the *baseline* is restored, over a programmable number of points. If the *decay time* (analogous to pole zero in the analogue system) is properly set up, the baseline restoration is perfect. The amplitude between the baseline and the filtered signal at the *peaking time* is the actual measurement of the energy. The trapezoid height will be obtained by averaging the trapezoid flat top over a programmable width (*peak mean*).

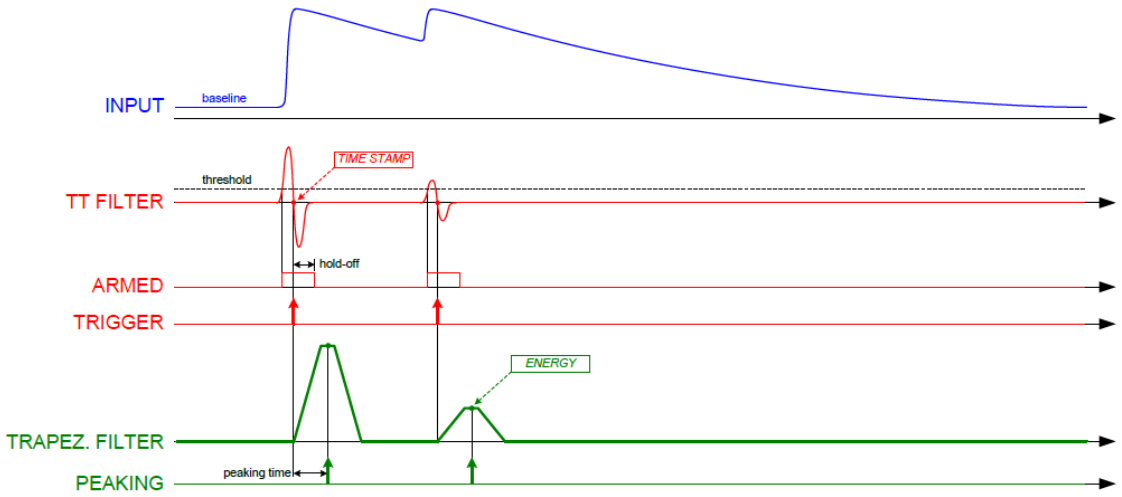

Figure 43: Signal stages during the treatment. CAEN user manual picture.

2.2.2.3 Acquisition System comparison

The digital approach given by the DPP is the most promising acquisition system for our setup, however it has to be tested and compared with the well-established analogue system in order to demonstrate at least equivalent performance. With this aim we performed full RBS experiments, including RBS-channelling, using both acquisition systems. It was reported as a part of the SPRITE project[28]. The experiments were performed at the ALTAÏS tandem accelerator (Université de Namur, UNAMUR, Belgium). Since the objective was to test the acquisition system a standard RBS configuration was used, with a Passivated Implanted Planar Silicon detector (PIPS) collimated to 1mm and placed at 165° and standard Canberra preamplifier and bias power supply. The analogue acquisition was the standard system used at the ALTAÏS laboratory (as explained above) while for the digital acquisition we used CAEN DPP (model DT5724) with MC²A multichannel analyser software provided by that company. The beam was $^{4}He^{+}$ at 1500 keV. The beam fluence was measured through a current integrator connected to the chamber as a faraday cup, as usual, and one of the DPP input channels was used to count the charge pulses, providing then not just the beam charge value but a time stamp for each beam charge pulse. Two samples were studied; a bismuth thin layer ($5.53 \cdot 10^{15}$ cm^{-2}) implanted in silicon (classical RBS reference sample) and Bi_2Se_3 (Topological Insulator, TI, that will be treated below, Chapter 3) epitaxially grown on GaAs, capped with ZnSe and lightly doped with Fe.

[28] Milestone 2.2: Enhanced digital acquisition in collaboration with CAEN Spa

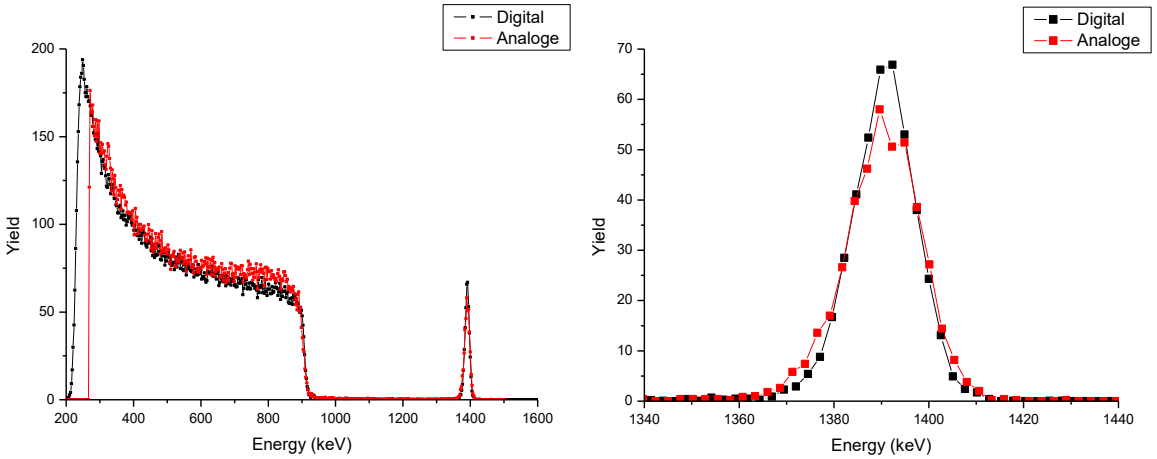

Figure 44: Bismuth on silicon substrate RBS spectra; black line is the full digital acquisition spectrum whereas the red line is the classical analogue one. On the left is shown the spectra overview, on the right the zoom in the Bi peak.

The Figure 44 shows the digital and analogue normalised[29] spectra taken on the Bi/Si sample. Equivalent appearance and quantification can be observed in both cases. The Bi peak areas are 1068 (±33) and 1066 (±32) total counts in the digital and analogue spectrum respectively. However measuring the Full Width at Half Maximum (FWHM) in the Bi peak, which corresponds to the energy resolution of the measurement, we obtain 15.4 keV for digital and 18.2 for the analogue, which is a significant improvement due to the easier way to manage the different parameters in order to optimize the acquisition given by the digital approach. Note that there is a slight difference in the Si substrate around 800 keV, where the analogue spectra has more counts. That might be explained by channelling effect in the Si <1 0 0> crystal in the digital measurement and some small variation in the experimental environment.

A similar comparison was made in the TI sample. In this case we investigate the system results in an RBS-channelling experiment. The main experiment was an ion lattice damage study through channelling (explained in Subsection 1.1.2), where the aim is to measure the $\chi_{\min}$, which is a crystallographic order indicator, at different ion fluences– from 39.8 nm^{-2} (5 μC deposited in a 1 mm diameter beam spot) to 835.6 nm^{-2} (105 μC) – trying to induce Type I damage (Annex II: Ion Damage). In Figure 45 are the two different system spectra obtained; it demonstrates the at least equivalent behaviour and reliability for the full digital acquisition, validating the system for routine use in an IBA laboratory.

Since the scientific interest of this experiment was the atomic disorder evaluation as a beam fluence function, we also performed a comparison of the χ evolution[30] in both system as is shown in Figure 46. The equivalence is still there for both systems in the values and the

[29] The spectra normalisation is the ratio yield/fluence.

[30] Here is not strictly true to call χ_{min} since the disorder is too high to be in the monocrystal range, as will be explained in Chapter 3, hence the correct nomenclature has to be just χ.

tendencies[31], where the increment is a result of generated nuclear Type I damage due to the beam.

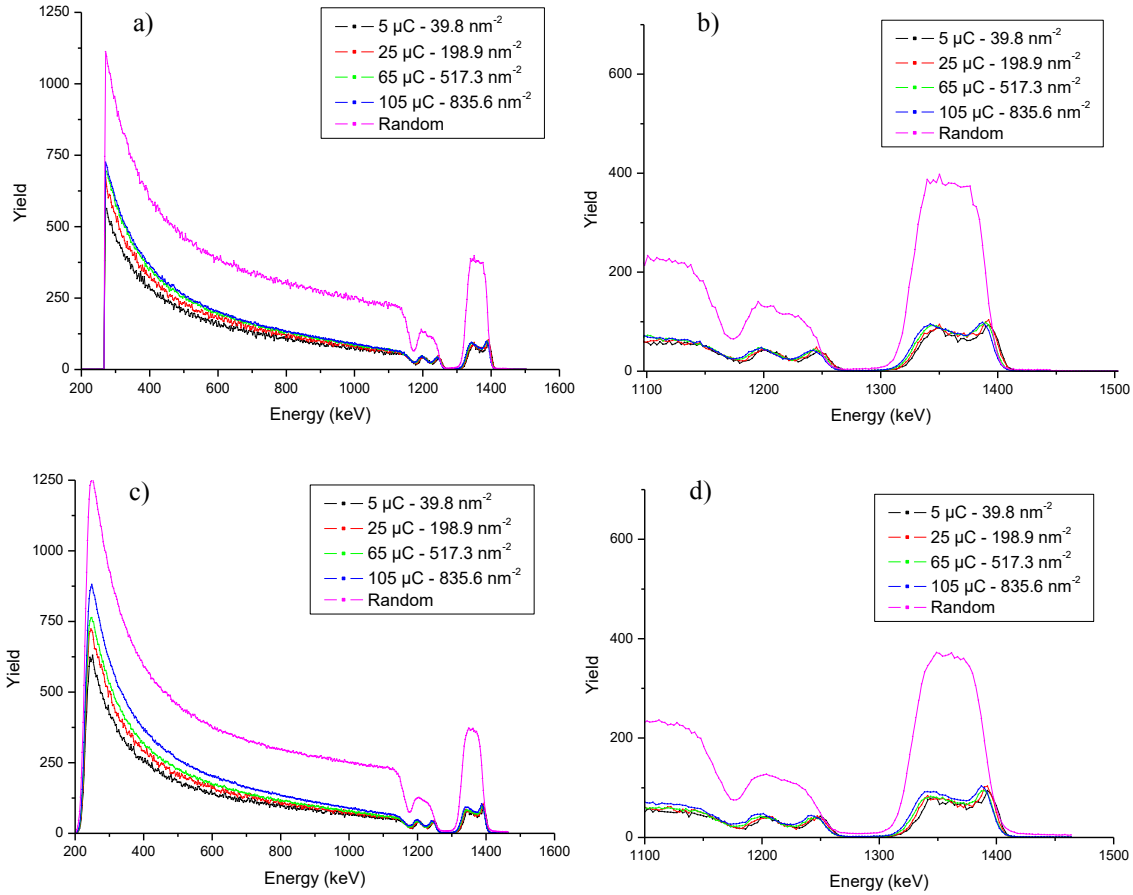

Figure 45: a) and b) analogue and c) and d) digital RBS-channelling spectra for lightly Fe doped Bi_2Se_3 on GaAs with a capping layer of ZnSe

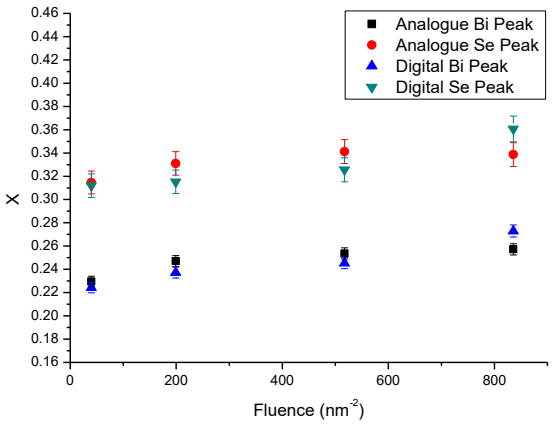

Figure 46: Disorder evolution as a fluence function for the Bi and Se peak compared between the two acquisition systems.

[31] The highest fluence value in Bi is not quantitative equivalent, however, comparing with the Se graph, the tendency is right.

3. IBA in Topological Insulators

The first system to be studied with the SegDet were the Topological Insulators (TI). As explained above (Section 1.2), the TI are a new interesting electronic state of the matter in which the conduction in the surface is helical due to the strong spin orbit coupling. The Topological Surface States (TSS) ruling that behaviour are expressed as Dirac Hamiltonian equation solution with massless carriers, which is expressed in the electronic bands as a gapless Dirac cone and protected by time-reversal symmetry. The spin dependence in the electronic current direction makes these materials a great candidate to be used as spintronic technology material. One of the most promising TI materials object of extensive research efforts is Bi_2Se_3, which is a canonical second generation TI example [49]. However the knowledge about them is still in developing process and there are many questions, some of them basic ones, opened to be studied by IBA techniques.

Within this chapter will be presented the motivations to apply our detection system in these compounds (Section 3.1), as well as the sampling used (Section 3.2). Two different phases were done in the study. A first set of RBS and RBS-channelling experiments was made using a standard setup (single PIPS detector and analogue data acquisition). The results of this study were presented at 22nd International Conference on Ion Beam Analysis[32] and Section 3.3 is the subsequently published article. In the second phase an in-depth study was made with more samples, techniques and the complete new detection and acquisition system operative (Section 3.4). The final conclusions and future perspectives are commented in Section 3.5.

3.1 Motivation

The IBA techniques can give us direct measurement information about composition and depth profile (RBS, PIXE, NRA), and also atomic lattice order and evolution of ion beam induced damage (RBS-Channelling). In our case due to our enhanced IBA system we approach this research for two main reasons:

1. To be able to manage the TSS it is necessary to magnetically dope the surfaces. Then the Dirac cone can be opened and the states made controllable [73]. Also, non-magnetic doping can be useful in order to move the Dirac cone centre (known as Dirac point) to the same value as the Fermi level and thus decrease the bulk conduction contribution to measurements of the surfaces state conduction [74]. Using the SegDet, the low amounts of doping materials may be measured due to its large solid angle.

2. The Bi_2Se_3 has a Quintuple Layer (QL) structure, with the bond between QLs rules by Van der Waals forces. These forces are relatively weak[33] hence could be sensitive to nuclear damage Type I (Annex II: Ion Damage) created in the crystal lattice by the analysing alpha particle beam. A large solid angle would reduce such damage for a given analysis.

[32] These results were also the object of an oral presentation at Ion Beam Analysis Francophone 2014

[33] In a rough estimation $F_{VdW} \propto 10^{-12}\ N$, while $F_{ionic} \propto 10^{-6}\ N$ and $F_{covalent} \propto 10^{-9}\ N$

3.2 Samples and Experimental Setup

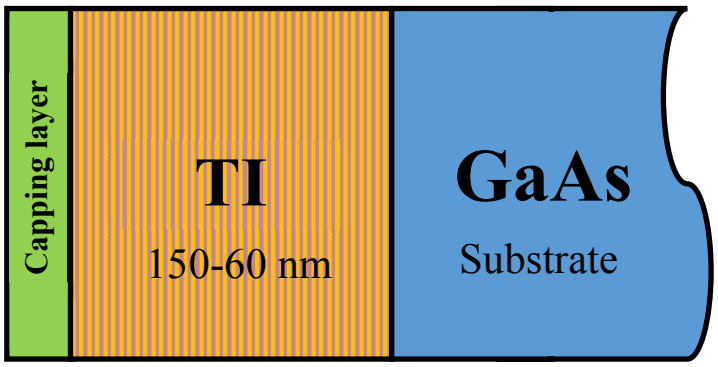

Figure 47: Samples layout schema

The samples (Figure 47) were grown by Molecular Beam epitaxy (MBE) in our own laboratory, INSP (Institute de NanoScience de Paris), where some previous work has been undertaken within the Growth and Properties of Thin Layer Hybrid Systems (Croissance et Propriétés de Systèmes Hybrides en Couches Mince) team. The growth procedure is explained elsewhere [75]. The study concerned thin undoped and Fe-containing[34] Bi_2Se_3 samples with various nominal amounts of Fe which was incorporated during growth (these were just qualitatively known before the IBA experiments). They were grown epitaxially on (111) GaAs substrate and capped with ZnSe, Se or Au to avoid oxidation or degradation of the first TI layer. In Table 2 we give the sample nomenclature used throughout this chapter as well as the layer composition. The sample growth method results in TI behaviour, as it was proved in [76].

Table 2: Fe free and Fe containing Bi_2Se_3 samples. The capping layer is represented in the first term of the 2nd column. The iron index (Fe^x) represents the nominal relative iron amount ($[Fe^1] < [Fe^2] < [Fe^3]$).

Sample 1	Au/Bi_2Se_3/GaAs
Sample 2	Au/ Bi_2Se_3 (Fe^2)/GaAs
Sample 3	Au/ Bi_2Se_3 (Fe^3)/GaAs
Sample 4	Au/ Bi_2Se_3 (Fe^1)/GaAs
Sample 5	Se/ Bi_2Se_3/GaAs
Sample 6	Se/ Bi_2Se_3 (Fe^2)/GaAs
Sample 7	Se/ Bi_2Se_3 (Fe^3)/GaAs
Sample 8	Se/ Bi_2Se_3 (Fe^1)/GaAs
Sample 9	ZnSe/ Bi_2Se_3/GaAs
Sample 10	ZnSe/ Bi_2Se_3 (Fe^3)/GaAs
Sample 11	ZnSe/ Bi_2Se_3 (Fe^1)/GaAs
Sample 12	ZnSe/Bi_2Se_3(5QL)/GaAs
Sample 13	Bi_2Se_3/GaAs

[34] Throughout the text we used "Fe-containing" instead "Fe-doped", since below we show that substitutional doping was not achieved in most cases

Section 3.4 presents the results obtained in several laboratories. During the renovation work on the laboratory building we started the experiments presented in Section 3.3 using the 2 MV tandem ion accelerator facility ALTAÏS at Université de Namur (UNAMUR), where we used a classical IBA setup, i.e. analogue acquisition chain and single PIPS detector. For RBS and RBS-Channelling experiments we used a $^4He^+$ beam at energies between 1500 and 2000 keV with a backscattering angle between 140° to 162°.

PIXE experiments included in Subsection 3.4.1 were performed at the 3 MV tandem accelerator from Centro Nacional de Aceleradores (CNA) facility at Universidad de Sevilla (US), with simultaneous RBS measurements using an analogue data acquisition system and $^4He^+$ ion beam at 2000 keV with 165° backscattering angle for the silicon detector and 145° for the PIXE SiLi detector. The analysis is done using data from both Namur and Sevilla. The RBS-channelling measurements in Subsection 3.4.2 are the same as those presented in the publication, but more detailed.

Attempts to implement the SegDet in Namur and at the Surrey Ion Beam Centre of the University of Surrey[35] proved to be very difficult, mainly due to the short time available to overcome various mechanical difficulties and to successfully identify and mitigate electronic noise sources. We therefore decided to mount and test the SegDet in our laboratory in Paris and wait until the SAFIR was reinstalled and operational in the renovated laboratory. Here the electronic and mechanical environment is well controlled daily by ourselves and the test possibilities for the new system were more fluid. Therefore Subsection 3.4.3 shows the results taken with full DDA and SegDet in SAFIR 2 MV Van de Graaff single ended ion accelerator facility, using a $^4He^+$ ion beam at 2000 keV with the segmented detector centre placed at 155° (angle range from 165° to 146°).

In all the cases the beam spot diameter was 0.5-1 mm and the beam current lower than 50 nA, allowing us to neglect pile-up events.

[35] The author had a SPRITE internship there in order to try and mount the SegDet for tests, and to obtain advanced experience in using the NDF DataFurnace software.

3.3 Results: Publication II[36]

Nuclear Instruments and Methods in Physics Research B 371 (2016) 224–229

Contents lists available at ScienceDirect

Nuclear Instruments and Methods in Physics Research B

journal homepage: www.elsevier.com/locate/nimb

Rutherford Backscattering Spectrometry analysis of iron-containing Bi_2Se_3 topological insulator thin films

V. Alarcon-Diez [a,*], M. Eddrief [a,b], I. Vickridge [a,b]

[a] Sorbonne Universités, UPMC Univ Paris 06, UMR7588, INSP, F-75005 Paris, France
[b] CNRS, UMR7588, INSP, F-75005 Paris, France

ARTICLE INFO

Article history:
Received 6 July 2015
Received in revised form 18 September 2015
Accepted 25 November 2015
Available online 11 December 2015

Keywords:
RBS
Topological insulators
Bi_2Se_3
Fe–Se intergrowth

ABSTRACT

Fe-containing Bi_2Se_3 topological insulators (TI) thin films have been grown to investigate the intricate interplay between topological order and the incorporation of ferromagnetic atoms. Here we present the quantitative characterisation of the Bi_2Se_3 thin films with up to 16 at% Fe incorporated during the growth process on GaAs (1 1 1) substrate by Molecular Beam Epitaxy. We report the elemental composition and depth profiles of the Bi_2Se_3:Fe films obtained using Rutherford Backscattering Spectrometry (RBS) and their formed crystalline phase obtained by X-ray diffraction (XRD). Resistance of the TI to beam-induced damage was investigated by channelling RBS. Using the elemental composition from RBS and the thickness from XRD measurements the Fe-free film density was deduced. For Fe-containing samples, the diffraction reveals the formation of two distinct crystalline phases, as well as their intergrowth pattern, in which the basal planes of Bi_2Se_3 coexist with an additional Fe–Se phase. This intergrown composite, with chemical compatibility of the Fe–Se phase with the crystalline Bi_2Se_3 structure, preserves the intrinsic topological surface states of the TI component despite the inhomogeneous distribution of the constituent phases. RBS analysis gives the stoichiometry of the Bi_2Se_3, and Bi_2Se_3:Fe samples (estimated between 0 and 16 at% Fe) and gives insights into the composition of $FeSe_x$ phases present.

© 2015 Elsevier B.V. All rights reserved.

1. Introduction

In three-dimensional topological insulators (TIs), the strong intrinsic spin-orbit coupling generates an insulator band inversion with spin-momentum locking leading to creation of protected topological surface states (TSS) due to time-reversal (TR) symmetry [1]. These surface states are described by the relativistic Dirac Hamiltonian – Dirac cone – with massless Dirac fermions as charge carriers. The charge carriers are characterised by their helicity property and the topological order of their surface states, meaning that opposing electron spin states generate opposing currents without backscattering effects. These states are very robust under TR variations [2]. The topological nature with its spin texture is extremely interesting not only from the technological perspective, for example in quantum computing and spintronic devices, but also in fundamental particle physics (Majorana fermions, axions, magnetic monopoles…) [3]. However for such applications it is necessary to be able to form a ferromagnetic TSS, breaking TR symmetry and thus opening the Dirac cone and creating a band gap in the TSS. This may be attempted through doping with a magnetic dopant [4,5], to give for example Bi_2Se_3:Fe. Bi_2Se_3 has been used due to the band structure, with just one Dirac cone in the TSS and the bulk energy band gap compatible with ambient temperature, together with a well-defined crystal structure.

In this work, we have quantitatively studied the elemental composition of Bi_2Se_3:Fe topological insulator thin films. The Bi_2Se_3 samples were epitaxially grown by Molecular Beam Epitaxy (MBE) on GaAs (1 1 1) substrates and including varying concentrations of Fe in the growth process to obtain Bi_2Se_3:Fe samples, with Fe/(Bi + Se + Fe) atomic ratios up to 16% (reported in Table 1 below). The films were 100 nm thick, either uncapped or capped to protect from oxidation. We will show that the Fe reacts with the Se, forming $FeSe_x$, this intergrowth compound having no influence on the topologic gapless surface state. Rutherford Backscattering Spectrometry (RBS) was applied to determine film elemental compositions and concentration depth profiles. To our knowledge, these are the first direct quantitative determinations of the elemental composition of such thin Bi_2Se_3:Fe films.

* Corresponding author. Tel.: +33 1 44 27 46 88.
E-mail address: victor.alarcon@insp.upmc.fr (V. Alarcon-Diez).

http://dx.doi.org/10.1016/j.nimb.2015.11.031
0168-583X/© 2015 Elsevier B.V. All rights reserved.

[36] With permission from I. Vickridge, M. Eddrief. Rutherford BackscatteringSpectrometry Analysis of iron-containing Bi_2Se_3 topological insulator thin films. Nuclear Instruments and Methods in Physics Research Section B, volume B371, pp224-229, Elsevier, 2016.

2. Methodology

The Bi_2Se_3 samples are grown by MBE on GaAs (1 1 1) substrate and either left uncapped or capped with one of three layers: ZnSe, Se or Au. More details of the epitaxy and characterisation of the Fe-free Bi_2Se_3 films are given in [6]. For the RBS analysis presented here, Au capping was used in order to avoid overlapping the signals from the TI with that of the capping layer. Growth is conducted under Se-rich conditions – similar to the case of the GaAs buffer layer grown under As rich condition – since the substrate temperature during growth is greater than that at which Se (or As) evaporates. In the Bi_2Se_3:Fe samples, Fe was evaporated at the same time as the Bi and Se, with the nominal Fe content being controlled through the Fe flux, which was varied via the temperature (T_{Fe}) of the Fe Knudsen cell.

Elemental composition was obtained by Rutherford Backscattering Spectrometry (RBS) using an $^4He^+$ ion beam of energies between 1500 and 2000 keV, with 5–20 nA in a 0.5–1 mm beam spot. Under these conditions deadtime was less than 1% and pileup was negligible. The backscattering angle varied between 145° and 165°. X-ray diffraction (XRD) was also undertaken as a complementary technique, using monochromatic Cu Kα X-rays. The Bi_2Se_3 structure consists of a 5-layer unit cell dominated by covalent bonds, with the stack of 5-layer units (quintuple-layers, or QL) held together via van der Waals forces. Since the van der Waals forces are weak, we also investigated the stability under the analysis beam of the TI layers by channelling RBS.

The NDF DataFurnace code (NDFv9.6a and WiNDFv9.3.76) [7] was used to fit the RBS spectra. Spectra were taken at several points on each sample. All of the spectra from a given sample were fitted simultaneously with NDF in order to improve the statistics and increase the representivity of the studied area. SRIM-2003 stopping power was used [8]. We found it necessary to apply a correction of 0.9 to the stopping power of gallium in order to obtain adequate fits of the substrate plateau height. This correction produces the correct plateau height in a GaAs bulk sample. The Chu model was used for the straggling [9], Andersen for screening [10] and Molodtsov and Gurbich for pile-up correction [11]. Double scattering was implemented in order to get good fits to the GaAs substrate signal at low energies [12] in the spectra. In all cases the detector dead layer (determined elsewhere) was included in the fit model.

3. Results and discussion

3.1. He beam damage

Possible beam damage was assessed from channelling spectra. The beam was aligned with the GaAs ⟨1 1 1⟩ axis, which corresponds to ⟨0 0 1⟩ in Bi_2Se_3, and aligned spectra were acquired for increasing incident beam charge. Angular scans showed that the Bi_2Se_3 ⟨0 0 1⟩ axis was aligned with the GaAs ⟨1 1 1⟩ axis. Fig. 1 shows the random spectrum, and a series of channelled spectra accumulated for increasing incident beam charge (expressed in ions/nm^2). The random spectra were obtained by summing several spectra obtained from pseudo-random orientations. The disorder in the lattice has been parameterized by the random/channelled ratio (chi, χ) which is 0.23 in the Bi peak and 0.32 in Se at the lowest beam fluence. Whilst in an ideal well-ordered crystal χ would be less than 0.05, in these samples significantly larger disorder was observed. We also note higher χ in the Se peak than in the Bi peak. Further channelling studies aimed at understanding this are underway, however this shows the robustness of the TI, since all the studied samples show TSS [6,13] even with this degree of disorder. The damage evolves slightly with the deposited charge, as shown in Fig. 2, where it is possible to observe a slight increase in χ as the fluence increases from 31 ions/nm^2 (5 μC in 1 mm beam diameter) to 656 ions/nm^2 (105 μC). The fluence used for experiments reported here was never greater than 93 ion/nm^2 (15 μC) and we conclude that beam damage may safely be neglected for these composition measurements, which are all obtained for random orientation of the samples.

3.2. Composition

In the case of uncapped layers, uncontrolled oxidation occurred, and in the case of Se and ZnSe capped layers, contributions to the spectrum from the capping layer contributed significant uncertainty to the estimation of the amount of Se in the TI layer itself. We present here only RBS results for three gold-capped Bi_2Se_3 layers, which gave the best analysis conditions for NDF Data Furnace. In sample 1, no Fe was introduced during the growth. In samples 2 and 3, Fe was evaporated at temperatures T_{Fe} of 1360 °C and 1370 °C respectively during growth.

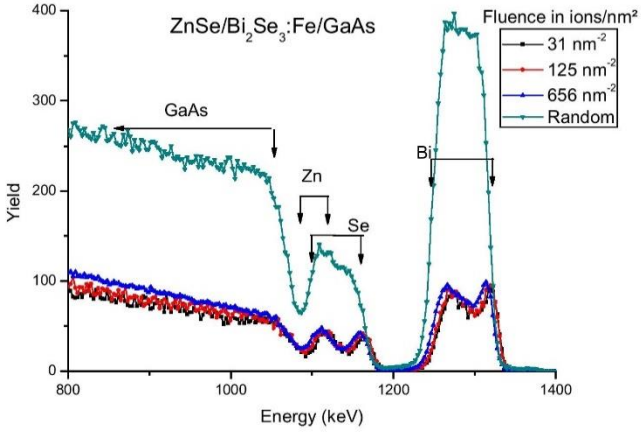

Fig. 1. RBS-channelling spectra obtained from slightly Fe incorporated amount in Bi_2Se_3, capped with ZnSe and on GaAs substrate, for increasing ion beam fluences. The signal from the iron is between 1000 and 1050 keV, however it is too small to be measured here.

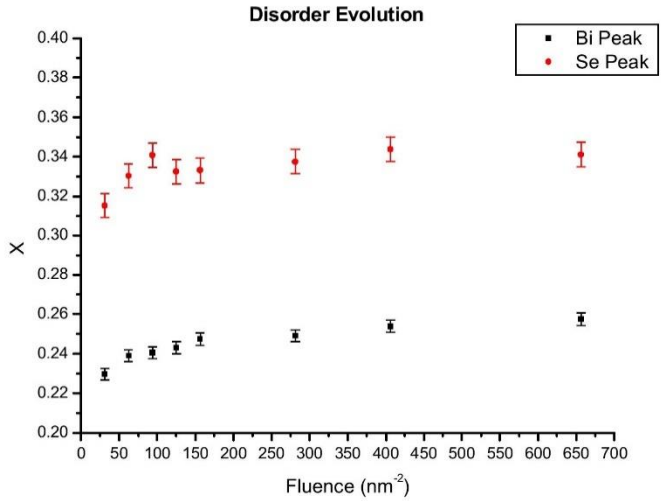

Fig. 2. Disorder evolution; random/channelled ratio (chi, χ) chi vs incident ion fluence.

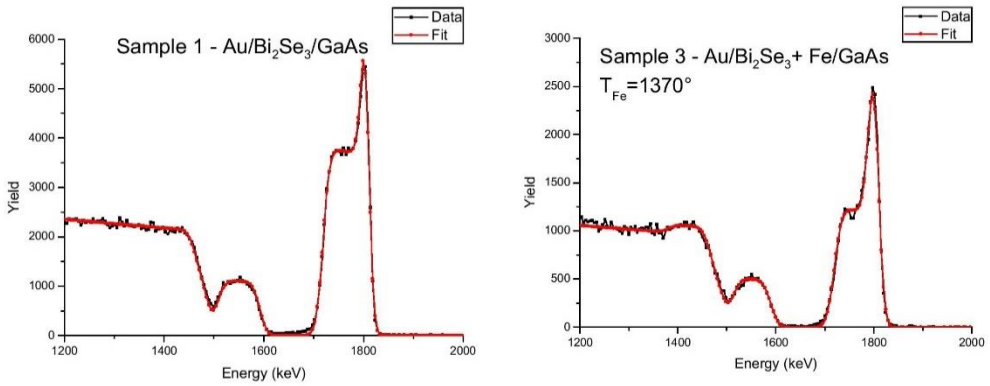

Fig. 3. Sample 1 (Fe-free) and sample 3 spectra (black) and fits (red). (For interpretation of the references to colour in this figure legend, the reader is referred to the web version of this article.)

In all cases, spectra from several points and/or measured at different angles and incident beam energies were simultaneously fitted with NDF, yielding areal densities for Fe, Bi and Se, as shown in Fig. 3. Once the optimum fit was obtained, the uncertainty for each fit was assessed by re-fitting the spectra with the Bi/Se ratio and Fe content constrained to a desired value (leaving NDF free to optimise charge, gain, detector angle etc, as was the case for the unconstrained fitting). Goodness of fit was then judged by eye and the range of Bi/Se ratios and Fe content consistent with the data was judged from the range of these constrained fits that were consistent with the data. An example of such a series of constrained fits is given in Fig. 4. Note that these uncertainties are only those associated with the fitting process and the information contained in the spectra: systematic uncertainties (e.g. uncertainties in screening corrections or stopping powers) are not considered, but will be common to all measurements.

The summary of the fitted results and range of values found is given in Table 1.

We first note that in all cases the films are rich in selenium, since in stoichiometric Bi_2Se_3 Bi/Se would be 0.67. Careful attention was paid to obtaining good random spectra so that undesired

Table 1
Fitted results. Thickness as total number of atoms – is expressed in Thin Film Unit (TFU), where 1 TFU = 10^{15} atoms/cm^2 – and in nm.

	Bi/Se	Fe (%)	Thickness (TFU)	Thickness (nm)
Sample 1 (no Fe)	0.59 ± 0.02	0	489 ± 3	137.7 ± 0.9
Sample 2 (T_{Fe} 1360 °C)	0.51 ± 0.03	14 ± 2	295 ± 5	83.1 ± 1.4
Sample 3 (T_{Fe} 1370 °C)	0.43 ± 0.02	16 ± 2	472 ± 3	133.0 ± 0.9

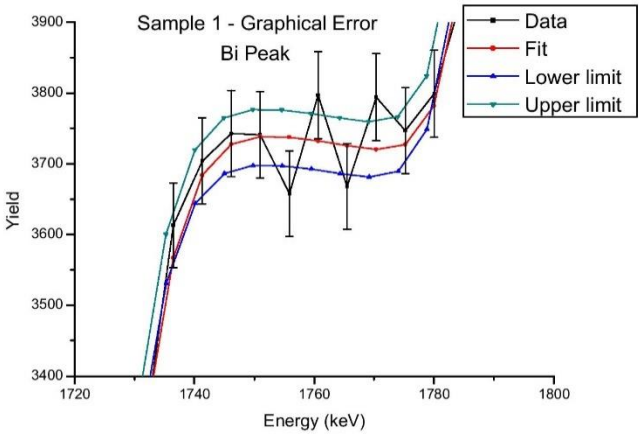

Fig. 4. Sample 1 optimal fit (red), lower (blue) and upper (cyan) limit. (For interpretation of the references to colour in this figure legend, the reader is referred to the web version of this article.)

channelling effects are negligible here. The MBE is undertaken under Se-rich conditions, however the films have well-defined X-ray diffraction peaks for undistorted Bi_2Se_3 (blue line in Fig. 6) and no local perturbations are observed by Transmission Electron Microscopy (TEM, not shown here). This implies that any excess selenium is in sites that do not disturb the lattice structure. The Fe-free film displays the expected TSS behaviour and the Dirac cones are observed in ARPES [6,13] so the selenium excess is not having a significant effect on these properties of the system either. Similar composition has been found in uncapped samples and samples with different capping layers, always obtaining an excess of Se although with greater uncertainties as mentioned above. We note that the RBS spectra indicate homogeneous concentration with depth, which is shown in Fig. 5 for the Bi_2Se_3 sample. RBS spectra from the Bi_2Se_3:Fe samples also indicate constant composition with depth, including for the Fe for which a signal is also visible in the spectra.

We can reformulate the compound as $Bi_2Se_3 + Se_{excess}$. For the Fe-free sample Se_{excess} is 11 ± 3% of the total amount of Se. This surprising result will require further characterisation in order to understand where the excess Se is, however this result is consistent with the channelling spectra obtained during the beam damage investigation. The Bi channelling yield is about 23% of that of the random yield whilst the Se channelling yield is about 32%. If the sample were to be just disordered Bi_2Se_3 we might expect to have similar disorder in the two sublattices, with Se also having a channelling yield around 23%. It is intriguing that the Se channelling yield is equal to that of the Bi plus 9% more of the total Se yield – close to the 11% overall Se excess observed in random RBS spectra.

The small difference in temperature for the Fe Knudsen cell between samples 2 and 3 corresponds to 8% difference in Fe vapour pressure [14] and thus Fe flux arriving at the growth surface, which is consistent with the difference in Fe concentration observed.

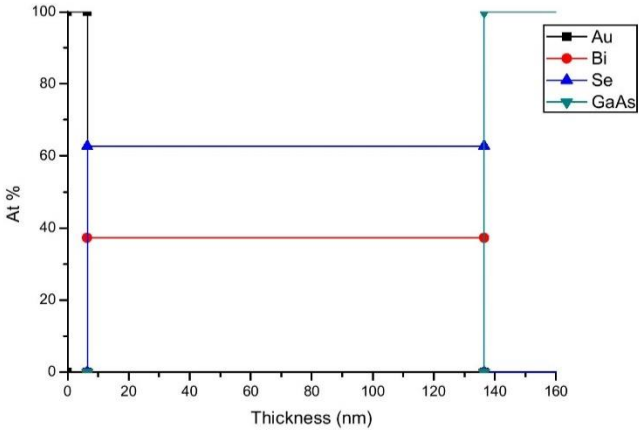

Fig. 5. Sample 1 Bi_2Se_3 depth profile, using ideal Bi_2Se_3 atomic density calculation.

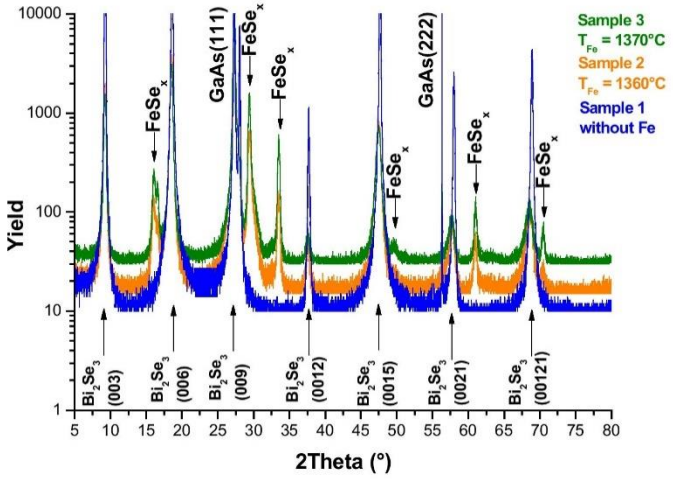

Fig. 6. X-ray diffraction spectra (monochromatic Cu Kα). In blue is the sample 1 with Bi_2Se_3 peaks well defined; around 23° there is a parasitic peak which may be ignored. Orange and green lines are sample 2 and 3 respectively, where the Bi_2Se_3 peaks are less intense and broadened, probably due to the presence of $FeSe_x$ phases. (For interpretation of the references to colour in this figure legend, the reader is referred to the web version of this article.)

Finally, we note that as the Fe content increases, the Bi/Se ratio decreases. This suggests the possible presence of Fe–Se phases, which we denote $FeSe_x$. The Fe–Se phase diagram is complex [15] however XRD of Fe-rich films shows peaks consistent with $FeSe_x$ phases (orange and green lines in Fig. 6). Due to the complexity of the phase diagram and the associated complexity in indexing the XRD peaks we cannot know with certainty the number and identity of all the phases, since it is not possible to index them all using ordinary methods. We noted that the primary pattern is from Bi_2Se_3, whose expected Bragg peak positions are marked with ticks – $(00l)$ reflections, which obey the rhombohedral diffraction condition $l = 3n$, whilst the indexation of $FeSe_x$ phase peaks remains yet to be determined. However substantial disorder has been found in Bi_2Se_3:Fe samples since the Bi_2Se_3 Bragg peaks are broader for these samples than those obtained from the Fe-free sample. Furthermore, the Fe–Se alloy peak positions are the same between the two samples, indicating that in the two samples the basal planes of the $FeSe_x$ phases have the same alignment with respect to the Bi_2Se_3 planes. Nevertheless the $FeSe_x$ planes are probably different due to an inhomogeneous distribution with different texture orientations. The XRD measurements also gave a measure of the physical thickness of the Fe-free film, through the Laue oscillations observed in the wings of the Bi_2Se_3 Bragg peaks.

Under this scenario it is possible to consider the quantity of Se as the sum of three different contributions: that related to Bi forming Bi_2Se_3 (Se_{Bi}), that in excess Se_{excess}, and that forming an alloy $FeSe_x$ (Se_{Fe}) so that we consider the film to be composed of $Bi_2Se_3 + Se_{excess} + FeSe_x$. Furthermore, angle-resolved photoemission spectrometry (ARPES) measurements (not shown here) on these Fe-rich samples show that the Dirac cone has not been opened, suggesting that there is little or no Fe substitution into the Bi_2Se_3 lattice. Although the Fe–Se phases are not yet known, the results found by RBS can be used to calculate the overall index x for this alloy, as the Se/Fe ratio. This calculation has been based on the formulation $Bi_2Se_3 + Se_{excess} + FeSe_x$ and the results extracted by NDF fits with all the conceivable values of x, taking several possible values for Bi/Se_T (where $Se_T = Se_{Bi} + Se_{excess} + Se_{Fe}$) and the Fe content, within the uncertainty limits, and averaging them to find the best estimate for x. Two extreme hypotheses are presented in Table 2. At one extreme, we assume that the percentage Se excess in the Bi_2Se_3:Fe samples is the same as that experimentally determined in the Bi_2Se_3 sample ($Se_{excess} = 11\%$). At the other extreme, we assume that all excess Se is associated with $FeSe_x$ phases ($Se_{excess} = 0$). In both cases, $x < 1$ (Fe-rich) for $T_{Fe} = 1360$ °C, and $x > 1$ (Se-rich) for $T_{Fe} = 1370$ °C. The resulting estimates of the atomic percentage of $FeSe_x$ in Fe rich samples are 21% for sample 2 and 33% for sample 3 when $Se_{excess} = 11\%$ (experimental value reported above for the Bi_2Se_3 film) and 27% and 39% when a perfect stoichiometry of Bi_2Se_3 is assumed ($Se_{excess} = 0$).

Table 2
FeSe index calculation. Two extreme hypotheses were assumed: Bi/Se obtained experimentally from the sample 1 (Fe-free), and Bi/Se equal to the stoichiometric value.

	Bi/Se	Se_{excess}/Se_T	x = Se/Fe	
			Sample 2	Sample 3
Experimental fitting	0.59	0.11	0.51 ± 0.15	1.02 ± 0.23
Stoichiometry	0.67	0	0.94 ± 0.19	1.32 ± 0.26

Furthermore the atomic and mass densities for the Bi_2Se_3 iron free sample can be calculated from the number of atoms and physical thickness obtained in RBS and XRD respectively. We find $\rho_{atomic} = (3.88 \pm 0.15) \cdot 10^{22}\ cm^{-3}$ and $\rho_{mass} = 8.22 \pm 0.32\ g\ cm^{-3}$, when taking into account the total number of atoms measured ($Bi_2Se_3 + Se_{excess}$). On the other hand, if we just count the number of Se atoms that would be required to form stoichiometric Bi_2Se_3 and ignore Se_{excess}, we obtain $\rho_{atomic} = (3.62 \pm 0.18) \cdot 10^{22}\ cm^{-3}$ and $\rho_{mass} = 7.88 \pm 0.39\ g\ cm^{-3}$. The first result is significantly greater than the expected density for an ideal Bi_2Se_3 crystal which may be calculated from the unit cell, giving $3.55 \cdot 10^{22}\ cm^{-3}$ and $7.71\ g\ cm^{-3}$ atomic and mass density respectively, whereas the second result is in good agreement, further underlining the view that the excess Se is present in such a way as to not disturb the Bi_2Se_3 lattice.

4. Conclusions

RBS-channelling showed that the Bi_2Se_3 layers are sufficiently robust to allow RBS analysis without significant beam induced damage. The initial amount of disorder, with the smallest value of χ observed to be 0.23, is significantly greater than that expected for a defect-free crystal.

The elemental composition extracted by RBS in combination with XRD of the Bi_2Se_3 films, shows an excess in Se (Se_{excess}) of $11 \pm 3\%$, which we describe as $Bi_2Se_3 + Se_{excess}$. Nevertheless neither the lattice structure measured by XRD nor the electronic properties are different from those expected for an ideal Bi_2Se_3 TI. Moreover the density calculations also suggest that the Se excess does not significantly disrupt the Bi_2Se_3 structure. Bi_2Se_3:Fe samples show a decreasing Bi/Se ratio as a function of the amount of incorporated Fe. The presence of Fe–Se phases is shown by XRD spectra and the great majority of Fe atoms are within this $FeSe_x$ alloy, hence Fe atoms are probably not diluted within Bi_2Se_3. The alloy has been expressed as $FeSe_x$, where x is Se/Fe ratio. Whatever hypothesis is retained for the distribution of the Se not incorporated into stoichiometric Bi_2Se_3, the composition determined by RBS allows us to deduce that overall the $FeSe_x$ phases are Fe-rich ($x < 1$) for sample 2 ($T_{Fe} = 1360$ °C) and Se-rich ($x > 1$) for sample 3 ($T_{Fe} = 1380$ °C).

Further experiments are planned using other Ion Beam Analysis (IBA) techniques, such as Particle Induce X-ray Emission (PIXE), in order to study samples with smaller Fe concentrations, and using a large solid angle segmented detector in order to reduce uncertainty through improved statistics. Since such a detector will also produce spectra for a range of detection angles, this will also reduce the mass/depth ambiguity in samples capped with Se or ZnSe, allowing more meaningful composition studies to be performed by RBS with such samples. Channelling studies of Bi_2Se_3 and Bi_2Se_3:Fe films are also likely to shed further light on the nature of the disorder in the films and could provide further clues about the nature of the excess Se.

Acknowledgements

This work has been supported by Marie Curie Actions – Initial Training Networks (ITN) as an Integrating Activity Supporting Postgraduate Research with Internships in Industry and Training Excellence (SPRITE) under EC contract No. 317169. We are very grateful to the ALTAÏS accelerator team from Namur University in Belgium, where the IBA experiments took place, and to Emrick Briand and Sebastien Steydli of INSP for efficient technical assistance with the RBS measurements. We are also very grateful to Sarah Hidki of INSP, for the excellent XRD experiments.

References

[1] L. Fu, C.L. Kane, E.J. Mele, Topological insulators in three dimensions, Phys. Rev. Lett. 98 (2007) 1–4.
[2] M.Z. Hasan, C.L. Kane, Colloquium: topological insulators, Rev. Mod. Phys. 82 (4) (2010) 3045–3067.
[3] L.A. Wray, Device physics: topological transistor, Nat. Phys. 8 (10) (2012) 705–706.
[4] Q. Liu, C.-X. Liu, C. Xu, X.-L. Qi, S.-C. Zhang, Magnetic impurities on the surface of a topological insulator, Phys. Rev. Lett. 102 (15) (2009) 156603.
[5] J.-M. Zhang, W. Zhu, Y. Zhang, D. Xiao, Y. Yao, Tailoring magnetic doping in the topological insulator Bi_2Se_3, Phys. Rev. Lett. 109 (26) (2012) 266405.
[6] M. Eddrief, P. Atkinson, V. Etgens, B. Jusserand, Low-temperature Raman fingerprints for few-quintuple layer topological insulator Bi_2Se_3 films epitaxied on GaAs, Nanotechnology 25 (24) (2014) 245701.
[7] N.P. Barradas, C. Jeynes, Advanced physics and algorithms in the IBA DataFurnace, Nucl. Instr. Meth. Phys. Res. Sect. B 266 (8) (2008) 1875–1879.
[8] J.F. Ziegler, SRIM-2003, Nucl. Instr. Meth. Phys. Res. Sect. B 219–220 (2004) 1027–1036.
[9] W.K. Chu, Calculation of energy straggling for protons and helium ions, Phys. Rev. A 13 (6) (1976) 2057–2060.
[10] H.H. Andersen, F. Besenbacher, P. Loftager, W. Möller, Large-angle scattering of light ions in the weakly screened Rutherford region, Phys. Rev. A 21 (6) (1980) 1891–1901.
[11] S.L. Molodtsov, A.F. Gurbich, Simulation of the pulse pile-up effect on the pulse-height spectrum, Nucl. Instr. Meth. Phys. Res. Sect. B 267 (20) (2009) 3484–3487.
[12] N.P. Barradas, Double scattering in grazing angle Rutherford backscattering spectra, Nucl. Instr. Meth. Phys. Res. Sect. B 225 (3) (2004) 318–330.
[13] F. Vidal, M. Eddrief, B. Rache Salles, I. Vobornik, E. Velez-Fort, G. Panaccione, M. Marangolo, Photon energy dependence of circular dichroism in angle-resolved photoemission spectroscopy of Bi_2Se_3 Dirac states, Phys. Rev. B 88 (24) (2013) 241410.
[14] D.R. Lide, CRC Handbook of Chemistry and Physics, 84th ed., CRC Press, 2003, ISBN 9780849304842.
[15] H. Okamoto, The FeSe (Iron-Selenium) system, J. Phase Equilib. 12 (3) (1991) 383–389.

3.4 Results: Non-published

Beyond the work presented and published above, further experiments were performed, using different samples or the same ones and performing more techniques. The majority of them were done after the publication; which makes, in some cases, more detailed and accurate results.

3.4.1 Composition quantification: NDF Fitting

The RBS spectra in the different TI samples were treated afterwards with NDF DataFurnace, a fitting spectra software tool which uses the so called simulated annealing algorithm. If it is wisely implemented the results obtained can have a great accuracy in both element amount and depth profile. The PHD (dead layer, see Subsection 2.1.1), stopping power[37], straggling, screening and pile-up coefficients and corrections are the same as in the previous Section. The RBS spectra for gold capped samples are shown in Figure 48; the gold and bismuth peak (around 1700 – 1850 keV), the selenium peak (around 1550-1600 keV) and the GaAs substrate (below 1500 keV) there can be observed).

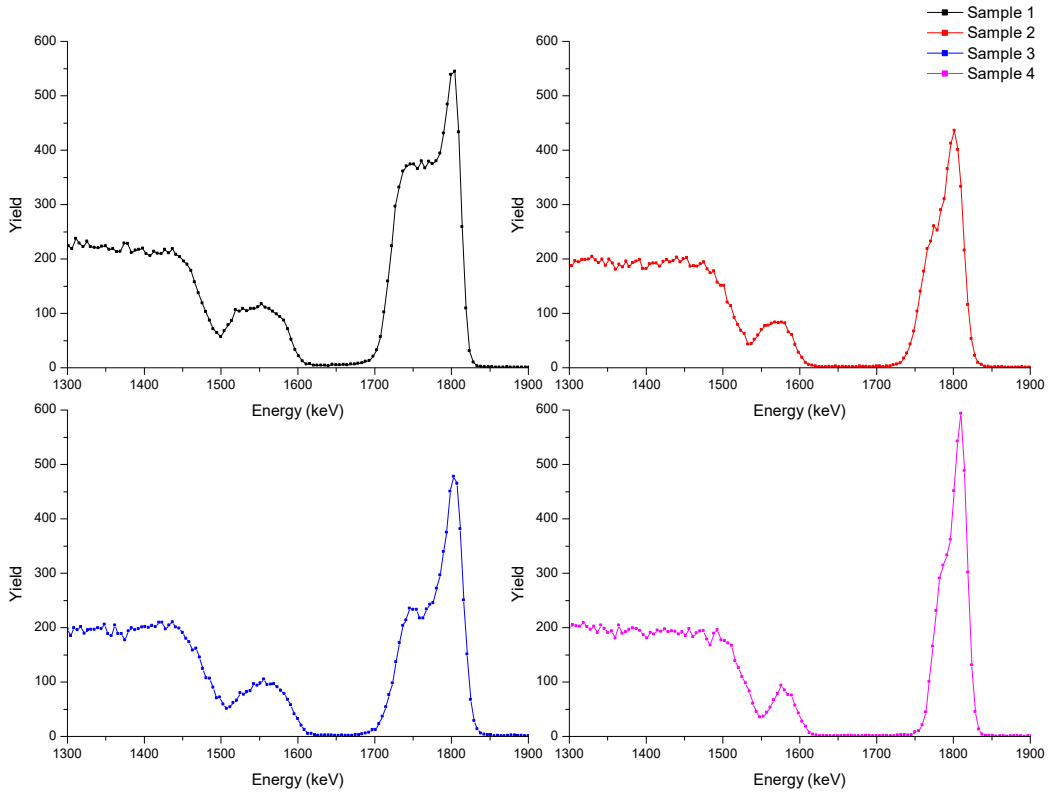

Figure 48: 2000 keV $^{4}He^{+}$ RBS spectra for TI samples with Au capping layer.

The iron signal can be identified in Sample 2 and 3 (around 1450 keV), but it is not as visible for the Sample 4 (Sample 1 has not iron at all). Therefore an extra technique with a better iron sensitivity is required in those samples to determine the Fe content; in our case PIXE was the

[37] Note that Ga stopping power has been corrected by 0.9 times the SRIM one, which results in a reduction in the total stopping power of GaAs of 5%. This is consistent with the measured stopping power reported in [109].

best solution. The characteristic PIXE X-ray peaks for the majority of the elements are overlapped or poorly separated, however the iron K X-rays are completely isolated (Figure 49). The possibility to get a self-consistent result using several RBS spectra (at different angles, for example) and the PIXE through NDF was a very seductive idea, so we moved to CNA (Sevilla, Spain) to perform the PIXE experiments since in that time our facility was not operative. NDF cannot fit the X-ray spectra, however it takes the result file from another software specifically dedicated to PIXE, which is compatible with NDF. NDF needs the elemental peak areas and their uncertainties. GUPIX [33] was the tool chosen since is can implement pile-up corrections, accurate bremsstrahlung and any other background subtraction to obtain the real peak area.

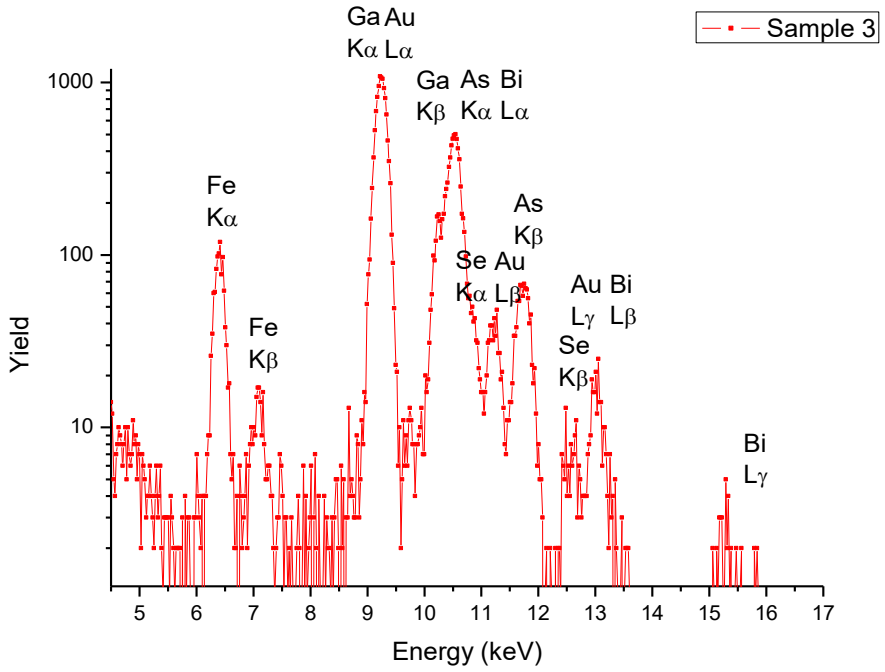

Figure 49: 2000 keV $^{4}He^{+}$ beam PIXE spectra for Sample 3.

The TI samples provided for this study have a remarkable elemental complexity, giving several overlapping elemental RBS signals from the capping layer, the TI layer, and the GaAs substrate where the iron is overlapped. Reliable analysis thus requires judicious choice of the experimental parameters and the sample type. Taking in account those requirements the optimal RBS samples are the 1 to 4, since the gold capping layer can be discriminated more easily, following by Samples 5 to 7 Se capped, where the Bi information is clean (that peak is isolated) while the Se peak is less reliable since is not possible to separate the Se in capping and in the TI. Note that Samples 1 to 8 were grown simultaneously and the capping layer was deposited afterwards (i.e. Sample 1 and 5 are equivalent in Bi and Se within the TI layer, Sample 2 and 6 are equivalent as well and so on). The remaining samples, uncapped or capped with ZnSe, are completely discarded due to the extra difficulty of the Zn signal within the substrate background and the Se for the ZnSe capped, and uncontrolled oxidation/contamination in the uncapped sample. Thus the fitting strategy had three components: the main fitting is done in Au capped samples, the Bi amount is more accurately established in Se capped samples and Fe is characterised by PIXE simultaneously done with the RBS. In some cases the Se capped results

have disagreements with the Au capped (such as greater Bi in Sample 5 than in 1, it not proving possible to get the same results in both using the same sample structure; or very low Fe amount in Sample 7, which is probably due to the $FeSe_x$ patch formation which generates some material inhomogeneity). In these cases the Au capped results are taken as the more reliable ones.

In contrast to the previous Section, the uncertainty in the atomic values has been calculated here by the Bayesian Inference uncertainty estimation included in NDF. The uncertainty (1σ) in the TI layer atomic thickness is around 0.4% (very similar to the 0.6% found in the previous Section) and 0.6-0.9 % in the Bi/Se ratio (much better than the 3% stated in the published work). The Fe uncertainty is much bigger around 3-6%, due to the complexity in that spectrum zone.

Table 3: Au capped samples elemental composition

	Layer 1	**Layer 2**	**Bi/Se**	**Fe %**
	Capping (TFU)	**TI (TFU)**		
Sample 1	39.6 ± 0.7	496.0 ± 1.8	0.596 ± 0.004	0
Sample 2	53.0 ± 0.8	304.6 ± 1.1	0.479 ± 0.010	12.96 ± 0.68
Sample 3	64.7 ± 0.8	486.0 ± 1.5	0.424 ± 0.006	15.70 ± 0.49
Sample 4	39.7 ± 0.8	223.0 ± 0.9	0.687 ± 0.009	3.20 ± 0.19

The detailed results are slightly different from the published ones, since more sampling and geometries have been fitted, and the PIXE brings new information, but the overall results and conclusions are confirmed. For Au capped samples we observe an excess in Se ($Bi/Se<0.667$) in the samples 1 to 3, in the same way as was previously reported. Sample 4 is different, it has a closer Bi/Se stoichiometric ratio, which may be an indication of better Fe dilution and the absence of excess Se incorporation. [In Subsection 3.4.3, using the SegDet, we are going to come back to try and explain this observation.]

The results for the Sample 5 to 8 follow the same general tendency. As in the reported work, there is a reduction in the Bi/Se ratio when the iron (when Fe>12%) is incorporated, supporting the idea that $FeSe_x$ is formed. Calculation of the Se/Fe ratio (x) is also attempted under the two possibilities reported in the paper, i.e. assuming an ideal Bi/Se stoichiometry or assuming that found Sample 1 (no Fe). In the publication we managed the hypothesis of the Se_{exc} found in the iron-free sample has not a real role in the TI behaviour, it would be due to the Se rich environment needed for MBE growth conditions. The evolution in the index x with the iron amount gives us another perspective, since the for a nominal perfect stoichiometry the indexation is increasing in the Samples 2 and 3, as is shown in the publication, however it changes dramatically in Sample 4, where the Se excess amount can be considered zero. The tendency using the measured stoichiometry is completely different, the index softly arises with the Fe amount.

However the overall x value is kept in the same tendency as the reported results: for the nominal stoichiometry the predominant element is Se ($x>0$) whereas using the experimental stoichiometry is Fe ($x<0$) as well as was presented in the publication. The discussion continues

in the Subsection 3.4.3 where the results using improvements in the experimental set-up may shed some light in the analysis and its interpretation.

3.4.2 Channelling

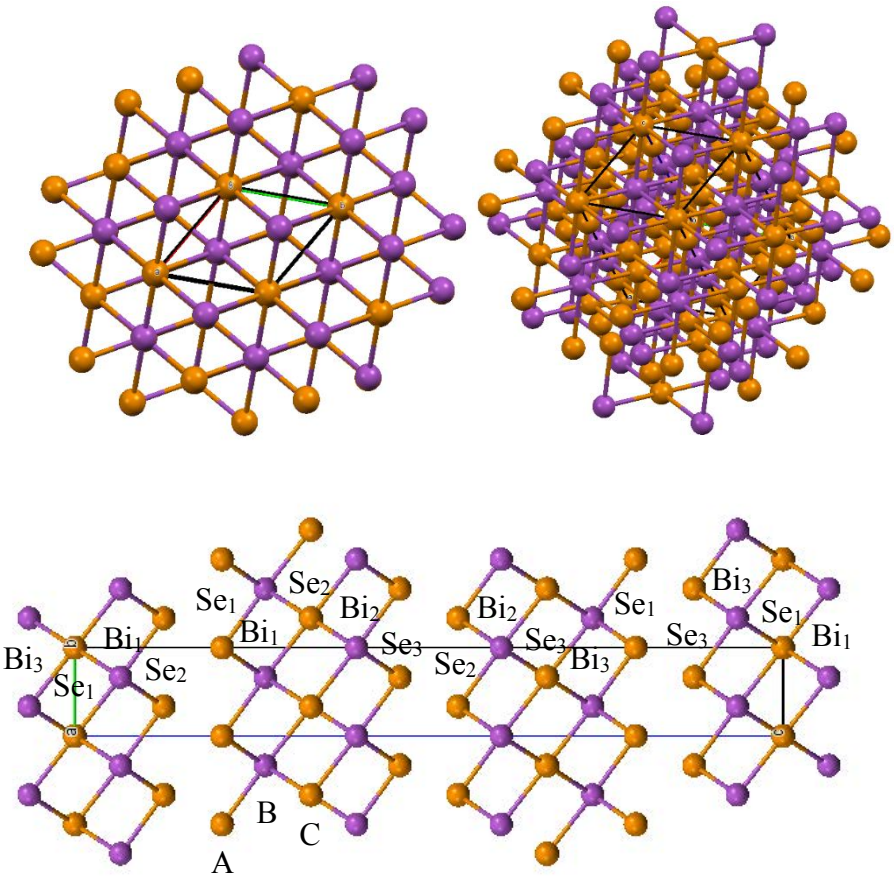

Figure 50: On the top-left, the atomic structure of Bi_2Se_3 when it is aligned in <0 0 1> with rhomboidal geometry ($a = b = 4.1$ Å). On the top-right, a pseudo-random atomic structure. On the bottom the (0 1 0) plane with the Bi_2Se_3 atomic structure, composed by three positions (A, B and C) that needs series of 3QL ($c = 28.6$ Å) for the complete description.

In the published Paper II has been shown that using an ion fluence up to the 40 nm^{-2} (5 μC in 1 mm beam diameter) the disorder generated by the beam is represented as a $\chi = 0.23$ in the case of the bismuth, which is far greater than the typical $\chi_{min} = 0.05$ that could be easily found in a silicon monocrystal using 80 nm^{-2} beam fluence. That can gives an idea of how robust are the TSS under even very high atomic disorder, since the samples were proven to be TI [76]. Moreover we demonstrated that the nuclear beam damage, indicated by the disorder evolution, can be neglected in the fluence range usually used in a standard RBS measurement. Note that the sample under study in the published channelling experiment was the so called Sample 11.

Higher disorder was also observed in the selenium peak, which we proposed to be due to the Se excess. However the capping layer presented in Sample 11 contains Se and that could modify

the Se peak behaviour (as well as Sample 9, 10 and 12). Encouraged to prove that hypothesis we performed another channelling experiment on Sample 1 and 9, which have the same TI composition (no iron, see Table 2) but different capping layers (Au and ZnSe respectively). In Figure 51 are both random and channelling spectra, where can be observed the TI layer thickness differences (Sample 9 is thinner than Sample 1) as well as the capping layers (Figure 51.a) and the comparison of random and channelling spectra (Figure 51.b and c).

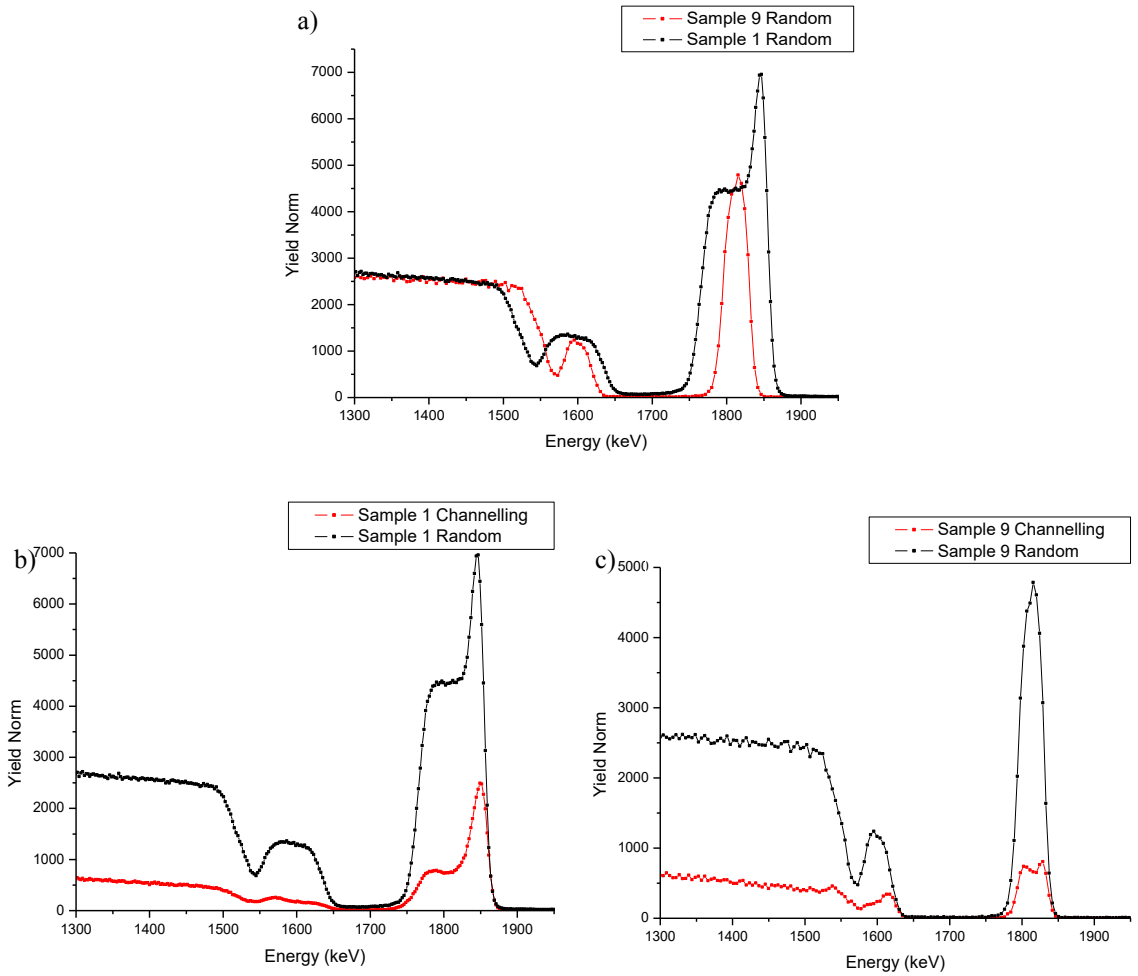

Figure 51: a) Sample 9 and 1 RBS spectra ($^4He^+$ at 2000 keV and 165° backscattering angle) in random configurations. b) and c) random and channelling spectra for Sample 1 and 8 respectively.

The χ for the complete peak area in Bi is 0.390±0.004 for Sample 1[38], while in the Sample 8 is 0.200±0.010. In other hand, the Se peak χ is 0.258±0.006 and 0.271±0.023 for Sample 1 and 8 respectively. The capping layer role in the χ calculation can have a critical impact; the χ difference for Bi is 0.19 (huge influence due to Au presence) while the differences in Se is around 0.02 (less influence due to ZnSe). Thus a more careful analysis has to be done to evaluate the real atomic disorder. In Figure 52, the different zones of the channelling spectra are shown. There it is possible to recognize where the surface capping layers are and using the fitting results

[38] Actually it is the combined Bi and Au peak.

discussed above, extract those zones from the χ area calculations and have a more realistic estimate of the atomic disorder within the samples.

Both capping layers have similar thickness; Sample 1 Au capping layer is 6.7 nm thick, which corresponds to 39.6 TFU, and Sample 9 ZnSe thickness is 5.6 nm (28.7 TFU); therefore the differences in χ have to be in the capping layer crystallisation stage.

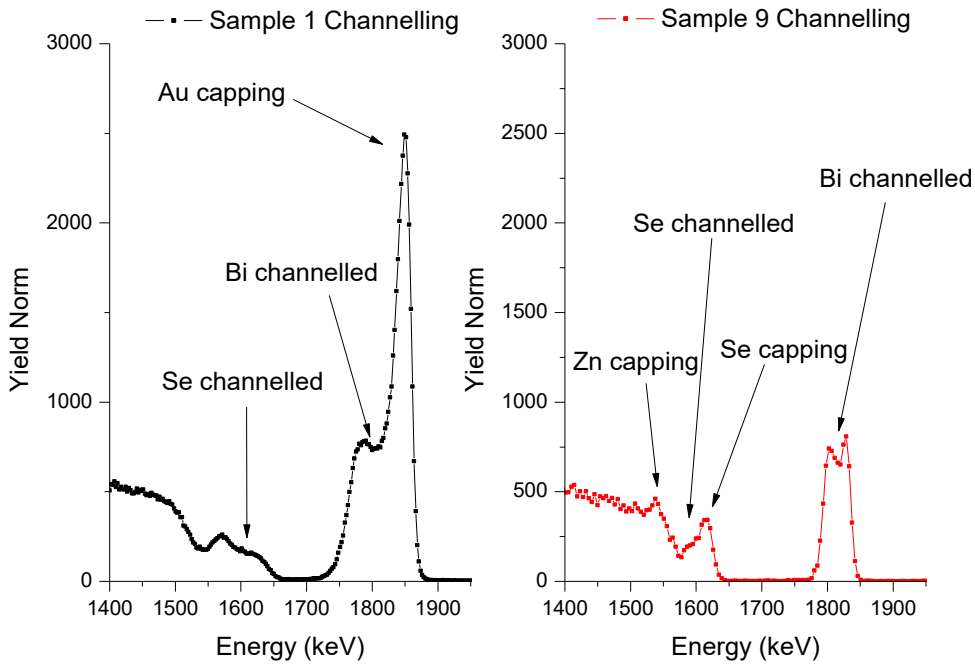

Figure 52: Sample 1 and 9 channelling spectra with different zones identified.

In Sample 1, subtracting the normalised number of counts which correspond to NDF fitted energy range Au signal (we are also subtracting some Bi counts) in the channelling and random spectra the χ is 0.282±0.005. Moreover we can subtract the Au signal by using the fitted area for Au peak and supposing that is the same in random and channelling spectra. There the χ obtained is 0.280±0.003. As both are the same we can conclude that the Au capping layer is amorphous and it has to be eliminated in the disorder characterisation, and that it can induce some disorder in the first Bi_2Se_3 layers.

In Sample 9 it is more complicated to extract the ZnSe capping layer from the spectra. Here ZnSe is probably crystallised and it could exhibit channelling. Moreover the Zn is hidden below the background – slightly mixed with the Se peak – and the capping Se is mixed with the Se from TI, consequently the best method to subtract the capping layer from the disorder calculation is taking out the areas within the Se+Zn peak in the energy range where the capping layer is not, as was done secondly on the Au signal. Once again we used the NDF fitting results to identify the Zn energy position and the capping Se proportion of the whole Se represented in spectrum peak. Defining then the 'capping layer free' energy range, we obtained χ for Se of 0.264±0.026, a similar value to the complete peak integration. Thus we can determine that ZnSe is fairly well crystallised compared with the TI since the inferred disorder is independent of whether or not the capping layer is included.

The same treatment has been applied to the remaining ZnSe capped samples (Sample 10 and 11) which also contain iron. The results are shown in Table 4, where an increment in the atomic disorder with the amount of iron can be observed. This is reasonable since as was shown above the Fe is probably present as randomly distributed and oriented $FeSe_x$ inclusions. Note that Sample 1 has smaller uncertainty, which is just due to the better statistical measurement (longer measurement and bigger solid angle).

Table 4: Disorder evaluated in the samples with different amounts of ion.

	Fe %	χ_{Bi}	χ_{Se}
Sample 1	0	0.281±0.005	0.251±0.004
Sample 9	0	0.200±0.010	0.271±0.023
Sample 10	3.3±0.3	0.265±0.011	0.323±0.021
Sample 11	16±2	0.297±0.011	0.419±0.022

Different behaviour is observed depending on the capping layer. In ZnSe capped samples the Se has bigger disorder than the Bi, while in the Au capped sample has been found the opposite. That can be a consequence of the capping layer suppression in Au and the wrong assumption of well channelled ion in the ZnSe. In the next Subsection we attempted to answer the question about Au capped sample, decreasing the uncertainly in the Au position in the RBS spectrum using the SegDet. Also the Se capped samples are evaluated.

3.4.3 Segmented Detector in TI

The interest in using the SegDet for the TI was based on the small amount of ferromagnetic doping that has to be introduced to reach the exotic states from TI by breaking the Dirac cone, and the possible fragility under ion beam irradiation due to the weak Van der Waals bonding between QL. However the lowest amount of iron that can be measured by RBS is limited to about 10% and PIXE offers a useful alternative in such cases. The samples with higher Fe concentrations (Samples 2 and 3) have been demonstrated to be non-doped, the Fe being incorporated as $FeSe_x$ patches rather than as substitutional dopants. Furthermore the material has proven to be rather robust against beam-induced structural damage. Nevertheless there remain interesting aspects than can be studied through the new acquisition system.

Ideally, in the SegDet configuration using the digital acquisition anticoincidence rejection is required in order to have a clean spectrum, removing pulses where the induced charge is shared between adjacent segments or a segment and the common guard ring. This feature is not yet completely developed and integrated in the multichannel analyser software, with the result that extra signals are given by the charges collected in the GR. The left side of the Figure 53 shows the spectrum of charge induced in the GR during collection of the spectra (those of S6 and S10 are also shown on the Figure) from the SegDet. There can be seen an extra contribution in the GaAs signal and the Se; the contribution for each segment (supposing that the GR signal is equally generated by all of the segments and dividing the GR spectrum by 15) is about 1% extra signal for GaAs and even smaller in the Se, which is in good agreement with the values measured by IBIC in Subsection 2.1.2.1. However on the right side of the Figure 53 is compared

at the equivalent angles. There the differences in the GaAs and Se can be up to 30%. The source of this signal increment is still under study and outside of this thesis scope.

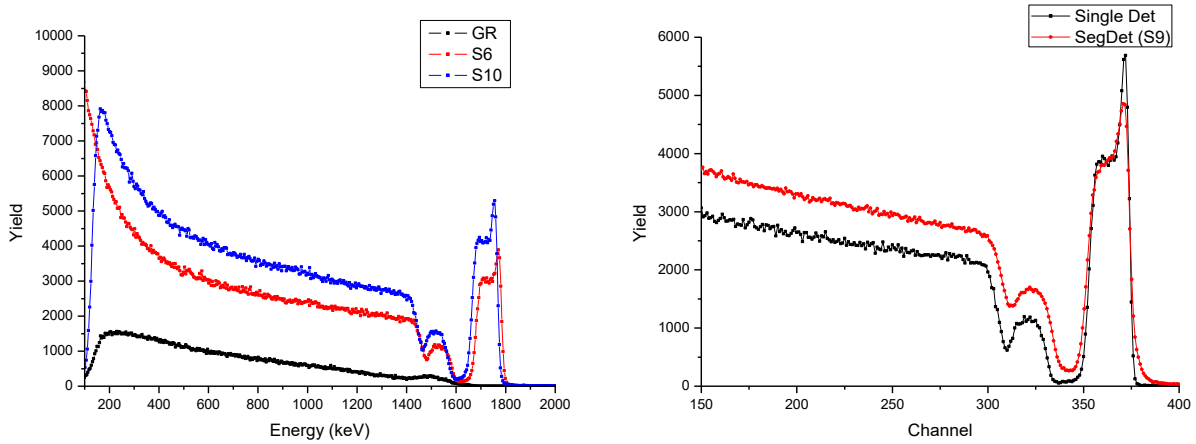

Figure 53: On the left the spectra for two consecutive segments (S6 and S10) and the signal taken by in the GR. On the right the Sample 1 spectra comparison between a single detector and the Segment 9 from the SegDet both at 146°.

We can attempt to analyse such spectra by using an ad hoc yield correction on the Se and GaAs signals, taking the Bi-Au peak as a reference and correcting the SegDet spectra according to the well-known PIPS single detector spectra. It possible to extend the correction for one segment to the remaining segments since as is shown in Figure 54 the variations in the yield are very similar for the two single detector spectra at the appropriate angles and the spectra from segments at equivalent angles in the SegDet. In this case the correction for the GaAs is 20%, the Se low energy zone 30% and high energy 40%.

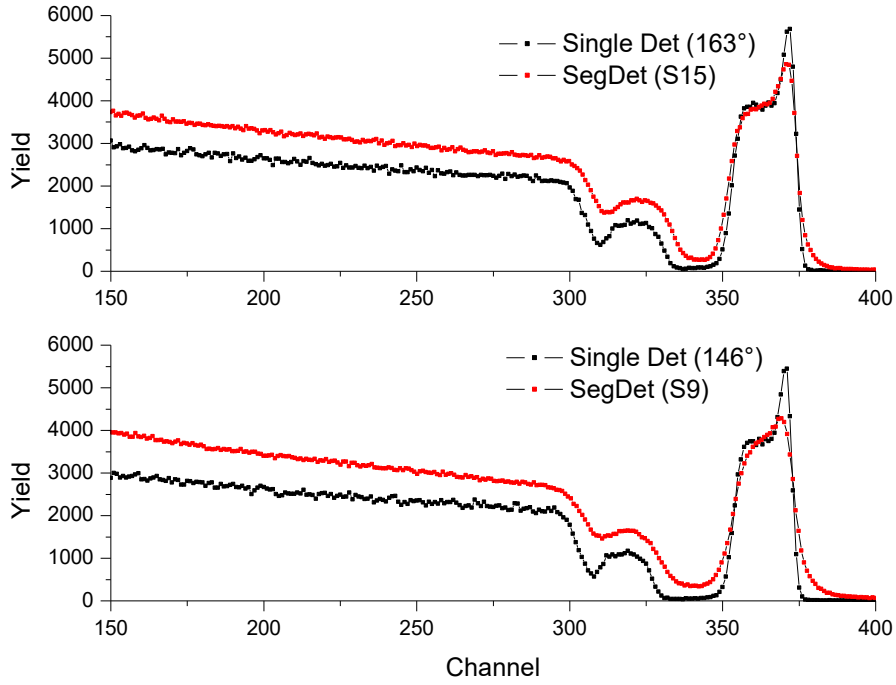

Figure 54: Comparison between the single detector at wo different angles with their equivalent segment angle in the SegDet (S15 and S9)

The quantitative analysis using NDF in these conditions is too complicated and the corrections taking place can substantially degrade the reliability of the results. We therefore focus on the analysis in the RBS-channelling configuration since it is less sensitive to mathematical corrections.

3.4.3.1 Channelling with SegDet

Previously we have shown RBS-channelling results for the Au and ZnSe capped samples. In both cases the capping layer is perturbing the χ values; in the Au capped due to angular scattering occurring in the amorphous Au surface layer, and in the ZnSe due to the Zn signal (between the GaAs and the Se) and the ambiguity in the Se part of the capping. Using the SegDet and the Se capped sample those issues are solved. Figure 55 shows the channelling and the random spectra for the Segment 7. There the Se capping layer surface can be easily seen and then subtracted to calculate the χ for Se. Since we have the spectra from 8 segments in this case, we can do the average to have a better measurement of the disorder present in the sample.

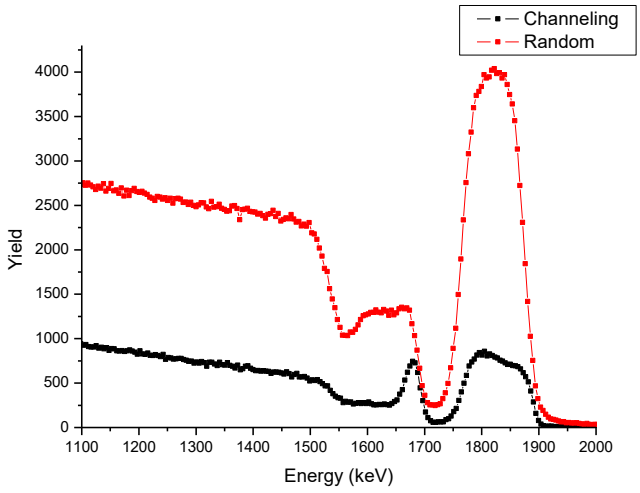

Figure 55: 2 MeV 4He+ spectra in channelling and (pseudo)random configuration from Segment 7 of SegDet in Sample 5.

Applying the corrections mentioned above only in the GaAs substrate and the Se signal for the random spectrum, since the background much reduced in the channelled spectrum, we found that the average value for χ_{Bi} is 0.253±0.002 and for χ_{se} is 0.332±0.007 after the surface peak subtraction, with a remarkable improvement in the uncertainty[39]. These values are around 0.05 higher than the values found previously in the ZnSe capped samples. In both cases the capping layer could well be hexagonally crystallised, the lattice parameter (4.3 nm for Se [77] and 4.1 nm for ZnSe [78]) matches quite well that of the TI (4.1 nm [79]) and their thicknesses are smaller than 10 nm; hence the observed difference in χ is not coming from there. On the other hand, the thickness of the ZnSe capped TI is 193 TFU whereas that of the Se capped is 489 TFU, 2.5 times bigger, therefore the presence of disorder increases with the layer thickness.

[39] The uncertainty has been calculated through standard deviation of the 8 segments.

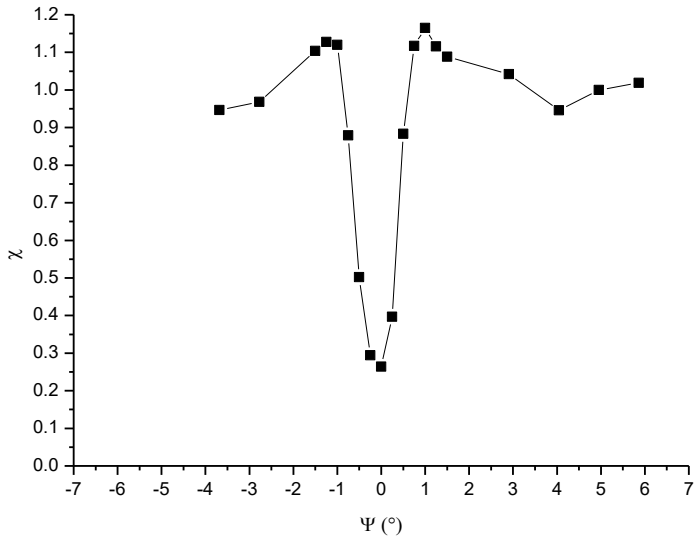

Figure 56: χ in function of the incident angle for the Bi signal.

An angular scan of the Bi signal about the <0 0 1> axis for the Bi contribution is shown in Figure 56. Here we can see the angular width at the half minimum, $2 \cdot \Psi_{1/2}$, where the $\chi = 1/2$, is 0.77° (0.48° on the left and 0.29° on the right) and the critical angle, Ψ_C, is slightly smaller than 1° (0.97° on the left side and 0.79° on the right side), which both are in agreement with the single crystal behaviour.

We can compare these observations with the previsions of the continuous model explained in Subsection 1.1.2.2. Using Equation 1.31 is possible calculate the critical angle assuming the atomic row has a $Z_2 = 0.6 \cdot Z_{Se} + 0.4 \cdot Z_{Bi}$, the interatomic distances given by [79] and the estimation of $r_{min} = 0.4$ Å. The value obtained is 1.14°. Taking out the 20% overestimation of the continuous model, the value is 0.91°, which is in pretty good agreement.

Moreover the continuous model allows us to calculate the theoretical χ_{min} as well. Through the Equation 1.33 and using the same parameters as above is obtained 0.03, adding the factor 3 correction for the underestimation of the model the final result is $\chi_{min} = 0.08$; which is much lower than the experimental results.

3.5 Conclusions and perspectives concerning TI

We summarize here the main conclusions that can be reached from the TI study. Firstly, the channelling measurements of the lattice disorder as a function of ion fluence showed that the Bi_2Se_3 is very resistant to the $^4He^+$ ion beam. The Van der Waals forces between the QL are able to keep the layers bonded and the beam is not generating significant nuclear damage. Despite the presence of substantial disorder in the TI atomic lattice the TSS are present, demonstrating the high robustness of those states.

The measured Bi/Se ratio is systematically smaller than the stoichiometry expected value of 0.667. Using the classical RBS and PIXE data acquisition configuration, the Se excess is considered to be a result of the growth process, since a Se rich environment is needed to overtake the characteristic problems that the Se atoms have to be incorporated into the lattice.

In the Fe-containing samples the Se interacts with the Fe forming the $FeSe_x$ compound and dramatically decreasing the Bi/Se ratio. This is especially the case for the high Fe concentrations (Fe>12%). The samples containing the smallest concentrations of Fe have a completely different behaviour. The RBS analysis shows that the Bi/Se ratio is close to the stoichiometric one, which suggests a change in the TI atomic growth mechanisms and establishes a limit to the formation of $FeSe_x$ and suggests the possibility to really introduce ferromagnetic doping. However since the Dirac cone was not opened, the doping may only be of the bulk, and not the first few QL's. The depth resolution of RBS is insufficient to see such an effect.

In a later publication of our collaborators in this work, the $FeSe_x$ stoichiometry could be measured by X-ray absorption fine structure (EXAFS) [80]. There the Fe-Se alloy found was Fe_3Se_4, in the nomenclature used here $FeSe_{1.33}$. It is in very good agreement with the calculated results given in the Table 2 of the Publication II (Section 3.3) for the theoretical stoichiometry in the Bi_2Se_3. Therefore in the Fe-Se-Bi interaction during the MBE process the excess in Se presented in the free-iron samples is forming $FeSe_{1.33}$ in the vast majority.

The RBS-channelling results for the iron-free samples (Samples 1, 5 and 9) from both single PIPS detectors and the SegDet present a χ bigger than could be expected for a Bi_2Se_3 single crystal – calculated by the corrected continuous model – which indicates substantial structural disorder within the sample. The Se and ZnSe capped samples present higher χ in the Se signal than the Bi one, and that may be a sign of the Se excess found in the RBS measurements. The Au capped signal has a different behaviour and it is the χ_{Bi} which is bigger. That can be explained by an overestimation of the Bi signal, which overlapped with the Au capping, furthermore the Au is in amorphous phase which will induce angular spread before the beam enters the TI, while the Se and ZnSe are crystallised. In the iron containing samples χ increases with the Fe concentration, consistent with the XRF measurements which show deterioration of the crystal structure due to the $FeSe_x$ clusters.

The Se capped iron-free samples were measured with the segmented detector, therefore the results are statistically better and the uncertainty lower than the measurements done with a single detector. Focusing on this sample, the critical angle measured is in good agreement with that calculated by the corrected continuous model, meaning that the crystal structure is well defined, which was also confirmed by the XRF experiments, but at the same time the high χ reveals a great number of the atomic defects in the sample, such as interstitials or the already reported twins [81], that increases with the sample thickness.

The TI's are at a very early stage of development, so this research remains open providing motivation to improve our system to go beyond the classical IBA limitations. The time and the sample accessibility have been completely determinate to the possibility to get a much deeper understanding on the material. Some of the future possibilities to continue the study with such as IBA system are proposed in the following lines.

There are others ferromagnetic transition metals doping that may be easier to dilute within the Bi_2Se_3 lattice; there are some works in which chromium [82], manganese [83] or cobalt [84]

doping have been already attempted, but with some limitations (for example some of them are just proven to be a TI in the low temperature regime). The characterisation of the atomic doping in those cases remains far from clear and accurate hence the IBA techniques – with our enhanced acquisition system – may be one of the keys in this topic.

Electronic measurements are complicated in the TI's since the bulk is not a trivial insulator, rather it is a narrow (0.35 eV) band gap n-type semiconductor. Therefore introducing non-ferromagnetic acceptor doping in the bulk can suppress the n-type behaviour and facilitate the electronic characterisation, as well providing more control of the material response for future developed tuning systems. Once again IBA can determine better than any other technique the needed amount to have an electronically neutral TI bulk.

There are other TI materials such as Bi_2Te_3, Sb_2Te_3 or ternary Bi:Te:Se compounds, citing just some possibilities that have been theoretically and/or experimentally reported, which could easily be studied by our system. The GaAs substrate does not lead to the most atomically ordered TI lattice and other substrates may have better performance here. Using a lighter elemental or compound substrate for the RBS measurements of the doping elements would be even more accurate, since the signal of interest would not be overlapping the substrate signal.

The measurements by RBS-channelling can contribute to localize point defects in the ferromagnetically free (non-doped) TI's. It can be an interesting point to study the interstitial defects which some theoretical works claim to have a crucial role in the n-type semiconductor behaviour of the Bi_2Se_3 [85]. For the doped TI's – ferromagnetic for surface state tuning or non-magnetic to avoid bulk carriers – the channelling can give information about where the doping is taking place. However the growth system has to be enhanced in order to improve the crystallographic order of the epitaxial films, the ideal being to use TI bulk monocrystals[40].

[40] There are some reports of the growth of such crystals, although their crystalline quality has not been clearly demonstrated.

4. MoO_x and Organic Semiconductors Devices

Characterisation of organic semiconductor devices is an interesting application to take advantage of the benefits in the SegDet capabilities. The low energy consumption, potential low manufacturing price and environmental impact are the strongest reason to study the electronic behaviour in these materials. As Section 1.3 previously shows, the OPV is a promising organic semiconductor application, however there are some difficulties (environmental degradation, charged carriers mobility, etc.) in both the organic donor compounds and the hole extractors that have to be overcome. Furthermore, new TMO growth techniques are under study in order to achieve optimal manufacturing strategies to improve stoichiometric stability and reduce price. In this direction, IBA techniques can strongly contribute through the elemental characterisation – and the lateral distribution – that can be related to the electrical behaviour.

In collaboration with NanoSYD, University of Southern Denmark (Sønderborg, Denmark) we undertook IBA characterisation of externally oxidised MoO_x sputtered thin films in order to shed some light on that process; measuring the stoichiometry for different x values, and oxygen uptake and diffusion under oxidising conditions[41].

This chapter is structured in a similar way to the previous one: Section 4.1 presents the motivations and advantages of using the SegDet and DDA system; Section 4.2 shows the samples involved in the study; Section 4.3 shows and discusses the results found through NDF; and Section 4.4 summarises the results and gives some conclusions.

4.1 Motivation

The SegDet with DDA is the most convenient system to analyse ionisation sensitive materials through IBA techniques, such as the organic semiconductors, and the tiny amounts of matter on the classical substrate background, as it was shown in Section 2.1.2; both circumstances are combined in the OPV technology. The organic compounds have been excluded from IBA characterisation due to their weak molecular bonding and light element composition (basically hydrogen, carbon and oxygen), however the new SegDet system can overcome those limitations. We have demonstrated that using this kind of system, oxygen and carbon characterisation is possible without major losses in the studied sample.

Moreover we attempted to characterise the oxidation process in the MoO_x charge injector/extractor material – a hole extractor in this case, for the OPV functionality. The measurement is extremely difficult to perform without a large solid angle detector, since the oxygen is on the substrate background (silicon in this case) and amount is very small, from 40 to 100 TFU. IBA, RBS in this case, is very useful due to the possibility of depth profiling, hence

[41] The measurements were included in a talk given by André L. Fernandez-Cauduro in the international workshop International Summit on Hybrid and Organic PV Stability (ISOS-9).

the oxidation can be studied as a function of depth, knowing if it is placed on the surface or deeper in the sample.

These reasons demonstrate the usefulness of our system, being the very first results of a SegDet with full DDA experimental setup and a publication is in preparation for submission after the end of the thesis.

4.2 Samples and Experimental Setup

Two materials were analysed separately here: the organic compound tetraphenyldibenzoperiflanthene (DBP) and the MoO_x TMO with three as-grown stoichiometric compositions (x=2.57, 3.00 and 3.16) and two deposition techniques (sputtering and thermal deposition). The sample preparation has been undertaken by our collaborators at NanoSYD and it is detailed elsewhere [86]. The nominal compositions of the samples analysed here are based on RBS measurements of thicker samples grown under the same deposition conditions, as detailed in [86]. Table 5 below shows the sample nomenclature used in this chapter.

Table 5: TMO samples deposited by sputtering and thermally with different stoichiometry and organic DBP sample. Note that thermal deposited sample (Sample 3) has unknown stoichiometry that will be solved in the analysis.

Name/kind	Deposition process	Stoichiometry
Sample 1 - MoO_x	Sputtering Ar=20:O_2=10	x=2.57
Sample 2 - MoO_x	Sputtering Ar=20:O_2=12	x=3.00
Sample 3 - MoO_x	Thermal deposition	x<3
Sample 4 - MoO_x	Sputtering Ar=20:O_2=20	3.16
Sample 5 - DBP $C_{64}H_{36}$/Si	Organic Molecular Beam Deposition (OMBD)	
Sample 6 - DBP $C_{64}H_{36}$/ITO/SiO_2	Organic Molecular Beam Deposition (OMBD)	

Since our interest in the TMO samples is the external oxidation process, it was necessary to discriminate the oxygen already within the as-grown sample from oxygen originating from the environment. Due to the isotopic sensitivity of RBS, we decided to incorporate ^{18}O through the pressure controlled furnace available at INSP. The *as deposited* samples, were packed under vacuum conditions and they were not opened until the pre analysis treatment took place, minimising uncontrolled environmental oxidation.

For each sample, in addition to keeping aside one 'as deposited' sample, three different treatments were made: just surface cleaning pre-treatment, ^{18}O exposure with cleaning pre-treatment and ^{18}O exposure after pre-cleaning and MoO_x crystallisation. The pre-treatment consists of a two-step surface cleaning process: 1) 30 mins at 150°C and 2) 30 mins at 200°C under vacuum conditions. The isotopic oxidation was made in pure $^{18}O_2$ at 300°C under 200 mbar pressure and crystallisation was induced by treatment at 500°C for 5 minutes with 2

minutes ramp-up temperature[42]. Table 6 summarises the samples analysed with the treatment used in each.

Table 6: Sampling nomenclature with the treatment procedure used.

Sample Name	Description	Procedure
Sample 1.1	Sputtered MoO_x; x=2.57	Direct measurement, no treatment.
Sample 1.2		Cleaning
Sample 1.3		Cleaning. ^{18}O exposure.
Sample 1.4		Cleaning. Crystallisation. ^{18}O exposure.
Sample 2.1	Sputtered MoO_x; x=3	Direct measurement, no treatment.
Sample 2.2		Cleaning
Sample 2.3		Cleaning. ^{18}O incorporation.
Sample 2.4		Cleaning. Crystallisation. ^{18}O exposure.
Sample 3.1	Thermal deposited MoO_x; x<3	Direct measurement, no treatment.
Sample 3.2		Cleaning
Sample 3.3		Cleaning. ^{18}O incorporation.
Sample 3.4		Cleaning. Crystallisation. ^{18}O exposure.
Sample 4.1	Sputtered MoO_x; x=3.16	Direct measurement, no treatment.
Sample 4.2		Cleaning
Sample 4.3		Cleaning. ^{18}O incorporation.
Sample 4.4		Cleaning. Crystallisation. ^{18}O exposure.

The IBA techniques applied in MoO_x were RBS; using $^4He^+$ ion at 2060 keV with the SegDet centre (between segments 4 and 12, S4 and S12) placed at 156° from the incident beam and around 75 mm from the sample holder, therefore the backscattering angle range was from 165° to 146°; and NRA through the reaction $^{18}O(H^+,{}^4He^+)^{15}N$ (Q=3980 keV), with H^+ incident beam at 750 keV, where the $^4He^+$ produced was detected by the SegDet centre placed at 156° with a 12 μm mylar foil in front of it[43]. Two DT5725 (8 input channels) digitisers, optically daisy chained and connected to the acquisition PC, acquired the data by DPP-PHA. In all cases the detector bias voltage was between -30 V and -40 V and the beam spot diameter 1 mm. The detector energy resolution (20-50 keV) was limited here due to noise generated in the power supply for the DT's provided by CAEN, and could be improved with better power supplies.

In the organic compound DBP (Samples 5 and 6), the basic idea in the experiment is to demonstrate the SegDet capabilities for fragile materials under energetic ion beam conditions. We attempt to determine the nuclear damage that can be characterised by the IBA (see Annex II: Ion Damage) by measuring the evolution of the RBS carbon signal with beam fluence. If there is type I damage (carbon loss), the C signal will decrease when the ion fluence increases.

[42] This is a result from our collaborators which is not published yet.

[43] Those backscattering angles and incident ion energy values are estimates, since the SegDet is mobile and these can vary by up to about 1 degree or 2 keV for experiments performed on different days.

The procedure was to use the channelling configuration in the substrate, reducing then the Si signal in order to have a clean C signal from the DBP. Thus we could perform RBS in the DDA in list mode which gives a time stamp for each arriving particle. From the list mode file, we can extract spectra for given time window and thus examine the time evolution of desired spectrum features – such as C peak integral area. The time-ion fluence relationship has been measured through the current integrator connected to the vacuum chamber which generates the trigger for a pulse generator which is connected to a digitiser channel that can store them with their time stamp, giving the time-fluence relationship.

The experiments were performed with a $^{4}He^{+}$ ion beam at 2010 keV with the same data acquisition devices used in the MoO_x measurements. The beam spot used here was 0.5x2 mm².

4.3 Results and Discussion

This section divides our work in two parts. Firstly (Subsection 4.3.1) is the RBS and NRA analysis of the TMO MoO_x to confirm the nominal stoichiometry (or measure it in the case of Sample 3) and external ^{18}O oxidation measurements. These results will be presented in an article mentioned above. Subsection 4.3.2 shows the comparison between the RBS analysis using a classical single detector and the SegDet in the organic compound DBP.

4.3.1 MoO_x oxidation: stoichiometry and external oxygen characterisation

Figure 57 shows the appearance of typical spectra from 3 segments – one at the centre and one each from the outermost available segments (S4, S8 and S14, see Figure 28) with normalised yield and energy calibrated. At the top is Sample 2.1 and at the bottom Sample 2.4. These are our first results using the SegDet and acquiring data in 13 segments simultaneously[44]. The higher energy peak corresponds to the Mo (1600-1800 keV), while the O signal is on the Si substrate (600-800 keV). In the bottom graph the ^{18}O peak is discernible, around 800 keV, the peak area for a single segment is very small (around 200 normalised counts subtracting the Si substrate background) so the solid angle enlargement is needed to be able to characterise properly the oxygen content.

In this case the extra signal for the SegDet observed in the TI experiments is not a problem, since the elements involved here have smaller atomic mass and are present in thinner layers. It is possible to recognise the slightly higher background between the Si and Mo signal, however the spectra may be quantitatively analysed through NDF.

Note that energy resolution is not homogeneous in all the segments and it can vary slightly from one segment to another. This is the case of S4 and S14 in Sample 2.1, where Mo peaks are higher and narrower than in S8, the resolution in those are twice better. The bias voltage used there is -30 V, which does not improve the resolution as well as -40 V used in the bottom graph and in the vast majority of the taken spectra.

[44] Actually 14 segments are available, however the S16 is partially hidden for the mask edge and has not been into account for the NDF analysis.

We observed slight variations in the solid angle/beam fluence product between measurements. This may be due to small imperfections in the beam current integration process, since the detector mounting required exposure of some earthed components in the interior of the chamber which could provide slightly compromise its function as an ideal Faraday cup.

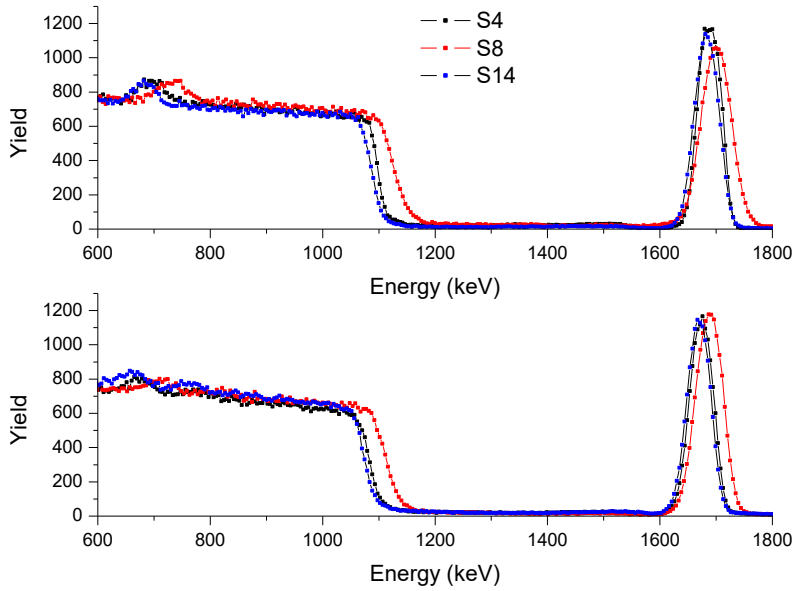

Figure 57: Sample 2.1 (top) and 2.4 (bottom) – just clean and ^{18}O treated – normalised spectra for segments S4, S8 and S14 (middle and outer availed detector segments)

Figure 58 shows 14 spectra for Sample 4.1 corresponding to the available segments. Technical problems related to the signal collection (broken gold wires) made the Segment 1 and 15 unavailable. Nevertheless using 14 segments per measurement is already a great improvement in the data collection and the solid angle has been increased by a factor of about 100 in comparison with the typical RBS setup installed in SAFIR (and other IBA systems).

NDF DataFurnace was the fitting tool used in the sample analysis; as we have shown previously, its use is more than justified when the SegDet data has to be treated. We used SRIM-2003 stopping power [8], Chu straggling model [87], Andersen screening [6] and Molodstov and Gurbich pile-up correction [70]. Furthermore some spectra present channelling effects in the Si substrate. To improve the fit we used the ad-hoc channelling corrections available in NDF. The PHD is assumed to be due to a 180 nm silicon dead layer. NDF fitting treatment finds the best self-consistent result through simulated annealing and local research; the criteria used to select the good fitted result was $\chi^2 < 50$ for the averaged fitted spectra (see Annex I: NDF DataFurnace and Total IBA). For the ^{18}O peaks the Simulated Annealing is not sufficient to provide a realistic fit, even using the NRA spectra (i.e. simultaneously fitting 14 RBS spectra and 14 NRA spectra). Therefore the fitting process was more complicated in those samples; SA was used to find the MoO_x profile and a good approximation for the fitting parameters (energy gain, charge, solid angle, backscattering angle…), then the ^{18}O profile was adjusted manually and iterated as many times as necessary to have a good fit verifiable by graphical observation in the spectra (paying special attention to the peaks areas) and the χ^2 given by NDF.

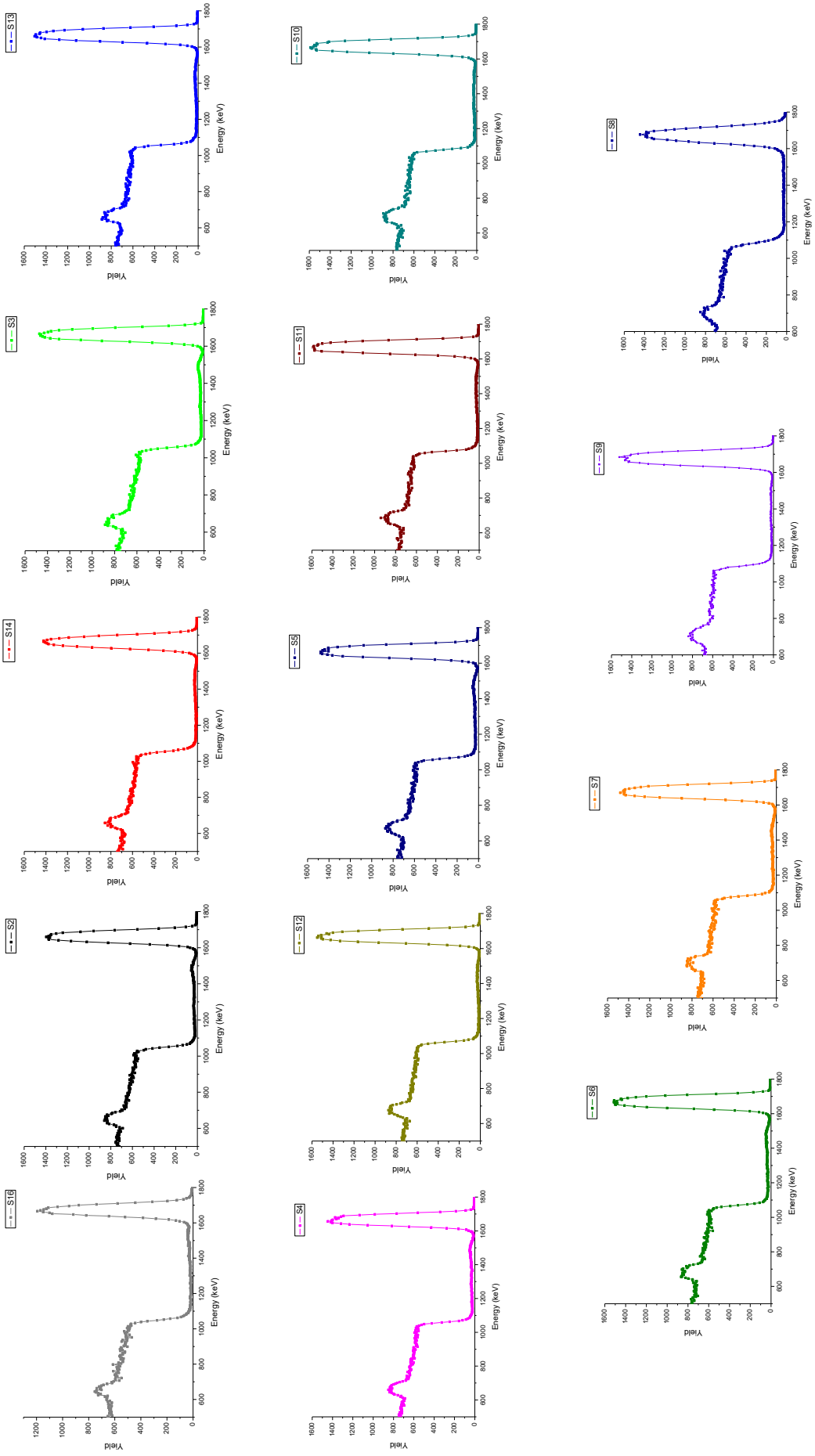

Figure 58: Sample 4.1 spectra for all the available segments. They are organised from the bigger backscattering angle (S16 at 164.8°) to the smallest (S8 at 146.7°)

Figure 59 shows an example of the data/fit appearance. Note that not all the spectra are fitted as perfectly as those shown here. The statistical NDF treatment gives the best result taking into account the overall input data, however the peak areas are in all cases equivalent[45]. Fitting of the $^{18}O_2$ treated samples (Samples X.3 and X.4) takes in account the NRA spectra as well (not shown here). Actually NRA fixes the ^{18}O amount within the sample (which must be compatible with the RBS spectra) whereas RBS indicates in addition the depth profile.

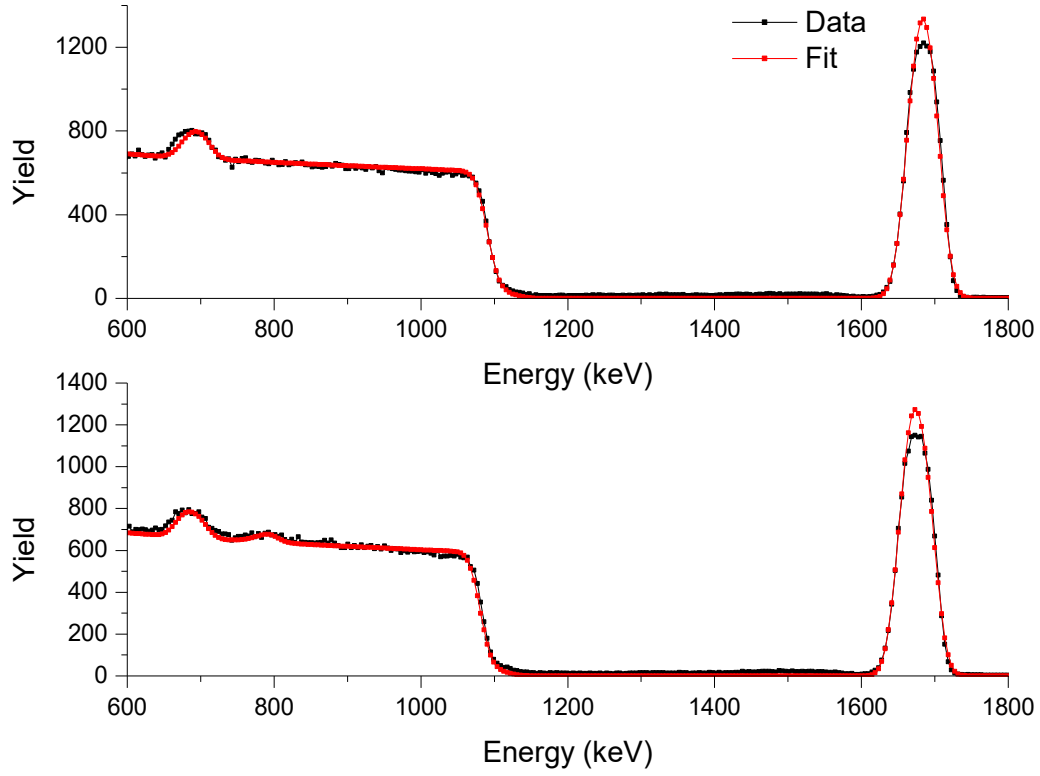

Figure 59: Sample 1.2 (top) and 1.3 (bottom) spectra corresponding to S4 (black dots-lines) and the fitting results given by NDF (red dots-lines).

Table 7 summarises the results obtained maintaining the nomenclature used in Table 6. The first question we had to answer was whether the nominal stoichiometry was the actual one. Leaving the oxygen amount as a free parameter the fitted results are quite close to the nominal ones, so we decided to use the given stoichiometry as a fixed parameter for the untreated sample, in order to reduce one degree of freedom and obtain more reliable fitting. The results reported here have been fitted in this way with the exception of the Sample 3, in which the stoichiometry was unknown, so NDF fitted its value, getting x=2.9 as the optimal result.

The differences in the Data/Fit ratio in the peak areas is on average smaller than 3%. The statistical uncertainty, calculated through BI, is 1%; although this value can underestimate the uncertainty contribution for the detector resolution, the beam current integration and

[45] The deviations from the experimental data are in terms of energy calibration, offset and backscattering angle. The main problem here lies in the inability of NDF to limit or correlate degrees of freedom for the individual segments, as is commented in Chapter 5.

channelling corrections; the most reliable uncertainty estimation for the values is estimated from the Data/Fit difference. Then the global uncertainty is estimated to be 3%.

The best fits are found for an abrupt sample/substrate interface, with no extension beyond the depth resolution of the measurements (80 nm for Mo).

Table 7: NDF results summary. The element amounts are given in TFU, Thin Film Unit, where 1 TFU = 10^{15} atoms/cm².

Sample Name	Mo (TFU)	O (TFU)	Mo+O (TFU)	^{18}O (TFU)	Total (TFU)	^{18}O (%)	O/Mo	^{18}O+O/Mo
Sample 1.1	117.10	300.90	418.00	0.00	418.00	0.00	2.57	2.57
Sample 1.2	119.20	306.40	425.60	0.00	425.60	0.00	2.57	2.57
Sample 1.3	118.90	305.70	424.60	79.64	504.24	0.16	2.57	3.24
Sample 1.4	119.10	306.00	425.10	99.25	524.35	0.19	2.57	3.40
Sample 2.1	110.00	329.90	439.90	0.00	439.90	0.00	3.00	3.00
Sample 2.2	122.20	366.70	488.90	0.00	488.90	0.00	3.00	3.00
Sample 2.3	109.60	328.80	438.40	40.74	479.14	0.09	3.00	3.37
Sample 2.4	108.80	326.40	435.20	110.20	545.40	0.20	3.00	4.01
Sample 3.1	137.60	399.00	536.60	0.00	536.60	0.00	2.90	2.90
Sample 3.2	134.40	390.10	524.50	0.00	524.50	0.00	2.90	2.90
Sample 3.3	129.40	375.20	504.60	57.15	561.75	0.10	2.90	3.34
Sample 3.4	140.20	406.70	546.90	74.76	621.66	0.12	2.90	3.43
Sample 4.1	191.60	605.40	797.00	0.00	797.00	0.00	3.16	3.16
Sample 4.2	182.50	576.80	759.30	0.00	759.30	0.00	3.16	3.16
Sample 4.3	189.50	598.70	788.20	53.98	842.18	0.06	3.16	3.44
Sample 4.4	181.60	573.80	755.40	96.84	852.24	0.11	3.16	3.69

We first observe that there is no systematic variation (loss …) of Mo or ^{16}O amounts as a result of the $^{18}O_2$ anneals, and the O/Mo ratio remains constant. This indicates that there is no exchange between the O in the MoO_x and the oxygen from the gas. There are small variations in the total amounts of Mo and ^{16}O, however we ascribe this to small thickness differences amongst the samples cut from different parts of the as-received MoO_x/Si films, which may be judged from the third column (Mo+O). For the Samples 1 and 4 this is almost negligible (maximum differences are 2% and 5% respectively) whereas in Samples 2 and 3 slightly higher (11% and 8% respectively) lateral thickness inhomogeneity is observed.

Comparing the Samples X.1 and X.2, i.e. as deposited and cleaned samples, no significant environmental oxidation is found, the stoichiometry is maintained in both cases and the fitting results are largely satisfying. This indicates that environmental oxidation is negligible during the few minutes of exposure between breaking the vacuum packaging from NanoSYD and introducing the sample into the furnace, and/or between removing the sample from the furnace and placing it under vacuum of the analysis chamber.

Samples X.3 and X.4 have the first indication of external oxidation, where we can see the relationship between the stoichiometry and the incorporated ^{18}O. In all cases the final stoichiometry is greater than the as-received. The charge mobility in the MoO_x is due to O vacancies [88], and since the as-received films are conducting and therefore have significant oxygen vacancy concentrations, it is not surprising that further oxygen can be incorporated. However the ^{18}O incorporation was in all cases greater in the crystallised samples than that observed in the amorphous samples, as can be seen in the ^{18}O percentage column. The crystalline films do not show evidence of ion channelling and so are polycrystalline. They thus have a large number of grain boundaries which could be preferential diffusion paths for oxygen. Oxidation kinetics studies (beyond the scope of this thesis) would provide a test of this hypothesis. A further test would be to undertake charged carrier mobility measurements and to link conduction behaviour with the oxidation (reduction of oxygen vacancy concentration).

The capacity to include extra oxygen can be observed in last column, where the total oxygen stoichiometry is given. In the Samples X.3, the values seem to increase with x, however taking account the uncertainty in the Mo, O and ^{18}O amount and using the error propagation, we obtain around $\pm$ 0.20 in those values, therefore for these results the total oxygen ($O+^{18}O$) stoichiometry is equivalent for all of them and the average value is 3.35 ± 0.20. This results may be interpreted as a limit to the oxidation of the amorphous MoO_x. Sample X.4 show two kinds of behaviour. When $x < 3$, the extra oxygen capacity is perhaps slightly higher than that of the amorphous samples (around 3.40 ± 0.20) but could even be considered as equivalent[46]; however this capacity tends to increase in the $x \geq 3$ between 9% to 18%, giving an oxidation stoichiometry up to 4.00 ± 0.20. This may indicate a preferential ability of the grain boundaries to not only provide enhanced diffusion pathways, but also to incorporate further oxygen in the grain

[46] This equivalence is taking the overall samples where $x < 3$ through ^{18}O+O/Mo column. Do not mix with the previous observation of higher oxidation capacity in crystal phase, which is done by comparison in the same sample in the ^{18}O percentage.

boundaries themselves, or of a different crystalline structure (grain size, phase, orientation) depending on the initial oxygen content.

For ^{18}O containing samples, Samples X.3 and X.4, the ^{18}O depth profile was also a critical physical quantity that has to be carefully taken into account. If we suppose that all of the ^{18}O is uniformly distributed throughout the film, the fit to the RBS spectra was not satisfactory. The best solution was found by assuming an ^{18}O depth profile, with the concentration decreasing from a maximum at the surface. Due to the energy resolution limitations, the quantitative depth profile information is limited, however an example of the qualitative behaviour is shown in Figure 60, in the fitted depth profile for the Sample 2.3.

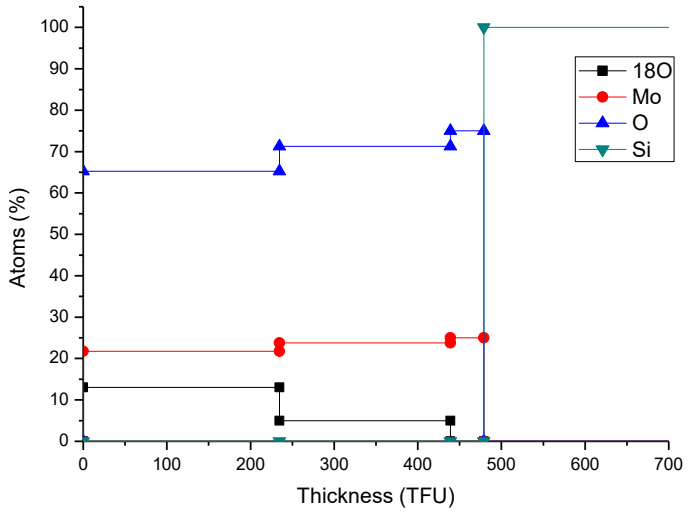

Figure 60: Depth profile for the Sample 2.3, where the black line is the diffusion pattern for the ^{18}O incorporated during the $^{18}O_2$ thermal treatments.

4.3.2 Organic semiconductor: overcoming classical RBS limitations

The great enhancement brought by the SegDet is the possibility to analyse organic materials using IBA that otherwise, using the classical acquisition system, would be impossible due to the damage generated by the ion beam. Here we demonstrate the statistical power of the SegDet measuring the damage generated by the ion beam as a function of fluence and, therefore, establishing the ion fluence limitation for RBS of the organic compound DBP on two different substrates: Silicon (Sample 5) and ITO (Sample 6).

In this experiment the setup has to be chosen carefully since the integrated DDA list mode gives the time stamp for each detected particle but our interest is in the ion fluence stamp. Therefore an extra parameter, i.e. beam charge deposited, has to be taken into account. The vacuum chamber works as a Faraday cup where the current generated by the ion beam can be measured using a current integrator. In the set up used in this experiment the output signal from the integrator triggers a pulse generator, giving pulses which can be treated by the DDA. Thus we are able to measure and store the fluence and the beam current as function of time (Figure 61).

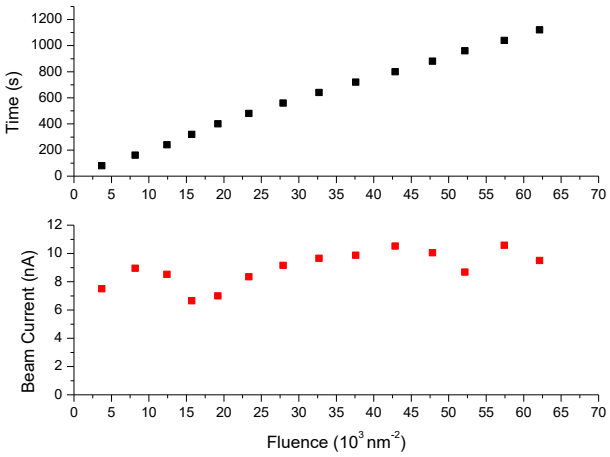

Figure 61: On the top the fluence vs time stamp. On the bottom the current evolution with the fluence.

Thus the experimental set up is prepared for the spectrum representation for any given time-fluence window. Figure 62 shows the spectrum from S2 of the SegDet for the complete $62.1 \cdot 10^3$ nm^{-2} fluence measurement. The Si is not completely channelled but the C signal is perfectly visible between 500 keV (c_1) and 600 keV (c_2). It is due to the large thickness of the DBP, nominally 100 nm.

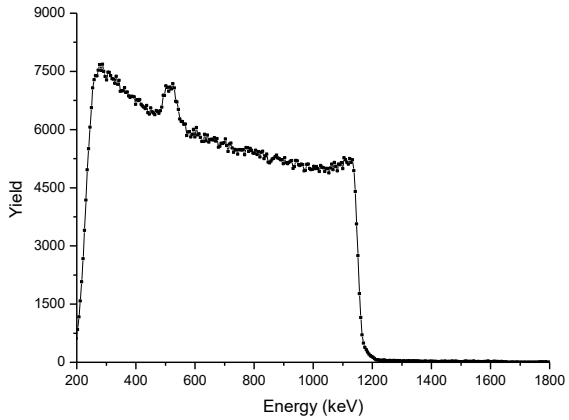

Figure 62: RBS spectrum from the SegDet (S2) on the Sample 5 using 2 MeV $^4He^+$ ions after $62.1 \cdot 10^3$ nm^{-2} (10 μC in 1 mm^2 beam spot)

Figure 63.a shows the damage evaluation of the DBP represented as the addition of the C peak area, C_{Area}, for the all the used segments as a function of fluence. In order to calculate an approximation of the substrate line shape, the silicon signal below the carbon was eliminated through the difference of the 45 keV (10 channels) before and after the C signal, $C_{Area} = A_{(c_1,c_2)} - A_{(c_1,c_1-45)} - A_{(c_2,c_2+45)}$. Then the uncertainty is the sum of the square root for all the areas involved. No significant trend in the C peak area is observed during the measurement. Furthermore Figure 63.b compares the spectra from the first and last 80s acquisition times, corresponding to around $4 \cdot 10^3$ ions nm^{-2}: we cannot observe changes in the C peak here either. We conclude that the 2 MeV $^4He^+$ is not generating Type I damage (see Annex II: Ion Damage). However beam spot traces in the beam impact point are observable by eye, with the film eventually becoming transparent. Although the carbon is still there the organic compound has been damaged (Type II damage), probably releasing hydrogen and generating C double bonds.

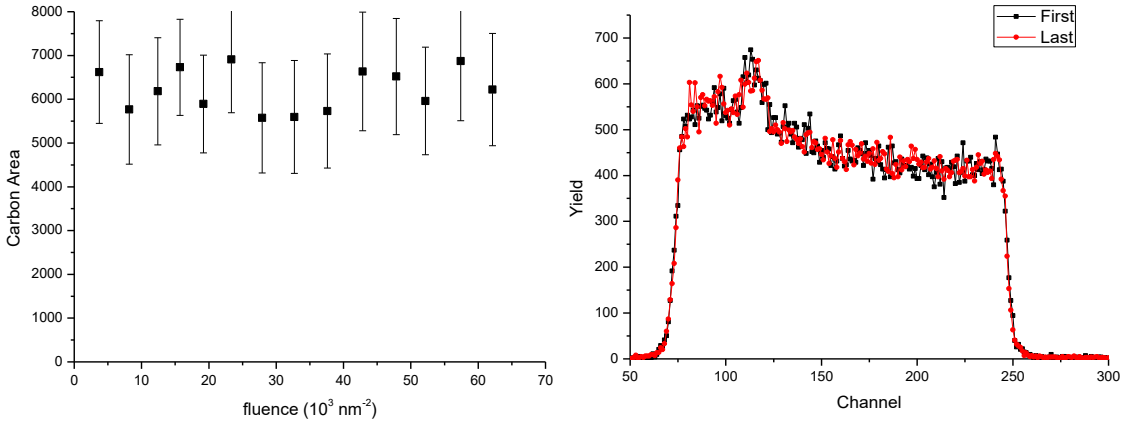

Figure 63: On the left, number of C atoms evolution as a fluence function; on the right, RBS spectra from S4 in the SegDet for Sample 5 for the first and last $4 \cdot 10^3$ nm^{-2} ion fluence.

Sample 6 substrate, ITO and quartz, is transparent in the visible light, therefore we can establish a fluence limitation before generating observable damage. Figure 64 shows a photo of Sample 6 irradiated at several points (from A to J) at increasing ion fluence, from $0.6 \cdot 10^3$ nm^{-2} to $25.9 \cdot 10^3$ nm^{-2} (0.1 μC to 4 μC in 1 mm^2 beam spot). The image has been treated to improve visibility of the beam impact points – the dark areas are in reality transparent. Points A and B correspond to $0.6 \cdot 10^3$ nm^{-2} and $1.2 \cdot 10^3$ nm^{-2} with a current below to 10 nA and the damage can be considered as negligible. Points C and D are for the same fluence but higher current (around 30 nA) where there is perhaps slightly more damage than for the lower current points. More pronounced transparent traces are seen in E, at $3.7 \cdot 10^3$ nm^{-2}, and from there the damage increases.

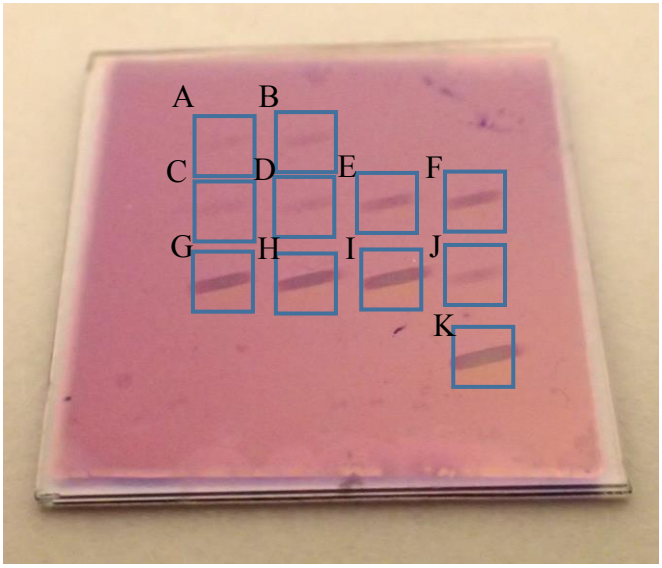

Figure 64: Sample 6 after being irradiated. Point A at 0.6 nm^{-2} (0.1 μC); B at 1.2 nm^{-2} (0.2 μC), both with less than 10 nA beam current; the remaining points were irradiated with 25-30 nA, point C at 0.6 nm^{-2} (0.2 μC), D at 1.2 nm^{-2} (0.1 μC); E at 3.7 nm^{-2} (0.6 μC); F at 6.2 nm^{-2} (1 μC); G at 9.4 nm^{-2} (1.6 μC); H at 12.4 nm^{-2} (2 μC); I at 18.6 nm^{-2} (3 μC); J the fluence was not well measured but it has to be around 2 nm^{-2} (0.3 μC) and K at 24.9 nm^{-2} (4 μC). The contrast and the brightness in the image has been increased to make it clearer (the dark traces are in reality transparent).

We noticed that points A, B, C and D had more pronounced damage traces just after being taken out of the vacuum chamber. Some self-repair or oxidation is taking place over several minutes when the sample is exposed to air.

Assuming an extremely small upper limit of $1.2 \cdot 10^3$ nm^{-2} for the fluence, the carbon peak from the Sample 5[47] segments in the SegDet can be calculated subtracting the silicon signal using an equivalent method to that used above. In this case the number of channels before and after the C signal vary depending on the best fit between the spectrum substrate and the line defined on each side of the C area (on the left by c_1 and $c_1 - x$, and on the right by c_2 and $c_2 + y$) following the equation:

$$C_{Area} = A_{(c_1,c_2)} - \left(\frac{A_{(c_1,c_1-x)}}{x} - \frac{A_{(c_2,c_2-y)}}{y}\right)\frac{c_2 - c_1}{2} \qquad 4.1$$

The addition of the peak areas from the 6 segments used gives a total carbon area of 1188±745, the uncertainty then is about 60%. On the other hand we can simulate the spectrum form a classical single PIPS detector using the SimNRA and adding Poisson noise. There the peak area found for this fluence is 90±89, a 98% of uncertainty. Figure 65 shows the spectra for the SegDet S3 and the PIPS detector simulation.

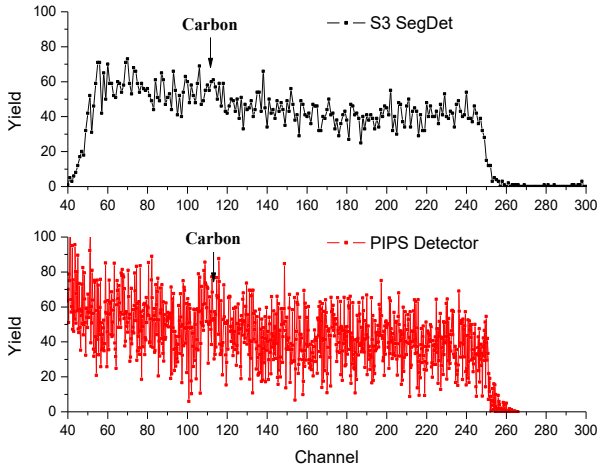

Figure 65: RBS spectra for $1.2 \cdot 10^3$ nm^{-2} fluence of the SegDet S3 (top) and simulated 2 msr PIPS detector (bottom).

4.4 Conclusions of the MoO_x/DBP study

We have demonstrated the convenient use of the SegDet, DDA and NDF for the RBS and NRA study of the oxidation process in the TMO MoO_x and the DBP organic semiconductor molecule. Fourteen simultaneous spectra have been successfully taken in this work, increasing more than 100 times the overall solid angle in comparison with the classical RBS installation in SAFIR (106 msr for the 14 segments vs 1 msr for the single PIPS detector typically used). Even with the energy resolution limitation (due to the digitiser power supplies), the SegDet has been confirmed to be a powerful instrument for IBA measurements.

[47] We used the Sample 5 since the RBS spectra is simpler.

The huge amount of data and the potential segment inhomogeneities (gain and resolution variability) from the SegDet has to be interpreted via a specialised tool, of which at present NDF is the only one available to manage the multiple spectra obtained. NDF Simulated Annealing has shown very strong capabilities, however also some weaknesses when tiny signals are involved. These kind of signals have to be fitted by a hybrid manual-automatic local search to get the minimum difference between data and fit, and obtain an optimal solution.

The samples show the nominal stoichiometry even when they were not pretreated by a cleaning process, therefore the short-term stability (around 10 minutes) in air has been proven. The lateral homogeneity is also quite stable, given a maximum disagreement in measured thickness of 11%.

The data analysis reveals that the amorphous oxidised samples reach an overall stoichiometric limit of $x = 3.35 \pm 0.20$ for the incorporation of ^{18}O. This observation could be completed by extending the thermodynamic range of the study, for example by observing the pressure and temperature dependence of the oxidation process.

The crystallised samples always incorporate at least as much oxygen (between 3% to 16% more), as the amorphous samples, suggesting the presence of enhanced oxygen diffusion via grain boundaries. However they show different behaviour depending on the initial as deposited stoichiometric value. When the nominal x values is less than 3 the stoichiometric value for the total oxygen (^{18}O and nominal divided by Mo) is 3.40 ± 0.20, which is only marginally greater than the limit found previously for the amorphous samples. However if the nominal value of x is greater than 3 then the oxidation uptake is up to 18% greater than for $x<3$. This difference in behaviour between MoO_x crystallised from low and higher initial oxygen concentrations may be a sign that the crystallisation behaviour itself depends on the initial oxygen concentration.

Qualitatively, the ^{18}O incorporation is observed to have a depth profile, higher at the surface than in the volume of the layer although the depth resolution is insufficient to make a more quantitative statement. Higher resolution depth profiling of ^{18}O could be with NRA resonance depth profiling [89], that can improve greatly the current results in terms of oxidation depth description. In principle this technique can be fitted simultaneously with RBS using NDF as well, through the same nuclear reaction at 150 keV where a sharp resonance takes place [90], [91].

The hypotheses about the oxidation capacity, role of oxygen vacancies and crystal electronic behaviour have to be more deeply studied and eventually confirmed by carrier mobility experiments. Furthermore, understanding the oxidation mechanisms will be facilitated by extending the thermodynamic range explored on the ^{18}O thermal treatments to a greater range of times and temperatures.

We demonstrate the SegDet capabilities IBA on the organic compounds characterisation in comparison with a classical single PIPS detector. The DDA list mode features brings the opportunity to store the acquired spectrum chronologically, making possible to represent any spectra for a given time or frame. Furthermore the spectra can be represented by the fluence

using the Faraday cup charge integrator and a pulse generator that can stablish a relationship between time and fluence.

The DBP organic semiconductor shows no observable Type I damage under beam irradiation, however the samples present Type II damage, probably through hydrogen loss and carbon bond re-organisation. We characterise the ion damage by visual effects, finding a fluence limitation before observable damage of between 1 nm^{-2} and 2 nm^{-2}. The samples further evolve after some minutes on the air environment, becoming less transparent. Within the fluence limitation ranges the SegDet can get 60% uncertainty using 6 segments, whereas a single classical PIPS detector cannot give any better statistical uncertainty than 95%. The estimations using the 16 segments and a more refined silicon signal subtraction gives the half of this uncertainty, 30%, which is enough statistics to be able to analyse by IBA techniques the organic compound. Using an accumulated spectrum for several impact points the experiment can be as reliable as any inorganic RBS analysis.

5. Conclusions and Perspectives

We have implemented and demonstrated the operation of a Segmented Detector with 16 segments and 760 mm² active area for several IBA applications. The detector design, with the segmentation and the use of an appropriate bias on the Guard Ring keeps the capacitance and the leakage current low, which is critical for obtaining the energy resolution required in depth profiling IBA techniques. An extensive IBIC investigation has shown that the shared collection of charge from particles that enter the detector in the interstrip region is sufficiently small to be ignored and that the detector may be operated without intricate shielding to prevent particles from impinging on the interstrip region. The detector is larger than a standard PIPS detector and more susceptible to pick up, however the noise can be controlled adequately using the same shielding and earthing techniques as have been implemented for decades with classical single PIPS detectors.

We show that it is highly desirable to associate such a device with Digital Data Acquisition in order to be able to acquire the spectra in a clean, reproducible and economical way. We demonstrate that CAEN Digitisers can reach the performance required by the IBA community. The digital system is shown to have at least the performance of the classical analogue systems, and even better energy resolution, particle counting and pile-up rejection can be expected. We note that the energy resolution is worse with the DT5725 than with DT5724, probably due to a different input stage of the DT5725 which has a digitally controlled input gain.

Due to the great amount of data acquired the analysis tool has to be prepared for its management. NDF DataFurnace has proven to be a very useful tool, probably the only one available today, for obtaining self-consistent results from multiple spectra given by the multiple detector segments.

The overall experimental setup is almost ready to be used systematically in an IBA facility such as SAFIR. The large solid angle available with the SegDet opens a new possibility for single ended accelerators to use the very low currents of doubled charged ions produced by the RF ion source. This effectively doubles the available ion beam energy and so opens new research perspectives in application of non-Rutherford elastic scattering that would otherwise require a much larger machine. The spectra obtained in this thesis constitute a proof-of-principle, however there is undoubtedly room to improve the intensity and purity of the $^{4}He^{2+}$ beam for routine use. Neither the ion source parameters nor the beam transport were subject to a concerted optimisation effort. In addition, the ion source itself may be modified quite simply, for example by optimising the magnetic field around the source bottle to maximise ionisation in the plasma, and choosing an appropriate material for the ion source exit canal, where significant ionisation can take place [92].

Moreover we used this enhanced IBA system to study two systems of high current interest: Topological Insulators, which have just received the 2016 Nobel Prize in Physics, and organic semiconductor devices with application as organic photovoltaic devices, of great importance for sustainable development and renewable energy sources, one of the most challenging

subjects that our generation has to deal with. In both cases the SegDet capabilities were tested with interesting results (detailed conclusions concerning the TI and MoO_x studies are given in the appropriate chapters above), but also suggesting promising further avenues to be explored.

The prototype system experimented here seems to be the next step in the IBA community, so improvement in performance will continue and the technical aspects will be refined. The possibilities have just started to be opened and the systems are already being used in current works within the INSP, such as a channelling study in TiO_2, giving the first example of applications outside this thesis.

In the TI study we discovered a weakness in the acquisition system. The heavier atomic masses in the substrate (GaAs in comparison with the Si used in the other studies and tests) and the bigger layer thicknesses in the medium-heavy elements (up to 300 TFU of Se in the TI as compared to some tens in Bi in RBS reference sample or the 100 of Mo in the MoO_x study) used there generates significant spectrum background from the substrate signal and the medium weight elements (Se in the TI case). The results obtained by IBIC and further tests in the GR signal show that this background is not coming from the particles arriving in the GR zone. Moreover we noticed that background is not found in the channelled spectra for those samples, which is a clear reflection of the count rate dependency of this effect. However comparing the spectra for two different fluences, 6μC and 0.2μC, the background remains the same, hence there is not a fluence dependency. The source of this effect is unclear and it could be due to several combined factors. One possibility is a failure in the signal filtering for the DDA system that can change the input bandwidth giving some distortions in the spectrum for the higher count rate experiments. Incomplete charge collection in the SegDet could also produce such effects as well, but it cannot come from the depletion thickness since we worked in a bias voltage between -30V to -50V which gives more than enough depletion zone thickness. To solve this issue it is necessary to characterise more precisely the causes; some clues have been reported here: atomic mass, layer thickness and count rate dependency and fluence independency. These bring us ideas for further experiments in order to understand this behaviour. Using samples composed of a heavy element on the top of a light substrate, Au on C for instance, and varying the heavy element layer thickness depth could help to characterise the nature of the background. The results can be compared with a single PIPS detector, other DDA modules (here DT5781 and DT5724 are also available) and analogue acquisition systems, in order to be able to identify the SegDet or DDA origin for the undesirable background.

Nevertheless, once the system is completely operative, some perspectives can be explored in the short-term. The DDA can process a great number of events (250 Msample/s in DT5724-25) and the input voltage of each channel can be adjusted via software. This allows us to adapt individual channels to specific experimental needs. Both features can be used to measure nuclear reaction products without the foil used to prevent elastically scattered primary beam from the detector, since the system may be able to measure both backscattered particles and reaction products without severe pile-up. The limitation here would be the capability of the detector depletion thickness; in SegDet this is around 250 μm which gives an energy limitation of around 5 MeV for protons, 7 MeV for deuterons, and 22 MeV for alpha particles.

Another aspect to be explored in the near future is the data visualisation for the analyst. A software tool with an easy way to introduce the energy gain and charge collected in each segment can be very useful for the first view of the data acquired since the preamplifiers and backscattering angles are very reproducible.

The NDF DataFurnace is the most reliable and convenient tool to use with a SegDet, however it could be slightly developed for this kind of application. In the fitting process the backscattering angles have to be free variables to get the correct result. This idea works perfectly in case of independent detectors, but for the SegDet there is one degree of freedom less since the angular step between each segment is known and fixed. Furthermore, it is known that the ion fluence is identical for each spectrum, however this too is a free variable for each spectrum in NDF. The analysis would be much easier if these relationships are directly taken in account in the software, otherwise the analyst has to be aware of the geometry files fitting for each individual segment, which is a tedious work.

Annex I: NDF DataFurnace and Total IBA

The spectrum analysis tool used in this thesis has been NDF DataFurnace. It is based on the idea of generating a self-consistent answer by fitting at once multiple spectra from IBA. In our case this is mandatory, since we had to deal with 16 spectra – one per segment – for every individual sample measurement where, obviously, the sample structure has to be common for all the spectra. Moreover with NDF EBS, NRA and ERDA spectra can be fitted as well; and when is combined with results from some PIXE fitting tools the material characterisation can be extremely accurate and unambiguous [2].

DataFurnace mechanisms

The basic algorithm is Simulated Annealing (SA), which can be understood by analogy with the annealing process in steel or ceramics, where heating the atoms increases their energy which allows them to explore the most energetically favourable positions, followed by slow cooling so that the material is crystallised; the size of the crystals is controlled by the cooling time ramp.

Unlike the classical RBS fitting tools, NDF results are not calculated through a simulation but rather proceed without an a priori sample structure. In the classical fitting tool, the depth structure is simulated from certain geometrical parameters and structure input which, afterwards, are fitted by trial and error in order to have the closest match between the simulation and the measured spectrum. Instead, SA calculates the depth profile for a given experimental spectrum using just initial experimental parameters (such as energy gain and offset, ion fluence or solid angle). Thus, the fitting concept here is working in the inverse way to the classical fitting systems.

Mathematically, SA is defined as *global optimisation* for a given function [93]. That means that SA is able to find the minimum possible value in a continuous function using some initial criteria. The SA consists of five concepts: forward model, objective function, Markov chain, acceptance criterion and cooling schedule. The *forward model* is, basically, how all the simulation IBA fitting tools work. It takes the experimental data as a function and converts it to a result function. In RBS, the experimental spectrum ($Y(E)$) is converted into the sample depth profile through the stopping power ($F(x)$).The *objective function* is the object to optimize. In the RBS case, the function represents the distance between theoretical and experimental data spectra (Y), whose variable is the depth profile (x), and it is represented by $O(Y, x)$. However there is not a unique number of possible solutions (or depth profiles), the space where are all the solutions are randomly positioned, $S\{x\}$, can be organised by a *Markov chain* $M_s = \{x_0, x_1, x_2, \dots x_m\}$. Then the *acceptance criterion* is applied to include or exclude the potential solution within the Markov chain. The probability of it is given by the Metropolis criterion:

$$P \propto \exp -\frac{\Delta O}{T} \qquad \text{AI.1}$$

Where ΔO is the difference between two consecutive objective functions and the *transition distribution* is T, where $T(x_i) = x_{i+1}$. This probability is very similar to the Boltzmann distribution, hence an analogy with the thermodynamics through the Boltzmann factor can be easily done where the transition parameter represents the temperature. That is the reason to call it an "annealing" process. Finally, the *cooling schedule* is the "temperature" reduction ramp which has to be long enough to reach the "thermodynamic equilibrium". Then we can redefine the objective function as $\chi^2_{min}(Y,x) = \sum(Y_{data} - Y_{fit})^2$ in order to link the SA with the IBA spectra. Figure 66 shows a simplified diagram for the SA process.

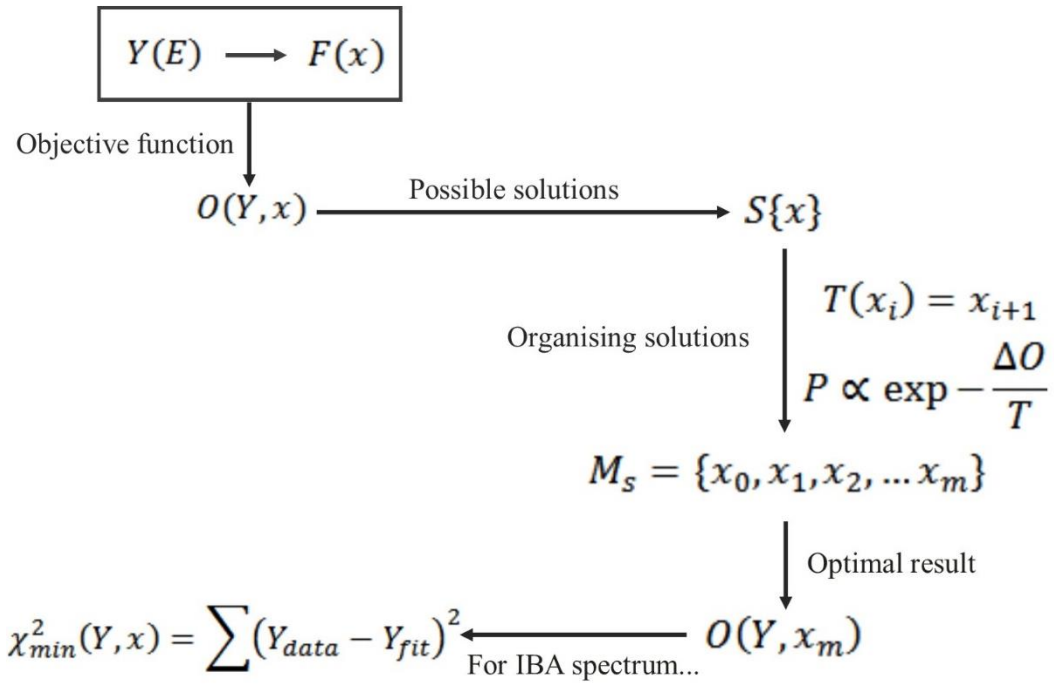

Figure 66: Simulated Annealing flow diagram.

NDF implements SA which gets the global minimum of the O for the optimum depth profile. Initial input parameters (such as energy gain, solid angle/fluence product or backscattering angle) have to be introduced to prepare the SA fitting. Nevertheless *local minimum search* is also implemented to get more refined fitting. It uses grid search optimisation based on the previous SA solution. More extended and deeper explanations and some experimental applications can be found in elsewhere [1], [93], [94]. These references also include descriptions of the different corrections that can be implemented in the NDF fitting such as *Double Scattering* [95] and the *ad-hoc Multiple Scattering and channelling corrections* [94] used in this thesis.

Bayesian Inference

Bayesian Inference (BI) is an alternative to calculate the results for a given spectrum. BI is able to quantify the accuracy for depth profiles, through a range of optimal solutions. These solutions are averaged and then it is possible to calculate the standard deviation which is, ultimately, the

uncertainly in the spectrum depth profile. The combination between the SA, to get the profile, and the BI, to get the uncertainty, is a powerful method to describe a sample by IBA techniques.

The main idea in BI is to construct a density of states function through the possible results obtained by the *Markov Chain Monte Carlo* (MCMC) algorithm, where the probability states distribution, $\rho(x|Y)$ is created using the forward model, Poisson statistics and the prior distribution that is given by the SA result (number of layers information). The probability states distribution gives a statistical way to calculate the profile average, $\langle x \rangle$, and the standard deviation associated, $\sigma(x)$, which is the uncertainty representation for the measurement; therefore it is the *confidence interval* for the equilibrium distribution. Deeper explanation and examples are shown in [94], [96].

The BI is purely statistical approach and it gives, actually, the value of the information quality within an spectrum, hence there is needed to interpret the SA and BI results to have more realistic uncertainly evaluation. In the studied systems above, we the SA and local searching result as the real depth profile, and then, applying BI we played with the parameters until the SA result was inside the standard deviation range. Here has to be noted that the uncertainty values are not absolute, they are evaluated without real information about the absolute uncertainty in fluence, energy beam and the remain experimental parameters. The absolute uncertainty evaluation has to be done by costly (in time and effort) uncertainty budget methods [97]–[101] which were not manageable to make within this thesis.

Annex II: Ion Damage

Typically IBA techniques are considered non-destructive and the material under study is not going to be damaged. However it is just partially true. The sample has not to be handled harshly; it is not needed to break it down to measure the depth profile, put it under extreme environmental conditions or change its chemical nature. Moreover – depending on the case – if the sample must be left functional (if it is an electronic device, for example) after the measurement. This is reason to call them non-destructive techniques. Nonetheless, what we have in IBA is an ion beam interacting with the matter and we measure the backscattered ions, but the most of these incident ions are not backscattered, indeed the cross section of the IBA experiments (ionisation for PIXE, Rutherford for RBS…) delimitates the ratio between counted events and incident ions to less than 0.05%. Therefore we induce a great number of nuclear collisions which are inevitably modifying the target material through ionisation, beam heating or atomic displacements. Here are established two basic kinds of damage [102]:

- Type I: which can be observed in situ. It is related to sputtering, physical deformation or crystal atoms displacement (just observable in channelling)

- Type II: this is associated to the material internal properties, such as electronic, optic or magnetic behaviour. It just can be measured separately after the IBA experiment. These kind of damage (and crystal displaced atoms) can be eventually recovered through thermal annealing.

The damage induced by the ion beam is strongly related to the electronic and nuclear stopping power. In the *nuclear electronic* point of view – ionising damage – the ion passes through the sample generates an ionised track below, which excites the localised atomic electrons around it and the Plasmon modes. Afterwards those electrons loss their extra energy in the phonons, which can create *colour centres*[48] and heat up the sample. Two facts have to be taken in account here: the ion/target atomic weight and the sample electronic state nature.

Using light ions, the heat created will recover the damage (totally or almost) since the energy gained by localised electron through the ion excitation is quickly transferred to the Plasmon modes (recombination), while when heavy ions are used the damage process is bigger and more complex. Their stopping power is bigger and the charge is not constant, so the charge state has to be taken in account. The generation of nuclear recoils also is bigger and, as will be shown below, they can produce nuclear cascades which induce extra ionisation in their path. In Figure 67 are SRIM calculations [8] for the ionisation with a light incident ion ($^{4}He^{+}$) and heavy one ($^{132}Xe^{+}$) on silicon. The thermal spike model [103] has been demonstrated reasonably valid for the ionising damage, but it is still an open topic.

[48] The color centers are electron defects, in which an atom – or various – in the material is extra charged.

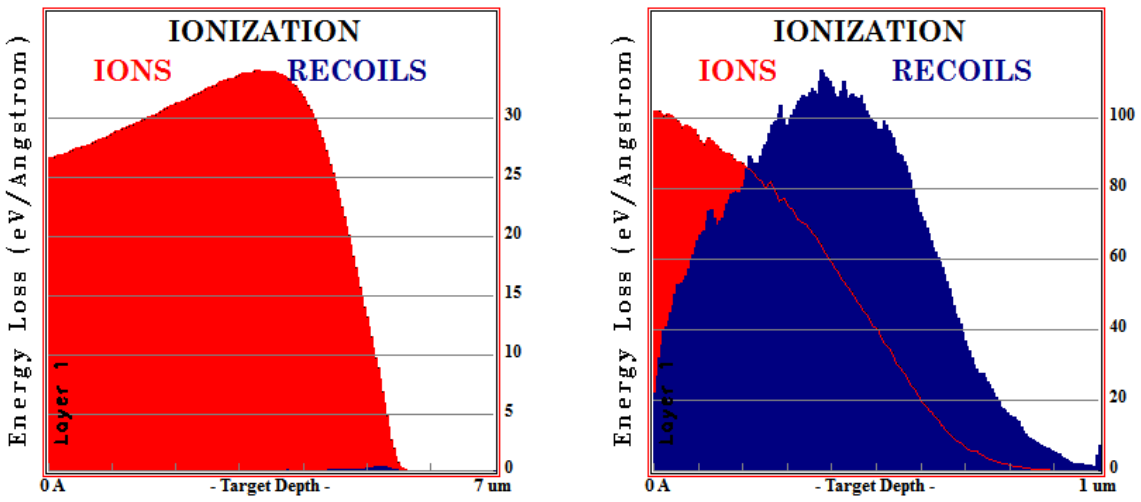

Figure 67: Ionisation SRIM calculations. In the left $^{4}He^{+}$ ions on Si and in the right $^{123}Xe^{+}$ ions in Si, both at 1500 keV.

The number of free electrons, i.e. electronic state, of the studied material has also a role on the ionising damage. The possibility to fill up a hole left by an excited electron is obviously bigger in the conductors than in any other material. In semiconductors, the ionising damage depends strongly on the incident ion properties and the recombination time in the sample. In the other hand, for insulator materials, the slow recombination can heat sample up since the phonons gain the no recombined energy, hence the sample can be burned and the chemical bounds completely destroyed.

Nonetheless in this thesis we have used – principally – light incident ions so the electronic contribution can be neglected when the material under study is metal or semiconductor. The potential ionising damage done in the organic materials involved within the text has not been characterised, we have been interested in the element composition so there are not repercussions about that kind of damage.

The *nuclear stopping damage* is related to the direct interaction ions-nucleus and the atomic defects. When the energy of one of these collisions is enough to displace a target atom, there is created a dislocated atom which leaves behind a *vacancy*. This dislocation can be placed in a interstitial permanent position, there will be created a *Frenkel pair*, which corresponds to interstitial atom and the vacancy, also it can be placed in an original vacancy (*Schottky pair*) or replaced a primitive atom site (*substitutional* or *anti-site*), just in the same way as the defects are classified in [11]. In the other hand, the dislocated nucleus – and sometimes the incident ions as well – can collide several times, generating atomic *cascades* along the ion track within the material. They are initiated by the *primary knock-on atom* (PKA) and the overall effect of them is represented by the number of *displaced atoms* (n_{disp}). To model and simulate these cascades is necessary to use Monte Carlo calculations, as it is done in SRIM. These cascades can generate the same kind of defects as the commented above but in a secondary interaction. However after certain time, the picture will change, and the generated defects in the material will search the most favourable energetic configuration since the temperature is giving some mobility to them, and the sample can be self-healed through internal annealing.

The ion weight and the energy also play here a main role. Cascades are easier to start when the ion is bigger and they can go farther if the energy is more elevated, as we can see in the SRIM code shown in Figure 68.

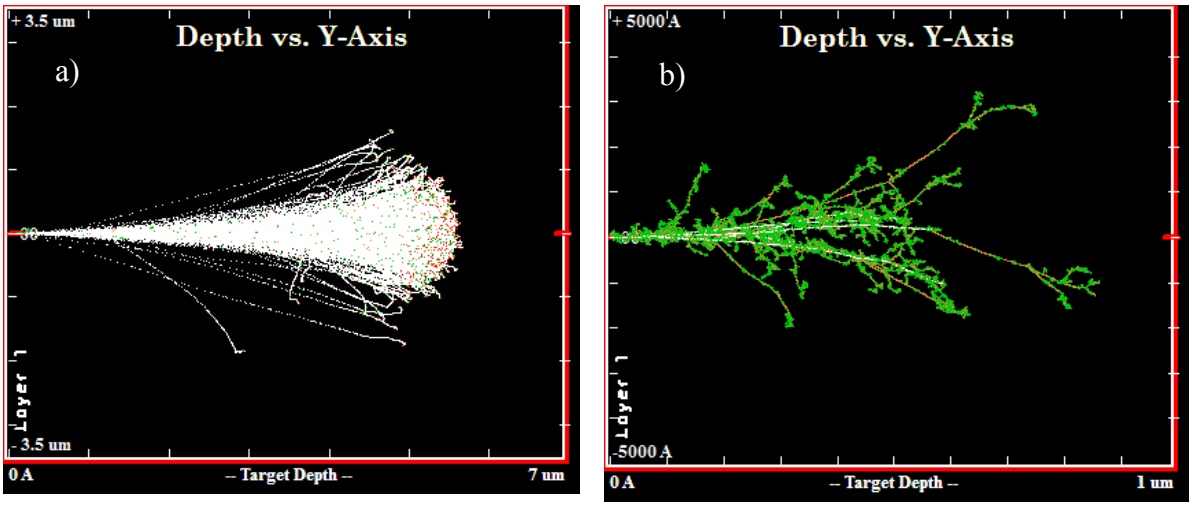

Figure 68: SRIM simulation for Si 100 µm thick target with incident ions a) 3000 $^{4}He^{+}$ and b) 5 $^{132}Xe^{+}$ at 1500 keV. The white lines are the ion trajectory while the green are the cascades.

Summarising, the ion beam induces two damage in two different ways: by electronic excitation (ionising), which depends on the electronic stopping power and by nuclear interaction, which displaces the target nucleus giving rise to eventual nuclear cascades. In terms of material behaviour, the damage can be classify in two: type I, where the damage has consequences in the IBA measurement and type II in which the material response is within the internal behaviour.

Bibliography

[1] N. P. Barradas and C. Jeynes, "Advanced physics and algorithms in the IBA DataFurnace," *Nucl. Instruments Methods Phys. Res. Sect. B Beam Interact. with Mater. Atoms*, vol. 266, no. 8, pp. 1875–1879, Apr. 2008.

[2] C. Jeynes, M. J. Bailey, N. J. Bright, M. E. Christopher, G. W. Grime, B. N. Jones, V. V. Palitsin, and R. P. Webb, "'Total IBA' – Where are we?," *Nucl. Instruments Methods Phys. Res. Sect. B Beam Interact. with Mater. Atoms*, vol. 271, pp. 107–118, 2012.

[3] H. Bethe, "Zur Theorie des Durchgangs schneller Korpuskularstrahlen durch Materie," *Ann. Phys.*, vol. 397, no. 3, pp. 325–400, 1930.

[4] F. Bloch, "Bremsvermögen von Atomen mit mehreren Elektronen," *Zeitschrift für Phys.*, vol. 81, no. 5–6, pp. 363–376, May 1933.

[5] J. F. Ziegler and J. M. Manoyan, "The stopping of ions in compounds," *Nucl. Instruments Methods Phys. Res. Sect. B Beam Interact. with Mater. Atoms*, vol. 35, no. 3–4, pp. 215–228, Dec. 1988.

[6] H. H. Andersen, F. Besenbacher, P. Loftager, and W. Möller, "Large-angle scattering of light ions in the weakly screened Rutherford region," *Phys. Rev. A*, vol. 21, no. 6, pp. 1891–1901, Jun. 1980.

[7] J. L'Ecuyer, J. A. Davies, and N. Matsunami, "How accurate are absolute rutherford backscattering yields," *Nucl. Instruments Methods*, vol. 160, no. 2, pp. 337–346, 1979.

[8] J. F. Ziegler, "SRIM-2003," *Nucl. Instruments Methods Phys. Res. Sect. B Beam Interact. with Mater. Atoms*, vol. 219–220, pp. 1027–1036, Jun. 2004.

[9] K. Nordlund, "Molecular dynamics simulation of ion ranges in the 1–100 keV energy range," *Comput. Mater. Sci.*, vol. 3, no. 4, pp. 448–456, Mar. 1995.

[10] D. Schmaus and I. Vickridge, "MeV Ion Beam Analytical Methods," in *Analytical Methods in Corrosion Science and Engineering*, P. Marcus and F. Mansfeld, Eds. New York: CRC Press, Taylos & Francis, 2006, pp. 103–132.

[11] N. W. Ashcroft and N. D. Mermin, *Solid State Physics*. Philadelphia: Holt-Saunders International Edition, 1976.

[12] C. Cohen-Tannoudji, B. Diu, and F. Laloê, *Mecanique Quantique Vol. I*. Hermann, 1997.

[13] E. Kaxiras, *Atomic and Electronic Structure of Solids*. Cambridge: Cambridge University Press, 2003.

[14] L. C. Feldman, J. W. Mayer, and S. T. Picraux, "Interaction of ion beams with surfaces," in *Materials Analysis by Ion Channeling*, Elsevier, 1982, pp. 12–36.

[15] J. H. Barrett, "Monte Carlo Channeling Calculations," *Phys. Rev. B*, vol. 3, no. 5, pp. 1527–1547, Mar. 1971.

[16] M. N. Yongqiang Wang, *Handbook of Modern Ion Beam Materials Analysis*. Materials

Research Society, 2010.

[17] J. Lindhard, “Influence of crystal lattice on motion of energetic charged particles,” *Math. meddelelser*, vol. 34, no. 14, 1965.

[18] L. C. Feldman, J. W. Mayer, and S. T. Picraux, “Front Matter,” in *Materials Analysis by Ion Channeling*, Elsevier, 1982, p. iii.

[19] A. Vantomme, “50years of ion channeling in materials science,” *Nucl. Instruments Methods Phys. Res. Sect. B Beam Interact. with Mater. Atoms*, vol. 371, pp. 12–26, Mar. 2016.

[20] M. B. H. Breese, D. N. Jamieson, and P. J. C. King, *Materials analysis using a nuclear microprobe*. New York: John Wiley & Sons, Ltd., 1996.

[21] R. D. Deslattes, E. G. K. Jr., P. Indelicato, L. de Billy, E. Lindroth, J. Anton, J. S. Coursey, D. J. Schwab, C. Chang, R. Sukumar, K. Olsen, and R. A. Dragoset, “NIST X-Ray Transition Energies,” *National Institute of Standards and Technology*, 2005. [Online]. Available: http://www.nist.gov/pml/data/xraytrans/index.cfm. [Accessed: 31-May-2016].

[22] M. Hsiung Chen and B. Crasemann, “Relativistic cross sections for atomic K- and L-shell ionization by protons, calculated from a Dirac-Hartree-Slater model,” *At. Data Nucl. Data Tables*, vol. 33, no. 2, pp. 217–233, Sep. 1985.

[23] M. H. Chen and B. Crasemann, “Atomic K-, L-, and M-shell cross sections for ionization by protons: A relativistic hartree-slater calculation,” *At. Data Nucl. Data Tables*, vol. 41, no. 2, pp. 257–285, Mar. 1989.

[24] H. Paul and J. Sacher, “Fitted empirical reference cross sections for K-shell ionization by protons,” *At. Data Nucl. Data Tables*, vol. 42, no. 1, pp. 105–156, May 1989.

[25] J. H. Hubbell, P. N. Trehan, N. Singh, B. Chand, D. Mehta, M. L. Garg, R. R. Garg, S. Singh, and S. Puri, “A Review, Bibliography, and Tabulation of K, L, and Higher Atomic Shell X-Ray Fluorescence Yields,” *J. Phys. Chem. Ref. Data*, vol. 23, no. 2, p. 339, Mar. 1994.

[26] I. Orlic, C. H. Sow, and S. M. Tang, “Experimental L-Shell X-Ray Production and Ionization Cross Sections for Proton Impact,” *At. Data Nucl. Data Tables*, vol. 56, no. 1, pp. 159–210, Jan. 1994.

[27] J. L. Campbell, “Fluorescence yields and Coster–Kronig probabilities for the atomic L subshells. Part II: The L1 subshell revisited,” *At. Data Nucl. Data Tables*, vol. 95, no. 1, pp. 115–124, Jan. 2009.

[28] J. L. Campbell, “Fluorescence yields and Coster–Kronig probabilities for the atomic L subshells,” *At. Data Nucl. Data Tables*, vol. 85, no. 2, pp. 291–315, Nov. 2003.

[29] T. Papp, J. L. Campbell, and S. Raman, “Experimental test of Dirac-Fock versus Dirac-Hartree-Slater L X-ray intensity ratios,” *J. Phys. B At. Mol. Opt. Phys.*, vol. 26, no. 22, pp. 4007–4017, Nov. 1993.

[30] K. Ishii, H. Yamazaki, S. Matsuyama, W. Galster, T. Satoh, and M. Budnar, "Contribution of atomic bremsstrahlung in PIXE spectra and screening effect in atomic bremsstrahlung," *X-Ray Spectrom.*, vol. 34, no. 4, pp. 363–365, Jul. 2005.

[31] I. V. Mitchell and K. M. Barfoot, "Particle induced X-ray emission analysis application to analytical problems," *Nucl. Sci. Appl., Sect. B*, vol. 1, no. 2, pp. 99–162, 1981.

[32] J. A. Maxwell, W. J. Teesdale, and J. L. Campbell, "Ifi The Guelph PIXE software package II," *Nucl. Instruments Methods Phys. Res. Sect. B Beam Interact. with Mater. Atoms*, vol. 43, no. 94, pp. 218–230, 1995.

[33] J. L. Campbell, N. I. Boyd, N. Grassi, P. Bonnick, and J. A. Maxwell, "The Guelph PIXE software package IV," *Nucl. Instruments Methods Phys. Res. Sect. B Beam Interact. with Mater. Atoms*, vol. 268, no. 20, pp. 3356–3363, 2010.

[34] C. G. Ryan, D. R. Cousens, S. H. Sie, W. L. Griffin, G. F. Suter, and E. Clayton, "Quantitative pixe microanalysis of geological matemal using the CSIRO proton microprobe," *Nucl. Inst. Methods Phys. Res. B*, vol. 47, no. 1, pp. 55–71, 1990.

[35] K. S. Krane, "Introductory Nuclear Physics," *Introd. Nucl. Physics, by Kenneth S. Krane, pp. 864. ISBN 0-471-80553-X. Wiley-VCH , Oct. 1987.*, vol. 1, p. 845, 1987.

[36] A. F. Gurbich, "SigmaCalc recent development and present status of the evaluated cross-sections for IBA," *Nucl. Instruments Methods Phys. Res. Sect. B Beam Interact. with Mater. Atoms*, vol. 371, pp. 27–32, Mar. 2016.

[37] G. Amsel and B. Maurel, "High resolution techniques for nuclear reaction narrow resonance width measurements and for shallow depth profiling," *Nucl. Instruments Methods Phys. Res.*, vol. 218, no. 1, pp. 183–196, 1983.

[38] I. C. Vickridge, "Depth resolution and narrow nuclear resonance profiling," *Curr. Appl. Phys.*, vol. 3, no. 1, pp. 51–55, 2003.

[39] G. Amsel and W. A. Lanford, "Nuclear Reaction Techniques in Materials Analysis," *Annu. Rev. Nucl. Part. Sci.*, vol. 34, no. 1, pp. 435–460, Dec. 1984.

[40] G. Dearnaley and D. C. Northrop, *Semiconductor Counters for Nuclear Radiations*. Wiley, 1966.

[41] G. H. Döhler and H. Heyszenau, "Conduction in the relaxation regime," *Phys. Rev. B*, vol. 12, no. 2, pp. 641–649, Jul. 1975.

[42] W. Shockley, "Currents to Conductors Induced by a Moving Point Charge," *J. Appl. Phys.*, vol. 9, no. 10, p. 635, Apr. 1938.

[43] S. Ramo, "Currents Induced by Electron Motion," *Proc. IRE*, vol. 27, no. 9, pp. 584–585, Sep. 1939.

[44] J. B. Gunn, "A general expression for electrostatic induction and its application to semiconductor devices," *Solid. State. Electron.*, vol. 7, no. 10, pp. 739–742, Oct. 1964.

[45] M. B. H. Breese, E. Vittone, G. Vizkelethy, and P. J. Sellin, "A review of ion beam

induced charge microscopy," *Nucl. Instruments Methods Phys. Res. Sect. B Beam Interact. with Mater. Atoms*, vol. 264, no. 2, pp. 345–360, Nov. 2007.

[46] F. B. McLean and T. R. Oldham, "Charge Funneling in N- and P-Type Si Substrates," *IEEE Trans. Nucl. Sci.*, vol. 29, no. 6, pp. 2017–2023, 1982.

[47] F. D. M. Haldane, "Model for a quantum hall effect without landau levels: Condensed-matter realization of the 'parity anomaly,'" *Phys. Rev. Lett.*, vol. 61, no. 18, pp. 2015–2018, Oct. 1988.

[48] C. L. Kane and E. J. Mele, "Quantum Spin Hall Effect in Graphene," *Phys. Rev. Lett.*, vol. 95, no. 22, p. 226801, Nov. 2005.

[49] M. Z. Hasan and C. L. Kane, "Colloquium: Topological insulators," *Rev. Mod. Phys.*, vol. 82, no. 4, pp. 3045–3067, Nov. 2010.

[50] J. Tian, I. Childres, H. Cao, T. Shen, I. Miotkowski, and Y. P. Chen, "Topological insulator based spin valve devices: Evidence for spin polarized transport of spin-momentum-locked topological surface states," *Solid State Commun.*, vol. 191, pp. 1–5, Aug. 2014.

[51] L. A. Wray, S.-Y. Xu, Y. Xia, D. Hsieh, A. V. Fedorov, H. Lin, A. Bansil, Y. S. Hor, R. J. Cava, and M. Z. Hasan, "How robust the topological properties of Bi2Se3 surface are : A topological insulator surface under strong Coulomb, magnetic and disorder perturbations," *Nat. Phys.*, vol. 7, no. 1, p. 14, Jan. 2011.

[52] Y. L. Chen, J.-H. Chu, J. G. Analytis, Z. K. Liu, K. Igarashi, H.-H. Kuo, X. L. Qi, S. K. Mo, R. G. Moore, D. H. Lu, M. Hashimoto, T. Sasagawa, S. C. Zhang, I. R. Fisher, Z. Hussain, and Z. X. Shen, "Massive Dirac fermion on the surface of a magnetically doped topological insulator.," *Science*, vol. 329, no. 5992, pp. 659–662, Aug. 2010.

[53] C.-Z. Z. Chang, J. Zhang, X. Feng, J. Shen, Z. Zhang, M. Guo, K. Li, Y. Ou, P. Wei, L.-L. L. Wang, Z.-Q. Q. Ji, Y. Feng, S. Ji, X. Chen, J. Jia, X. Dai, Z. Fang, S.-C. C. Zhang, K. He, Y. Wang, L. Lu, X.-C. C. Ma, and Q.-K. K. Xue, "Experimental Observation of the Quantum Anomalous Hall Effect in a Magnetic Topological Insulator," *Science (80-.).*, vol. 340, no. 6129, pp. 167–170, Apr. 2013.

[54] H. Zhang, C.-X. Liu, X.-L. Qi, X. Dai, Z. Fang, and S.-C. Zhang, "Topological insulators in Bi2Se3, Bi2Te3 and Sb2Te3 with a single Dirac cone on the surface," *Nat. Phys.*, vol. 5, no. 6, pp. 438–442, May 2009.

[55] 17F and 41C Authors and editors of the volumes III 17E, "Bismuth selenide (Bi2Se3) crystal structure, chemical bond, lattice parameter (including data of related compounds), pp. 4," *Non-Tetrahedrally Bond. Elem. Bin. Compd. I*, pp. 1–4, 2001.

[56] O. Materials and R. Prize, "Introduction : Organic Electronics and Optoelectronics," vol. 107, no. 4, pp. 1985–1987, 2007.

[57] H. Bässler and A. Köhler, "Charge transport in organic semiconductors," *Top. Curr. Chem.*, vol. 312, pp. 1–65, 2012.

[58] J. Meyer, S. Hamwi, M. Kröger, W. Kowalsky, T. Riedl, and A. Kahn, "Transition metal

oxides for organic electronics: Energetics, device physics and applications," *Advanced Materials*, vol. 24, no. 40. WILEY-VCH Verlag, pp. 5408–5427, 23-Oct-2012.

[59] M. T. Greiner, M. G. Helander, W.-M. Tang, Z.-B. Wang, J. Qiu, and Z.-H. Lu, "Universal energy-level alignment of molecules on metal oxides," *Nat. Mater.*, vol. 11, no. 1, pp. 76–81, Nov. 2012.

[60] M. A. Green, K. Emery, Y. Hishikawa, W. Warta, and E. D. Dunlop, "Solar cell efficiency tables (version 48)," *Prog. Photovoltaics Res. Appl.*, vol. 24, no. 7, pp. 905–913, Jul. 2016.

[61] X. Xiao, J. D. Zimmerman, B. E. Lassiter, K. J. Bergemann, and S. R. Forrest, "A hybrid planar-mixed tetraphenyldibenzoperiflanthene/C70 photovoltaic cell," *Appl. Phys. Lett.*, vol. 102, no. 7, p. 73302, 2013.

[62] T. Kirchhuebel, M. Gruenewald, F. Sojka, S. Kera, F. Bussolotti, T. Ueba, N. Ueno, G. Rouillé, R. Forker, and T. Fritz, "Self-Assembly of Tetraphenyldibenzoperiflanthene (DBP) Films on Ag(111) in the Monolayer Regime," *Langmuir*, vol. 32, no. 8, pp. 1981–1987, Mar. 2016.

[63] H. Zhong, "Review of the Shockley–Ramo theorem and its application in semiconductor gamma-ray detectors," *Nucl. Inst. Methods Phys. Res. A*, vol. 463, no. 1–2, pp. 250–267, 2001.

[64] F. Munnik, A. J. M. Plompen, J. Räisänen, and U. Wätjen, "Stopping powers of 200–3000 keV 4He and 550–1750 keV 1H ions in Vyns," *Nucl. Instruments Methods Phys. Res. Sect. B Beam Interact. with Mater. Atoms*, vol. 119, no. 4, pp. 445–451, Dec. 1996.

[65] H. Spieler, *Semiconductor Detector Systems*. OUP Oxford, 2005.

[66] U. Fano, "Ionization yield of radiations. II. the fluctuations of the number of ions," *Phys. Rev.*, vol. 72, no. 1, pp. 26–29, Jul. 1947.

[67] W. Van Roosbroeck, "Theory of the yield and fano factor of electron-hole pairs generated in semiconductors by high-energy particles," *Phys. Rev.*, vol. 139, no. 5A, pp. A1702–A1716, Aug. 1965.

[68] S. O. W. Antman and D. A. Landis, "Measurements of the Fano factor and the energy per hole-electron pair in germanium," *Nucl. Instruments Methods*, vol. 40, no. 2, pp. 272–276, 1966.

[69] S. Theorem, "Semiconductor detector," pp. 1–4, 2005.

[70] S. L. Molodtsov and A. F. Gurbich, "Simulation of the pulse pile-up effect on the pulse-height spectrum," *Nucl. Instruments Methods Phys. Res. Sect. B Beam Interact. with Mater. Atoms*, vol. 267, no. 20, pp. 3484–3487, Oct. 2009.

[71] G. Amsel, E. Girard, G. Vizkelethy, G. Battistig, Y. Girard, and E. Szilágyi, "High pulse rate and pileup handling in precision RBS," *Nucl. Instruments Methods Phys. Res. Sect. B Beam Interact. with Mater. Atoms*, vol. 64, no. 1–4, pp. 811–816, Feb. 1992.

[72] V. T. Jordanov and G. F. Knoll, "Digital synthesis of pulse shapes in real time for high

resolution radiation spectroscopy," *Nucl. Instruments Methods Phys. Res. Sect. A Accel. Spectrometers, Detect. Assoc. Equip.*, vol. 345, no. 2, pp. 337–345, Jun. 1994.

[73] Q. Liu, C.-X. Liu, C. Xu, X.-L. Qi, and S.-C. Zhang, "Magnetic Impurities on the Surface of a Topological Insulator," *Phys. Rev. Lett.*, vol. 102, no. 15, p. 156603, Apr. 2009.

[74] Z. Wang, T. Lin, P. Wei, X. Liu, R. Dumas, K. Liu, and J. Shi, "Tuning carrier type and density in Bi[sub 2]Se[sub 3] by Ca-doping," *Appl. Phys. Lett.*, vol. 97, no. 4, p. 42112, 2010.

[75] M. Eddrief, P. Atkinson, V. Etgens, and B. Jusserand, "Low-temperature Raman fingerprints for few-quintuple layer topological insulator Bi2Se3 films epitaxied on GaAs.," *Nanotechnology*, vol. 25, no. 24, p. 245701, Jun. 2014.

[76] F. Vidal, M. Eddrief, B. Rache Salles, I. Vobornik, E. Velez-Fort, G. Panaccione, and M. Marangolo, "Photon energy dependence of circular dichroism in angle-resolved photoemission spectroscopy of Bi 2 Se 3 Dirac states," *Phys. Rev. B*, vol. 88, no. 24, p. 241410, Dec. 2013.

[77] Collaboration: Authors and editors of the volumes III/17E-17F-41C, "Selenium (Se) crystal structure, lattice and cell parameters, monoclinic selenium (alpha, beta, gamma)," in *Non-Tetrahedrally Bonded Elements and Binary Compounds I*, Berlin/Heidelberg: Springer-Verlag, pp. 1–5.

[78] Collaboration: Authors and editors of the volumes III/17E-22A-41B, "Zinc telluride (ZnTe) crystal structure, lattice parameters, thermal expansion," in *II-VI and I-VII Compounds; Semimagnetic Compounds*, vol. 971, no. 1, Berlin/Heidelberg: Springer-Verlag, 1999, pp. 1–8.

[79] Collaboration: Authors and editors of the volumes III/17E-17F-41C, "Bismuth selenide (Bi2Se3) crystal structure, chemical bond, lattice parameter (including data of related compounds), pp. 4," in *Non-Tetrahedrally Bonded Elements and Binary Compounds I*, Berlin/Heidelberg: Springer-Verlag, 2001, pp. 1–4.

[80] H. M. do Nascimento Vasconcelos, M. Eddrief, Y. Zheng, D. Demaille, S. Hidki, E. Fonda, A. Novikova, J. Fujii, P. Torelli, B. R. Salles, I. Vobornik, G. Panaccione, A. J. de Oliveira, M. Marangolo, and F. Vidal, "Magnetically Hard Fe3Se4 Embedded in Bi2Se3 Topological Insulator Thin Films Grown by Molecular Beam Epitaxy," *ACS Nano*, vol. 10, no. 1, pp. 1132–1138, 2016.

[81] N. V Tarakina, S. Schreyeck, T. Borzenko, S. Grauer, C. Schumacher, G. Karczewski, C. Gould, K. Brunner, H. Buhmann, and L. W. Molenkamp, "Microstructural characterisation of Bi 2 Se 3 thin films," *J. Phys. Conf. Ser.*, vol. 471, no. 1, p. 12043, Nov. 2013.

[82] L. J. Collins-McIntyre, S. E. Harrison, P. Schönherr, N. J. Steinke, C. J. Kinane, T. R. Charlton, D. Alba-Veneroa, A. Pushp, A. J. Kellock, S. S. P. Parkin, J. S. Harris, S. Langridge, G. van der Laan, and T. Hesjedal, "Magnetic ordering in Cr-doped Bi2Se3 thin films," *Eur. Lett.*, vol. 107, no. 5, p. 57009, Sep. 2014.

[83] R. Tarasenko, M. Vališka, M. Vondráček, K. Horáková, V. Tkáč, K. Carva, P. Baláž, V. Holý, G. Springholz, V. Sechovský, and J. Honolka, "Magnetic and structural properties

of Mn-doped Bi2Se3 topological insulators," *Phys. B Condens. Matter*, vol. 481, pp. 262–267, 2016.

[84] B. Irfan and R. Chatterjee, "Magneto-transport and Kondo effect in cobalt doped Bi2Se3 topological insulators," *Appl. Phys. Lett.*, vol. 107, no. 17, p. 173108, Oct. 2015.

[85] M. A. Tumelero, R. Faccio, and A. A. Pasa, "The role of interstitial native defects in the topological insulator Bi 2 Se 3," *J. Phys. Condens. Matter*, vol. 28, no. 42, p. 425801, Oct. 2016.

[86] A. L. Fernandes Cauduro, Z. E. Fabrim, M. Ahmadpour, P. F. P. Fichtner, S. Hassing, H.-G. Rubahn, and M. Madsen, "Tuning the optoelectronic properties of amorphous MoOx films by reactive sputtering," *Appl. Phys. Lett.*, vol. 106, no. 20, p. 202101, May 2015.

[87] W. K. Chu, "Calculation of energy straggling for protons and helium ions," *Phys. Rev. A*, vol. 13, no. 6, pp. 2057–2060, Jun. 1976.

[88] Y. Guo and J. Robertson, "Origin of the high work function and high conductivity of MoO3," *Appl. Phys. Lett.*, vol. 105, no. 22, p. 222110, Dec. 2014.

[89] I. Vickridge and G. Amsel, "SPACES: A PC implementation of the stochastic theory of energy loss for narrow-resonance depth profiling," *Nucl. Instruments Methods Phys. Res. Sect. B Beam Interact. with Mater. Atoms*, vol. 45, no. 1, pp. 6–11, 1990.

[90] G. Battistig, G. Amsel, E. d'Artemare, and I. Vickridge, "A very narrow resonance in 18O(p, α)15N near 150 keV: Application to isotopic tracing. II. High resolution depth profiling of 18O," *Nucl. Instruments Methods Phys. Res. Sect. B Beam Interact. with Mater. Atoms*, vol. 66, no. 1, pp. 1–10, 1992.

[91] G. Battistig, G. Amsel, E. d'Artemare, and I. Vickridge, "A very narrow resonance in 18O(p, α)15N near 150 keV: Application to isotopic tracing: I. Resonance width measurement," *Nucl. Instruments Methods Phys. Res. Sect. B Beam Interact. with Mater. Atoms*, vol. 61, no. 4, pp. 369–376, 1991.

[92] E. J. Knystautas, "Extending the Energy Range of a 7 MV Van de Graaff Using Triply-Charged Beams: Applications to Neon and Argon Ions," *IEEE Trans. Nucl. Sci.*, vol. 26, no. 1, pp. 1470–1471, Feb. 1979.

[93] S. Kirkpatrick, C. D. Gelatt, and M. P. Vecch, "Optimization by Simulated Annealing," *Science (80-.).*, vol. 220, no. 4598, pp. 671–680, 2007.

[94] C. Jeynes, N. P. Barradas, P. K. Marriott, G. Boudreault, M. Jenkin, E. Wendler, and R. P. Webb, "Elemental thin film depth profiles by ion beam analysis using simulated annealing - a new tool," *J. Phys. D. Appl. Phys.*, vol. 36, no. 7, pp. R97–R126, Apr. 2003.

[95] N. P. Barradas, "Double scattering in grazing angle Rutherford backscattering spectra," *Nucl. Instruments Methods Phys. Res. Sect. B Beam Interact. with Mater. Atoms*, vol. 225, no. 3, pp. 318–330, Sep. 2004.

[96] N. P. Barradas, C. Jeynes, M. Jenkin, and P. K. Marriott, "Bayesian error analysis of Rutherford backscattering spectra," *Thin Solid Films*, vol. 343, pp. 31–34, 1999.

[97] K. . Sjöland, F. Munnik, and U. Wätjen, “Uncertainty budget for Ion Beam Analysis,” *Nucl. Instruments Methods Phys. Res. Sect. B Beam Interact. with Mater. Atoms*, vol. 161, pp. 275–280, 2000.

[98] J. L. Colaux and C. Jeynes, “High accuracy traceable Rutherford backscattering spectrometry of ion implanted samples,” *Anal. Methods*, vol. 6, no. 1, pp. 120–129, Dec. 2014.

[99] J. L. Colaux and C. Jeynes, “Accurate electronics calibration for particle backscattering spectrometry,” *Anal. Methods*, vol. 7, no. 7, pp. 3096–3104, Mar. 2015.

[100] J. L. Colaux, C. Jeynes, K. C. Heasman, and R. M. Gwilliam, “Certified ion implantation fluence by high accuracy RBS,” 2015.

[101] J. L. Colaux, G. Terwagne, and C. Jeynes, “On the traceably accurate voltage calibration of electrostatic accelerators,” *Nucl. Instruments Methods Phys. Res. Sect. B Beam Interact. with Mater. Atoms*, vol. 349, pp. 173–183, Apr. 2015.

[102] D. Benzeggouta and I. Vickridge, “Handbook on Best Practice for Minimising Beam Induced Damage during IBA,” no. March, 2011.

[103] W. J. Weber, D. M. Duffy, L. Thomé, and Y. Zhang, “The role of electronic energy loss in ion beam modification of materials,” *Curr. Opin. Solid State Mater. Sci.*, vol. 19, no. 1, pp. 1–11, Feb. 2015.

[104] E. Rutherford, “LXXIX. The scattering of α and β particles by matter and the structure of the atom,” *Philos. Mag. Ser. 6*, vol. 21, no. 125, pp. 669–688, May 1911.

[105] H. Geiger and E. Marsden, “On a Diffuse Reflection of the Formula-Particles,” *Proc. R. Soc. A Math. Phys. Eng. Sci.*, vol. 82, no. 557, pp. 495–500, Jul. 1909.

[106] N. Bohr, “I. On the constitution of atoms and molecules,” *Philos. Mag. Ser. 6*, vol. 26, no. 151, pp. 1–25, Jul. 1913.

[107] N. Bohr, “XXXVII. On the constitution of atoms and molecules,” *Philos. Mag. Ser. 6*, vol. 26, no. 153, pp. 476–502, Sep. 1913.

[108] N. Bohr, “LXXIII. On the constitution of atoms and molecules,” *Philos. Mag. Ser. 6*, vol. 26, no. 155, pp. 857–875, Nov. 1913.

[109] M. Rajatora, K. Väkeväinen, T. Ahlgren, E. Rauhala, J. Räisänen, and K. Rakennus, “Stopping powers of GaAs for 0.3-2.5 MeV 1H and 4He ions,” *Nucl. Instruments Methods Phys. Res. Sect. B Beam Interact. with Mater. Atoms*, vol. 119, no. 4, pp. 457–462, Dec. 1996.

Figures

Figure 1: Ion interactions with matter. 22
Figure 2: RBS ($^4He^+$ - 1500 keV incident beam at 165° scattering angle) spectra of bismuth thin film (peak between 1300-1350 keV) on silicon substrate (lower energy, up to 800 keV). 23
Figure 3: Schema elastic collision. Where $E0,1,2$ is energy, $M1,2$ mass and $v0,1,2$ velocity for the incident particle and target, while θ and ϕ are angles, in the laboratory frame..... 23
Figure 4: Three element/compound (A, B, C) thin layers on thick layer substrate target; incident and backscattered ion beam. $\Delta E = E0 - En = A, B, C$ 24
Figure 5: Example of electronic stopping power using the Bethe formula for incident high energetic $^4He^+$ in Ni [10]. 25
Figure 6: a) General RBS schema: the incident ion beam impact with the sample (target) and ions are backscattered to the detector with a frequency given by $d\sigma/d\Omega$; b) incident beam zone in target; beam surface S and x is penetrating; N is the number of atoms per unit volume..... 27
Figure 7: GaAs atomic structure a) in random configuration, b) channelled in axis <0 0 1>, c) channelled in axis <1 0 1> and d) plane [0 0 1] 28
3 Figure 8: Scattering interaction between ion and first atomic layer 29
Figure 9: Incident ion fluence distribution in the two first layers 31
Figure 10: RBS-Channelling spectrum for 2 MeV He^+ ion beam on Pt <1 1 0> axis. Striped area corresponds to the atoms in the surface [16]. 33
Figure 11: Channelling geometries a) axial channelling, where the axis z generates the linear potential in the ion M_1 and b) planar channelling, where the plane x-z generates the planar potential in M_1. 33
Figure 12: Incident ion momenta schema 34
Figure 13: Yield in function of the incident angle, $\chi(\psi)$, for 480 keV protons on W crystal along <1 0 0> axis [14] 35
Figure 14: ion beam and particle detector aligned with two different crystal axis to generate the blocking effect. 36
Figure 15: PIXE basic interaction: a) a sample atom in repose, b) incident ion (red ball and its path is the red line) removes an inner electron, c) an outer electron takes the removed electron place emitting an X-ray (yellow line) 37
Figure 16: Atomic x-rays transmission 38

Figure 17: Ion-Nucleus reaction scheme for $^{18}O(H^+,^4He^+)^{15}N$. Blue balls are neutrons and protons are yellow ones. This reaction is exothermic with a Q=3979.9 keV. 40
Figure 18: Charge induction schema. The ion creates the electron-hole pair which is instantly break through the electric field and an inducted charge is generated. The signal is amplified and converted to voltage signal through a charge sensitive preamplifier. 41
Figure 19: A Topological Insulator has an insulator behaviour in the bulk (purple) and conductive beaviour on the surfaces (yellow), the electron movement there is fixed in two direction depending on the electron spin..... 44
Figure 20: Topological insulators band structure. The bulk contribution (blue) is a trivial insulator while the Topologic Surface States (TSS) are a gapless Dirac cone (red lines) with spin-orbit locked massless Dirac fermions..... 45
Figure 21: Bi_2Se_3 atomic lattice structure 45
Figure 22: OPV layout; MoOx is the TMO working as a hole extractor for the DBP organic p-type semiconductor, BCP Bathocuproine is the electron extractor for the Fullerene C60 n-type organic semiconductor. Au and ITO are the device anode/cathode. 47
Figure 23: a) p-n junction schema. b) Reverse bias applied in p-n junction. 49
Figure 24: Electron-hole generation through the ion path due to ionising excitation. 50
Figure 25: Angle spread schema. θ is the backscattering angle and $\Delta\theta = \theta f - \theta i$ is the detector window width. 52
Figure 26: SegDet appearance. a) SegDet and housing schema, b) SegDet and print circuit picture, c) SegDet completely mounted 53
Figure 27: Guard Ring and interstrip region microscopic view (left) and a cross section schema (right)..... 54
Figure 28: Segment organisation within SegDet..... 68
Figure 29: Segment energy resolution for several segment and guard ring configurations in the SegDet using a pulse generator and -40 V bias voltage. The non-shown segments were not available due to broken gold wire connection. 69
Figure 30: spectra taken simultaneously from four segments of the SegDet. Two from the centre segments (left, red and black) and two far away between each other (right, blue and orange). RBS done using $^4He^+$ at 800 keV on SiO_2 on C substrate. 70
Figure 31: Bi (5.53 TFU) on Si substrate spectrum with a classical single PIPS detector (25mm²) for 4 MeV $^4He^{2+}$ ion beam. The channels up to 90 are HH^+ beam contribution at 2 MeV which is mixed with $^4He^{2+}$. 71

Figure 32: $Au_{0.78}Ag_{0.15}Cu_{0.07}$ (3.77 TFU) on C substrate spectra from SegDet, segment 5 on top and 12 on bottom, for 4 MeV $^4He^{2+}$ ion beam. 72
Figure 33: RBS and annular segmented detector schema. 73
Figure 34: On the top-left is the annular detector design. The detector active area is blue and the detector mounting boards with copper signal paths are grey. On the top-right is a detector section on the PCB. On the bottom is shown the proposed pattern for fabrication of 6 detector sectors in a 77.6 x 39.5 mm silicon wafer 74
Figure 35: Interstrip schema: guard ring and passivated zone. Detector active areas are in left and right sides..... 74
Figure 36: On the top-left, PCB front side where are the pad-hole connections in the insulator part (grey) – with geometrical dimensions – and cooper covered for the back detector side grounding. On the top-right, PCB back side with a common ground connection. On the bottom, Contact pad-hole schema for detector output signal, input guard ring voltage and detector back side grounding connection. 76
Figure 37: Data acquisition system schema. 77
Figure 38: Preamplifier circuit. Input detector voltage, Vi, induced by the charge deposited and the output voltage, Vo, would be prepared to the shaping. Rf and Cf are the op amp positive feedback to increase de voltage and Rd is the detector bias resistor. 78
Figure 39: a) INSP-Nolam preamp board picture. b) Cremat CR-110 preamplifier..... 78
Figure 40: Analogue data acquisition system. Red lines are the signal shape after each step. The current integrator is used to measure the charge deposited, the input comes from the chamber and the output goes to A/D Convertor. 79
Figure 41: Digital acquisition system using the digitiser provided by CAEN S.p.A..... 81
Figure 42: Digital signal treatment schema..... 81
Figure 43: Signal stages during the treatment. CAEN user manual picture. 83
Figure 44: Bismuth on silicon substrate RBS spectra; black line is the full digital acquisition spectrum whereas the red line is the classical analogue one. On the left is shown the spectra overview, on the right the zoom in the Bi peak. 84
Figure 45: a) ad b) analogue and c) and d) digital RBS-channelling spectra for lightly Fe doped Bi25Se3 on GaAs with a capping layer of ZnSe..... 85
Figure 46: Disorder evolution as a fluence function for the Bi and Se peak compared between the two acquisition systems..... 85
Figure 47: Samples layout schema..... 87
Figure 48: 2000 keV $^4He^+$ RBS spectra for TI samples with Au capping layer. 95

Figure 49: 2000 keV $^4He^+$ beam PIXE spectra for Sample 3. 96
Figure 50: On the top-left, the atomic structure of Bi_2Se_3 when it is aligned in <0 0 1> with rhonboedal geometry ($a = b = 4.1$ Å). On the top-right, a pseudo-random atomic structure. On the bottom the (0 1 0) plane with the Bi_2Se_3 atomic structure, composed by three positions (A, B and C) that needs series of 3QL ($c = 28.6$ Å) for the complete description. 98
Figure 51: a) Sample 8 and 1 RBS spectra ($^4He^+$ at 2000 keV and 165° backscattering angle) in random configurations. b) and c) random and channelling spectra for Sample 1 and 8 respectively. 99
Figure 52: Sample 1 and 9 channelling spectra with different zones identified. 100
Figure 53: On the left the spectra for two consecutives segments (S6 and S10) and the signal taken by in the GR. On the right the Sample 1 spectra comparison between a single detector and the Segment 9 from the SegDet both at 146°. 102
Figure 54: Comaprison between the single detector at wo different angles with their equivalent segment angle in the SegDet (S15 and S9) 102
Figure 55: 2 MeV 4He+ spectra in channelling and (pseudo)random configuration from Segment 7 of SegDet in Sample 5. 103
Figure 56: χ in function of the incident angle for the Bi signal. 104
Figure 57: Sample 2.1 (top) and 2.4 (bottom) – just clean and ^{18}O treated – normalised spectra for segments S4, S8 and S14 (middle and outer avaible detector segments) 111
Figure 58: Sample 4.1 spectra for all the available segments. They are organised from the bigger backscattering angle (S16 at 164.8°) to the smallest (S8 at 146.7°) 112
Figure 59: Sample 1.2 (top) and 1.3 (bottom) spectra corresponding to S4 (black dots-lines) and the fitting results given by NDF (red dots-lines). 113
Figure 60: Depth profile for the Sample 2.3, where the black line is the diffusion pattern for the ^{18}O incorporated during the $^{18}O_2$ thermal treatments. 116
Figure 61: On the top the fluence vs time stamp. On the bottom the current evolution with the fluence. 117
Figure 62: RBS spectrum from the SegDet (S2) on the Sample 5 using 2 MeV $^4He^+$ ions after $62.1 \cdot 10^3$ nm^{-2} (10 μC in 1 mm^2 beam spot) 117
Figure 63: a) Number of C atoms evolution as a fluence fuction; b) RBS spectra from S4 in the SegDet for Sample 5 for the first and last $4 \cdot 10^3$ nm^{-2} ion fluence. 118
Figure 64: Sample 6 after being irradiated. Point A at $0.6 \cdot 10^3$ nm^{-2} (0.1 μC); B at at $1.2 \cdot 10^3$ nm^{-2} (0.2 μC), both with less than 10 nA beam current; the remaining points were irradiated with

25-30 nA, point C at at $0.6 \cdot 10^3$ nm^{-2} (0.2 μC), D at at $1.2 \cdot 10^3$ nm^{-2} (0.1 μC); E at $3.7 \cdot 10^3$ nm^{-2} (0.6 μC); F at $6.2 \cdot 10^3$ nm^{-2} (1 μC); G at $9.4 \cdot 10^3$ nm^{-2} (1.6 μC); H at $12.4 \cdot 10^3$ nm^{-2} (2 μC); I at $18.6 \cdot 10^3$ nm^{-2} (3 μC); J the fluence was not well measured but it has to be around $2 \cdot 10^3$ nm^{-2} (0.3 μC) and K at at $24.9 \cdot 10^3$ nm^{-2} (4 μC). The contrast and the brightness in the image has been increased to make it clearer (the dark traces are in reality transparent). 118
Figure 65: RBS spectra for $1.2 \cdot 10^3$ nm^{-2} fluence of the SegDet S3 (top) and simulated 2 msr PIPS detector (bottom). 119
Figure 66: Simulate Annealing schema. 126
Figure 67: Ionisation SRIM calculations. In the left $^4He^+$ ions on Si and in the right $^{123}Xe^+$ ions in Si, both at 1500 keV. 129
Figure 68: SRIM simulation for Si 100 μm thick target with incident ions a) 3000 $^4He^+$ and b) 5 $^{132}Xe^+$ at 1500 keV. The white lines are the ion trajectory while the green are the cascades. 130

Tables

Table 1: Segment specifications. R (max and min) is segment radius, r is segment width, and area is calculated for the segment from one of the 5 sectors. The sold angle (Ω) of each segment is calculated for the segment from one of the 5 sectors for a target-detector distance of 70 mm. 75

Table 2: Fe Free and Fe containing Bi_2Se_3 samples. The capping layer is represented in the first term of the 2nd column. The iron index (Fe^x) represents the nominal relative iron amount ($[Fe^1] < [Fe^2] < [Fe^3]$). 87

Table 3: Au capped samples elemental composition 97

Table 4: Disorder evaluated in the samples with different amounts of ion. 101

Table 5: TMO samples deposited by sputtering and thermally with different stoichiometry and organic DBP sample. Note that thermal deposited sample (Sample 3) has unknown stoichiometry that will be solved in the analysis. 108

Table 6: Sampling nomenclature with the treatment procedure used. 109

Table 7: NDF results summary. The element amounts are given in TFU, Thin Film Unit, where 1 TFU = 10^{15} atoms/cm². 114

This thesis presents new developments in charged particle detection and digital pulse processing for application in analysis with fast ion beams - Ion Beam Analysis (IBA). In particular a charged particle detector array, consisting of 16 independent charged particle detectors on a single silicon chip is implemented giving an overall solid angle of detection around two orders of magnitude greater than the standard charged particle detectors used in IBA. Sixteen parallel data acquisition channels are implemented using a fully digital approach for nuclear pulse processing. The overall system has an energy resolution equivalent to that of standard detectors. The large amount of data generated is handled in a self-consistent way by spectrum fitting with a simulated annealing algorithm via the NDF DataFurnace.
The large solid angles thus achieved are exploited in Rutherford Backscattering Spectrometry (RBS) and ion channelling studies of the topological insulator Bi_2Se_3 enriched in Fe, in view of studies of the thermo-electric effect, spintronics and quantum computing, and in RBS and Nuclear Reaction Analysis (NRA) studies of organic photovoltaic materials based on tetraphenyldibenzoperiflanthene (DBP) as the photo-absorber and transition metal oxide charge injectors.

Keywords: Ion Beam Analysis, charged particle detection, Topological Insulators, Organic Photovoltaic

Cette thèse présente de nouveaux développements en détection de particules chargées et traitement tout-numérique d'impulsions pour application à l'analyse avec des faisceaux d'ions rapides (IBA). Un ensemble de 16 détecteurs gravés sur une puce de Si est mis en œuvre, ce qui fournit un angle solide de détection environ 100 fois plus grande que celle des détecteurs utilisés auparavant pour l'IBA. Seize chaines d'acquisition sont également mises en œuvre avec une approche 'tout-numérique' pour le traitement des signaux issus des détecteurs. Dans son ensemble, le système ainsi développé a une résolution en énergie équivalent à celle des détecteurs standards. La considérable quantité d'information ainsi générée est traitée de manière cohérente en ajustant des spectres en énergie simulé aux spectres mesurés grâce à un algorithme de recuit simulé, avec le NDF DataFurnace.
Les grandes angles solides disponibles sont exploitées pour des études par rétrodiffusion de Rutherford (RBS) et canalisation d'ions de l'isolant topologique Bi_2Se_3 enrichi en fer en vue d'études de l'effet thermoélectrique, de spintronique ou encore la computation quantique, ainsi que pour des études par RBS et analyse par réactions nucléaires (NRA) de matériaux pour la photovoltaïque organique, basés sur tetraphenyldibenzoperiflanthene (DBP) comme photo-absorbant avec oxydes de métaux de transition pour injection de charge.

Mots-clés : Analyse par Faisceaux d'Ions, Détection de Particules Chargés, Isolants Topologiques, Photovoltaïque Organique